University of Tennessee, Knoxville

TRACE: Tennessee Research and Creative Exchange

Doctoral Dissertations

Graduate School

5-2017

Modulation of Cell Behaviors on Photo-crosslinked Polymer Networks and Polymer Spherulites

Jinbo Dou
University of Tennessee, Knoxville, jdou@vols.utk.edu

Follow this and additional works at: https://trace.tennessee.edu/utk_graddiss

Part of the Polymer and Organic Materials Commons

Recommended Citation

Dou, Jinbo, "Modulation of Cell Behaviors on Photo-crosslinked Polymer Networks and Polymer Spherulites. " PhD diss., University of Tennessee, 2017.
https://trace.tennessee.edu/utk_graddiss/4457

This Dissertation is brought to you for free and open access by the Graduate School at TRACE: Tennessee Research and Creative Exchange. It has been accepted for inclusion in Doctoral Dissertations by an authorized administrator of TRACE: Tennessee Research and Creative Exchange. For more information, please contact trace@utk.edu.

To the Graduate Council:

I am submitting herewith a dissertation written by Jinbo Dou entitled "Modulation of Cell Behaviors on Photo-crosslinked Polymer Networks and Polymer Spherulites." I have examined the final electronic copy of this dissertation for form and content and recommend that it be accepted in partial fulfillment of the requirements for the degree of Doctor of Philosophy, with a major in Materials Science and Engineering.

Shanfeng Wang, Major Professor

We have read this dissertation and recommend its acceptance:

Roberto S. Benson, Peter K. Liaw, Mei-zhen Cui

Accepted for the Council:

Dixie L. Thompson

Vice Provost and Dean of the Graduate School

(Original signatures are on file with official student records.)

Modulation of Cell Behaviors on Photo-crosslinked Polymer Networks and Polymer Spherulites

A Dissertation Presented for the

Doctor of Philosophy

Degree

The University of Tennessee, Knoxville

Jinbo Dou

May 2017

Copyright © 2017 by Jinbo Dou

All rights reserved.

Acknowledgements

I would like to express my sincere appreciation and thanks to my advisor, Dr. Shanfeng Wang. It is a great honor for me to work with him and have him as my advisor. He is professional and knowledgeable, and one of the top scientists in polymer science. His advices and help on both projects design and manuscripts preparation in these years have been invaluable.

I would also like to thank my committee members, Dr. Benson, Dr. Liaw, and Dr. Cui for reviewing my thesis and serving on my committee. I also thank all the professors who taught me in the engineering field, including Dr. Wang, Dr. Sickafus, Dr. Pharr, Dr. Morris, Dr. Mandrus, and Dr. Bhat. I also thank the professors who helped me when I was the teaching assistant, including Dr. Wang, Dr. Liaw, Dr. Rawn, Dr. Zhuravleva, and Dr. Meek. I also thank Dr. Keppens, Dr. Benson, and Dr. Sickafus for their help.

I would like to thank my colleagues: Dr. Lei Cai, Dr. Xiaohui Wu, Dr. Xifeng Liu, Charles Sprague, Dr. Anchao Feng, Qingya Zeng, Hui Zou, Tianyu Li, and Sirui Ge. I also thank my coworkers for their collaboration, discussion, and assistance to my dissertation: Dr. Xifeng Liu (Chapter 2 and 3), Timothy Mickens (Chapter 3), Qingya Zeng (Chapter 4), Hannah Simpson (Chapter 6 and 9), Hannah South (Chapter 7), Juliana de Menezes (Chapter 8), Codi Ferree (Chapter 9), and Cody Legg (Chapter 9).

I am grateful to our collaborators Dr. Jingyan Dong, and Dr. Li Zhang at North Carolina State University, and Dr. Cui from the Department of Biomedical and Diagnostic Sciences at UT. I would also like to thank Dr. Chao Pu, Dr. Haoyan Diao, Luis Casillas, Dr. Caitlin Taylor, Dr. Shuangcheng Tang, and Dr. Lu Huang for their help in my research, and all the other friends who give me support and help. I would also like to thank Dr. Bin Zhao from Department of Chemistry

at UT, Dr. John Dunlap of Microscopy Facility at UT, Dr. Maulik Patel, Chris Wettland, and all the staff of MSE department for their valuable help.

Finally, I give my greatest appreciation to my parents for their support and love.

Abstract

This dissertation presents novel biodegradable and photo-crosslinkable poly(ε-caprolactone) acrylates (PCLAs) to achieve polymer networks with controllable surface chemistry, stiffness, and topographical features, as well as crystallization-induced PCL, poly(3-hydroxybutyrate) (PHB) and poly(L-lactic acid) (PLLA) surfaces for investigating cell-material interactions. Chapter I reviews the recent progress of injectable polymeric biomaterials in the last decade for various tissue engineering applications. Chapter II investigates the variation of thermal and mechanical properties of PCL triacrylate (PCLTA) networks with different crosslinking time, and further studies the smooth muscle cell (SMC) responses to these networks. Chapter III studies the SMC responses to hydrolyzed PCLTA/methoxyl polyethylene glycol monoacrylate (mPEGA) networks, and the *in vitro* degradation of the crosslinked PCLTA and PCLTA/mPEGA networks. Chapter IV introduces the synthesis, and characterization of four-arm and six-arm PCLAs, and further demonstrates SMC responses to tunable stiffness of the photo-crosslinked PCLA networks. Chapter V investigates the roles of microgroove dimensions in promoting SMC functions on photo-crosslinked PCLA substrates, and further reveals SMC migration can be altered by microgroove dimensions. Chapter VI presents a facile method to synthesize photo-crosslinkable polyhedral oligomeric silsesquioxane (POSS)-PCL diacrylate (POSS-PCLDA) elastomers using POSS as initiator for potential applications in cardiovascular and peripheral nerve regeneration. The crystallinity of PCL network was compressed by POSS molecule, and the amorphous POSS-PCLDA networks were elastomeric at physiological temperature. Chapter VII describes the epitaxial crystallization and surface segregation in modulating pre-osteoblastic cell behavior on PCL/PEG substrates. PCL/PEG films had different morphologies on different substrates, and introduced different cell behaviors. Chapter VIII investigates the SMC responses to PHB

spherulites. Instead of the banded structures, the cracks on the PHB films were found to be more important in regulating cell alignment. Chapter IX presents the role of PLLA crystallization in regulation cell behaviors. Rougher surfaces of PLLA were found to be worse in supporting cell attachment and proliferation.

Table of Contents

Chapter I. Introduction 1
1.1 Introduction of injectable polymeric systems 2
1.2 Materials 3
1.2.1 PPF-based injectable polymeric systems. 3
1.2.2 PCL-based injectable polymeric systems. 9
1.2.3 PEG-based injectable polymeric systems. 12
1.2.4 Injectable polymer composites/hybrid systems. 13
1.3 Fabrication of structures 17
1.3.1 Surface patterns. 17
1.3.2 3D structures. 19
1.4 Applications 22
1.4.1 In vitro cell regulation. 22
1.4.2 In vivo animal implantation. 27
1.5 Conclusions and perspectives 28
References 30
Chapter II. Smooth Muscle Cell Responses to Poly(ε-caprolactone) Triacrylate Networks with Different Crosslinking Time 33
Abstract 34
2.1 Introduction 35
2.2 Materials and Methods 36
2.2.1 Photo-crosslinking and characterization of PCLTAs. 36
2.2.2 In vitro SMC attachment and proliferation. 38
2.2.3 Characterization of focal adhesions (FAs). 39
2.2.4 Statistical analysis. 40
2.3 Results and Discussion 40
2.3.1 Gel fraction and swelling ratio. 40
2.3.2 Thermal and mechanical properties. 42
2.3.3 In vitro SMC attachment and proliferation. 47
2.3.4 Focal adhesions. 50
2.3.5 Further discussion. 50
2.4 Conclusions 54
References 55
Chapter III. Smooth Muscle Cell Responses to Hydrolyzed Poly(ε-caprolactone) Triacrylate/Methoxyl Polyethylene Glycol Monoacrylate Networks 57
Abstract 58
3.1 Introduction 59
3.2 Materials and Methods 61
3.2.1 Photo-crosslinking and characterization of PCLTA and mPEGA/PCLTA networks. . 61
3.2.2 In vitro SMC attachment and proliferation. 63

3.2.3 Characterization of focal adhesions (FAs). 64
3.2.4 In vitro degradation. 64
3.2.5 Statistical analysis. 65
3.3 Results and Discussion 65
3.3.1 Thermal and mechanical properties. 65
3.3.2 In vitro SMC attachment and proliferation. 67
3.3.3 Focal adhesions. 70
3.3.4 In vitro degradation. 73
3.3.5 Further discussion. 75
3.4 Conclusions 78
References 79
Chapter IV. Four-arm and Six-arm Poly(ε-caprolactone) Acrylates: Synthesis, Characterization, and Smooth Muscle Cells Responses to Tunable Stiffness 83
Abstract 84
4.1 Introduction 85
4.2 Materials and Methods 87
4.2.1 Synthesis. 87
4.2.2 Photo-crosslinking of PCLAs. 89
4.2.3 Material characterization. 89
4.2.4 Protein adsorption. 90
4.2.5 In vitro SMC attachment and proliferation. 91
4.2.6 Characterization of focal adhesions. 92
4.2.7 Gene expression. 92
4.2.8 Statistical analysis. 93
4.3 Results and Discussion 93
4.3.1 Structure characterization and photo-crosslinking. 93
4.3.2 Thermal properties. 97
4.3.3 Mechanical and rheological properties. 100
4.3.4 In vitro SMC attachment and proliferation. 104
4.3.5 Focal adhesions and gene expression. 107
4.3.6 Further discussion. 112
4.4 Conclusions 113
References 115
Chapter V. Roles of Microgroove Dimensions in Promoting Smooth Muscle Cell Functions on Photo-crosslinked Poly(ε-caprolactone) Acrylate Substrates 118
Abstract 119
5.1 Introduction 120
5.2 Materials and Methods 122
5.2.1 Materials. 122
5.2.2 Photo-crosslinking of PCLA flat samples and microgrooves. 122

5.2.3 In vitro SMC attachment, proliferation and alignment. 123
5.2.4 Focal adhesions. 124
5.2.5 Gene expression..... 124
5.2.6 Single cell migration..... 125
5.2.7 Statistical analysis. 126
5.3 Results and Discussion..... 126
5.3.1 Characterization of microgrooved substrates. 126
5.3.2 In vitro SMC attachment and proliferation. 128
5.3.3 Focal adhesions and gene expression. 133
5.3.4 SMC migration. 133
5.3.5 Further discussion..... 138
5.4 Conclusions 140
References 142
Chapter VI. Biodegradable Elastomers Based on POSS-Initiated Poly(ε-caprolactone) for Cardiovascular and Peripheral Nerve Repair..... 146
Abstract 147
6.1 Introduction 149
6.2 Materials and Methods 151
6.2.1 Synthesis of POSS-PCL diols and POSS-PCLDAs. 151
6.2.2 Photo-crosslinking of POSS-PCLDAs. 153
6.2.3 Characterization of photo-crosslinked POSS-PCLDAs. 154
6.2.4 In vitro SMC attachment and proliferation. 155
6.2.5 Characterization of focal adhesions (FAs) in SMCs. 156
6.2.6 In vitro PC12 cell attachment, proliferation, and differentiation. 156
6.2.7 Statistical analysis. 157
6.3 Results and Discussion..... 157
6.3.1 Structure characterization and photo-crosslinking. 157
6.3.2 Thermal and mechanical properties..... 160
6.3.3 In vitro SMC attachment and proliferation. 168
6.3.4 Focal adhesions in SMCs. 168
6.3.5 In vitro PC12 cell attachment, proliferation, and differentiation. 171
6.3.6 Fabrication of nerve conduits. 173
6.3.7 Further discussion..... 176
6.4 Conclusions 179
References 180
Chapter VII. Epitaxial Crystallization and Surface Segregation in Modulating Pre-osteoblastic Cell Behavior on Polymer Substrates 184
Abstract 185
7.1 Introduction 186
7.2 Experimental Section 189

7.2.1 Film preparation and characterization. 189
7.2.2 Protein adsorption. 190
7.2.3 In vitro MC3T3-E1 cell attachment and proliferation. 190
7.2.4 Focal adhesions (FAs) in MC3T3-E1 cells. 191
7.2.5 Statistical analysis. 192
7.3 Results and Discussion 192
7.3.1 Surface roughness and hydrophilicity. 192
7.3.2 Protein adsorption. 196
7.3.3 Cell attachment and proliferation. 199
7.3.4 Focal adhesions. 201
7.3.5 Further discussion. 203
7.4 Conclusions 205
References 206
Chapter VIII. Smooth Muscle Cell Responses to PHB Spherulites 211
Abstract 212
8.1 Introduction 213
8.2 Experimental Section 214
8.2.1 Materials and sample preparation. 214
8.2.2 Polymer characterizations. 214
8.2.3 In vitro SMC attachment, proliferation, and alignment. 215
8.2.4 Gene expression. 216
8.2.5 Statistical analysis. 217
8.3 Results and Discussion 217
8.3.1 Characterizations of PHB spherulites. 217
8.3.2 Cell attachment, proliferation and alignment. 223
8.3.3 Gene expression of contractile markers. 228
8.3.4 Cell nuclear shape and distribution. 228
8.3.5 Further discussion. 231
8.4 Conclusions 234
References 235
Chapter IX. Cell Responses to Poly(L-lactic acid) Banded and Non-banded Spherulites 238
Abstract 239
9.1 Introduction 240
9.2 Experimental Section 242
9.2.1 Materials. 242
9.2.2 Polymer characterization. 242
9.2.3 In vitro SMC attachment and proliferation. 244
9.2.4 In vitro MC3T3-E1 cell attachment, proliferation, and alignment. 245
9.2.5 In vitro PC12 cell attachment, proliferation, and differentiation. 245
9.2.6 Statistical analysis. 246

9.3 Results and Discussion 246
9.3.1 Characterizations of PLLA spherulites. 246
9.3.2 Cellular responses to PLLA spherulites. 250
9.3.3 Cell nuclear shape and distribution. 253
9.3.4 Further discussion. 256
9.4 Conclusions 259
References 260
Chapter X. Conclusions 263
Vita 270

List of Tables

Table 2.1 Thermal properties of the crosslinked PCLTAs with different crosslinking time..... 43

Table 3.1 Thermal properties of PCLTA and mPEGA/PCLTA networks with different NaOH hydrolysis time..... 76

Table 4.1 Molecular characteristics and thermal properties of the PCL-OHs and PCLAs. 95
Table 4.2 Thermal and mechanical properties (37 °C) of crosslinked PCLAs..... 99

Table 6.1 Molecular characteristics and thermal properties of the polymers 158
Table 6.2 Thermal properties and mechanical properties of crosslinked PCLAs at 37 °C 162

Table 7.1 Surface roughnesses and water contact angles of the polymer samples..... 197

Table 9.1 Molecular weight change of the PLLA homoblends after melting and annealing process 242
Table 9.2 Band widths (μm) of the PLLA spherulites prepared under different T_cs..... 247

List of Figures

Figure 1.1 Chemical structures of the injectable and biodegradable polymers discussed in this chapter. 5
Figure 1.2 Tensile modulus of crosslinked PPF, PCLDAs, and PPF/PCLDA blends at 37 °C. Schematic changes in crosslinked PPF/PCLDA blends as the composition of PCLDA increases. Solid and dotted curves denote polymer chains in a chemical network and physical associations formed by crystalline domains, respectively. Two components of PPF and PCLDA are not differentiated from each other in the schematic chemical networks. (Adapted from [18], with copyright permission) 8
Figure 1.3 Chemical structures of photo-polymerizable mPEGA and PLL. 10
Figure 1.4 Chemical structures of three different POSS molecules used to incorporate with photo-crosslinkable polymers 14
Figure 1.5 Representative 2D photo-crosslinked PCLTA substrates with (a) honey-comb pores, (b) concentric microgrooves, and (c) parallel microgrooves, and 3D structures such as (d) a salt-leached porous bone scaffold of photo-crosslinked PPF-*co*-PCL (Φ_{PCL} = 31%), (e) a thermally crosslinked PPF/HA nanocomposite scaffold from a wax mold, and (f) a photo-crosslinked PCLF2000 neve conduit. Scale bars are 30 μm, 200 μm, 50 μm, 1 mm, 0.6 mm, and 1 mm in (a-f), respectively. (Adapted from references [2,34,35,38], with copyright permission) 18
Figure 1.6 Representative fluorescent images of MC3T3-E1 cells cultured on photo-crosslinked PCLTA10k substrates with concentric microgrooves (groove width: 7.5 μm, groove depth: 10 μm) at 4 h, stained with rhodamine-phalloidin and 4',6-diamidino-2-phenylindole (DAPI) (a), and DAPI-stained cell nuclei at day 4 on the intersection area (b) with a red dotted curve to mark the boundary between the flat margin (left) and the microgrooved area (right). Coronal section of photo-crosslinked PPF-*co*-PCL (Φ_{PCL} = 31%) scaffold implanted in a rat femoral bone defect for eight weeks, stained with methylene blue and basic fuchsin (c) and midpart cross section of a crosslinked PPF-*co*-PCL (Φ_{PCL} = 90%) single-lumen nerve conduit after 16 weeks of implantation, stained with toluidine blue (d). Scale bars are 100 μm, 100 μm, 1 mm, and 500 μm in (a-d). (Adapted from references [15,35], with copyright permission) 25

Figure 2.1 Crosslinked PCLTAs with different crosslinking time. 37
Figure 2.2 Gel fractions (a) and swelling ratios (b) of PCLTAs with different crosslinking time. Gel fractions (c) and swelling ratios (d) of 4arm and 6arm PCLAs (4arm-10k, 4arm-14k, 6arm-10k and 6arm-20k) with different crosslinking time. 41
Figure 2.3 DSC curves of crosslinked PCLTAs with different crosslinking time 44
Figure 2.4 Storage modulus G' (solid symbols), and loss modulus G'' (open symbols) vs. frequency for PCLTAs (a, 8k; b, 10k; c, 20k) with different crosslinking time at 37 °C. Viscosity (lines) vs. frequency for PCLTAs (d, 8k; e, 10k; f, 20k) with different crosslinking time at 37 °C. 46

Figure 2.5 (a) Tensile modulus of PCLTAs (8k, 10k, and 20k) with different crosslinking time. Tensile stress-strain curves of PCLTAs (b, 8k; c, 10k; d, 20k) with different crosslinking time. 46
Figure 2.6 AFM 3D height images of PCLTAs with different crosslinking time. 48
Figure 2.7 (a) Normalized SMC attachment at 4 h post seeding. (b) SMC areas at day 1 post-seeding. (c-e) SMC numbers at days 1, 2, and 4 post-seeding on the PCLTAs with different crosslinking time, respectively. *: $p < 0.05$ between the samples marked with the symbol with the corresponding data on the same PCLTA with crosslinking time of 0, 1, and 3 min. #: $p < 0.05$ between the samples marked with the symbol with the corresponding data on the same PCLTA with crosslinking time of 0, 1, 3, and 5 min. ^: $p < 0.05$ between the samples marked with the symbol. 49
Figure 2.8 SMC images at days 1, 2, and 4 post-seeding stained using RP (red) and DAPI (blue) on PCLTAs with different crosslinking time. Scale bar of 200 μm is applicable to all. 51
Figure 2.9 Characterizations of FAs in SMCs at day 1 post-seeding on PCLTAs with different crosslinking time (0, 3, and 60 min). (a) Immunofluorescence images of FAs in the cells with vinculin stained green, and F-actin stained red. Scale bar of 50 μm is applicable to all. Quantification of FAs in terms of (b) FA density, and (c) FA area. *: $p < 0.05$ between two samples marked with the same symbol. 52

Figure 3.1 Photo-crosslinking of PCLTA and mPEGA/PCLTA networks. 62
Figure 3.2 SEM images of PCLTA and mPEGA/PCLTA networks with different NaOH hydrolysis time. Scale bar of 50 μm is applicable to all. 66
Figure 3.3 Water contact angles of PCLTA and mPEGA/PCLTA networks with different NaOH hydrolysis time. 66
Figure 3.4 SMC attachment and proliferation on PCLTA and mPEGA/PCLTA networks with different NaOH hydrolysis time. (a) Normalized SMC attachment at 4 h post-seeding. (b) SMC numbers at days 1, 2, and 4 post-seeding. (c) SMC areas at day 1 post-seeding. (d) SMC circularities. *: significantly higher ($p < 0.05$) than the corresponding data on 0 h samples. #: significantly higher ($p < 0.05$) than the corresponding data on 24 h samples. ^: significantly higher ($p < 0.05$) than the corresponding data on 48 h samples. +: significantly higher ($p < 0.05$) than the corresponding data on the PCLTA network with the same NaOH hydrolysis time. 68
Figure 3.5 SMC images at days 1, 2, and 4 post-seeding stained using RP (red) and DAPI (blue) on PCLTA (a) and mPEGA/PCLTA (b) networks with different NaOH hydrolysis time. Scale bar of 200 μm is applicable to all images. 69
Figure 3.6 (a) Fluorescent images of SMC nuclei stained with DAPI on PCLTA and mPEGA/PCLTA networks with different NaOH hydrolysis time at day 1 post-seeding. (b) Average area and (c) circularity of SMC nuclei on these substrates. *: $p < 0.05$ compared to the corresponding data on 0 h samples. Scale bar of 200 μm is applicable to all, and the scale of embedded images are 70 μm. 71

Figure 3.7 Characterizations of FAs in SMCs on crosslinked PCLTA and mPEGA/PCLTA networks with different NaOH hydrolysis time at day 1 post-seeding. (a) Immunofluorescence images of FAs in the cells with vinculin stained green, and F-actin stained red. Scale bar of 50 μm is applicable to all. Quantification of FAs in terms of (b) FA density (c) FA area, and (d) FA elongation. *: $p < 0.05$ compared to the corresponding data on 0 h samples. #: $p < 0.05$ compared to the corresponding data on 24 h samples. ^: $p < 0.05$ relative to the PCLTA network with the same NaOH hydrolysis time. 72
Figure 3.8 Weight fraction of PCLTA and mPEGA/PCLTA networks with different NaOH hydrolysis time (a) and PBS hydrolysis time (b). DSC curves of PCLTA (c) and mPEGA/PCLTA (d) networks with different NaOH hydrolysis time. Water adsorption of PCLTA and mPEGA/PCLTA networks with different PBS hydrolysis time (e). 74

Figure 4.1 Synthesis of PCL-OHs and PCLAs. 88
Figure 4.2 ^{1}H NMR (300 MHz, $CDCl_3$, reference TMS) spectra of PCL-OHs and PCLAs (a, 4arm PCL-OH; b, 4arm PCLA; c, 6arm PCL-OH; d, 6arm PCLA). S = solvent. Asterisk denotes the signals due to the residue of CH_2Cl_2. 96
Figure 4.3 DSC curves of 4arm (a, c) and 6arm (b, d) PCL-OHs, PCLAs, and crosslinked PCLAs. 98
Figure 4.4 Storage modulus G' (solid symbols), and loss modulus G'' (open symbols) vs. frequency for crosslinked PCLAs at 37 °C (a, 4arm PCLA; c, 6arm PCLA) and 60 °C (b, 4arm PCLA; d, 6arm PCLA). Viscosity (lines) vs. frequency for crosslinked PCLAs at 37 °C (e, 4arm PCLA; f, 6arm PCLA) and 60 °C (g, 4arm PCLA; h, 6arm PCLA). (i) Temperature dependence of zero-shear viscosity for PCLAs. 101
Figure 4.5 Tensile stress-strain curves of crosslinked PCLAs at 37 °C. (a) 4-arm and (b) 6-arm. 103
Figure 4.6 (a) AFM 3D height images of compressed crosslinked PCLA disks. (b) Water contact angles and protein adsorptions on crosslinked PCLA disks. 105
Figure 4.7 (a) Normalized SMC attachment at 4 h post-seeding, (b) SMC numbers at days 1, 2, and 4 post-seeding on the crosslinked PCLA disks, and (c) SMC areas at day 1 post-seeding. *, #: $p < 0.05$ between any two samples marked with the same symbol. 106
Figure 4.8 SMC images at days 1, 2, and 4 post-seeding stained using RP (red) and DAPI (blue). 108
Figure 4.9 (a) Confocal microscope images of SMC filaments and vinculin antibody stained focal adhesions at day 1 post-seeding. (b) FA density, and area. *: $p < 0.05$ between any two samples marked with the same symbol. 109
Figure 4.10 Gene expression levels of (a) smoothlin, (b) calponin, (c) transgelin, and (d) SM-MHC relative to GAPDH in SMCs at day 4 post-seeding on crosslinked PCLA disks. *: $p < 0.05$ between any two samples marked with the same symbol. 111

Figure 5.1 SEM images of the microgrooves with widths of 5 and 15 μm and depths of 1 and 12 μm on crosslinked 4arm-25k PCLA. Scale bar of 100 μm is applicable to a, b, c and d. Scale bar of 40 μm is applicable to e, f, g and h. 127
Figure 5.2 SMC numbers at 4 h, days 1, 2, and 4 post-seeding on the microgrooved PCLA disks. *: $p < 0.05$ between the samples marked with the same symbol with the corresponding data on microgrooved disks of 12 μm depth and 5 μm width at day 4 post-seeding. 129
Figure 5.3 SMCs images at days 1 and 4 post-seeding stained using RP (red) on the flat and microgrooved PCLA disks. Scale bar of 200 μm is applicable to all. 129
Figure 5.4 SMC circularity, major/minor axis ratio, area and alignment at day 1 post-seeding on the flat and microgrooved substrates of photo-crosslinked PCLA (a, 4arm-25k; b, 6arm-30k). *: $p < 0.05$ between the samples marked with the same symbol. 130
Figure 5.5 (a) Fluorescent images of SMC nuclei stained using DAPI (blue) on the microgrooved substrates of photo-crosslinked PCLA 4arm-25k. Scale bar of 200 μm is applicable to all. SMC nuclear circularities (b), and locations (c) at day 4 post-seeding on the microgrooved PCLA disks. *: $p < 0.05$ between the samples marked with the same symbol. 132
Figure 5.6 Confocal microscope images of SMC filaments and vinculin antibody stained focal adhesions. Scale bar of 50 μm is applicable to all. 134
Figure 5.7 Gene expression levels of smoothlin, calponin, SM-MHC, and transgelin relative to GAPDH in SMCs at day 4 post-seeding on the flat and microgrooved PCLA disks (a, 4arm-25k; b, 6arm-30k). *: $p < 0.05$ between the samples marked with the same symbol. $^{\#}$: $p < 0.05$ between the samples marked with the symbol and flat sample. 134
Figure 5.8 SMC migration on flat PCLA 4arm-7k and 4arm-25k substrates, and microgrooved PCLA 4arm-25k substrates, compared with at 12 h (a) and day 2 (b) post-seeding. The migration vector of cells on microgrooves after 30 min expressed as a dot. 136
Figure 5.9 SMC migration speeds on flat PCLA 4arm-7k and 4arm-25k substrates, and microgrooved PCLA 4arm-25k substrates at 12 h (a) and day 2 (b) post-seeding. *: $p < 0.05$ between the samples marked with the same symbol. 137
Figure 5.10 SMC migration directions on flat PCLA 4arm-7k and 4arm-25k substrates, and microgrooved PCLA 4arm-25k substrates at 12 h (a) and day 2 (b) post-seeding. 137

Figure 6.1 Synthesis scheme (a), and GPC curves of POSS-PCL diols (b) and POSS-PCLDAs (c). (d) ^{1}H NMR (300 MHz, $CDCl_3$, reference TMS) spectra of POSS-PCL diols and POSS-PCLDAs. S = solvent. Asterisk denotes the signals due to the residue of CH_2Cl_2 152
Figure 6.2 DSC heating (a) and cooling (b) curves of POSS-PCL diols, POSS-PCLDAs, and crosslinked POSS-PCLDAs. (c) TGA curves of crosslinked POSS-PCLDAs. 161
Figure 6.3 Storage modulus G' (solid symbols), and loss modulus G" (open symbols) vs. frequency for crosslinked POSS-PCLDAs at 37 °C (a) and 60 °C (b). Viscosity (lines) vs. frequency for crosslinked POSS-PCLDAs at 37 °C (c) and 60 °C (d). (e) Tensile stress-strain curves for crosslinked POSS-PCLDAs at 37 °C. (f) Cyclic stress–strain curve (cycle = 2) for POSS-

PCLDA (Φ_{POSS} = 34%). (g) Tensile modulus, melting temperature, and crystallinity degree change based on POSS compositions of crosslinked POSS-PCLDAs. 165
Figure 6.4 (a) Optical images of crosslinked POSS-PCLDA disks at 25, 37, and 60 °C. (b) AFM 3D height images and (c) water contact angles of compressed crosslinked POSS-PCLDA disks. 167
Figure 6.5 (a) SMCs images at days 1, 2, and 4 post-seeding stained using RP (red). Scale bar of 200 μm is applicable to all. (b) Normalized SMC attachment at 4 h post-seeding. (c) SMC numbers at days 1, 2, and 4 post-seeding on the crosslinked POSS-PCLDA disks. *: $p < 0.05$ between any two samples marked with the same symbol..... 169
Figure 6.6 (a) Confocal microscope images of SMC filaments and vinculin antibody stained focal adhesions. Scale bar of 100 μm is applicable to all. (b) FA density, FA area, and FA elongation. *, #, ^: $p < 0.05$ between the samples marked with the same symbol. 170
Figure 6.7 (a) PC12 cell images at days 1, 4, and 7 post-seeding stained using RP. Scale bar of 200 μm is applicable to all. (b) PC12 cell numbers at 12 h, days 1, 2, and 4 post-seeding on the crosslinked POSS-PCLDA disks. *: $p < 0.05$ between the sample marked with the symbol and POSS-PCLDAs (Φ_{POSS} = 30%, 32%, 34% and 36%). ^: $p < 0.05$ between the sample marked with the symbol and POSS-PCLDA (Φ_{POSS} = 30%). 172
Figure 6.8 (a) Fluorescent images of NGF-induced PC12 cell differentiation stained using RP (red) and DAPI (blue) at day 7 post-seeding. Scale bar of 200 μm is applicable to all. (b) Quantification of PC12 neurites at day 7 using the number of neurites per cell, percentage of differentiated cells, and neurite lengths. *: $p < 0.05$ between the marked samples and any other samples. ^: $p < 0.05$ between the marked samples and POSS-PCLDA (Φ_{POSS} = 10% and 20%). 174
Figure 6.9 SEM images of (a) a crosslinked POSS-PCLDA (Φ_{POSS} = 32%) conduit and (b) the cross sections. 175

Figure 7.1 Polymer films coated on different substrates 188
Figure 7.2 POM images of the spherulites on different substrates 193
Figure 7.3 AFM images of the interfaces in the PCL/PEG films on glass (a), Si (b), and PTFE (c). The scale of the images is 100 μm. Top surfaces of films on glass and Si have the height of 600 nm, bottom surfaces of films on glass and Si have the height of 400 nm. Top surfaces of films on PTFE have the height of 1 μm, bottom surfaces of films on PTFE have the height of 2 μm. (d) Surface roughness of the polymer films. *: $p < 0.05$ relative to the bottom surface of the same film. +: $p < 0.05$ relative to the bottom surfaces of 5% and 10% films on same substrates. #: $p < 0.05$ relative to the Si counterparts. ^: $p < 0.05$ relative to the glass and Si counterparts..... 195
Figure 7.4 (a) Water contact angles of the polymer films. *: $p < 0.05$ relative to the bottom surface of the same film. +: $p < 0.05$ relative to the top or bottom surfaces of 5% and 10% films on same substrates. ^: $p < 0.05$ relative to the glass and Si counterparts. (b) Protein adsorptions of the polymer films. *: $p < 0.05$ relative to the 0% top surface, 5% and 10% bottom surfaces on

same substrates. #: p < 0.05 between any two samples marked with the same symbol. ^: p < 0.05 relative to the glass and Si counterparts except the 0% top. 198
Figure 7.5 (a) Fluorescent images of MC3T3-E1 cells stained with RP (red) and DAPI (blue) on the PCL/PEG films at day 2 post-seeding. Scale bar of 200 μm is applicable to all. (b) Normalized MC3T3-E1 cell attachment at 4 h post-seeding on the PCL/PEG films. (c) MC3T3-E1 cell proliferation indicated by cell numbers at days 1, 2, and 4 post-seeding on the PCL/PEG films. (d) MC3T3-E1 cell areas at day 1 post-seeding on PCL/PEG films. *: p < 0.05 relative to the bottom surface of the same film. +: p < 0.05 between two samples marked with the same symbol. ^: p < 0.05 relative to the PTFE counterparts. 200
Figure 7.6 Confocal microscope images of MC3T3-E1 cell filaments and vinculin antibody stained focal adhesions, on the surfaces of the PCL/PEG films crystallized on the (a) glass, (b) Si, and (c) PTFE substrates. Scale bar of 50 μm is applicable to all. (d-f) FA density, FA area, and FA elongation of the MC3T3-E1 cell of a-c, respectively. *: p < 0.05 relative to the bottom surface of the same film. ^: p < 0.05 relative to the top or bottom surfaces of 0% films on same substrates. +: p < 0.05 relative to the bottom surface of 5% films on same substrates. 202

Figure 8.1 (a) DSC curves of PHB crystallized at different conditions. (b-h) POM images of the PHB spherulites crystallized with different conditions, T_c= b: 45 °C; c: 65 °C; d: 80 °C without circular cracks; e: 90 °C without circular cracks; g: 80 °C with circular cracks; h: 90 °C with circular cracks. Scale bar of 200 μm is applicable to all images. 219
Figure 8.2 Formation of circular cracks during the crystallization process of PHB at 80 °C for (a) 30 s, (b) 90 s, (c) 3 min, and (d) cooling down to room temperature. Scale bar of 200 μm in (d) is applicable to all images. 221
Figure 8.3 Circular cracks on PHB spherulites crystallized at 80 °C (a,c), and at 90 °C (b,d). . 221
Figure 8.4 (A) AFM images of flat PHB film, and PHB films crystallized at 45 and 65 °C. (B) AFM images of PHB films (with and without circular cracks) crystallized at 80 and 90 °C. The scales of unmarked images are 50 μm. (C) Height curves (a, b, c, and d) were corresponding to the line in the AFM images (B). 222
Figure 8.5 (a) Normalized SMC attachment at 4 h post-seeding on the PHB films crystallized at different conditions. (b) SMC proliferation indicated by cell numbers at days 1, 2, and 4 post-seeding on the PHB films crystallized at different conditions. SMC areas (c) and circularities (d) at day 1 post-seeding on PHB films. *: $p < 0.05$ between two samples marked with the same symbol..... 224
Figure 8.6 Fluorescent images of SMCs stained with RP (red) and DAPI (blue) on the PHB films at days 1, 2, and 4 post-seeding. Scale bar of 200 μm is applicable to all images. 225
Figure 8.7 SMC alignment on PHB films with and without circular cracks crystallized at 80 and 90 °C. Scale bar of 200 μm is applicable to all images. 227
Figure 8.8 SEM images of SMCs on the flat PHB films (a), PHB films without circular cracks crystallized at 80 °C (b), and PHB films with circular cracks crystallized at 80 °C (c: large scale, and d: small scale). Scale bar of 200 μm is applicable to a, c, and d..... 229

Figure 8.9 Relative gene expression levels of four contractile gene markers of SMCs on flat PHB films, and PHB films with and without circular cracks crystallized at 80 °C. *: $p < 0.05$ between two samples marked with the same symbol. 230
Figure 8.10 SMC nuclear distribution at day 2 post-seeding on banded PHB spherulites with and without circular cracks crystallized at 80 and 90 °C, respectively. Merged image of polarizing optical micrograph as the background, and fluorescent image of DAPI-stained cell nuclei. Scale bar of 100 μm is applicable to all images. 232

Figure 9.1 POM images of the PLLA spherulites prepared under different crystallized temperatures. (a) Without annealing at 160 °C. (b) Annealing at 160 °C. 247
Figure 9.2 AFM images of PLLA (Φ_{PLLA3k} = 30%) spherulites with different T_cs. (a) Height images of the spherulites. (b) Height curves corresponding to the lines in (a). Height and phase images of valley (c) and ridge (d) in (a). Scale bar of 2 μm is applicable to all images in (c) and (d). 249
Figure 9.3 (a) SMC images at days 1, 2, and 4 post-seeding stained using rhodamine-phalloidin (red) on PLLA spherulites. Scale bar of 200 μm is applicable to all. (b) Normalized SMC attachment at 4 h post-seeding. (c) SMC numbers at days 1, 2, and 4 post-seeding. *, ^: significantly smaller ($p < 0.05$) than the corresponding data on the other samples. #: $p < 0.05$ between the samples marked with the same symbol. 251
Figure 9.4 (a) MC3T3-E1 cell images at days 1, 2, and 4 post-seeding stained using RP (red) on PLLA spherulites. Scale bar of 200 μm is applicable to all. (b) Normalized MC3T3-E1 cell attachment at 4 h post-seeding. (c) MC3T3-E1 cell numbers at days 1, 2, and 4 post-seeding. *: significantly smaller ($p < 0.05$) than the corresponding data on the other samples. 252
Figure 9.5 (a) PC12 cell images at days 1, 4, and 7 post-seeding, and differentiation images at day 7 post-seeding stained using RP (red) on PLLA spherulites. Scale bar of 200 μm is applicable to all images. (b) Normalized PC12 cell attachment at 4 h post-seeding. (c) PC12 cell numbers at days 1, 4, and 7 post-seeding. (d) Quantification of PC12 neurites at day 7 post-seeding using the neurite lengths, percentage of differentiated cells, and number of neurites per cell. *: significantly lower ($p < 0.05$) than the other samples. 254
Figure 9.6 MC3T3-E1 and PC12 cell nuclear distribution at day 2 post-seeding on banded PLLA spherulites with different crystallization temperatures. Merged image of polarizing optical micrograph as the background, and fluorescent image of DAPI-stained cell nuclei. Scale bar of 150 μm is applicable to images of MC3T3-E1 cells, and 100 μm to images of PC12 cell. 255

Chapter I. Introduction

This chapter is revised based on a paper published by Jinbo Dou and Shanfeng Wang: Dou, J.; Sprague, C. H.; Chen, L.; Wang, Z.; Wang, S. Injectable polymeric biomaterials: a brief review. *Materials Technology* **2015**. *30*(sup8), B273-B282.

Reproduced with permission from [Dou, J.; Sprague, C. H.; Chen, L.; Wang, Z.; Wang, S. Injectable polymeric biomaterials: a brief review. *Materials Technology* **2015**. *30*(sup8), B273-B282.] Copyright Taylor & Francis.

1.1 Introduction of injectable polymeric systems

Polymeric biomaterials have emerged in the field of regenerative medicine to improve patients' life quality and alleviate the need of highly invasive surgical procedures. Injectable biomaterials offer exceptional healing benefits for patients suffering from diseased tissues or traumatic injuries. Advantages of using injectable polymeric biomaterials include their tunable physicochemical and topographical properties, injectability, which means that the system is a liquid above its softening point and can be used as an injectable matrix and then is able to harden *in situ* to fill irregularly shaped defects, and manufacturability into various structures for diverse tissue engineering applications [1-5]. In addition to physical gels that are prepared using non-covalent bonding, injectable polymeric biomaterials can be cured via photo-initiation, heat, or redox process. These injectable polymers are mostly biodegradable in order to enhance tissue integration and allow for viable substitutes for autografts and allografts [1,6-9].

Here I review a series of injectable polymeric biomaterials reported by Dr. Shanfeng Wang and his co-workers in the last decade for various tissue engineering applications. These injectable and biodegradable polymeric systems include homo-polymers, copolymers, and polymer blends developed on the basis of poly(propylene fumarate) (PPF), poly(ε-caprolactone) (PCL), and

poly(ethylene glycol) (PEG), and their composites with hydroxyapatite (HA) nanoparticles or polyhedral oligomeric silsesquioxane (POSS) nanocages. First, I will discuss their synthesis, structures, and physicochemical properties. Then I will discuss different methods of fabricating these injectable polymeric biomaterials into two-dimensional (2D) substrates with surface patterns such as parallel/concentric microgrooves and honey-comb pores, and three-dimensional (3D) structures such as porous bone scaffolds and nerve conduits. At last, the applications of these injectable polymeric biomaterials will be elaborated in terms of both *in vitro* regulation of cellular responses and *in vivo* tissue regeneration.

1.2 Materials

1.2.1 PPF-based injectable polymeric systems.

PPF [10-13]. PPF is an injectable, photo-crosslinkable, and biodegradable linear unsaturated polyester developed for orthopedic applications to replace clinically used non-degradable poly(methyl methacrylate) (PMMA)-based bone cement [10-13]. PPF has unique handling characteristics as it can be injected together with diluents such as its own monomer, diethyl fumarate (DEF), and crosslinked by ultraviolet (UV) light or thermal initiation to fill bone defects or fabricate 3D porous scaffolds with controllable pore size, porosity, and geometry [4,5].

As demonstrated in Figure 1.1, PPF has one fumarate segment in the repeating unit and can be modified or crosslinked through this carbon-carbon double bond. PPF is normally synthesized through a two-step polycondensation between DEF and 1,2-propane diol in presence of $ZnCl_2$ as the catalyst and hydroquinone as the crosslinking inhibitor at temperatures of 130-160 °C with assistance of vacuum. The molecular weight of PPF can be controlled by using different reaction times [12]. PPF is an amorphous polymer with the glass transition temperatures (T_g) of -30-30 °C

in the weight-average molecular weight (M_w) range of 1110-17900 g/mol and a strong molecular weight dependence exists when the number-average molecular weight (M_n) was lower than 5000 g/mol [12]. A variety of macroscopic physical properties and microscopic chain dimensions for both PPF melts with molecular weights in that range and solutions in DEF or tetrahydrofuran (THF) have been obtained and correlated with the molecular weight, which are very informative for practical uses of PPF [12]. Based on the M_n dependence of T_g, the T_g for the infinite molecular weight (T_g^{∞}) was calculated to be 31.9 °C for PPF, which is between room temperature and body temperature (37 °C), suggesting that the attempts to increase the molecular weight of PPF may not be beneficial because fabrication of force-bearing PPF scaffolds still requires crosslinking [12]. The on-set thermal degradation temperature (T_d) and density (ρ) of PPF were also found to increase with M_n but the dependence was much weaker [12]. The master curves of storage modulus (G') and loss modulus (G'') as functions of frequency (ω) showed that the PPF samples were unentangled even at the M_w of 17900 g/mol [12]. The zero-shear melt viscosity (η_0) of PPF also strongly depended on the molecular weight and the temperature dependence of η_0 was stronger at a higher molecular weight, which was attributed to the variance in T_g [12].

PPF-*co*-PCL [14,15]. To achieve polymeric biomaterials with a wide range of controllable physicochemical properties for diverse tissue engineering applications, a series of injectable, crosslinkable, and biodegradable multi-block PPF-*co*-PCL copolymers with PCL weight compositions (Φ_{PCL}) of 29-90% (Figure 1.1) have been synthesized via polycondensation of oligomeric PPF with PCL diols.[14] After introduction of more flexible PCL segments with a lower T_g of -60 °C, the copolymers had much lower T_g values, higher chain flexibility, and faster relaxation than those of PPF and these physicochemical characteristics were efficiently modulated

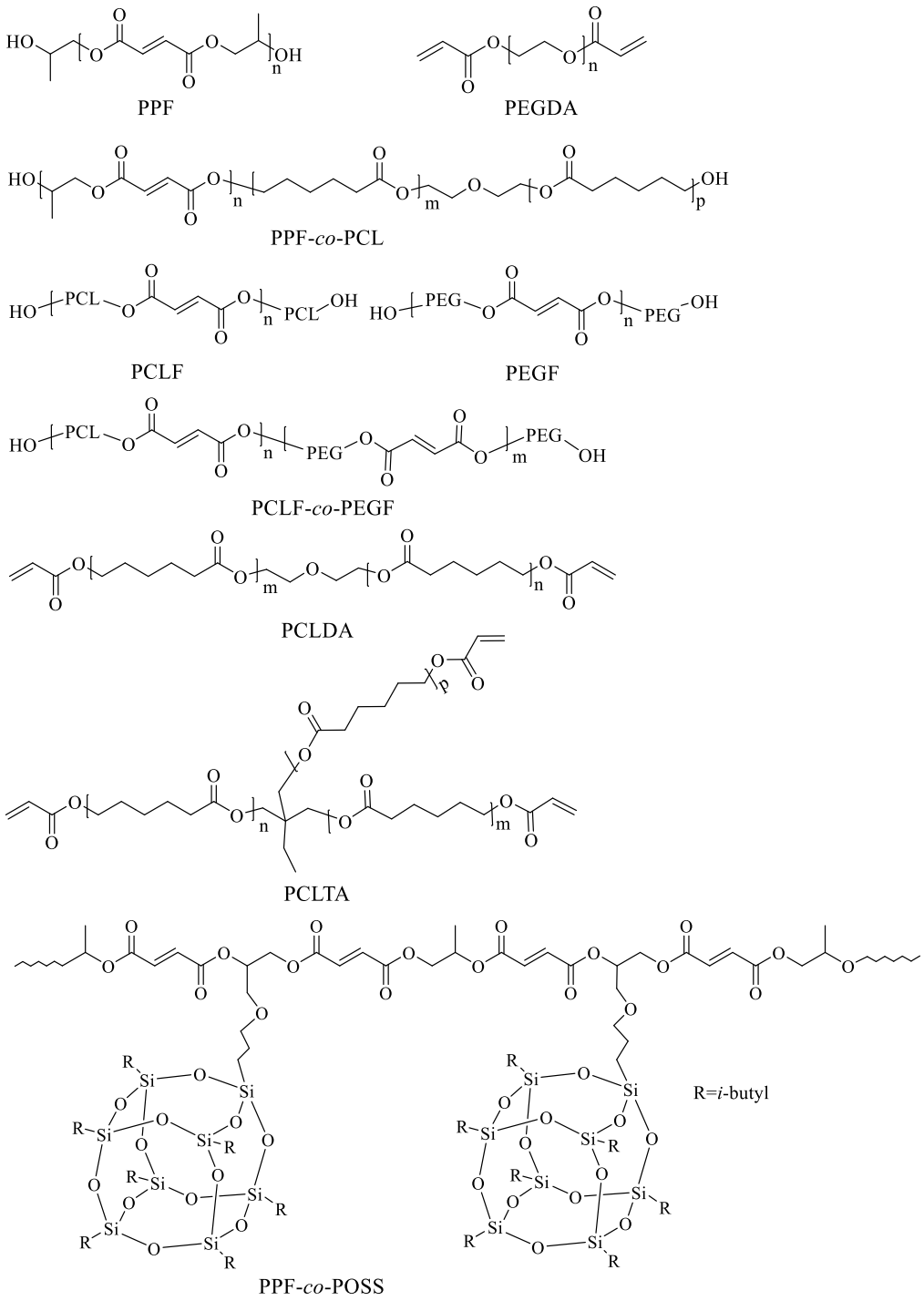

Figure 1.1 Chemical structures of the injectable and biodegradable polymers discussed in this chapter.

by using Φ_{PCL} [14]. At a high Φ_{PCL} of 90%, the copolymer was semi-crystalline and formed banded spherulites at room temperature [14]. For PPF-*co*-PCL copolymers, semi-crystalline PCL blocks were covalently linked in the backbone. Thus after crosslinking, the crystallinity was significantly suppressed and only crosslinked PPF-*co*-PCL (Φ_{PCL} = 90%) was still crystalline at room temperature. The swelling ratios of crosslinked PPF-*co*-PCLs in methylene chloride (CH_2Cl_2) and ethanol progressively increased with increasing Φ_{PCL} while little swelling was observed in water [15]. The thermal and mechanical properties of crosslinked PPF-*co*-PCLs were also efficiently regulated by Φ_{PCL}, and thus the stiffer networks were used for assisting bone regeneration while the softer networks were for peripheral nerve regeneration [15].

PPF/PCL blends [16]. To investigate the role of crosslinks in affecting mechanical and thermal properties at both room temperature and 37 °C, PPF (M_n = 2000 g/mol, M_w = 2800 g/mol) with a T_g of -0.2 °C was blended with a high-molecular-weight PCL (M_n = 98000 g/mol, M_w = 144000 g/mol) with a T_g of ~-60 °C and a T_m of ~55 °C. Before crosslinking, amorphous PPF softened PCL and the elastic modulus (*E*) decreased from 388 ± 24 MPa for the PCL to 38 ± 2.6 MPa for the blend with ϕ_{PPF} of 75% at room temperature. After crosslinking, although the crosslinks suppressed the crystallinity of PCL, the PPF network significantly strengthened the physical network formed among the PCL crystalline domains. A wide range of mechanical properties was thus achieved from a flexible material for uncrosslinked PPF/PCL to a stronger and stiffer material with *E* of 848 ± 62 MPa for crosslinked PPF/PCL with ϕ_{PPF} of 75% at room temperature. Meanwhile, surface segregation effect was evident as the more mobile component PPF in the uncrosslinked blends appeared more on the top surface to affect surface chemistry, topography, and cellular responses.

PPF/PCLF networks [17]. To achieve controllable thermal, rheological, and mechanical

properties, PPF (M_n = 3460 g/mol, M_w of 7910 g/mol) was blended and photo-crosslinked with PCL fumarate (PCLF, Figure 1.1), which was synthesized via condensation between PCL diol with a nominal molecular weight of 530 g/mol and fumaryl chloride (see Section 1.2.2), at various compositions. Blending with amorphous PPF could suppress the crystallinity of the PCLF completely when ϕ_{PPF} was 50% and photo-crosslinking further constrained crystallization and resulted in amorphous networks for all the samples including crosslinked PCLF. The crosslinked PPF/PCLF samples showed a progressive physical change from a flexible and weak material for crosslinked PCLF to a stiff but brittle material for crosslinked PPF. The blending method was much simpler than copolymerization of PPF-*co*-PCLs and the composition range could be wider.

PPF/PCLDA networks [18]. In PPF/PCLF networks discussed above, only one PCLF (i.e., PCLF530) was used and all the networks were amorphous. PCL diacrylates (PCLDAs, Figure 1.1) synthesized from PCL diols with three different nominal molecular weights of 530, 1250, and 2000 g/mol (see Section 1.2.2) were photo-crosslinked with PPF to form networks with simultaneously controllable crosslinking density and crystallinity, through which the mechanical properties could be tuned efficiently over a wide range (Figure 1.2). When semi-crystalline PCLDA1250 or 2000 were crosslinked with PPF, crystallinity and crosslinking density collectively regulated the mechanical properties of the networks and a non-monotonic or parabolic dependence of E on the blend composition was observed with a minimum at the PCLDA composition of 70% or 80%, respectively.

PPF/mPEGA networks [19]. Hydrophobicity is one limitation for crosslinked PPF in its applications because the wettability of medical devices is critical for allowing surrounding body fluids to penetrate and supply nutrients to cells and tissue that grow inside. Photo-crosslinked PPF has a water contact angle of ~90° at room temperature [17]. The bulk and surface properties of

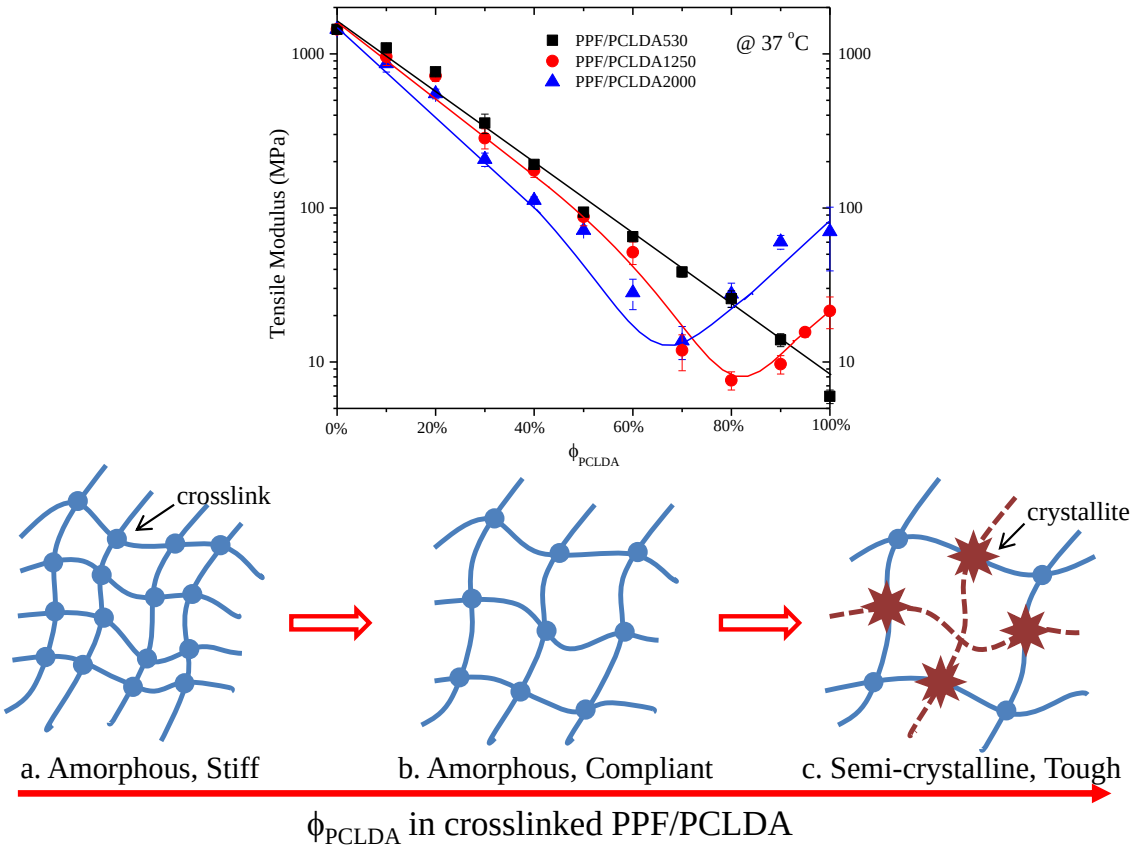

Figure 1.2 Tensile modulus of crosslinked PPF, PCLDAs, and PPF/PCLDA blends at 37 °C. Schematic changes in crosslinked PPF/PCLDA blends as the composition of PCLDA increases. Solid and dotted curves denote polymer chains in a chemical network and physical associations formed by crystalline domains, respectively. Two components of PPF and PCLDA are not differentiated from each other in the schematic chemical networks. (Adapted from [18], with copyright permission)

crosslinked PPF were modified by photo-crosslinking the blends of methoxyl PEG monoacrylate (mPEGA, Figure 1.3) and PPF at various weight compositions of mPEGA (Φ_m). Unlike PPF crosslinked with PEG dimethacrylate (PEGDMA) [20], the PEG dangling chains tethered in the PPF network did not swell in water but greatly increased surface hydrophilicity or wettability. Meanwhile, the tensile and compressive moduli, frictional coefficient, and protein adsorption decreased continuously with increasing Φ_m because of the reduced crosslinking density, surface hydration, and repulsion by the tethered PEG chains.

1.2.2 PCL-based injectable polymeric systems.

PCL is a widely used biodegradable polyester that has shown promising results in making suitable scaffolds for bone, cardiovascular, epithelial, and nerve repair [5]. PCL can be modified to enhance its physical properties and biocompatibility [3-5]. Injectable polymers have been developed by converting the hydroxyl end groups in PCL to fumarate or acrylate groups and these polymers have been further incorporated with POSS nanocages or HA nanoparticles [3-5,21-25].

PCLF [3,4,21]**.** PCLFs were synthesized from PCL diols with different molecular weights (and also different crystallinities and T_m) to achieve injectable and biodegradable biomaterials with mechanical properties that can be controlled through crystallinity and crosslinking. At first, trimethylamine (TEA) was used as the proton scavenger to remove the byproduct hydrochloride (HCl) in synthesizing PCLF but the resulted PCLF had a dark color. Then potassium carbonate (K_2CO_3) was used instead and the K_2CO_3 method resulted in clean PCLFs that were more suitable for photo-crosslinking. This method is also more convenient and less time-consuming in synthesis and purification. In addition, the use of K_2CO_3 can avoid colored, water-soluble, cytotoxic complexes formed between TEA and unsaturated acyl chlorides or anhydrides, which were the reason why the synthesized polymer was colorized. The complexes demonstrated the cytotoxicity

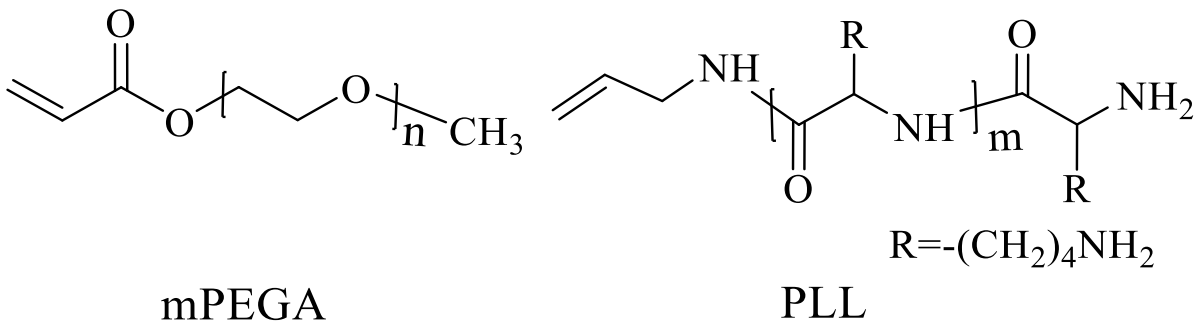

Figure 1.3 Chemical structures of photo-polymerizable mPEGA and PLL.

even at a very low concentration (0.01 g/L in culture medium) for human embryonic kidney 293 (HEK293) cells [26]. PCLF is able to self-crosslink among the unsaturated fumarate segments at 37 °C and hardens physically through crystallization when the temperature is lower than its T_m. The amount of photo-initiator bis(2,4,6-trimethyl benzoyl) phosphine oxide (BAPO) used in photo-crosslinking PCLF was found to affect the thermal, rheological, and mechanical properties of the PCLF networks by controlling both crosslinking density and crystallinity simultaneously. The gel fraction of the PCLF network increased while the swelling ratio in CH_2Cl_2 decreased almost monotonically with increasing the BAPO/PCLF ratio from 10 to 23.3 mg/g. The higher crosslinking density at a higher BAPO/PCLF ratio resulted in stiffer amorphous PCLF530 networks while less stiff PCL1250 and PCL2000 networks because the crystallinity was suppressed more by a tighter chemical network.

PCLF-*co*-PEGF [22]**.** Similar to PCLF, PEG fumarate (PEGF, Figure 1.1) or oligoPEG fumarate (OPF) was first synthesized by the Mikos group between PEG and fumaryl chloride using TEA as the proton scavenger [27,28]. PEGF can be photo-crosslinked into a water swellable network to form hydrogel and the crosslinking density can be controlled by the molecular weight of PEG precursor [27,28]. In the same report for synthesizing PCLF using the K_2CO_3 method, PEGF and amphiphilic PCLF-*co*-PEGF (Figure 1.1) were synthesized. PEGF-*co*-PCLF copolymers can be thermally crosslinked or photo-crosslinked into networks that can swell in both water and organic solvents, without the need of a crosslinker. The swelling ratios of thermally crosslinked PCLF-*co*-PEGF were 106% and 508% in water and CH_2Cl_2, respectively.

PCLAs [5]**.** There can be multiple fumarate segments in the PCLF backbone available for crosslinking. To control the formed networks more precisely, injectable and crosslinkable PCL acrylates (PCLAs) including PCLDAs and PCL triacrylates (PCLTAs, Figure 1.1) were also

synthesized via condensation between PCL diols or triols and acryloyl chloride using the K_2CO_3 method. Crosslinked PCLAs were excellent model polymer systems integrating a chemical network and a physical network of connected crystalline domains. The crystallinity and T_m of the PCLA network were controllable through varying the molecular weight of PCL precursor. Consequently, their mechanical and rheological properties, surface roughness and hydrophilicity also varied significantly with the molecular weight of PCL precursor. At first, when the molecular weight of PCL is low, the PCLA network is amorphous and stiff. When the molecular weight of PCL increases, the stiffness of the amorphous PCLA network decreases as the crosslinking density lowers. When the molecular weight of PCL increases further, the PCLA network becomes semi-crystalline and this physical network strengthens the chemical network.

PCLA/mPEGA networks [29]**.** Similar to the strategy used in PPF/mPEGA networks [19], mPEGA was also photo-crosslinked with semi-crystalline PCLDA2000 at Φ_m of 2-30% to modify its bulk and surface properties. The gel fraction of the PCLDA/mPEGA network varied gradually from ~80% to ~70% when Φ_m increased from 2% to 30% but little swelling was seen in water. The *E* and tensile stress at break of the network at 37 °C decreased while the tensile strain at break increased with increasing Φ_m. Surface characteristics such as frictional coefficient, hydrophobicity, and protein adsorption were greatly reduced by tethering PEG chains into the PCLA networks.

1.2.3 PEG-based injectable polymeric systems.

PEG is inherently inert to protein adsorption and cellular affinity. Chemical modification is necessary to improve the cytocompatibility and bioactivity of PEG-based hydrogels. Similar to PEGF, PEG diacrylates (PEGDAs) were synthesized using facile condensation between PEG with two hydroxyl end groups and acryloyl chloride in the presence of K_2CO_3 [30]. To achieve networks

with different crosslinking densities and consequently different swelling ratios in water and hydrogel stiffnesses, three different PEG precursors with nominal molecular weights of 1000, 3400, and 10000 g/mol were used in synthesizing PEGFs and PEGDAs [22,30]. Photo-polymerizable poly(L-lysine) (PLL, Figure 1.3) with one end-capped allyl group was synthesized via ring-opening polymerization of ε-carbobenzyloxy-L-lysine-*N*-carboxyanhydride using allylamine as the initiator [30]. Both photo-polymerizable PLL and [2-(methacryloyloxy)ethyl]-trimethylamoonium chloride were photo-crosslinked with PEGDA to incorporate positive charges into the hydrogels [30,31]. In addition to photo-crosslinkable PEGF and PEGDA for achieving hydrogels, photo-polymerizable mPEGA discussed earlier was synthesized via acrylation of methyoxyl PEG with one hydroxyl group in the presence of K_2CO_3 and crosslinked with photo-crosslinkable hydrophobic PPF or PCLDA to improve surface hydrophilicity/wettability [19,29].

1.2.4 Injectable polymer composites/hybrid systems.

Crosslinked PPF was stiff but brittle and this weakness limits its load-bearing applications [32,33]. To improve the mechanical properties and also biocompatibility while maintaining the injectability, POSS nanocages and HA nanoparticles have been mixed or copolymerized with PPF to prepare photo-crosslinkable, injectable, and biodegradable nanocomposites [1,14-18,32,33].

PPF/mPOSS [33]**.** Methacryl-POSS (mPOSS, Figure 1.4) with eight methacryl groups was blended with PPF samples having two different M_w of 1150 and 5200 g/mol to form injectable and photo-crosslinkable hybrid organic-inorganic composites. mPOSS behaved as a crosslinker to decrease the η_0 of PPF, expedite the photo-crosslinking, and increase the photo-crosslinking efficiency. Photo-crosslinked PPF/mPOSS had higher stiffness and faster hydrolytic degradation in 1 M NaOH aqueous solution. All the photo-crosslinked PPF/mPOSS disks were amorphous and transparent with similar surface roughnesses of ~10 nm. The networks prepared with the higher-

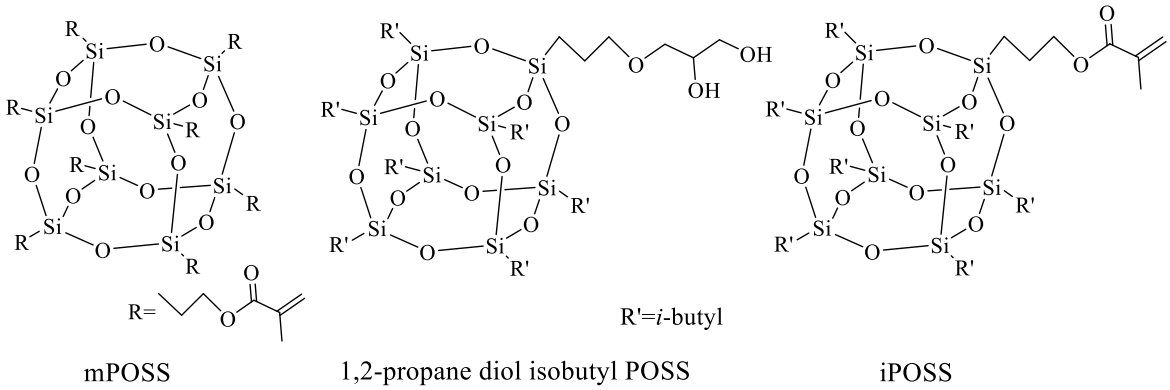

Figure 1.4 Chemical structures of three different POSS molecules used to incorporate with photo-crosslinkable polymers.

M_w PPF were always stiffer, regardless of the weight composition of mPOSS (ϕ_{mPOSS}). The surface hydrophilicity and protein adsorption did not vary significantly after adding mPOSS into PPF.

PPF-*co*-POSS [1]**.** Injectable and photo-crosslinkable PPF-*co*-POSS copolymers (Figure 1.1) with different POSS weight compositions (Φ_{POSS}) were synthesized via two-step polycondensation between DEF and monomers with two hydroxyl end groups: 1,2-propane diol and 1,2-propane diol isobutyl POSS (Figure 1.4). The tensile and compressive moduli and fracture toughness of photo-crosslinked PPF-*co*-POSS were enhanced simultaneously by increasing Φ_{POSS} up to 10%, in which the crystallinity of POSS was completely suppressed. The enhanced fracture toughness was attributed to the shear yielding of nanovoids formed between POSS nanoaggregates. Further incorporation of POSS decreased crosslinking density and induced brittleness from the crystalline regions of POSS, leading to decrease in stiffness and strain at break.

PCLTA/iPOSS [25]**.** In another study, PCLTAs having two different molecular weights of ~7000 and ~20,000 g/mol were mixed and photo-crosslinked with methacryl isobutyl POSS (iPOSS, Figure 1.4). Because of the different PCLTA molecular weights, one group had the amorphous polymer matrix of crosslinked PCLTA7k while the other had the semi-crystalline one of crosslinked PCLTA20k. Unlike mPOSS, iPOSS had only one reactive methacryl group to be incorporated with PCLTA networks and did not behave as a crosslinker. The POSS nanocages tethered in the PCLTA networks in general strengthened the polymer matrices and lowered the surface friction coefficient, but did not significantly alter the surface roughness, wettability, and the capability of adsorbing serum proteins. The PCLTA20k group always had much higher values in E, strain at break, and compressive modulus, regardless of the composition of iPOSS (Φ_{iPOSS}), and the effect of adding iPOSS became negative when Φ_{iPOSS} was higher than 10%.

PPF/HA [32]**.** Thermally crosslinked PPF/HA nanocomposites were prepared by mixing PPF

with HA nanoparticles and crosslinked at 60 °C to enhance the biocompatibility of PPF network. The thermal crosslinking procedure was performed using 1-vinyl-2-pyrrolidionone (NVP) as the crosslinker, benzoyl peroxide (BPO) as the free radical initiator, and *N*-dimethyl-*p*-toluidine (DMT) as the accelerator. In contrast with photo-crosslinked PPF/mPOSS, HA nanoparticles did not affect the compressive modulus of PPF networks but increased surface hydrophilicity and serum protein adsorption significantly because the nanocomposite disks were cut from cylinders and the HA nanoparticles were exposed sufficiently on the disk surface.

PCLF/HA [24]**.** PCLF530 and PCLF2000 were used as two polymer matrices to mix with HA nanoparticles and photo-crosslinked into nanocomposites with the HA weight compositions (Φ_{HA}) of 5%, 10%, 20%, and 30%. The preparation method was distinct from that for preparing thermally crosslinked PPF/HA nanocomposites, as the HA nanoparticles could be covered in the polymer matrix instead of being exposed, especially in the semi-crystalline one of PCLF2000. As the result, surface hydrophilicity and the capability of adsorbing serum proteins was not improved or even decreased. The G' and E values of photo-crosslinked PCLF/HA nanocomposites were all enhanced significantly but the compressive modulus did not change much for crosslinked PCLF2000/HA nanocomposites.

PCLDA/HA [23]**.** In order to elucidate how the exposure of HA nanoparticles affected the surface properties and biocompatibility of the composites, photo-crosslinked PCLDA/HA nanocomposites with Φ_{HA} of 10, 20, and 30% were also prepared using PCLDA530 and PCLDA2000. Unlike PPF/HA nanocomposites, the tensile, compressive and shear moduli were greatly enhanced by incorporating HA nanoparticles with the PCLDA matrices. HA nanoparticles were found to disperse unevenly from the top surface to the bulk, especially in semi-crystalline crosslinked PCLDA2000/HA nanocomposites, where crystallization occurred over HA

nanoparticles. Cutting the crosslinked PCLDA/HA using a blade exposed the embedded HA nanoparticles and resulted in higher surface hydrophilicity and higher protein adsorption, in contrast with the invariant surface hydrophilicity in the original surfaces of the crosslinked PCLDA/HA nanocomposites before exposure of the embedded HA nanoparticles.

1.3 Fabrication of structures

All the injectable and biodegradable polymers discussed in Section 2 have been photo-crosslinked into 2D disks with or without surface features and 3D structures that can be directly used for tissue regeneration (Figure 1.5). The surface features included honeycomb patterns with controllable pore sizes and concentric or parallel microgrooves with pre-designed groove dimensions. The 3D structures fabricated using these injectable polymers included nerve conduits and porous bone scaffolds.

1.3.1 Surface patterns.

Honeycomb patterns [34,33]**.** Honeycomb-patterned films of crosslinked PCLTA were fabricated by integrating the breath-figure method with photo-crosslinking (Figure 1.5a). Two pore sizes of 5.6 and 3.0 μm were achieved at the air flow rates of 0 and 50 mL/min, respectively. It is a facile method for generating substrates to mimic bone topography and enhance bone growth, and can be further extended to large-area stereolithographic production. Although the dry honeycomb films of photo-crosslinked PCLTA demonstrated higher hydrophobicity, this effect did not function as all the films were rinsed in culture media prior to cell seeding. The amounts of serum proteins adsorbed on the honeycomb-patterned films were significantly higher than that on the flat control, as attributed to the larger surface area instead of the surface chemistry of the porous films.

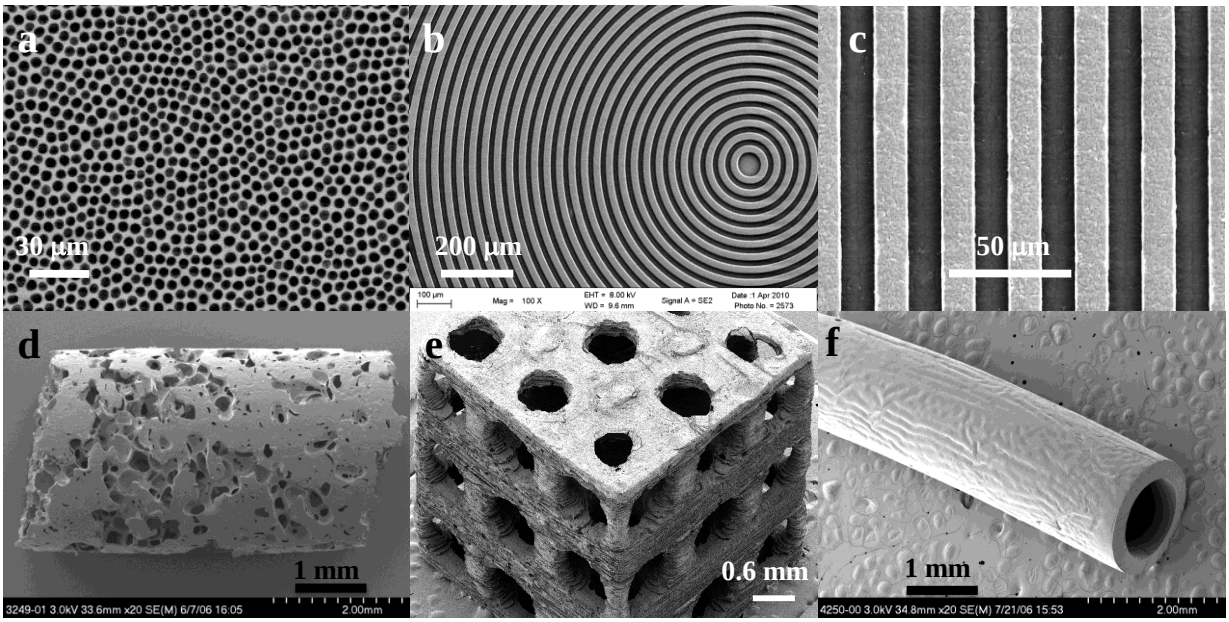

Figure 1.5 Representative 2D photo-crosslinked PCLTA substrates with (a) honey-comb pores, (b) concentric microgrooves, and (c) parallel microgrooves, and 3D structures such as (d) a salt-leached porous bone scaffold of photo-crosslinked PPF-*co*-PCL (Φ_{PCL} = 31%), (e) a thermally crosslinked PPF/HA nanocomposite scaffold from a wax mold, and (f) a photo-crosslinked PCLF2000 neve conduit. Scale bars are 30 µm, 200 µm, 50 µm, 1 mm, 0.6 mm, and 1 mm in (a-f), respectively. (Adapted from references [2,34,35,38], with copyright permission)

Microgrooved structures [2,35,36]**.** Both concentric (Figure 1.5b) and parallel (Figure 1.5c) microgrooved substrates of photo-crosslinked PCLTAs with various groove widths (same as the ridge width) of 5-90 μm and depths of 0.2-12 μm were fabricated through replica molding from silicon wafers with pre-designed patterns, which were made using a standard microfabrication procedure that included photo-lithography, physical vapor deposition, lift-off, and dry plasma etching processes. PCLTA with two molecular weights of ~7000 and ~10000 g/mol were used for comparison between a stiffer, semi-crystalline substrate and a more compliant, amorphous one. Using the same method, microgrooves with groove widths of 5 or 15 μm and a fixed depth of 5 μm were also incorporated with photo-crosslinked PCLTA20k/HA nanocomposites [36]. In these microgrooved nanocomposite substrates, the distribution of HA was controlled to be either uniform or "heterogeneous", meaning that HA was located only on the ridges or the groove bottom, by which surface chemistry, morphology, and stiffness were different in different regions.

1.3.2 3D structures.

Porous scaffolds [10,11,15,37,38]**.** Salt-leaching is an easy method to fabricate porous polymer scaffolds through mixing polymer solution with salt particles and leaching away the salt in water after polymer solidification. Both pore size and porosity can be regulated by the salt particle size and polymer/salt ratio; however, pore connectivity is poor and pore geometry is not controllable. Thermally crosslinked PPF and PPF/HA cubic porous scaffolds with a pore size of 300-500 μm and a porosity of 55% and photo-crosslinked PPF-*co*-PCL cylindrical porous scaffolds with a pore size of 300-400 μm and a porosity of 80% (Figure 1.5d) were fabricated using this method [15,38].

Stereolithography is an effective technique to fabricate photo-crosslinkable polymeric biomaterials into highly complex 3D scaffolds with controlled microstructures for tissue

engineering applications. Photo-crosslinked PPF scaffolds were fabricated using PPF/DEF resins with three different weight ratios and BAPO contents [10]. PPF molecular weight and the resin composition are critical for stereolithographical fabrication of 3D porous bone scaffolds because they determine the resin viscosity and the scaffold mechanical properties. When the PPF molecular weight and/or composition are too high, the resin viscosity is too high to be processed. If too low, photo-crosslinking is inefficient and the final scaffold is too weak. The fabricated PPF scaffolds were characterized in terms of external dimensions, porosity, mean pore size, and compressive modulus, and then compared to the computer-aided design (CAD) models. In xy-plane accuracy features were achieved and over-curing in z-axis was minimized.

A multi-nozzle-based versatile deposition system was developed to flexibly construct porous scaffolds using polymers with distinct physicochemical properties, for example, thermoplastics and photo-crosslinkable polymers [37]. Because the structural material is selectively deposited to a wax mold, it is convenient to use different materials at different layers and even at different desired locations in one layer. Using this deposition system supplemented with a UV-curing apparatus, PPF/DEF resin was fabricated into 3D porous bone scaffolds and characterized in terms of compressive mechanical properties, morphology, pore size, and porosity. In general, there is an inversely proportional relationship between porosity and compressive strength of the fabricated structure of a given polymer. By adjusting different structural parameters of porosity and pore size along with selection of desired materials, the mechanical strength of the designed scaffolds can be optimized.

3D printing and injection molding technique was used to fabricate 3D porous PPF scaffolds with assistance of pre-designed CAD models to control porosity, pore geometries, and pore dimensions [11]. First, a 3D phase-change ink jet printer, PatternMaster, was used to layer by layer

create a cube combining a building material, polystyrene (PS), and a support material, wax, which can dissolve in different solvents. After printing, PS was removed by dissolution in acetone and then the wax negative mold was ready for the polymerizing PPF resin to be thermally cured inside. PPF scaffolds were then obtained after the wax was dissolved in a cleaner solution. Crosslinked PPF/HA nanocomposite scaffolds (Figure 1.5e) were also fabricated using this method [38]. Compared with random salt-leached pores, the scaffolds had fully interconnected pores, leading to a significantly larger accessible void volume fraction.

Nerve conduits [3,15,29]**.** Based on their desirable mechanical properties (e.g., flexibility and tear resistance), PCLF, PCLDA, PPF-*co*-PCL (Φ_{PCL} = 90%), and mPEGA/PCLDA were selected to fabricate conduits for assisting peripheral nerve regeneration. To facilitate photo-crosslinking, a mold composed of a glass tube, a stainless-steel wire (or multiple wires), and two Teflon end-caps, was developed. Polymer/BAPO/CH_2Cl_2 solution was transferred into this mold and placed under a UV light to fabricate single-lumen and multi-lumen nerve conduits. Among three networks of PCLF530, PCLF1250, and PCLF2000, crosslinked PCLF2000 was the best candidate material for substituting autologous nerve conduit because it satisfied the major requirements in fabrication, degradation rate, flexibility, toughness, suturability/tear resistance, and biocompatibility. It is also convenient to incorporate crosslinked PCLF2000 nerve conduits (Figure 1.5f) with features such as multiple guidance channels, porous permeable wall structure, support cells, and nerve growth factor (NGF) [3].

In PCLDA/mPEGA networks, PEG chains were tethered not only onto the surface, but also inside the bulk. The method had advantages over other surface modification techniques, for example, self-assembled monolayers or surface-initiated polymerization, as PEG pendant chains were able to remain in the rest of the PCLDA/mPEGA networks even after degradation. Using

PCLDA/mPEGA, heterogeneous nerve conduits with a compositional gradient along the wall thickness were fabricated to address the feasibility of promoting nerve cell functions inside at an intermediate Φ_m of ~5% while prohibiting cell attachment outside at Φ_m of 30% [29]. In addition, lubricated surfaces with improved wettability by having a large amount of PEG pendant chains can facilitate implantation of nerve conduits and cause less wear between medical devices and surrounding tissues [29].

1.4 Applications

The above-discussed injectable polymeric systems were developed for bone, nerve, and cardiovascular tissue engineering applications. The 2D substrates and 3D structures fabricated using the injectable and biodegradable polymers were further evaluated in terms of regulating *in vitro* cellular responses and *in vivo* tissue regeneration.

1.4.1 *In vitro* cell regulation.

Cell-material interactions play a pivotal role in the design and evaluation of polymers for tissue engineering applications [9,39-41]. Among all the surface characteristics of polymeric biomaterials, surface chemistry, topography, and stiffness are most critical factors for controlling cell-material interactions [36,42]. Although most cells tend to favor stiffer substrates, it is important to note that when examining nerve cells, glial-type nerve cells such as Schwann cells showed favorability towards stiffer substrates whereas, neuronal-type cells showed preference to softer substrates [2]. Polymer thermal properties and crystallinity are also important in the performance of injectable polymeric biomaterials as these properties can be manipulated to influence the substrate stiffness, topography, and even chemistry. In addition to substrate stiffness, different surface patterns such as honeycomb structures [34] and microgrooved structures

[2,35,36], and 3D structures such as conduits [3,5,29] and porous scaffolds [10,11,37,38] have been studied with both *in vivo* animal implantation and *in vitro* cell regulation.

Different cell types have been used to evaluate the cytocompatibility of the above-discussed injectable and photo-crosslinkable polymeric systems and their interactions with the materials. These cell types included mouse pre-osteoblastic MC3T3-E1 cells and rat bone marrow stromal cells (BMSCs) for bone tissue engineering applications, primary rat aortic smooth muscle cells (SMCs) for cardiovascular tissue engineering applications, rat pheochromocytoma (PC12) cells, rat Schwann cell precursor line (SpL201) cells, and E14 mouse neural progenitor cells (NPCs) for nerve tissue engineering applications.

MC3T3-E1 cell behavior and functions were studied on the photo-crosslinked substrates of PCLAs [5], PPF/mPEGA blends [19], PPF/PCL blends [34], PPF-*co*-PCL copolymers [15], PPF-*co*-POSS copolymers [1], PPF/mPOSS blends [12], PPF/HA nanocomposites [32], PCLTA/iPOSS nanocomposites [25], and PCLDA/HA nanocomposites [23]. In general, MC3T3-E1 cells could better attach to and proliferate on stiffer and rougher substrates made of those polymeric systems. SMCs were studied on the PPF/PCL blends before and after photo-crosslinking [33] and BMSCs were studied on photo-crosslinked PPF/PCLF blends and PCLF/HA nanocomposites [24], in which similar results were received as the cells also preferred stiffer and/or rougher substrates. More studies on regulating SMCs on PCLA-based substrates done recently by the corresponding author have been presented in numerous conferences and are to be formally reported soon.

As one of surface chemical factors to affect cell-material interactions, surface hydrophilicity or surface energy was regulated by tethering PEG chains or incorporating HA nanoparticles into PPF networks, as discussed in Section 1.2. MC3T3-E1 cell attachment, spreading, proliferation, and differentiation on photo-crosslinked PPF/mPEGA substrates all exhibited parabolic

dependence on Φ_m and reached a maximum at Φ_m of ~5% [19]. In photo-crosslinked PPF/HA and PCLDA/HA nanocomposites, the exposed HA nanoparticles improved surface hydrophilicity and significantly promoted MC3T3-E1 cell attachment, proliferation, and mineralization [23,32]. The roles of Φ_{HA}, polymer crystallinity, and exposure of HA by cutting the samples in regulating surface characteristics and MC3T3-E1 cell behaviors are summarized and correlated [23].

MC3T3-E1 cells were also studied on honeycomb-patterned films of photo-crosslinked PCLTA [34] and microgrooved substrates of photo-crosslinked PCLTA and PCLTA/HA [35,36], as well as in crosslinked PPF and PPF/HA nanocomposite scaffolds [37,38]. Surface patterns mainly influence cell/nuclear phenotype/alignment, distribution, and migration through guidance. MC3T3-E1 cells on the honeycomb-patterned substrates of photo-crosslinked PCLTA attached, spread, and proliferated better with more filopodia and focal adhesions than on the flat control substrate, especially when the pore size was smaller. As the consequences, MC3T3-E1 cell mineralization and expression of integrin subunits of α_1, α_2, β_1, and gene markers of osteocalcin, osteopontin, and alkaline phosphatase, and collagen type I were all promoted by the honey-comb patterns, more prominently on smaller pores. On microgrooved substrates of PCLTAs, microgrooves did not affect MC3T3-E1 cell attachment and proliferation much, but significantly changed their phenotype and distribution. As shown in Figures 1.6a and 1.6b, MC3T3-E1 cells and nuclei were aligned along the microgrooves and showed better mineralization and higher osteocalcin expression levels than on the flat substrates, especially when the grooves were narrow and deep. In “heterogeneous” microgrooved substrates of photo-crosslinked PCLTA/HA nanocomposites, when HA nanoparticles only existed on the ridges, MC3T3-E1 cells had better attachment and proliferation. The cells could even spread perpendicular to the microgrooves and more nuclei could stay on the ridges and remain unaligned. In contrast, the “heterogeneous”

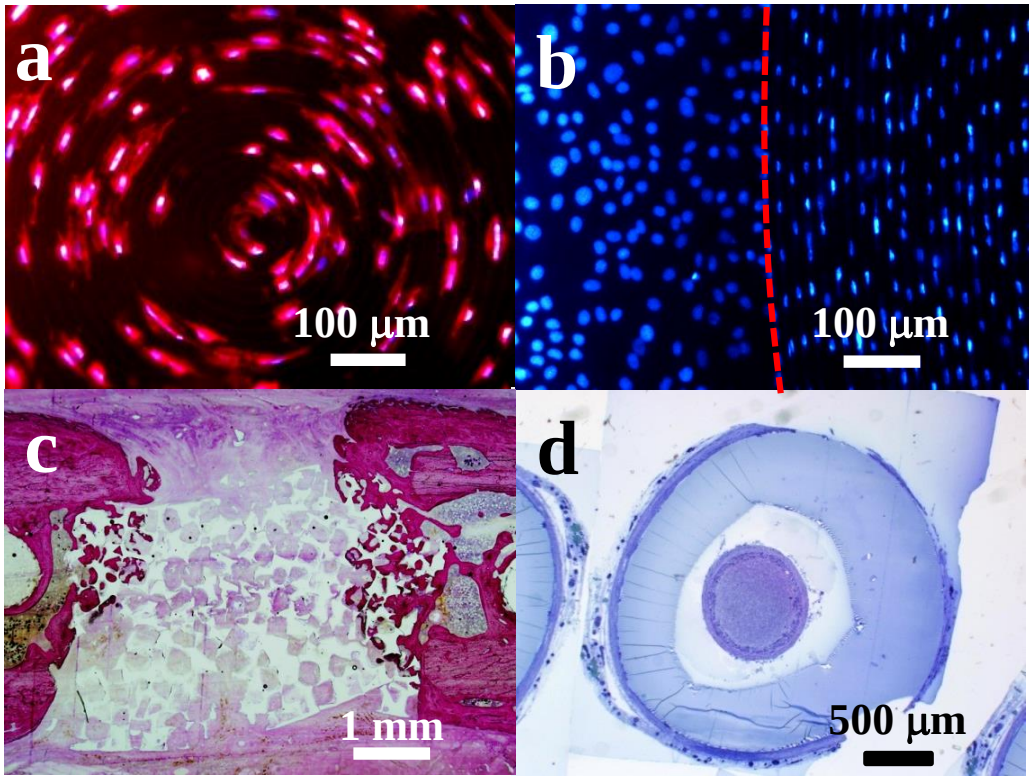

Figure 1.6 Representative fluorescent images of MC3T3-E1 cells cultured on photo-crosslinked PCLTA10k substrates with concentric microgrooves (groove width: 7.5 μm, groove depth: 10 μm) at 4 h, stained with rhodamine-phalloidin and 4',6-diamidino-2-phenylindole (DAPI) (a), and DAPI-stained cell nuclei at day 4 on the intersection area (b) with a red dotted curve to mark the boundary between the flat margin (left) and the microgrooved area (right). Coronal section of photo-crosslinked PPF-*co*-PCL (Φ_{PCL} = 31%) scaffold implanted in a rat femoral bone defect for eight weeks, stained with methylene blue and basic fuchsin (c) and midpart cross section of a crosslinked PPF-*co*-PCL (Φ_{PCL} = 90%) single-lumen nerve conduit after 16 weeks of implantation, stained with toluidine blue (d). Scale bars are 100 μm, 100 μm, 1 mm, and 500 μm in (a-d). (Adapted from references [15,35], with copyright permission)

substrates that contained HA on the groove bottom showed higher calcium content and ALP activity than those substrates with HA only in the ridges because MC3T3-E1 cells confined and aligned inside the microgrooves were more important for their differentiation. MC3T3-E1 cell attachment, proliferation, and ingrowth were better in the crosslinked PPF/HA nanocomposite scaffolds than in the PPF ones when the pore geometry and pore interconnectivity were the same. The values were the lowest in salt-leached scaffolds because of the lowest pore interconnectivity.

Neuronal-like PC12 cells have been widely studied as a model for neurite extension and cell communications. PC12 cells were studied on the photo-crosslinked substrates of PPF-*co*-PCL [15], PCLDA/mPEGA [29], and PCLTA [2]. Glial-type SpL201 cells were studied on the photo-crosslinked substrates of PCLF [3], PCLA [5], PCLTA [2], and PCLDA/mPEGA [29]. PC12 cells preferred softer substrates in attachment, proliferation, and NGF-induced differentiation, i.e., neurite extension, whereas SpL201 cells had better attachment and proliferation on stiffer substrates. On photo-crosslinked PCLDA/mPEGA substrates, surface hydrophilicity affected the proliferation rate for both cell types by first promoting it through improved surface hydrophilicity up to Φ_m of 5-7% and then inhibiting at higher Φ_m because of strong protein/cell repulsion from densely grafted PEG chains [29]. The microgrooved substrates of photo-crosslinked PCLTAs mainly affected the morphology and differentiation of both PC12 cells and SpL201 cells [2]. There were different threshold sensitivities of these two nerve cell types to topographical features when their cytoskeleton and nuclei were altered by varying the groove depth and width. Oriented SpL201 cells had a higher motility than the unaligned ones. SpL201 cells and PC12 cells demonstrated more differentiation on narrower microgrooves while the neurites extended from PC12 cells were more sensitive to narrower and shallower microgrooves [2]. NPCs, SpL201 cells, and PC12 cells were also studied on PEGDA hydrogels tethered with cationic PLL [30,31]. For all these three cell

types, their viability in encapsulation, attachment, proliferation, and differentiation on the hydrogel substrates were all enhanced by adding a suitable amount of PLL into neutral PEGDA hydrogels [30]. It should be noted that the optimal PLL weight percentage for NPC attachment, proliferation, and differentiation was 2-3% [31]. Meanwhile, the role of stiffness in regulating these nerve cells was examined on the hydrogels with different crosslinking densities and stiffnesses [30]. Again, SpL201 cells were found to prefer the stiffer substrates while both NPCs and PC12 cells preferred the softer ones [30].

1.4.2 *In vivo* animal implantation.

The tissue compatibility of crosslinked PCLF was evaluated by subcutaneous implantation in female Sprague-Dawley rats for 4 weeks [4]. No signs of chronic infection in the blood, abnormalities in the renal capsules or kidney glomerulus, or interstitial thickening around the blood vessels were observed. No activated macrophages were observed in the surrounding tissue. The thickness of the fibrous capsule around the sample was less than 100 µm, comparable to Gore artificial dura as the negative control. These results suggested good biocompatibility of the implanted crosslinked PCLF disks [4].

The injectable polymeric biomaterials were developed for two major purposes: bone and nerve regeneration. Thus *in vivo* animal implantation and histological analysis of the porous bone scaffolds and nerve conduits made from PCLF and PPF-*co*-PCL were performed [3,15]. After its crosslinking density and crystallinity were modulated, the PCLF2000 network supported SpL201 cell attachment and proliferation and was sufficiently strong to hold the suture while still suturable and flexible, and therefore was selected for evaluation in a 1 cm gap rat sciatic nerve model [3]. Histological evaluation demonstrated that the material was biocompatible with sufficient strength to hold sutures in place after 6 and 17 weeks of implantation and nerve cable with myelinated

axons was found in the crosslinked PCLF2000 nerve conduit [3]. Porous scaffolds and nerve conduits made from crosslinked PPF-*co*-PCLs with Φ_{PCL} of 31% and 90% were implanted in a rat femoral bone defect model and in bridging cut rat sciatic nerve tubes, respectively [15]. Only mild foreign body reaction to the implanted material was observed (Figure 1.6c) [15]. Newly formed bone extended from the original femur edges into the defect and had a woven appearance [15]. PPF-*co*-PCL (Φ_{PCL} = 31%) was also photo-crosslinked with poly(lactide-*co*-glycolide) (PLGA) microspheres containing recombinant human bone morphogenetic protein-2 (rhBMP-2) to form a controlled release scaffold system that resulted in healing rat femur bone defects in eight weeks. The structures of both single-lumen and seven-channel nerve conduits remained intact with only a small layer of fibroblast tissue around the conduits after 4 and 16 weeks of implantation (Figure 1.6d) [15]. Myelinated axons in the midpart of the nerve conduits were evident, especially after 16-week implantation [15].

1.5 Conclusions and perspectives

Injectable and photo-crosslinkable polymeric biomaterials with controllable physicochemical properties and degradation rates have demonstrated their great promise in regenerative medicine. In particular, three categories of injectable and biodegradable polymers based on PPF, PCL, and PEG, and their nanocomposites with HA and POSS have been developed for diverse tissue engineering applications. The thermal and mechanical properties, surface hydrophilicity/wettability, and morphology of these polymers can be well modulated before and after photo-crosslinking. In particular, simultaneously regulating crosslinking density and crystallinity in semi-crystalline polymer networks supplies an efficient approach to prepare biomaterials with controllable mechanical properties over a wide range. These polymeric

biomaterials have been fabricated into 2D substrates with or without surface features and 3D porous scaffolds and nerve conduits using different methods. Both *in vitro* cell regulation and *in vivo* animal implantation of these polymeric substrates and structures have been performed. The tailorability in material bulk and surface properties, readiness for being fabricated into biomedical devices, and their biocompatibility all demonstrate the promise of the injectable polymeric biomaterials in fulfilling tissue regeneration. To satisfy the growing needs in regenerative medicine and 3D fabrication methods, more novel injectable polymeric systems with multiple functionalities, advanced structural and physical properties, and convenient processability should be developed.

References

1. Cai, L.; Chen, J.; Rondinone A.; Wang, S. *Adv. Funct. Mater.* **2012**, *22*(15), 3181-3190.

2. Cai, L.; Zhang, L.; Dong, J.; Wang, S. *Langmuir* **2012**, *28*(34), 12557-12568.

3. Wang, S.; Yaszemski, M. J.; Knight, A. M.; Gruetzmacher, J. A.; Windebank A. J.; Lu, L. *Acta Biomater.* **2009**, *5*(5), 1531-1542.

4. Jabbari, E., Wang, S., Lu, L., Gruetzmacher, J. A., Ameenuddin, S., Hefferan, T. E., Currier, B. L., Windebank, A. J.; Yaszemski, M. J. *Biomacromolecules* **2005**, *6*(5), 2503-2511.

5. Cai, L.; Wang, S. *Polymer* **2010**, *51*(1), 164-177.

6. Khan, Y.; Yaszemski, M. J.; Mikos, A. G.; Laurencin, C. T. *J. Bone Joint Surg.* **2008**, *90*(S1), 36-42.

7. Yaszemski, M. J.; Payne, R. G.; Hayes, W. C.; Langer, R.; Mikos, A. G. *Biomaterials* **1996**, *17*(2), 175-185.

8. Schmidt, C. E.; Leach, J. B. *Annu. Rev. Biomed. Eng* **2003**, *5*(1), 293-347.

9. Wang, S.; Cai, L. *Int. J. Polym. Sci.* **2010**, 138686, 20 pages.

10. Lee, K. W.; Wang, S.; Fox, B. C.; Ritman, E. L.; Yaszemski, M. J.; Lu, L. *Biomacromolecules* **2007**, *8*(4), 1077-1084.

11. Lee, K. W.; Wang, S.; Lu, L.; Jabbari, E.; Currier, B. L.; Yaszemski, M. J. *Tissue Eng.* **2006**, *12*(10), 2801-2811.

12. Wang, S.; Lu, L.; Yaszemski, M. J. *Biomacromolecules* **2006**, *7*(6), 1976-1982.

13. X. F. Shi and A. G. Mikos: 'Poly(propylene fumarate)', in 'An introduction to biomaterials', (Eds: S. A. Guelcher, J. O. Hollinger), 205–218; 2006 CRC Press, Boca Raton, FL.

14. Wang, S.; Lu, L.; Gruetzmacher, J. A.; Currier, B. L.; Yaszemski, M. J. *Macromolecules* **2005**, *38*(17), 7358-7370.

15. Wang, S.; Kempen, D. H.; De Ruiter, G. C.; Cai, L.; Spinner, R. J.; Windebank, A. J.; Yaszemski, M. J.; Lu, L. *Adv. Funct. Mater.* **2015**, *25*(18), 2715-2724.

16. Wang, K.; Cai, L.; Hao, F.; Xu, X.; Cui, M.; Wang, S. *Biomacromolecules* **2010**, *11*(10), 2748-2759.

17. Wang, S.; Kempen, D. H.; Simha, N. K.; Lewis, J. L.; Windebank, A. J.; Yaszemski, M. J.; Lu, L. *Biomacromolecules* **2008**, *9*(4), 1229-1241.

18. Cai, L.; Wang, S. *Biomaterials* **2010**, *31*(29), 7423-7434.

19. Cai, L.; Wang, K.; Wang, S. *Biomaterials* **2010**, *31*(16), 4457–4466.

20. He, S.; Yaszemski, M. J.; Yasko, A. W.; Engel, P. S.; Mikos, A. G. *Biomaterials* **2000**, *21*(23), 2389-2394.

21. Wang, S.; Yaszemski, M. J.; Gruetzmacher, J. A.; Lu, L. *Polymer* **2008**, *49*(26), 5692-5699.

22. Wang, S.; Lu, L.; Gruetzmacher, J. A.; Currier, B. L.; Yaszemski, M. J. *Biomaterials* **2006**, *27*(6), 832-841.

23. Cai, L.; Guinn, A. S.; Wang, S. *Acta biomater.* **2011**, *7*(5), 2185-2199.

24. Wang, S.; Kempen, D. H.; Yaszemski, M. J.; Lu, L. *Biomaterials* **2009**, *30*(20), 3359-3370.

25. Cai, L.; Foster, C. J.; Liu, X.; Wang, S. *Polymer* 2014, *55*(16), 3836-3845.

26. Cai, L.; Wang, S. *Biomacromolecules* **2009**, *11*(1), 304-307.

27. Jo, S.; Shin, H.; Shung, A. K.; Fisher, J. P.; Mikos, A. G. *Macromolecules* **2001**, *34*(9), 2839-2844.

28. Temenoff, J. S.; Athanasiou, K. A.; Lebaron, R. G.; Mikos, A. G. *J. Biomed. Mater. Res.* **2002**, *59*(3), 429-437.

29. Cai, L.; Lu, J.; Sheen, V.; Wang, S. *Biomacromolecules* **2012**, *13*(2), 358-368.

30. Cai, L.; Lu, J.; Sheen, V.; Wang, S. *Biomacromolecules* **2012**, *13*(2), 342-349.

31. Cai, L.; Lu, J.; Sheen, V.; Wang, S. *Biomacromolecules* **2012**, *13*(5), 1663-1674.

32. Lee, K. W.; Wang, S.; Yaszemski, M. J.; Lu, L. *Biomaterials* **2008**, *29*(19), 2839-2848.

33. Wang, K.; Cai, L.; Wang, S. *Polymer* **2011**, *52*(13), 2827-2839.

34. Wu, X.; Wang, S. *Polymer* **2014**, *55*(7), 1756-1762.

35. Wang, K.; Cai, L.; Zhang, L.; Dong, J.; Wang, S. *Adv. Healthcare Mater.* **2012**, *1*(3), 292-301.

36. Henry, M. G.; Cai, L.; Liu, X.; Zhang, L.; Dong, J.; Chen, L.; Wang, Z.; Wang, S. *Langmuir* **2015**, *31*(9), 2851-2860.

37. Wei, C.; Cai, L.; Sonawane, B.; Wang, S.; Dong, J. *Biofabrication* **2012**, *4*(2), 025009.

38. Lee, K. W.; Wang, S.; Dadsetan, M.; Yaszemski, M. J.; Lu, L. *Biomacromolecules* **2010**, *11*(3), 682-689.

39. Harbers, G. M.; Grainger, D. W. In '*Introduction to biomaterials*', (Guelcher SA, Hollinger JO, editors), 15-45; 2005, Boca Raton: CRC Press.

40. W. M. Saltzman and T. R. Kyriakides: in 'Principles of tissue engineering', 3rd ed, (Lanza R, Langer R, Vacanti J, editors), 279-296; 2007, San Diego, Elsevier Academic Press.

41. Wang, S.; Cai, L. Chapter 3, In '*ACS Symposium Series on Biomaterials*', (A. S. Kulshrestha, A. Mahapatro, L. A. Henderson Eds.), 43-63; 2010, Washington DC, American Chemical Society.

42. Discher, D. E.; Janmey, P.; Wang, Y. L. *Science* **2005**, *310*(5751), 1139-1143.

Chapter II. Smooth Muscle Cell Responses to Poly(ε-caprolactone) Triacrylate Networks with Different Crosslinking Time

Abstract

To investigate the effect of crosslinking time on the polymer network properties and cellular behaviors, poly(ε-caprolactone) acrylates (PCLAs) with different molecular weights were crosslinked under UV light for time ranging from 1 to 60 min. The crosslinking efficiency of PCLA increased with decreasing the molecular weight and increasing crosslinking time could increase the gel fraction and network stiffness and decrease the swelling ratio. Then the PCLA networks crosslinked for different time were used as substrates for culturing rat aortic smooth muscle cells (SMCs). SMC attachment, proliferation, spreading, and focal adhesions all increased when the PCLTA molecular weight increased from 8k to 10k and then to 20k at the same crosslinking time. For the same PCLTA, SMC attachment, proliferation, spreading, and focal adhesions increased with increasing the crosslinking time, in particular, between the substrates crosslinked for less than 3 min and longer than 5 min.

2.1 Introduction

Poly(ε-caprolactone) (PCL) is a biodegradable semi-crystalline polymer that has been widely used in tissue engineering [1-5]. The crystalline structure offers PCL unique thermal and mechanical properties. After the hydroxyl end groups in PCL diols or triols are converted into crosslinkable functional groups, i.e. acrylate, maleic anhydride, or fumarate, they can be crosslinked into networks with controllable chemical and physical properties [6-14]. Compared to the other crosslinking methods through heat, irradiation, or redox process, photo-crosslinking is more efficient to control the polymerization heat evolution and fabricate complex structures [13-16]. Our research group has developed photo-crosslinkable PCL acrylates (PCLAs) such as PCL diacrylates (PCLDAs) and PCL triacrylates (PCLTAs) [17,18]. Depending on the molecular weight of PCL precursor in the synthesis of PCLA, amorphous and semi-crystalline PCL networks were prepared with elastic modulus (*E*) ranging from 1 to 200 MPa and controllable melting temperature (T_m) and crystallinity (χ_c) [18].

The crosslinks in the photo-crosslinked PCLAs suppressed and impeded the PCL crystallization, resulting in a reduced crystallinity. For photo-crosslinkable polymers, the crosslinking efficiency can be controlled by the density of crosslinkable groups, the concentration of photo-initiator, UV light intensity, and crosslinking time [14-16,19-23]. Among all these factors, sufficient crosslinking time should be given to ensure a polymer network with a high gel fraction and desirable mechanical properties without causing overcure and photo-scission problems [19,23]. For PCLAs, both crosslinking density and efficiency increase with increasing the density of acrylate end groups, which can be achieved by either decreasing the molecular weight of the PCL precursor with a certain architecture, or having multiple arms with more acrylate end groups in one polymer.

In this chapter, I studied the roles of crosslinking density and crystallinity in determining the physical properties, such as gel fraction, swelling ratio, and thermal, rheological, and mechanical properties, of photo-crosslinked PCLAs by varying both the crosslinking time and the molecular weight of PCL precursor. These PCLTA networks resulted from different crosslinking time were further used as substrates to regulate rat aortic smooth muscle cell (SMC) behaviors, including attachment, proliferation, spreading and focal adhesion.

2.2 Materials and Methods

2.2.1 Photo-crosslinking and characterization of PCLTAs.

Three PCLTAs with names of PCLTA8k, 10k, and 20k used in this chapter were synthesized according to our previous report and had number-average molecular weights (M_n) of 8460, 9750, and 20020 g/mol, respectively [18]. The PCLTAs were crosslinked into networks under UV light (SB-100P, Spectronics Corp., Westbury, NY, λ= 365 nm, Intensity: 4800 w/cm^2) for different crosslinking time of 1, 3, 5, 10, 20, 40, and 60 min, as shown in Figure 2.1. The gel fraction and swelling ratio in CH_2Cl_2 of the crosslinked PCLTAs were determined according to our previous report [17]. To compare with the PCLTAs in terms of gel fraction and swelling ratio, I also used 4arm and 6arm PCLAs with M_n of 9610, 14700, 10200, and 19900 g/mol, which were named 4arm-10k, 4arm-14k, 6arm-10k and 6arm-20k, respectively. These 4arm and 6arm PCLAs were synthesized via acrylation of PCL tetraols and PCL hexanols that were prepared through ring-opening polymerization of ε-caprolactone initiated with pentaerythritol and dipentaerythritol, respectively. Flat uncrosslinked PCLTA substrates (crosslinking time of 0) were prepared by compression and crystallization of the melt between two glass plates. Flat photo-crosslinked PCLTA substrates were soaked in acetone for two days to remove the sol fraction, dried in vacuum,

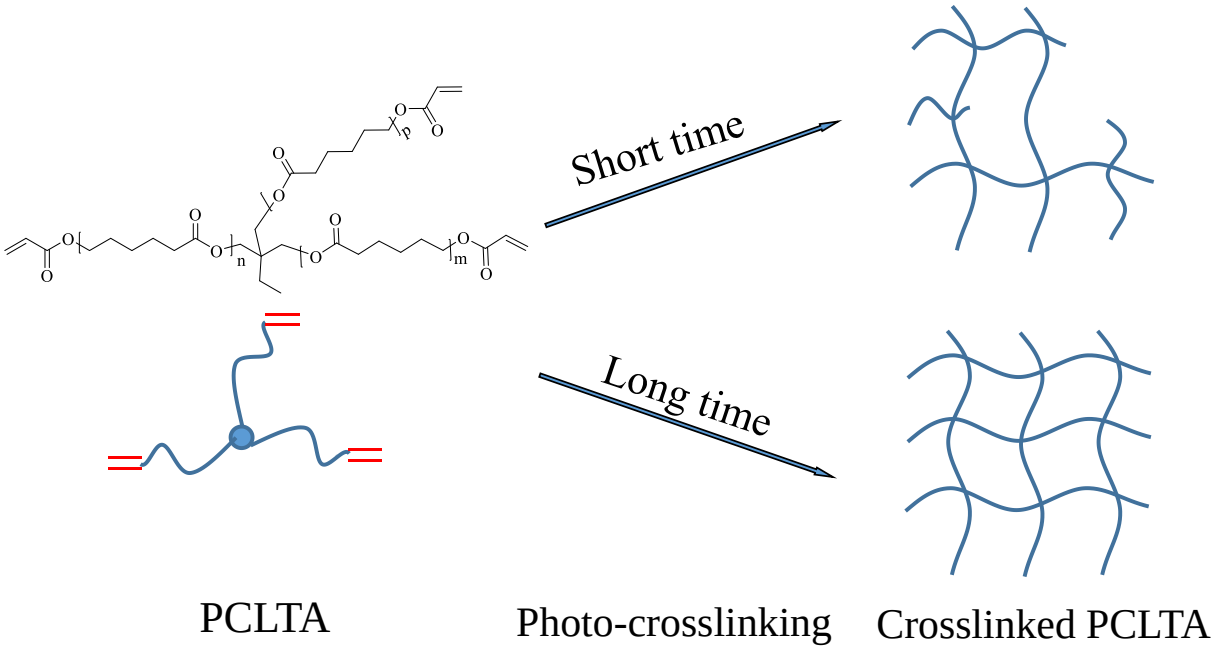

Figure 2.1 Crosslinked PCLTAs with different crosslinking time.

and compressed between two glass plates. The thermal properties of the photo-crosslinked PCLTAs were performed using differential scanning calorimeter (DSC, Q2000, TA instruments, New Castle, DE). The samples were first heated from room temperature to 100 °C and then cooled to -90 °C, followed by heating again to 100 °C at a rate of 10 °C/min in a dry nitrogen atmosphere. Linear viscoelastic properties of photo-crosslinked PCLTA disks (8 mm × 0.5 mm, diameter × thickness) were measured on a strain-controlled rheometer (RDS-2, Rheometric Scientific) at 37 °C. The tensile properties of photo-crosslinked PCLTA strips (0.5 mm × 0.8 mm × 10 mm, thickness × width × length) were tested using a dynamic mechanical analyzer (DMA, Q800, TA instruments) at 37 °C at a strain rate of 0.005/s. The surface morphologies of the photo-crosslinked PCLTAs were detected using a multi-mode atomic force microscope (AFM) with a Nanoscope III control system (Veeco Instruments, Santa Barbara, CA). A tapping mode over a scan area of 5 μm × 5 μm at a scan rate of 0.5 Hz was used. Root-mean-square surface roughness (R_{rms}) was measured from the height images using the Nanoscope 7.30 software (Veeco Instruments, Santa Barbara, CA).

2.2.2 *In vitro* SMC attachment and proliferation.

Photo-crosslinked PCLTA disks were sterilized in 70% ethanol solution and dried completely before cell studies. Rat primary aortic SMCs were cultured in a growth medium composed of Dulbecco's modified eagle medium (DMEM; Gibco, Grand Island, NY) supplemented with 10% fetal bovine serum (FBS; HyClone, Thermal Scientific) and 1% penicillin/streptomycin (Gibco, Grand Island, NY) in an incubator with 5% CO_2 and 95% relative humidity at 37 °C. SMCs were seeded onto PCLTA disks (10 × 0.5 mm, diameter × thickness) at a density of 15,000 cells/cm^2 and cultured for 4 h, 1, 2, and 4 days. A colorimetric cell metabolic assay (CellTiter 96 Aqueous One Solution, Promega, Madison, WI) was performed in each well to determine the number of

attached cells, which was correlated with the UV absorbance of the solution at 490 nm measured on the microplate reader (SpectraMax Plus 384, Molecular Devices, Sunnyvale, CA). Cell numbers were then quantified using the standard curve that was constructed using known cell numbers. SMCs attached on PCLTA disks were washed with phosphate buffered saline (PBS), fixed in 4% paraformaldehyde (PFA, Electron Microscopy Science) solution for 10 min at room temperature, washed with PBS twice, and then permeabilized with 0.1% Triton X-100 at room temperature for another 10 min. Cytoplasm was then stained using rhodamine-phalloidin (RP, Cytoskeleton Inc., Denver, CO) for 1 h at 37 °C, and cell nuclei were stained using 4',6-diamidino-2-phenylindole (DAPI) at room temperature. Then the cells were photographed using an Axiovert 25 light microscope (Carl Zeiss, Germany). From the cell images, cell area was determined on more than 50 non-overlapping cells at day 1 by using the ImageJ software (National Institutes of Health, Bethesda, MD).

2.2.3 Characterization of focal adhesions (FAs).

After day 1 post-seeding, SMCs attached on the PCLTA disks with crosslinking time of 0, 3, and 60 min were washed with PBS, fixed in 4% PFA solution, washed with PBS three times, and permeabilized with 0.1% Triton X-100 at room temperature for 10 min. Then the polymer disks with attached SMCs were incubated in 1% bovine serum albumin (BSA)/PBS at 37 °C for 30 min to reduce the background. After being washed with PBS three times, the polymer diskes with cells were incubated in monoclonal mouse antibody against vinculin (1:1000 in 1% PBS; Sigma) at room temperature for 2 h, and then washed with PBS three times again. Then the samples were cultured with goat anti-mouse IgG secondary antibody (1:200 in 1% PBS; Sigma) in dark at room temperature for 2 h. The samples were also stained using RP at 37 °C for another 1 h. The FAs were photographed using a Leica DM6000B fluorescent confocal microscope. The density, area,

and circularity (defined as $4\pi \times$ area/perimeter^2) of FAs were measured and averaged from 15 non-overlapping cells using ImageJ.

2.2.4 Statistical analysis.

Cell studies were performed in quadruplicates for each group at each time point. All values were expressed as mean ± standard deviation. The statistical significance ($p < 0.05$) in the difference between two groups was calculated using student's *t*-test.

2.3 Results and Discussion

2.3.1 Gel fraction and swelling ratio.

Crosslinking kinetics is important for understanding how a polymer network is formed and when crosslinking is sufficient for a variety of properties. The gel fraction and swelling ratio in CH_2Cl_2 of photo-crosslinked networks of the PCLTAs, 4arm and 6arm PCLAs with different crosslinking time are shown in Figure 2.2. Because the composition of acrylate groups was lower in PCLTA with a higher molecular weight, the gel fraction decreased from PCLTA8k to PCLTA10k and then PCLTA20k, at the same crosslinking time. For the same PCLTA, the gel fraction increased asymptotically with increasing the crosslinking time. The distance between two neighboring crosslinks in the network was determined by both the molecular weight of PCL precursor and crosslinking time [14,17,19]. Therefore, the swelling ratios increased from the range of 7.0-13.5 for PCLTA8k networks to 9.8-21.0 for PCLTA10k networks, and then 17.5-32.8 for PCLTA20k networks. For the same PCLTA, the swelling ratio of the network decreased with increasing the crosslinking time. The crosslinking efficiency was higher for PCLTA8k and PCLTA10k than for PCLTA20k. A crosslinking time of 10 min was needed to reach the highest gel fractions of 94% for PCLTA8k and 92% for PCLTA10k, while a longer crosslinking time of

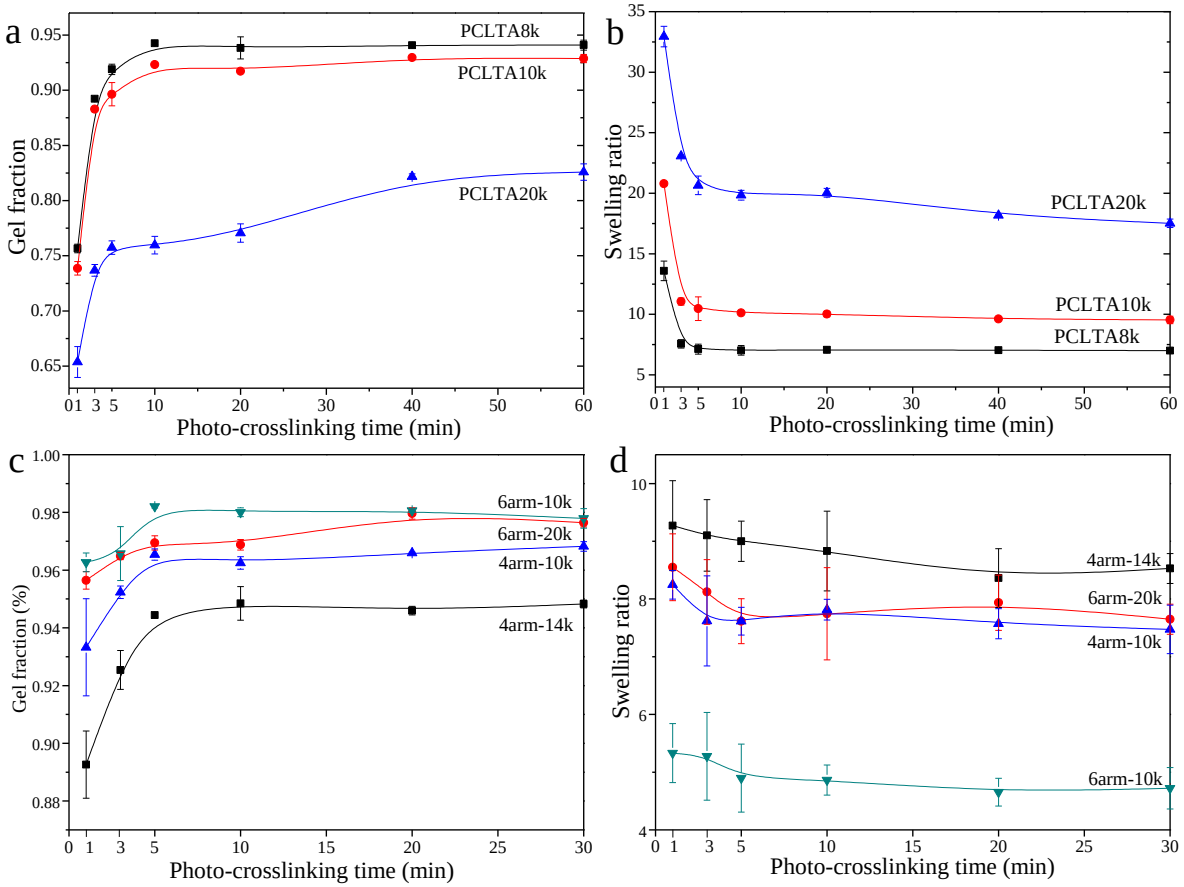

Figure 2.2 Gel fractions (a) and swelling ratios (b) of PCLTAs with different crosslinking time. Gel fractions (c) and swelling ratios (d) of 4arm and 6arm PCLAs (4arm-10k, 4arm-14k, 6arm-10k and 6arm-20k) with different crosslinking time.

40 min was needed for PCLTA20k to reach the highest gel fractions of 80%. When the crosslinking time increased from 1 to 3 min, the gel fraction increased and the swelling ratio decreased dramatically for all the PCLTAs with different molecular weights. When the crosslinking time was longer than 10 min, the increase in the gel fraction and the decrease in the swelling ratio of PCLTA8k and PCLTA10k could be barely noticeable, while the gel fraction increased and the swelling ratio decreased for PCLTA20k less sharply than the first 3 min.

Four PCLAs, i.e., 4arm-10k, 4arm-14k, 6arm-10k, and 6arm-20k, were used to compare with PCLTA10k in terms of the crosslinking rate (Figure 2.2). PCLA 4arm-10k and 6arm-10k had the same molecular weight while PCLA 4arm-14k and 6arm-20k had the same arm length as that in PCLTA10k. For the networks with the same molecular weight, PCLA 6arm-10k had the highest gel fractions and the lowest swelling ratios at all measured crosslinking time, followed by PCLA 4arm-10k and PCLTA10k. The highest gel fractions were 98% and 96% for PCLA 4arm-10k and 6arm-10k, respectively. For the networks with the same arm length, the PCLA 6arm-20k had the highest gel fraction and lowest swelling ratio at all measured crosslinking time, followed by PCLA 4arm-14k and PCLTA10k. The highest gel fractions were 97% and 94% for 4arm-14k and 6arm-20k PCLAs, respectively. Moreover, the crosslinking rates of 4arm and 6arm PCLAs were higher than those of PCLTAs, by showing that the highest gel fraction and lowest swelling ratio were reached at the crosslinking time shorter than 5 min. The results indicated that 4arm and 6arm PCLAs had higher crosslinking densities at the same crosslinking time.

2.3.2 Thermal and mechanical properties.

The thermal properties (T_m, ΔH_m, and χ_c) of photo-crosslinked PCLTAs for various crosslinking time in Table 2.1 were obtained from the DSC curves in Figure 2.3. T_m was the highest temperature of exothermal peaks during the heating round. χ_c was calculated using the equation of

Table 2.1 Thermal properties of the crosslinked PCLTAs with different crosslinking time.

Crosslinking time (min)	T_m (ºC)			ΔH_m (J/g)			χ_c (%)		
	8k	10k	20k	8k	10k	20k	8k	10k	20k
0	49.4	53.1	54.9	65.8	67.4	71.4	48.8	50.0	52.9
1	41.4	44.0	51.3	52.2	51.4	60.7	38.7	38.0	45.0
3	39.6	43.5	50.8	49.5	51.2	57.6	36.6	37.9	42.7
5	39.5	43.3	50.9	49.0	51.0	57.2	36.3	37.8	42.4
10	39.1	42.8	50.9	48.0	46.1	58.0	35.6	34.2	43.0
20	39.0	42.7	50.7	42.5	45.5	56.5	31.5	33.7	41.9
40	38.8	42.6	50.9	40.7	44.1	56.3	30.2	32.6	41.7
60	38.7	42.1	50.6	39.9	44.1	55.7	29.6	32.6	41.3

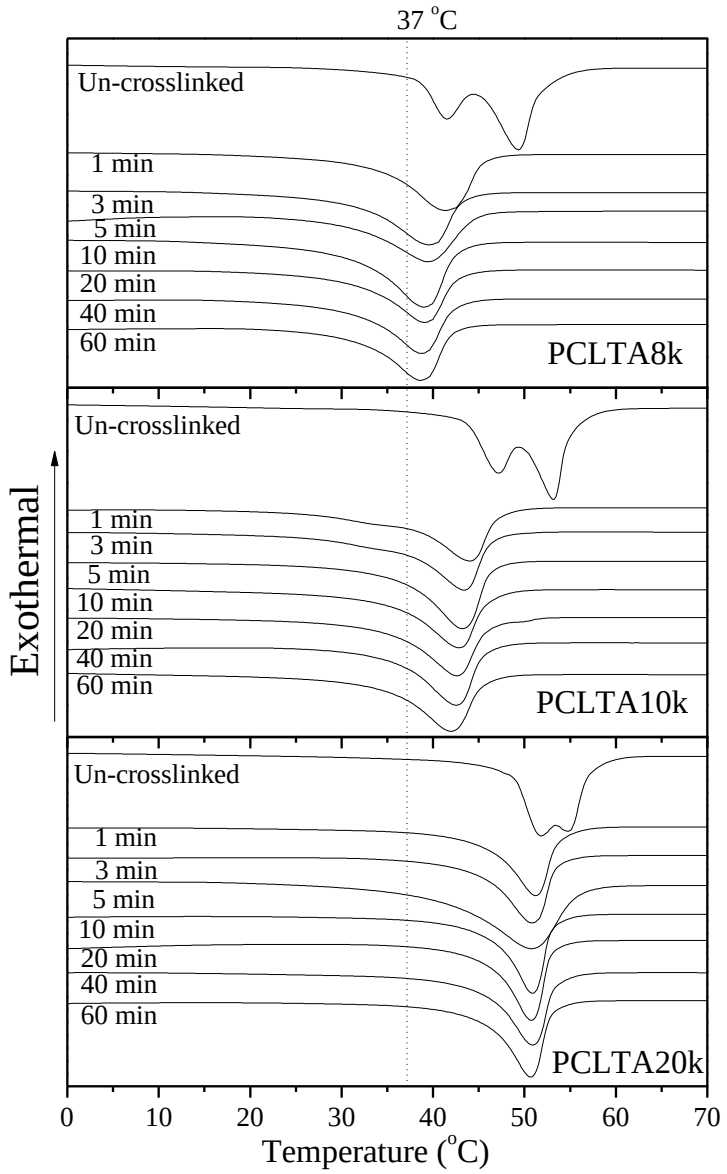

Figure 2.3 DSC curves of crosslinked PCLTAs with different crosslinking time.

$\chi_c = [\Delta H_m/(\Phi_{PCL} \cdot \Delta H_m^c)] \times 100\%$, where ΔH_m^c of completely crystalline PCL is 135 J/g [20]. All uncrosslinked PCLTAs were semi-crystalline with higher T_m and χ_c than the crosslinked counterparts as the crosslinks suppressed crystallinity. Nevertheless, all the crosslinked PCLTAs were still semi-crystalline at the physiological temperature (37 °C). At the same crosslinking time, both T_m and χ_c increased from PCLTA8k and PCLTA10k to PCLTA20k. The T_m of PCLTA10k was higher than that of PCLTA8k, while the difference in χ_c between PCLTA8k and PCLTA10k was insignificant. For the same PCLTA, T_m and χ_c decreased dramatically when the crosslinking time increased from 0 to 3 min. With increasing the crosslinking time further, χ_c still decreased but at a much lower rate while T_m only decreased slightly.

The rheological properties of the photo-crosslinked PCLTAs for various crosslinking time were measured at 37 °C using the dynamic frequency sweep mode. As shown in Figure 2.4, all curves showed that storage shear modulus (G') was much greater than loss shear modulus (G") and G' was independent of frequency. Meanwhile, η was approximately inversely proportional to frequency in the range of 1-100 rad/s, indicating the shear thinning behavior. At a low strain of 1%, uncrosslinked PCLTAs also showed the same phenomenon as the crosslinked PCLTAs, indicating that crystalline domains formed a physical network.

Tensile testing was performed at 37 °C to obtain the mechanical properties of photo-crosslinked PCLTAs at various crosslinking time. Representative stress-strain curves are shown in Figure 2.5. The E increased from the range of 15.1-41.0 MPa for PCLTA8k to 37.9-125.5 MPa for PCLTA10k, and then 74.1-257.2 MPa for PCLTA20k. Because PCLTA20k had a higher χ_c than those of PCLTA8k and PCLTA10k, the stiffness increased with the increase of molecular weight at the same crosslinking time. Different from crosslinked PCLTAs, uncrosslinked PCLTAs were extremely brittle, with the strain at break of less than 10%. For the same PCLTA, the stiffness

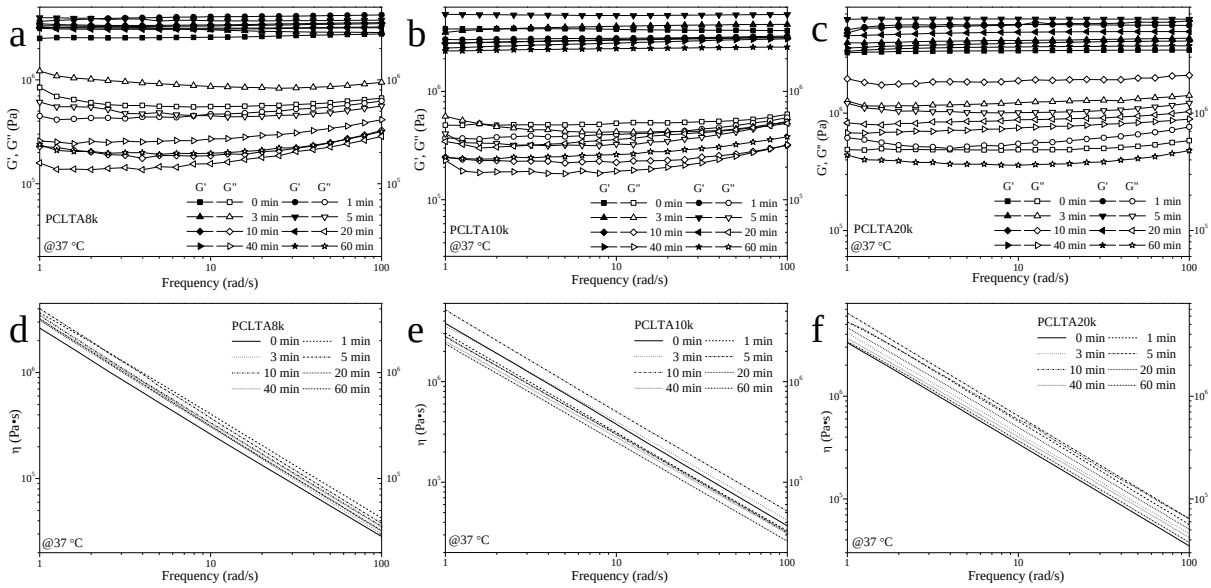

Figure 2.4 Storage modulus G' (solid symbols), and loss modulus G'' (open symbols) vs. frequency for PCLTAs (a, 8k; b, 10k; c, 20k) with different crosslinking time at 37 °C. Viscosity (lines) vs. frequency for PCLTAs (d, 8k; e, 10k; f, 20k) with different crosslinking time at 37 °C.

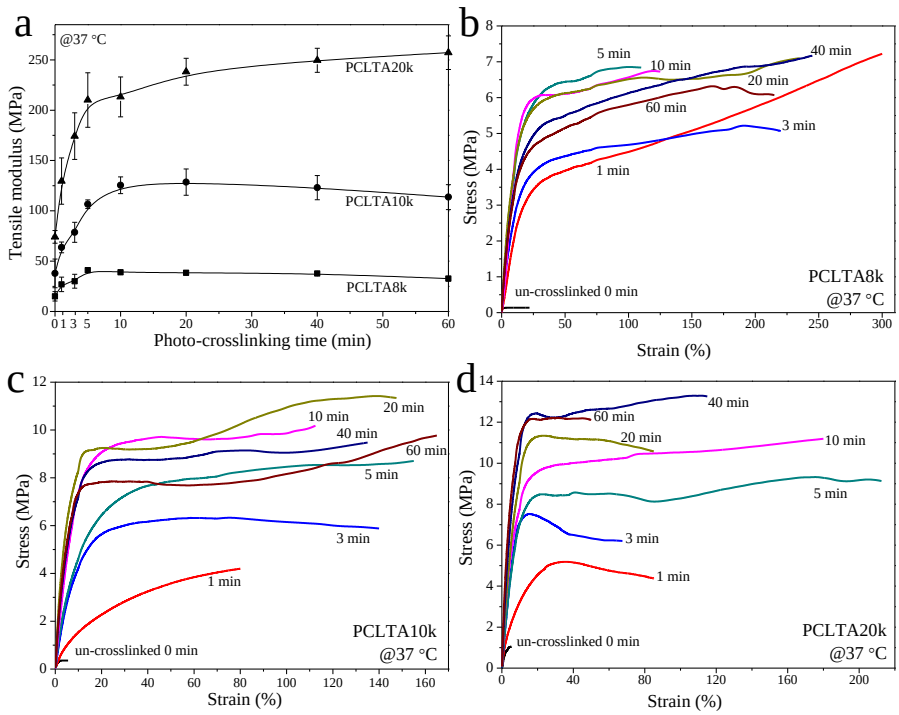

Figure 2.5 (a) Tensile modulus of PCLTAs (8k, 10k, and 20k) with different crosslinking time. Tensile stress-strain curves of PCLTAs (b, 8k; c, 10k; d, 20k) with different crosslinking time.

increased dramatically with increasing the crosslinking time from 0 to 5 min (15.1 to 41.0 MPa for PCLTA8k, 37.9 to 106.6 MPa for PCLTA10k, and 74.1 to 210.1 MPa for PCLTA20k), while the variance in stiffness was insignificant when the crosslinking time was longer than 10 min (41.0 to 32.6 MPa for PCLTA8k, 106.6 to 125.5 MPa for PCLTA10k, and 210.1 to 257.2 MPa for PCLTA20k). The stiffness of crosslinked PCLTA20k always increased with increasing the crosslinking time, while the highest stiffness of crosslinked PCLTA8k and 10k was observed at the crosslinking time of 5 and 10 min, respectively.

Similar to uncrosslinked PCLTAs, crosslinked PCLTA disks at various crosslinking time were compressed and smoothened between two glass plates, and the surface morphologies were detected using AFM (Figure 2.6). After the compression, the R_{rms} values of all the polymer disks were less than 20 nm without significant difference. Therefore, the effect of surface roughness on cell behaviors could be neglected.

2.3.3 *In vitro* SMC attachment and proliferation.

SMCs were seeded on the crosslinked PCLTA disks at various crosslinking time, and the results of cell attachment, proliferation, and area are shown in Figure 2.7. Consistent with the findings in previous studies [17,18,25-28], stiffer substrates could support SMC attachment and proliferation better, indicated by those on photo-crosslinked PCLTA20k were better than on photo-crosslinked PCLTA8k and PCLTA10k at the same crosslinking time. Specifically, the difference in SMC proliferation became more significant when the crosslinking time was longer than 5 min. For the same PCLTA, SMC attachment and proliferation were better when the crosslinking time was longer. Significant differences were found between the PCLTAs at crosslinking time longer than 10 min and shorter than 5 min. Among the crosslinking time of 0, 1, and 3 min, as well as 10,

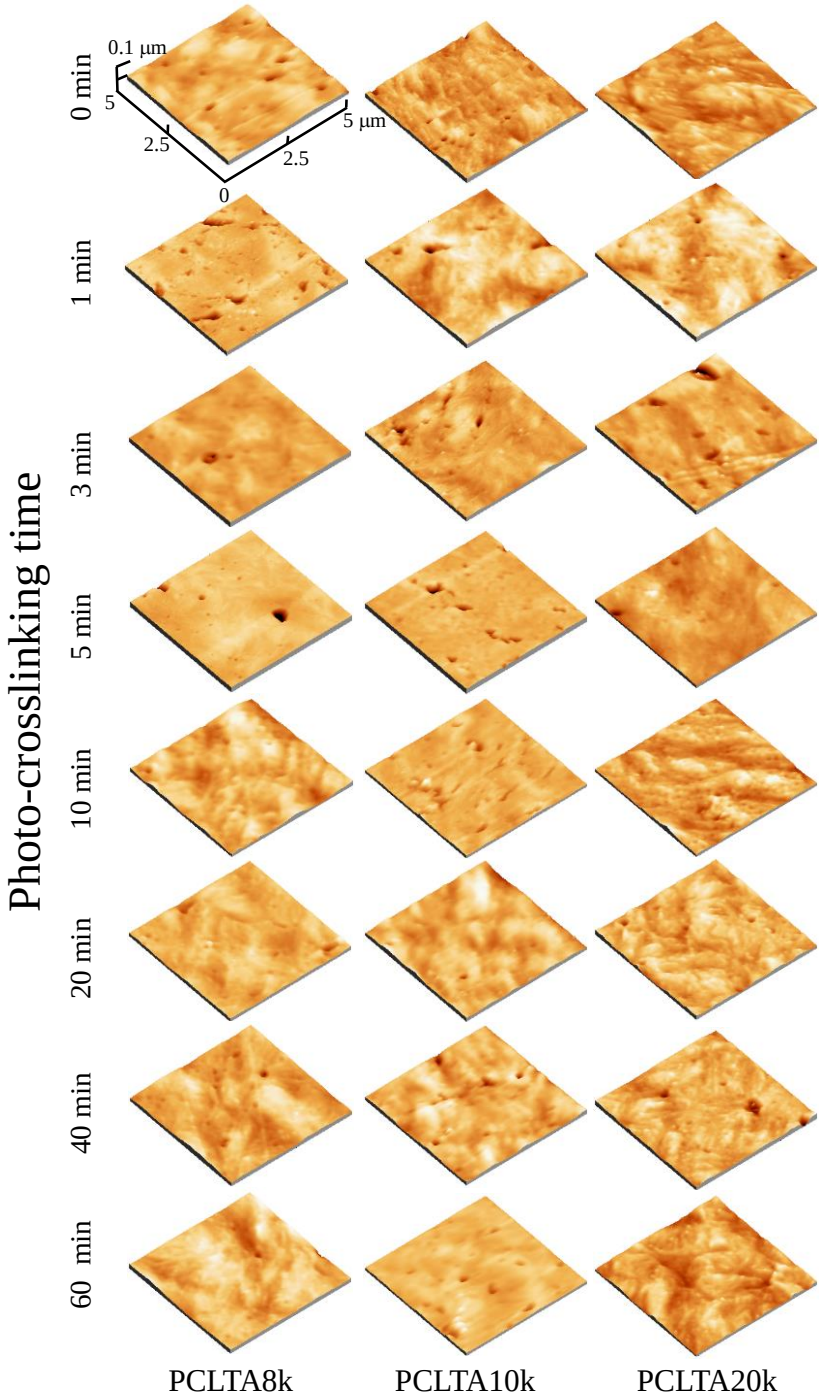

Figure 2.6 AFM 3D height images of PCLTAs with different crosslinking time.

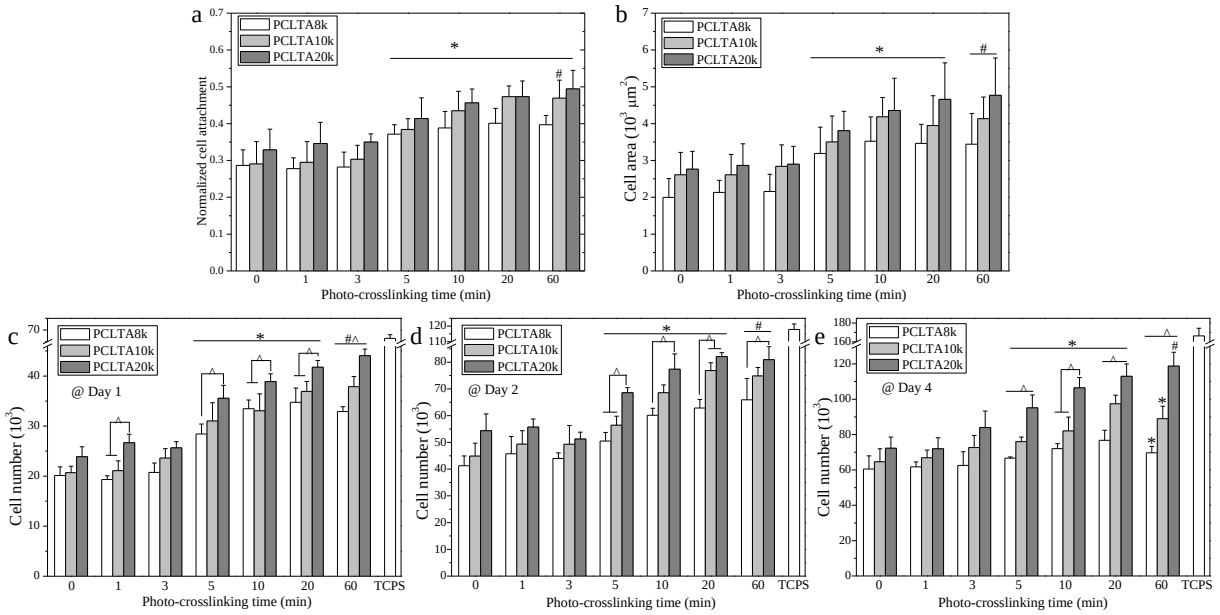

Figure 2.7 (a) Normalized SMC attachment at 4 h post seeding. (b) SMC areas at day 1 post-seeding. (c-e) SMC numbers at days 1, 2, and 4 post-seeding on the PCLTAs with different crosslinking time, respectively. *: $p < 0.05$ between the samples marked with the symbol with the corresponding data on the same PCLTA with crosslinking time of 0, 1, and 3 min. #: $p < 0.05$ between the samples marked with the symbol with the corresponding data on the same PCLTA with crosslinking time of 0, 1, 3, and 5 min. ^: $p < 0.05$ between the samples marked with the symbol.

20, and 60 min, SMC attachment and proliferation had no significant difference on the same PCLTA networks. The cell images stained with RP and DAPI (Figure 2.8) were consistent with the cell numbers obtained using the MTS assay. SMC spread areas also followed the same trend as in cell attachment and proliferation. However, no significant difference was found on different PCLTAs at the same crosslinking time. For the same PCLTA, when the crosslinking time was higher than 5 min, the increase in the cell area became more significant than on those at crosslinking time of 0, 1, and 3 min.

2.3.4 Focal adhesions.

FAs are able to respond to external mechanical signals and adjust their own properties and simultaneously trigger mechanotransduction for further regulation of cell growth and spreading [29,30], and therefore, were used to further evaluate cell adhesion to the polymer substrates. FAs in the SMCs cultured for one day on the crosslinked PCLTA8k, 10k, and 20k disks at crosslinking time of 0, 3, and 60 min were characterized and the results are shown in Figure 2.9. The FA density and area had the same trend as in the cell attachment and proliferation. For the same PCLTA, both FA density and area increased when the crosslinking time increased from 0 to 3, and 60 min. At the same crosslinking time, FA density increased from PCLTA8k to PCLTA10k and then PCLTA20k; however, the difference was only significant between PCLTA8k and the other two. Unlike FA density, FA area only increased with the increase of molecular weight, when the crosslinking time was 60 min. However, the FA circularity had no significant difference among all the crosslinked PCLTAs at different crosslinking time.

2.3.5 Further discussion.

The present chapter attempted to understand how to achieve various thermal and mechanical properties through controlled crystallinity and crosslinking density by using PCLA networks that

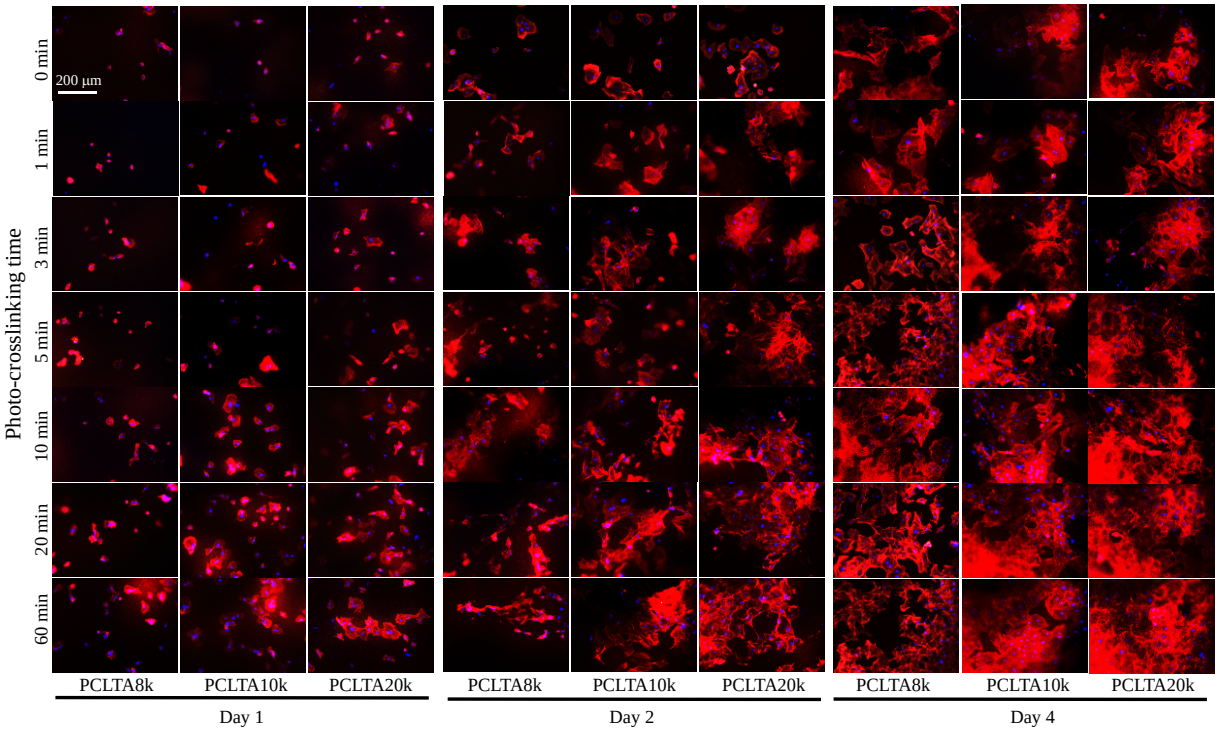

Figure 2.8 SMC images at days 1, 2, and 4 post-seeding stained using RP (red) and DAPI (blue) on PCLTAs with different crosslinking time. Scale bar of 200 µm is applicable to all.

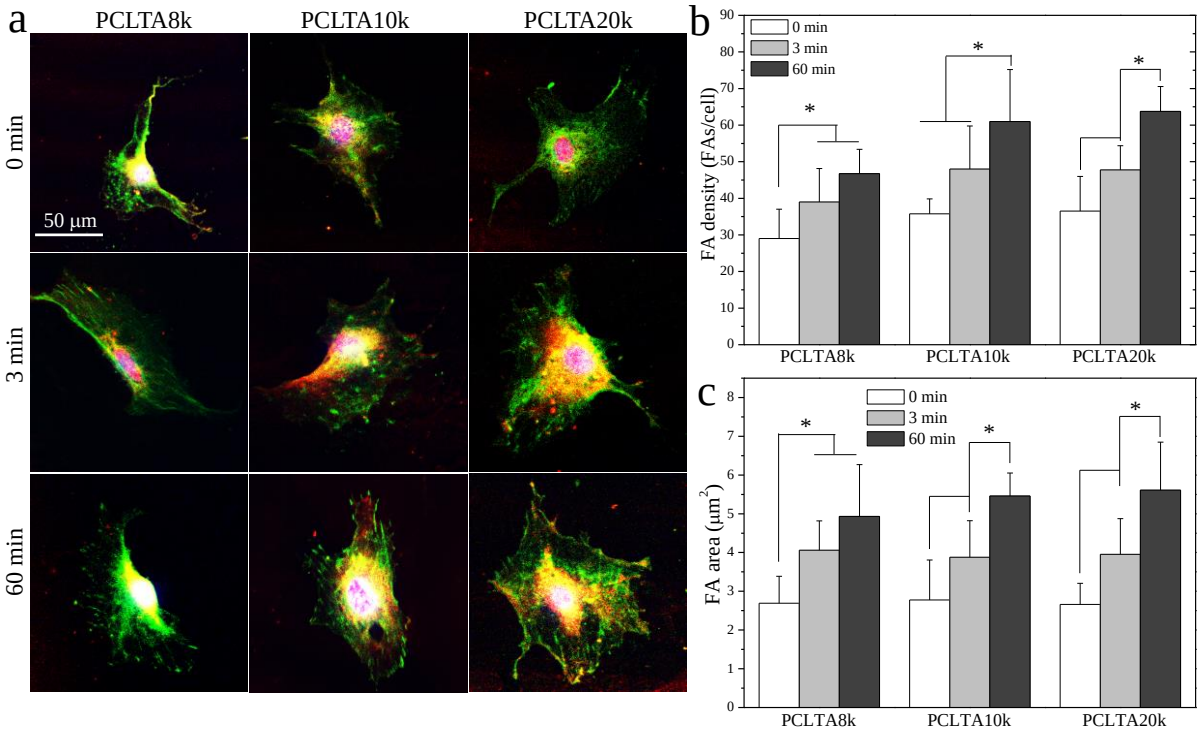

Figure 2.9 Characterizations of FAs in SMCs at day 1 post-seeding on PCLTAs with different crosslinking time (0, 3, and 60 min). (a) Immunofluorescence images of FAs in the cells with vinculin stained green, and F-actin stained red. Scale bar of 50 µm is applicable to all. Quantification of FAs in terms of (b) FA density, and (c) FA area. *: $p < 0.05$ between two samples marked with the same symbol.

were crosslinked for different time. Without showing detectable cytotoxicity, all the PCLTA networks could support SMC adhesion, proliferation, and spreading. Meanwhile, the molecular weight and crosslinking density of PCLAs resulted in different physical properties and consequently distinct SMC behaviors. Upon receiving the signals of the substrate materials, cells respond by adjusting their spreading, proliferation and other related processes [31].

In terms of crosslinking efficiency, difference was found between PCLTA20k and the other two PCLTAs with lower molecular weights. For PCLTA8k and PCLTA10k, crosslinking almost finished within 10 min of UV exposure, while for PCLTA20k, longer crosslinking time of 60 min could still increase the gel fraction and decrease the swelling ratio. The cell results showed the same trend with the gel fraction. With crosslinking time over 10 min, the densities of SMCs on crosslinked PCLTA8k and PCLTA10k disks did not vary too much. In contrast, the cell density on PCLTA20k still increased, although this increase was insignificant.

Different from crosslinked PCLTA10k and PCLA 4arm-10k, the crystallinity of crosslinked 6arm-10k was significantly suppressed by the crosslinks and demonstrated amorphous transparent characteristics at 37 °C even at the crosslinking time of 1 min. Although theoretically only one acrylate group is needed for participating in a network, having more arms or more acrylate end groups in one polymer architecture could improve crosslinking efficiency [21,32].

The cell responses to different crosslinked PCLA networks also provided the criteria of selecting biomaterials with sufficient crosslinking time to ensure appropriate crosslinking density and mechanical properties. PCLAs were proved to have high crosslinking efficiency under UV exposure for only 5-10 min, and therefore could be fabricated into two-dimensional substrates and three-dimensional scaffolds with better precision and controllability to fulfill different requirements for tissue engineering applications.

2.4 Conclusions

PCLTA8k, 10k, and 20k, PCLA 4arm-10k, 4arm-14k, 6arm-10k, and 6arm-20k were crosslinked under UV light for different time. A lower molecular weight and a longer crosslinking time resulted in a higher gel fraction, a lower swelling ratio, and a higher stiffness. At the same crosslinking time, 4arm and 6arm PCLAs had higher gel fractions and lower swelling ratios than PCLTA with the same arm length. Photo-crosslinking of PCLTA largely accomplished in the first 5 min of UV exposure. SMCs were cultured on these photo-crosslinked PCLTAs. At the same crosslinking time, PCLTA with a higher molecular weight could be crosslinked into substrates better supporting SMC attachment, proliferation, spreading, and focal adhesion. With the same molecular weight, better SMC attachment, proliferation, spreading and focal adhesion were found on the photo-crosslinked PCLTA substrates at a longer crosslinking time. The increments in SMC attachment, proliferation, and spreading were no longer significant after the crosslinking time was longer than 10 min.

References

1. Okada, M. *Prog. Polym. Sci.* **2002**, *27*(1), 87-133.

2. Perrin, D. E.; English, J. P. Polycaprolactone. In *Handbook of Biodegradable Polymers*; Domb, A. J.; Kost, J.; Wiseman, D., Eds.; Harwood Academic Publishers: Amsterdam, The Netherlands, 1997; pp 63-77.

3. Kweon, H.; Yoo, M. K.; Park, I. K.; Kim, T. H.; Lee, H. C.; Lee, H. S.; Oh, J. S.; Akaike, T.; Cho, C. S. *Biomaterials* **2003**, *24*(5), 801-808.

4. Nair, L. S.; Laurencin, C. T. *Prog. Polym. Sci.* **2007**, *32*(8), 762-798.

5. Lee, K. H.; Kim, H. Y.; Khil, M. S.; Ra, Y. M.; Lee, D. R. *Polymer* **2003**, *44*(4), 1287-1294.

6. Turunen, M. P. K.; Korhonen, H.; Tuominen, J.; Seppälä, J. V. *Polym. Int.* **2001**, *51*(1), 92-100.

7. Lendlein, A.; Schmidt, A. M.; Langer, R. *Proc. Natl. Acad. Sci. U.S.A.* **2001**, *98*(3), 842-847.

8. Nagata, M.; Kanechika, M.; Sakai, W.; Tsutsumi, N. *J. Polym. Sci. Part A Polym. Chem.* **2002**, *40*(24), 4523-4529.

9. Nagata, M.; Kato, K.; Sakai, W.; Tsutsumi, N. *Macromol. Biosci.* **2006**, *6*(5), 333-339.

10. Matsuda, T.; Mizutani, M.; Arnold, S. C. *Macromolecules* **2000**, *33*(3), 795-800.

11. Han, C.; Ran, X.; Su, X.; Zhang, K.; Liu, N.; Dong, L. *Polym. Int.* **2007**, *56*(5), 593-600.

12. Zhu, G.; Xu, Q.; Qin, R.; Yan, H.; Liang, G. *Radiat. Phys. Chem.* **2005**, *74*(1), 42-50.

13. Jabbari, E.; Wang, S.; Lu, L.; Gruetzmacher, J. A.; Ameenuddin, S.; Hefferan, T. E.; Currier, B. L.; Windebank, A. J.; Yaszemski, M. J. *Biomacromolecules* **2005**, *6*(5), 2503-2511.

14. Wang, S.; Yaszemski, M. J.; Gruetzmacher, J. A.; Lu, L. *Polymer* **2008**, *49*(26), 5692-5699.

15. Fisher, J. P.; Dean, D.; Engel, P. S.; Mikos, A. G. *Annu. Rev. Mater. Res.* **2001**, *31*(1), 171-181.

16. Ifkovits, J. L.; Burdick, J. A. *Tissue Eng.* **2007**, *13*(10), 2369-2385.

17. Cai, L.; Wang, S. *Polymer* **2010**, *51*(1), 164-177.

18. Liu, X. 2014. Phenotypic modulation of smooth muscle cells on biodegradable elastomeric substrates. Doctoral dissertation. The University of Tennessee, Knoxville.

19. Wang, K.; Cai, L.; Wang, S. *Polymer* **2011**,*52*(13), 2827-2839.

20. Wang, S.; Kempen, D. H.; Simha, N. K.; Lewis, J. L.; Windebank, A. J.; Yaszemski, M. J.; Lu, L. *Biomacromolecules* **2008**, *9*(4), 1229-1241.

21. Zhu, J. *Biomaterials* **2010**, *31*(17), 4639-4656.

22. Liu, Q.; Jiang, L.; Shi, R.; Zhang, L. *Prog. Polym. Sci.* **2012**, *37*(5), 715-765.

23. Venhoven, B. A. M.; De Gee, A. J.; Davidson, C. L. *Biomaterials* **1996**, *17*(24), 2313-2318.

24. Polymer Handbook. 3rd ed. Brandrup, J.; Immergut, E. H.; Eds.; Wiley: New York, 1989.

25. Wong, J. Y.; Velasco, A.; Rajagopalan, P.; Pham, Q. *Langmuir* **2003**, *19*(5), 1908-1913.

26. Discher, D. E.; Janmey, P.; Wang, Y. L. *Science* **2005**, *310*(5751), 1139-1143.

27. McDaniel, D. P.; Shaw, G. A.; Elliott, J. T.; Bhadriraju, K.; Meuse, C.; Chung, K. H.; Plant, A. L. *Biophys. J.* **2007**, *92*(5), 1759-1769.

28. Isenberg, B. C.; DiMilla, P. A.; Walker, M.; Kim, S.; Wong, J. Y. *Biophys. J.* **2009**, *97*(5), 1313-1322.

29. Parsons, J. T.; Horwitz, A. R.; Schwartz, M. A. *Nat. Rev. Mol. Cell Biol.* **2010**, *11*(9), 633-643.

30. Zamir, E.; Geiger, B. *J. Cell Sci.* **2001**, *114*(20), 3583-3590.

31. Jiang, F. X.; Yurke, B.; Schloss, R. S.; Firestein, B. L.; Langrana, N. A. *Biomaterials* **2010**, *31*(6), 1199-1212.

32. Matsuda, T.; Mizutani, M. *Macromolecules* **2000**, *33*(3), 791-794.

Chapter III. Smooth Muscle Cell Responses to Hydrolyzed Poly(ε-caprolactone) Triacrylate/Methoxyl Polyethylene Glycol Monoacrylate Networks

Abstract

Photo-crosslinked networks of poly(ε-caprolactone) triacrylate (PCLTA) and methoxyl polyethylene glycol monoacrylate (mPEGA)/PCLTA with a weight fraction of mPEGA of 5% were degraded in sodium hydroxide (NaOH) aqueous solution at 37 °C via expedited hydrolysis for different time periods of 24, 48 and 60 h to obtain different surface topographies and roughnesses. Longer NaOH hydrolysis time resulted in rougher surfaces and lower water contact angles for both PCLTA and mPEGA/PCLTA networks. These networks were used as substrates for culturing rat aortic smooth muscle cells (SMCs). At all hydrolysis time periods, SMCs were found to have better attachment, proliferation, spreading, and focal adhesions on mPEGA/PCLTA networks than on PCLTA networks, as the addition of a small amount of mPEGA increased surface hydrophilicity without significantly decreasing the stiffness. For both PCLTA and mPEGA/PCLTA networks, longer NaOH hydrolysis time resulted in better SMC attachment, proliferation, spreading, and focal adhesions. We also found that the mPEGA/PCLTA network degraded faster and had higher water adsorption than the PCLTA network in both phosphate buffered saline (PBS) and NaOH aqueous solution. Both PCLTA and mPEGA/PCLTA networks could be fully degraded in NaOH solution in 40 days while they were quite stable in PBS for over 16 months with weight residue of higher than 80%, and the both networks remained high degrees of crystallinity during the degradation.

3.1 Introduction

Poly(ε-caprolactone) (PCL) is a semi-crystalline, biodegradable polymer with a low glass transition temperature (T_g) of -60 °C and a low melting temperature (T_m) of ~60 °C, and has been widely used as a biomaterial [1-5]. PCL can be biodegraded by outdoor living organisms such as bacteria and fungi, but its degradation in animal and human bodies lacking suitable enzymes is via a much slower mechanism, hydrolysis [6]. The hydrolytic degradation process of PCL normally takes 2-4 years [6,7]. In hydrolytic degradation, random hydrolytic chain scissions occur and reduce the polymer molecular weight [7-10]. The hydrolytic degradation rates of PCL were found similar in molecular weight decrease and weight loss in both *in vitro* (saline) and *in vivo* (rabbit and rat) conditions [11,12]. In a basic medium such as sodium hydroxide (NaOH) aqueous solution, the hydrolysis of the ester bond is faster than in phosphate buffered saline (PBS) or animal/human bodies and thus the degradation of PCL can be accelerated [13,14].

The low degradation date of PCL via hydrolysis is attributed to the low hydrophilicity and high crystallinity, which restrict the capacity of water molecules to penetrate into the structure. The degradation rate of PCL can be affected by its molecular weight and morphology as the molecular weight determines the hydrophilicity and crystallinity and the morphology controls the surface area [7,8,15]. In our research group, several photo-crosslinked PCL-based networks were developed for regulating cellular responses and fabricating biomedical devices [16-18]. The degradation of crosslinked PCL network was different from PCL as the crystallinity of a PCL-based network was reduced by the crosslinks, accelerating the degradation in PBS or NaOH solution [19-21]. Meanwhile, the enzymatic degradation of PCL-based networks was found to be slower than that of PCL [21,22]. After hydrolysis, surface roughness and chemistry of PCL

substrates were altered and such change improved attachment and proliferation of mesenchymal stem cells, endothelial cells, smooth muscle cells (SMCs), cardiac cells, and osteoblasts [23-30].

To improve the hydrophobicity of PCL that limits degradation and cell proliferation, copolymers or blends containing PCL or PCL composites with inorganic fillers have been developed [31-35]. Among the components to enhance the surface hydrophilicity/wettability of PCL, polyethylene glycol (PEG) is one most commonly used polymer that can also inhibit immunogenic activities, promote biocompatibility, and accelerate the degradation [36-39]. In our research group, methoxyl PEG monoacrylates (mPEGAs) with different molecular weights was synthesized via acrylation of methoxyl PEGs in the presence of potassium carbonate (K_2CO_3) and photo-crosslinked into PCL-based networks as dangling chains [16,40]. Through this method, the grafted mPEGA chains not only appeared on the surface but also inside the bulk of the networks, rendering a uniform density of hydrophilicity even after degradation. Moreover, addition of mPEGA chains at the weight fraction of mPEGA (Φ_{mPEGA}) of 5% into PCL triacrylate (PCLTA) network was proved not to decrease the elastic modulus of the network [16,40].

The aim of the present chapter was to investigate the surface features and chemistry of PCLTA and mPEGA/PCLTA (Φ_{mPEGA} = 5%) networks with different hydrolysis time in 1 N NaOH aqueous solution and the rat aortic SMC responses to the degraded surfaces, including cell attachment, proliferation, spreading and focal adhesions. To compare with the accelerated hydrolysis in NaOH solution, the degradation of the PCLTA and mPEGA/PCLTA networks in PBS was also studied.

3.2 Materials and Methods

3.2.1 Photo-crosslinking and characterization of PCLTA and mPEGA/PCLTA networks.

PCLTA with a number-average molecular weight (M_n) of 9800 g/mol and a weight-average molecular weight (M_w) of 12300 g/mol and mPEGA with M_n of 330 g/mol and M_w of 420 g/mol used in this chapter were synthesized via our reported method [16,17]. Photo-initiator, phenyl bis(2,4,6-trimethyl benzoyl) phosphine oxide (BAPO, IRGACURE 819, Ciba Specialty Chemicals, Tarrytown, NY) was used in photo-crosslinking. PCLTA or mPEGA/PCLTA solutions mixed with BAPO (polymer/BAPO/CH_2Cl_2 solution, 1.5 g/15 mg/500 μL) were crosslinked with UV light (SB-100P, Spectronics Corp., Westbury, NY, λ= 365 nm, Intensity: 4800 w/cm^2) for 20 min (Figure 3.1). After crosslinking, crosslinked PCLTA and mPEGA/PCLTA disks were soaked in acetone for two days to remove the sol fraction, dried in vacuum, and compressed between two glass plates to smoothen them. [16,17]. Crosslinked PCLTA and mPEGA/PCLTA disks were immersed in 1 N NaOH aqueous solution at 37 °C for 24, 48 and 60 h. Then the polymer disks were soaked in distilled water for 2 days to remove the residual NaOH, followed by complete drying in vacuum. The surface morphologies of the polymer disks hydrolyzed for different time periods were characterized using scanning electron microscopy (SEM; S-3500, Hitachi Instruments, Tokyo, Japan) at a voltage of 2 kV. Water contact angles on the polymer disks hydrolyzed for different time periods were measured at 37 °C using a Ramé-Hart NRC C. A. goniometer (model 100-00-230). For each disk, 20 μL of distilled water (pH = 7.0) was injected onto the surface and equilibrated for 30 s before the measurement. A tangent method was used to read the water contact angle in degrees. Four disks were used for each sample to calculate the average and standard deviation using the ImageJ software (National Institutes of Health, Bethesda, MD).

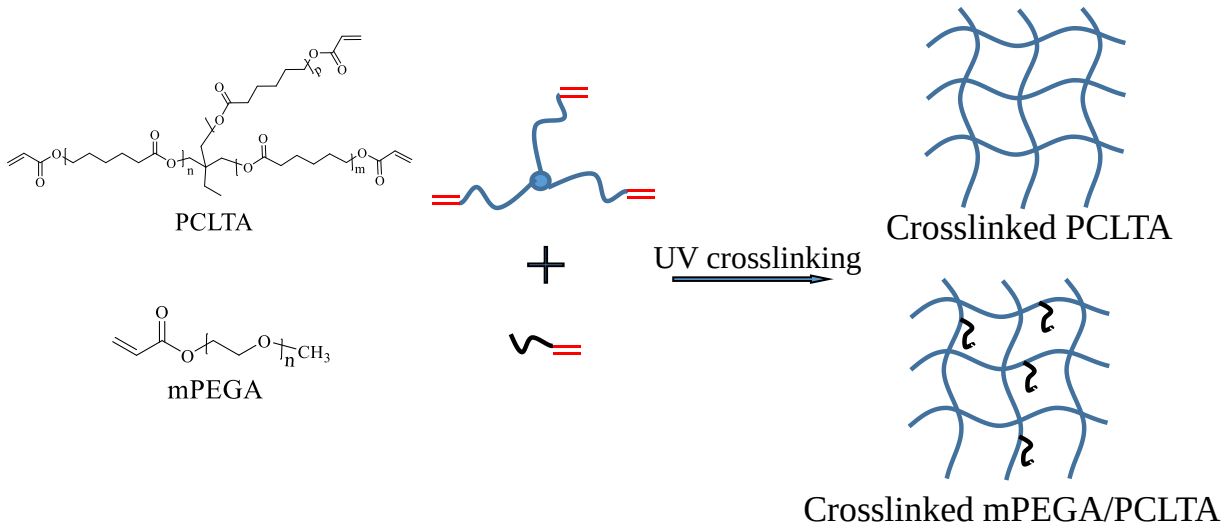

Figure 3.1 Photo-crosslinking of PCLTA and mPEGA/PCLTA networks.

3.2.2 *In vitro* SMC attachment and proliferation.

The polymer disks hydrolyzed for different time periods were sterilized in 70% ethanol solution and dried completely in vacuum before the cell studies. SMCs were cultured in a growth medium composed of Dulbecco's modified eagle medium (DMEM; Gibco, Grand Island, NY) supplemented with 10% fetal bovine serum (FBS; HyClone, Thermal Scientific) and 1% penicillin/streptomycin (Gibco) in an incubator with 5% CO_2 and 95% relative humidity at 37 °C. SMCs were seeded onto the polymer disks (10 × 0.5 mm, diameter × thickness) hydrolyzed for different time periods at a density of 15,000 cells/cm^2 and cultured for 4 h, 1, 2, and 4 days. A colorimetric cell metabolic assay (CellTiter 96 Aqueous One Solution, Promega, Madison, WI) was performed in each well to determine the number of attached cells, which was correlated to the UV absorbance of the solution at 490 nm measured on a microplate reader (SpectraMax Plus 384, Molecular Devices, Sunnyvale, CA). Cell numbers were then quantified using the standard curve constructed with known cell numbers. SMCs attached on the polymer disks were washed with PBS, fixed in 4% paraformaldehyde (PFA; Electron Microscopy Science) solution for 10 min at room temperature, washed with PBS twice, and then permeabilized with 0.1% Triton X-100 at room temperature for another 10 min. Cytoplasm was then stained using rhodamine-phalloidin (RP; Cytoskeleton Inc., Denver, CO) for 1 h at 37 °C, and cell nuclei were stained using 4',6-diamidino-2-phenylindole (DAPI) at room temperature. Then the cells were photographed using an Axiovert 25 light microscope (Carl Zeiss, Germany). From the cell images on the polymer disks, cell area and perimeter were measured on more than 25 non-overlapping cells at day 1 using ImageJ and cell circularity defined as $4\pi \times \text{area}/\text{perimeter}^2$ was calculated.

3.2.3 Characterization of focal adhesions (FAs).

After one-day culture, SMCs attached on the polymer disks hydrolyzed for different time periods were washed with PBS, fixed in 4% PFA solution, washed with PBS three times, and permeabilized with 0.1% Triton X-100 at room temperature for 10 min. Then the polymer disks with attached SMCs were incubated in 1% bovine serum albumin (BSA)/PBS at 37 °C for 30 min to remove the residue of PFA and Triton X-100 on the substrates. After being washed with PBS three times, the polymer disks with attached SMCs were incubated in monoclonal mouse antibody against vinculin (1:1000 in 1% PBS; Sigma) at room temperature for 2 h, and then washed with PBS three times again. Then the polymer disks with attached SMCs were cultured with goat anti-mouse IgG secondary antibody (1:200 in 1% PBS; Sigma) in dark at room temperature for 2 h. The samples were also stained using RP at 37 °C for another 1 h. The FAs in the cells were photographed on a Leica DM6000B fluorescent confocal microscope (Buffalo Grove, IL). The density, area, and circularity of the FAs were determined on more than 15 non-overlapping cells using ImageJ.

3.2.4 *In vitro* degradation.

In vitro degradation of both PCLTA and mPEGA/PCLTA networks was performed as follows. Photo-crosslinked PCLTA and mPEGA/PCLTA disks (~200 mg) were immersed in PBS or 1 N NaOH solution at 37 °C. After the degraded samples were fully washed and dried, the degraded weights (W_d) were measured and compared with their initial weights (W_i). The weight fraction left in the degraded polymer sample was calculated using the equation of $W_d/W_i \times 100\%$, every three days or one month for the polymer disks hydrolyzed in NaOH solution or PBS, respectively. Dried polymer disks hydrolyzed for different time periods were immersed in water at 37 °C for one day and weighed as W_w. The percentage of water absorption was determined by the equation of

$(W_w - W_d)/W_d \times 100\%$. The thermal properties of photo-crosslinked PCLTA and mPEGA/PCLTA disks hydrolyzed for 0, 3, 12, and 18 days were measured using differential scanning calorimeter (DSC, Q2000, TA Instruments, New Castle, DE). The samples were first heated from room temperature to 100 °C and then cooled to -80 °C, followed by another heating round to 100 °C at a rate of 10 °C/min in dry nitrogen.

3.2.5 Statistical analysis.

Cell studies were performed in quadruplicates for each group at each time point. All values were expressed as mean ± standard deviation. The statistical significance ($p < 0.05$) in the difference between two groups was calculated using the student's *t*-test.

3.3 Results and Discussion

3.3.1 Thermal and mechanical properties.

The surface morphologies of crosslinked PCLTA and mPEGA/PCLTA disks hydrolyzed for different time periods are shown in the SEM images in Figure 3.2. The original polymer disks were flat and smooth as they were compressed between two glass plates. After hydrolysis in NaOH aqueous solution, both crosslinked PCLTA and mPEGA/PCLTA disks showed rough surfaces with porous structures. The surfaces were rougher and the pores were larger at longer hydrolysis time. In addition, the surface of crosslinked mPEGA/PCLTA disk was always rougher and with larger pores than the surface of crosslinked PCLTA disk at the same hydrolysis time.

Surface energies of biomaterials are frequently correlated with the onset of biological processes such as protein adsorption and cell adhesion, and wettability when implanted [16,40,41]. Water contact angle on the surface of a biomaterial is used to evaluate surface energy and hydrophilicity. Figure 3.3 shows the water contact angles on the surfaces of crosslinked PCLTA

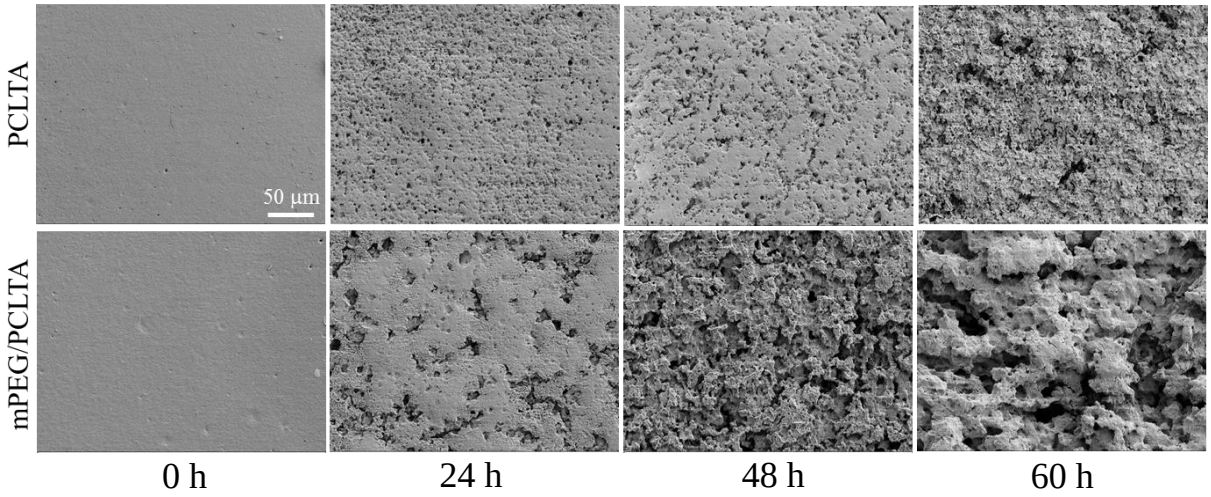

Figure 3.2 SEM images of PCLTA and mPEGA/PCLTA networks with different NaOH hydrolysis time. Scale bar of 50 μm is applicable to all.

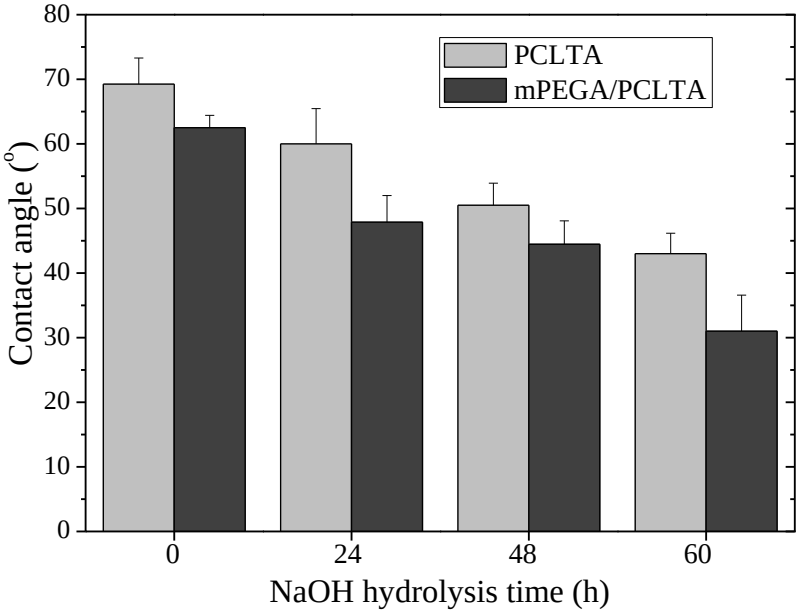

Figure 3.3 Water contact angles of PCLTA and mPEGA/PCLTA networks with different NaOH hydrolysis time.

and mPEGA/PCLTA disks. For both series, the water contact angle decreased on the disks hydrolyzed for longer time, and it was always higher on photo-crosslinked PCLTA disks than on photo-crosslinked mPEGA/PCLTA disks.

The water contact angle on the original photo-crosslinked PCLTA was 69 ± 4°, and the value decreased significantly to 60 ± 5°, 51 ± 3°, and 43 ± 3° for the disks hydrolyzed for 24, 48, and 60 h, respectively. These results indicated that the surface hydrophilicity was higher when the hydrolysis time was longer. A similar trend was found on photo-crosslinked mPEGA/PCLTA disks, by decreasing greatly from 63 ± 2° to 31 ± 6° with increasing the hydrolysis time from 0 to 60 h. Both surface hydrophilicity and roughness affect the capability of the surface to adsorb proteins from culture medium [42].

3.3.2 *In vitro* SMC attachment and proliferation.

SMCs were seeded on the photo-crosslinked PCLTA and mPEGA/PCLTA disks hydrolyzed for different time periods, and the results on SMC attachment at 4 h and 4-day proliferation are shown in Figure 3.4. Consistent with the previous study in our research group on the flat disks of photo-crosslinked PCLTA and mPEGA/PCLTA [16], photo-crosslinked mPEGA/PCLTA (Φ_{mPEGA} = 5%) better supported SMC attachment and proliferation than photo-crosslinked PCLTA at the same hydrolysis time. For both photo-crosslinked PCLTA and mPEGA/PCLTA disks, SMC attachment and proliferation were better when the polymer disks were hydrolyzed for longer time. On both polymer networks, the differences in SMC attachment and proliferation between the hydrolysis time of 48 and 60 h were not significant. The cell images stained with RP and DAPI are shown in Figure 3.5. SMC spread area also followed the same trend as in cell attachment and proliferation. However, the difference in the cell area between the PCLTA networks and the mPEGA/PCLTA networks at the same hydrolysis time was not significant. The SMC circularity

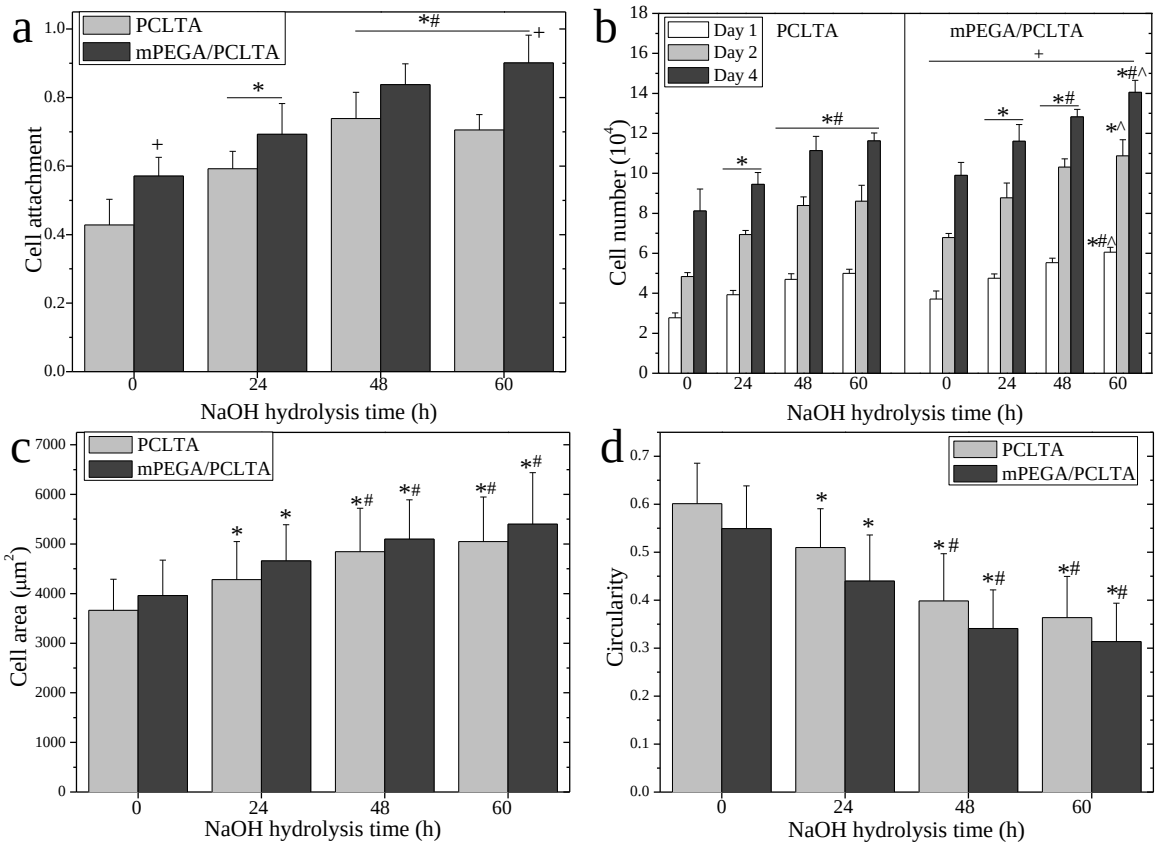

Figure 3.4 SMC attachment and proliferation on PCLTA and mPEGA/PCLTA networks with different NaOH hydrolysis time. (a) Normalized SMC attachment at 4 h post-seeding. (b) SMC numbers at days 1, 2, and 4 post-seeding. (c) SMC areas at day 1 post-seeding. (d) SMC circularities. *: significantly higher ($p < 0.05$) than the corresponding data on 0 h samples. $^{\#}$: significantly higher ($p < 0.05$) than the corresponding data on 24 h samples. ^: significantly higher ($p < 0.05$) than the corresponding data on 48 h samples. $^{+}$: significantly higher ($p < 0.05$) than the corresponding data on the PCLTA network with the same NaOH hydrolysis time.

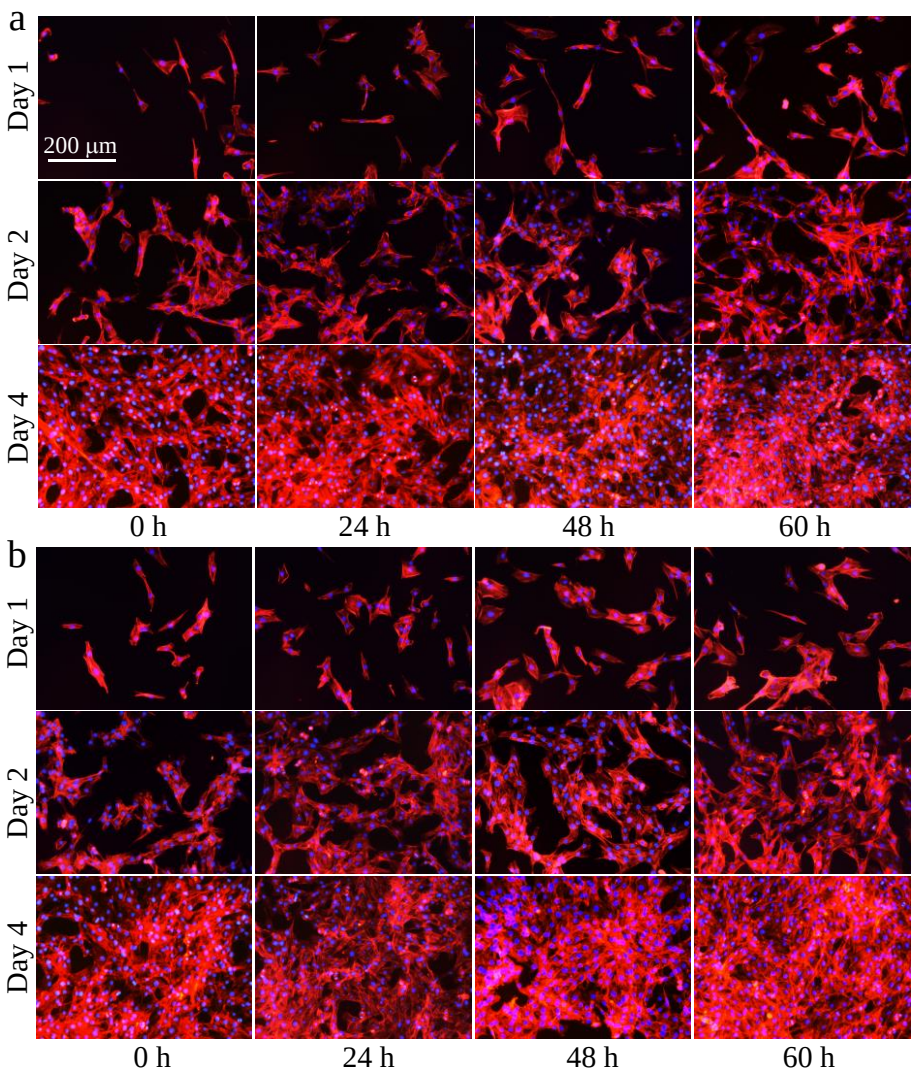

Figure 3.5 SMC images at days 1, 2, and 4 post-seeding stained using RP (red) and DAPI (blue) on PCLTA (a) and mPEGA/PCLTA (b) networks with different NaOH hydrolysis time. Scale bar of 200 μm is applicable to all images.

on the mPEGA/PCLTA network was always smaller than that on the PCLTA network at the same hydrolysis time. With increasing the hydrolysis time from 0 to 48 h, the SMC circularity on both PCLTA and mPEGA/PCLTA networks decreased significantly although there was no significant difference between the hydrolysis time periods of 48 and 60 h.

The nuclei of SMCs on the polymer disks hydrolyzed for different time periods were also characterized, as shown in Figure 3.6. The cell nuclear area was larger on the mPEGA/PCLTA network than that on the PCLTA network at the same hydrolysis time, and on the disks with longer hydrolysis time for both polymer series. Nevertheless, significant difference in the cell nuclear area was only found between the original polymer network and the hydrolyzed ones. Unlike the nuclear area, the nuclear circularity had no difference among all the samples although the values on the PCLTA networks were always slightly lower than on the mPEGA/PCLTA counterparts, suggesting that the surface morphologies caused by hydrolysis did not induce elongation of cell nuclei.

3.3.3 Focal adhesions.

FAs with functional diversity serve as the anchorage of a cell and signal carriers to report the ECM condition to cell nucleus and the feedback in turn affects the cell behavior [43,44]. The FAs in SMCs cultured for one day on the disks of photo-crosslinked PCLTA and mPEGA/PCLTA hydrolyzed for different time periods were characterized, as shown in Figure 3.7. With increasing the hydrolysis time from 0 to 60 h, the FA densities and areas on the hydrolyzed polymer disks were substantially larger than those on the original ones for both PCLTA and mPEGA/PCLTA networks. At longer hydrolysis time periods (> 48 h for FA density and > 24 h for FA area), the differences in FA densities and areas became insignificant. Meanwhile, the FA densities and areas were larger on the mPEGA/PCLTA networks than on the PCLTA networks at the same hydrolysis

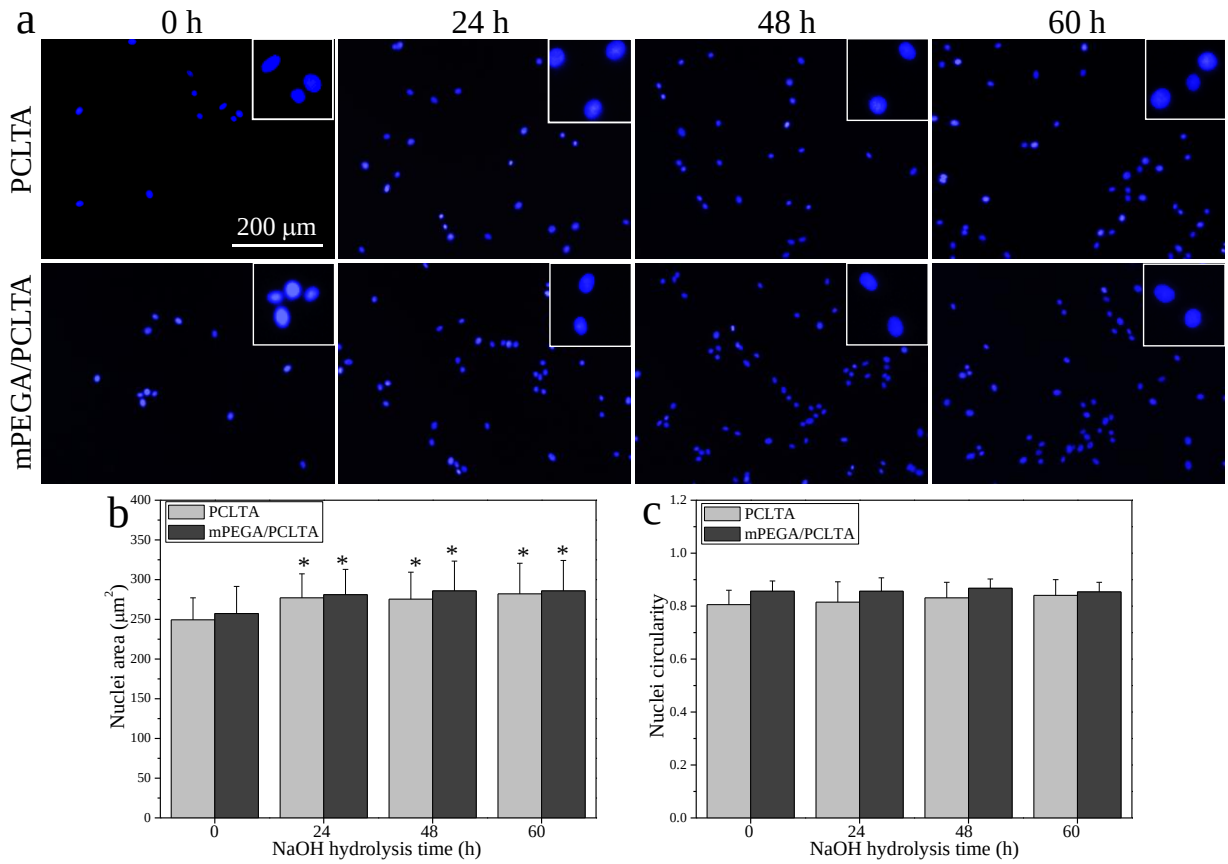

Figure 3.6 (a) Fluorescent images of SMC nuclei stained with DAPI on PCLTA and mPEGA/PCLTA networks with different NaOH hydrolysis time at day 1 post-seeding. (b) Average area and (c) circularity of SMC nuclei on these substrates. *: $p < 0.05$ compared to the corresponding data on 0 h samples. Scale bar of 200 μm is applicable to all, and the scale of embedded images are 70 μm.

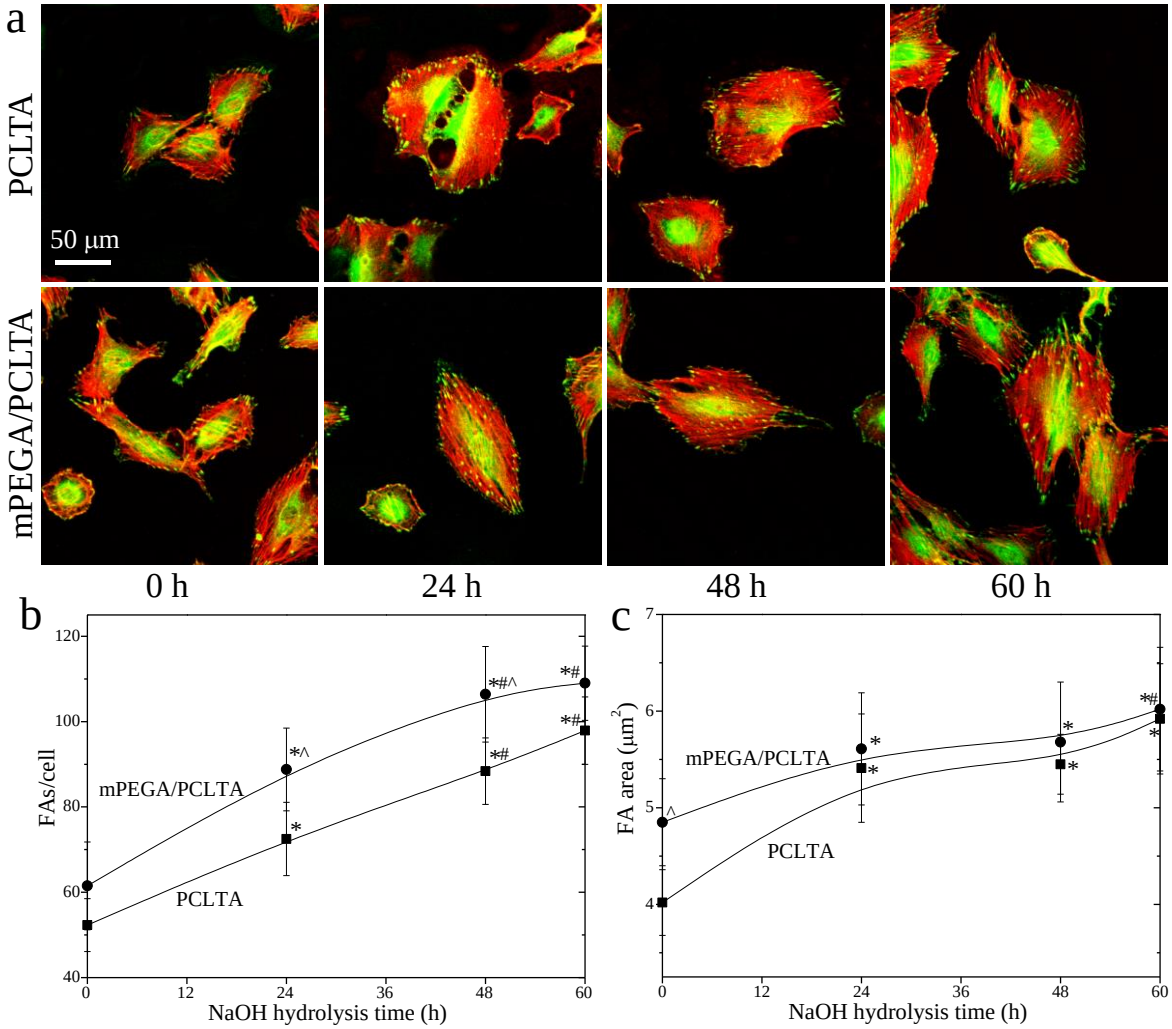

Figure 3.7 Characterizations of FAs in SMCs on crosslinked PCLTA and mPEGA/PCLTA networks with different NaOH hydrolysis time at day 1 post-seeding. (a) Immunofluorescence images of FAs in the cells with vinculin stained green, and F-actin stained red. Scale bar of 50 μm is applicable to all. Quantification of FAs in terms of (b) FA density (c) FA area, and (d) FA elongation. *: $p < 0.05$ compared to the corresponding data on 0 h samples. #: $p < 0.05$ compared to the corresponding data on 24 h samples. ^: $p < 0.05$ relative to the PCLTA network with the same NaOH hydrolysis time.

time. Unlike FA density and area, FA circularity (~0.66) had no difference among all the samples, suggesting that the elongation of FAs was not affected by the hydrolysis-induced surface morphological changes.

3.3.4 *In vitro* degradation.

To demonstrate degradability, I measured the weight losses of both PCLTA and mPEGA/PCLTA networks in 1 N NaOH solution via accelerated hydrolysis and in PBS via regular hydrolysis at 37 °C, as shown in Figures 3.8a and 3.8b, respectively. Addition of mPEGA could accelerate the hydrolytic degradation of the PCLTA network in both NaOH solution and PBS. Similar to photo-crosslinked PPF and PCLF [18,45], no detectable degradation could be seen in one week for both PCLTA and mPEGA/PCLTA networks in PBS at 37 °C, indicating there was no further degradation in both PCLTA and mPEGA/PCLTA networks during the cell study. In PBS, the mPEGA/PCLTA network degraded at a rate slightly higher than the PCLTA network, but only a decrease of 15-20% in weight fraction can be observed after 18 months for both series (Figure 3.8b). Meanwhile, the mPEGA/PCLTA network also had higher water absorption than the PCLTA network (Figure 3.8e).

As shown in Figure 3.8a, the degradation of both PCLTA and mPEGA/PCLTA networks in NaOH solution was much faster than that in PBS at 37 °C. The degradation rate of the PCLTA network was lower than that of the mPEGA/PCLTA network, and the difference in the weight fractions appeared to be significant after 15 days. Nevertheless, both PCLTA and mPEGA/PCLTA networks degraded completely within 40 days in NaOH solution at 37 °C.

The thermal properties of the PCLTA and mPEGA/PCLTA networks hydrolyzed in NaOH solution for 0, 3, 12, and 18 days were determined using DSC, as shown in Figures 3.8c and 3.8d, respectively. The crystallinity in this chapter was for the recrystallized samples after melting. T_m

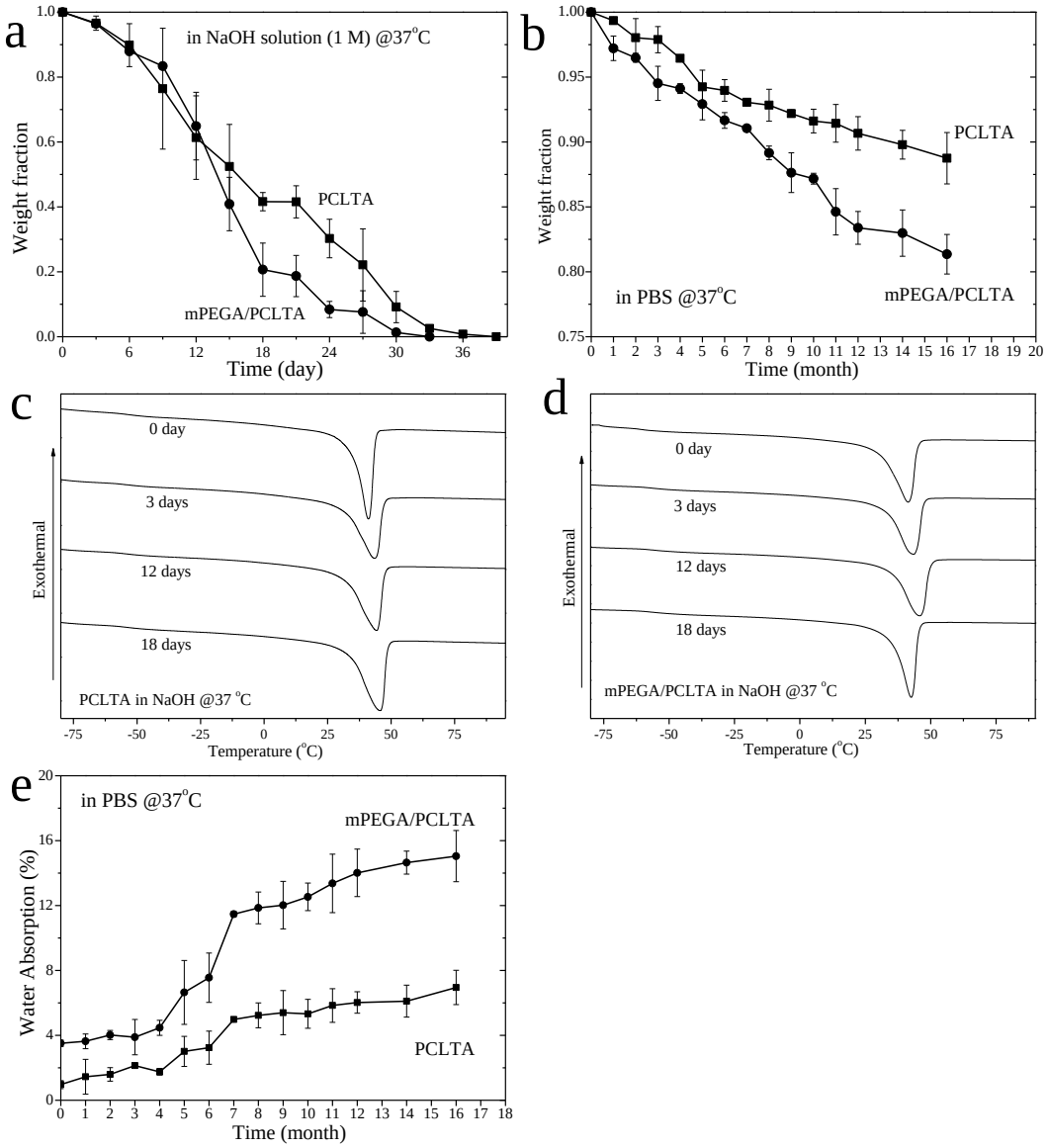

Figure 3.8 Weight fraction of PCLTA and mPEGA/PCLTA networks with different NaOH hydrolysis time (a) and PBS hydrolysis time (b). DSC curves of PCLTA (c) and mPEGA/PCLTA (d) networks with different NaOH hydrolysis time. Water adsorption of PCLTA and mPEGA/PCLTA networks with different PBS hydrolysis time (e).

was the highest peak temperature of the exothermal peaks during the heating process. Crystallinity (χ_c) was calculated using the equation of $\chi_c = [\Delta H_m/(\Phi_{PCL} \cdot \Delta H_m^c)] \times 100\%$, where ΔH_m^c of completely crystalline PCL is 135 J/g, and Φ_{PCL} was the weight fraction of caprolactone in the polymer [46]. The values of T_m, heat of fusion (ΔH_m), and χ_c are shown in Table 3.1. For the PCLTA network, both T_m and χ_c increased with increasing the degradation time. In contrast, for mPEGA/PCLTA network, T_m and χ_c first increased with increasing the hydrolysis time from 0 to 12 days, and then decreased at the hydrolysis time of 18 days. At the hydrolysis time of 12 days, the weight fractions of both PCLTA and mPEGA/PCLTA networks were ~60%, while the weight fractions of PCLTA and mPEGA/PCLTA networks were ~40% and ~20% with the hydrolysis time of 18 days, respectively. It was worthy to note that the crystallinity of mPEGA/PCLTA network was still high (~36.0%) even when the weight fraction was as low as 20%.

3.3.5 Further discussion.

The hydrolytic degradation of PCL is believed to involve chain scission to generate low-molecular-weight oligomers or segments, which eventually would be removed from the polymer. Copolymerizing and blending with other polymers caused the overall crystallinity to decrease and increased the accessibility of ester linkages, thus enhancing the rate of hydrolysis [34,35]. Our research group proved that although the addition of 5% mPEGA had no effect on the crystallinity of the PCLTA network, it improved the surface hydrophilicity [16,40]. Higher hydrophilicity also made water molecules diffuse into the polymer bulk and hydrolyze the chains more easily. Therefore, the mPEGA/PCLTA network had a higher degradation rate than the PCLTA network. Besides the increase of degradation rate by the introduction of mPEGA, the degradation of PCLTA networks was found to have no obvious increase in degradation rate compared with linear PCL. The degradation rate of the PCLTA network in PBS at 37 °C was in the same range of the *in vivo*

Table 3.1 Thermal properties of PCLTA and mPEGA/PCLTA networks with different NaOH hydrolysis time.

Samples	Days in NaOH	T_m (°C)	ΔH_m (J/g)	χ_c (%)
PCLTA	0	41.0	49.4	36.2
	3	43.6	50.7	37.2
	12	44.3	51.1	37.5
	18	45.6	53.8	39.5
mPEGA/ PCLTA	0	41.5	47.9	36.9
	3	43.5	49.1	38.6
	12	45.8	50.9	39.2
	18	42.5	46.7	36.0

degradation of linear PCL sutures in the literature [2]. However, the degradation of PCL-based network was different from that of linear PCL. For the network, not all the oligomers generated from chain scission could separate and diffuse out, as part of them were connected with the network. This was confirmed by the DSC results as the crystallinity increased with increasing the hydrolysis time before the weight residue was too low (mPEGA/PCLTA network at 18 days). It indicated more segments with lower molecular weights were generated during the degradation, which had higher chain mobility and could reorient the crystalline phase, and thus increased crystallinity, although the increase of crystallinity was limited. More remained segments also induced higher density of hydrophilic groups, and thus the hydrophilicity of the network increased with increasing the hydrolysis time in NaOH solution. As mentioned in literature, the initial surface degradation usually started in the amorphous regions of the PCL, and the crystalline regions had much lower degradation rates [34,35].

The original PCLTA and mPEGA/PCLTA networks were compressed to obtain smooth surfaces. The introduction of 5% mPEGA into the PCLTA network did not affect surface roughness [16,40]. Therefore, surface roughness in this chapter was mainly induced by the hydrolysis in NaOH solution. Different from surface roughness formed in crystallization, hydrolysis resulted in rougher surfaces with porous structures and the porosity increased with increasing the hydrolysis time [47,48]. The increases in surface roughness and porosity, together with the increase in surface hydrophilicity induced by the hydrolysis, were factors to improve SMC attachment, proliferation, and focal adhesions.

Besides of surface hydrophilicity and roughness, the stiffness of the polymer network was also important in regulating SMC behaviors. It has been reported that the stiffness of a polymer substrate would increase or decrease during the degradation [15,19,21]. In this chapter, at the

beginning, the amorphous phase in PCL was more susceptible to the hydrolysis. Faster degradation of the amorphous phase increased the crystallinity and therefore the stiffness of the polymer networks, although this increase was rather limited, as shown in Figures 3.8c and 3.8d, and Table 3.1. At longer degradation time, chain scission further decreased the crosslinking density and the molecular weight of PCL. Meanwhile, the hydrolytic degradation also increased porosity of the polymer networks. All of these factors would lead to the decrease in stiffness and make the polymer networks brittle. The change in the mechanical properties during the degradation is currently under investigation in our research group.

3.4 Conclusions

Photo-crosslinked PCLTA and mPEGA/PCLTA (Φ_{mPEGA} = 5%) disks were prepared, and increased surface hydrophilicity and roughness of the substrates were obtained through hydrolysis in 1 N NaOH aqueous solution. The mPEGA/PCLTA network could better support SMC attachment, proliferation, spreading and focal adhesion than the PCLTA network at the same hydrolysis time. Better SMC attachment, proliferation, spreading and focal adhesion, as well as smaller cell circularities were found on both PCLTA and mPEGA/PCLTA networks hydrolyzed for longer time. Both networks degraded with much higher degradation rates in NaOH solution than in PBS, and the addition of mPEGA also could accelerate the degradation.

References

1. Lee, K. H.; Kim, H. Y.; Khil, M. S.; Ra, Y. M.; Lee, D. R. *Polymer* **2003**, *44*(4), 1287-1294.

2. Perrin, D. E.; English, J. P. Polycaprolactone. In *Handbook of Biodegradable Polymers*; Domb, A. J.; Kost, J.; Wiseman, D., Eds.; Harwood Academic Publishers: Amsterdam, The Netherlands, 1997; pp 63-77.

3. Tian, H.; Tang, Z.; Zhuang, X.; Chen, X.; Jing, X. *Prog. Polym. Sci.* **2012**, *37*(2), 237-280.

4. Nair, L. S.; Laurencin, C. T. *Prog. Polym. Sci.* **2007**, *32*(8), 762-798.

5. Okada, M. *Prog. Polym. Sci.* **2002**, *27*(1), 87-133.

6. Vert, M. *J. Mater. Sci. - Mater. Med.* **2009**, *20*(2), 437-446.

7. Woodruff, M. A.; Hutmacher, D. W. *Prog. Polym. Sci.* **2010**, *35*(10), 1217-1256.

8. Woodward, S. C.; Brewer, P. S.; Moatamed, F.; Schindler, A.; Pitt, C. G. *J. Biomed. Mater. Res.* **1985**, *19*(4), 437-444.

9. Ali, S. A. M.; Zhong, S. P.; Doherty, P. J.; Williams, D. F. *Biomaterials* **1993**, *14*(9), 648-656.

10. Chen, D. R.; Bei, J. Z.; Wang, S. G. *Polym. Degrad. Stab.* **2000**, *67*(3), 455-459.

11. Pitt, C. G.; Chasalow, F. I.; Hibionada, Y. M.; Klimas, D. M.; Schindler, A. *J. Appl. Polym. Sci.* **1981**, *26*(11), 3779-3787.

12. Sun, H.; Mei, L.; Song, C.; Cui, X.; Wang, P. *Biomaterials* **2006**, *27*(9), 1735-1740.

13. Tsuji, H.; Ishida, T.; Fukuda, N. *Polym. Int.* **2003**, *52*(5), 843-852.

14. Lee, S. H.; Lee, J. H.; Cho, Y. S. *Tissue Eng. Regener. Med.* **2014**, *11*(6), 446-452.

15. Bosworth, L. A.; Downes, S. *Polym. Degrad. Stab.* **2010**, *95*(12), 2269-2276.

16. Liu, X. 2014. Phenotypic modulation of smooth muscle cells on biodegradable elastomeric substrates. Doctoral dissertation. The University of Tennessee, Knoxville.

17. Cai, L.; Wang, S. *Polymer* **2010**, *51*(1), 164-177.

18. Wang, S.; Yaszemski, M. J.; Knight, A. M.; Gruetzmacher, J. A.; Windebank, A. J.; Lu, L. *Acta biomater.* **2009**, *5*(5), 1531-1542.

19. Meseguer-Duenas, J. M.; Más-Estellés, J.; Castilla-Cortázar, I.; Ivirico, J. E.; Vidaurre, A. *J. Mater. Sci. - Mater. Med.* **2011**, *22*(1), 11-18.

20. Kweon, H.; Yoo, M. K.; Park, I. K.; Kim, T. H.; Lee, H. C.; Lee, H. S.; Oh, J. S.; Akaike, T.; Cho, C. S. *Biomaterials* **2003**, *24*(5), 801-808.

21. Castilla-Cortázar, I.; Más-Estellés, J.; Meseguer-Dueñas, J. M.; Ivirico, J. E.; Marí, B.; Vidaurre, A. *Polym. Degrad. Stab.* **2012**, *97*(8), 1241-1248.

22. Darwis, D.; Mitomo, H.; Enjoji, T.; Yoshii, F.; Makuuchi, K. *Polym. Degrad. Stab.* **1998**, *62*(2), 259-265.

23. Wang, Z. Y.; Lim, J.; Ho, Y. S.; Zhang, Q. Y.; Chong, M. S.; Tang, M.; Hong, M. H.; Chan, J. K.; Teoh, S. H.; Thian, E. S. *J. Biomed. Mater. Res. Part A* **2014**, *102*(7), 2197-2207.

24. Serrano, M. C.; Pagani, R.; Vallet-Regí, M.; Peña, J.; Comas, J. V.; Portolés, M. T. *Acta Biomater.* **2009**, *5*(6), 2045-2053.

25. Serrano, M. C.; Pagani, R.; Manzano, M.; Comas, J. V.; Portolés, M. T. *Biomaterials* **2006**, *27*(27), 4706-4714.

26. Spearman, B. S.; Hodge, A. J.; Porter, J. L.; Hardy, J. G.; Davis, Z. D.; Xu, T.; Zhang, X.; Schmidt, C. E.; Hamilton, M. C.; Lipke, E. A. *Acta Biomater.* **2015**, *28*, 109-120.

27. Chong, M. S. K.; Lee, C. N.; Teoh, S. H. *Mater. Sci. Eng., C* **2007**, *27*(2), 309-312.

28. Park, J. S.; Kim, J. M.; Lee, S. J.; Lee, S. G.; Jeong, Y. K.; Kim, S. E.; Lee, S. C. *Macromol. Res.* **2007**, *15*(5), 424-429.

29. Reichert, J. C.; Cipitria, A.; Epari, D. R.; Saifzadeh, S.; Krishnakanth, P.; Berner, A.; Woodruff, M. A.; Schell, H.; Mehta, M.; Schuetz, M. A.; Duda, G. N. *Sci. Transl. Med.* **2012**, *4*(141), 141ra93-141ra93.

30. Cipitria, A.; Skelton, A.; Dargaville, T. R.; Dalton, P. D.; Hutmacher, D. W. *J. Mater. Chem.* **2011**, *21*(26), 9419-9453.

31. Pitt, G. G.; Gratzl, M. M.; Kimmel, G. L.; Surles, J.; Sohindler, A. *Biomaterials* **1981**, *2*(4), 215-220.

32. Ye, W. P.; Du, F. S.; Jin, W. H.; Yang, J. Y.; Xu, Y. *React. Funct. Polym.* **1997**, *32*(2), 161-168.

33. Huang, M. H.; Li, S.; Hutmacher, D. W.; Coudane, J.; Vert, M. *J. Appl. Polym. Sci.* **2006**, *102*(2), 1681-1687.

34. Lam, C. X.; Hutmacher, D. W.; Schantz, J. T.; Woodruff, M. A.; Teoh, S. H. *J. Biomed. Mater. Res. Part A* **2009**, *90*(3), 906-919.

35. Lam, C. X.; Savalani, M. M.; Teoh, S. H.; Hutmacher, D. W. *Biomed. Mater.* **2008**, *3*(3), 034108.

36. Lee, J. H.; Lee, H. B.; Andrade, J. D. *Prog. Polym. Sci.* **1995**, *20*(6), 1043-1079.

37. Chaikof, E. L.; Merrill, E. W.; Callow, A. D.; Connolly, R. J.; Verdon, S. L.; Ramberg, K. *J. Biomed. Mater. Res.* **1992**, *26*(9), 1163-1168.

38. Nagaoka, S.; Mori, Y.; Takiuchi, H.; Tanzawa, H.; Nishiumi, S. In *Polymers as biomaterials*, Shalaby, S. W.; Hoffman, A. S.; Ratner, B. D.; Horbett, T. A., Eds.; Plenum Press: New York, 1984; pp 361-74.

39. Kingshott, P.; Griesser, H. J. *Curr. Opin. Solid State Mater. Sci.* **1999**, *4*(4), 403-412.

40. Cai, L.; Lu, J.; Sheen, V.; Wang, S. *Biomacromolecules* **2012**, *13*(2), 358-368.

41. Lin, L.; Wang, Y.; Huang, X. D.; Xu, Z. K.; Yao, K. *Appl. Surf. Sci.* **2010**, *256*(24), 7354-7364.

42. Harbers, G. M.; Grainger, D. W. In *Introduction to biomaterials*, Guelcher, S. A.; Hollinger, J. O., Eds.; CRC Press: Boca Raton, 2005; pp 15-45.

43. Pelham, R. J.; Wang, Y. L. *Pro. Natl. Acad. Sci. USA* **1997**, *94*, 13661-13665.

44. Burridge, K.; Chrzanowska-Wodnicka, M. *Annu. Rev. Cell Dev. Biol.* **1996**, *12*(1), 463-519.

45. Timmer, M. D.; Ambrose, C. G.; Mikos, A. G. *Biomaterials* **2003**, *24*(4), 571-577.

46. Polymer Handbook. 3rd ed. Brandrup, J.; Immergut, E. H.; Eds.; Wiley: New York, 1989.

47. Zhang, Q.; Jiang, Y.; Zhang, Y.; Ye, Z.; Tan, W.; Lang, M. *Polym. Degrad. Stab.* **2013**, *98*(1), 209-218.

48. Diban, N.; Haimi, S. P.; Bolhuis-Versteeg, L.; Teixeira, S.; Miettinen, S.; Poot, A. A.; Grijpma, D. W.; Stamatialis, D. *Macromol. Symp.* **2013**, *334*(1), 126-132.

Chapter IV. Four-arm and Six-arm Poly(ε-caprolactone) Acrylates: Synthesis, Characterization, and Smooth Muscle Cells Responses to Tunable Stiffness

Abstract

We synthesized 4arm and 6arm poly(ε-caprolactone) acrylates (PCLAs) with different molecular weights through acrylation of PCL tetraols and hexanols, which were prepared via ring-opening polymerization of ε-caprolactone initiated with pentaerythritol and dipentaerythritol, respectively. The multi-arm PCLAs showed high photo-crosslinking efficiency and the resulted PCLA networks had gel fractions higher than 82%. By varying the molecular weight of PCLA, both amorphous and semi-crystalline PCLA networks were obtained. Photo-crosslinked 4arm and 6arm PCLAs with number-average molecular weights higher than 10000 g/mol and 13000 g/mol were semi-crystalline at physiological temperature, which showed distinct thermal and mechanical properties. Compared to amorphous PCLA networks, semi-crystalline PCLA networks had higher stiffness, rougher surface, lower hydrophilicity and lower protein adsorption. Photo-crosslinked PCLA disks were used for modulating primary rat aortic smooth muscle cell (SMC) behavior. We found that among all the surface characteristics, other than surface hydrophilicity and roughness, substrate stiffness was the main factor in promoting SMC attachment, proliferation, spreading, focal adhesions, and contractile gene expression.

4.1 Introduction

In tissue engineering applications, biomaterials with desired properties provide a permissive environment for cell functions as extrinsic signals to cells from the surrounding extracellular matrix (ECM) are essential in guiding them through distinct development stages [1-4]. The mechanical, chemical, and morphological properties of the biomaterials need to be precisely controlled, as they are important in determining cell responses to ECM [5-10]. Curable or crosslinkable polymeric biomaterials have advantages such as their injectability and manufacturability using diverse fabrication methods and tailorable chemical structures and physicochemical properties for diverse tissue engineering applications. Crosslinkable polymers such as polypropylene fumarate (PPF) can be cured via photo-initiation, heat, irradiation, or redox process. Among these methods, photo-crosslinking has advantages such as high efficiency, easy to control heat evolution, and flexibility in preparing heterogeneous substrates and structures with variations in material type and properties [11-15].

A series of photo-crosslinkable polymeric biomaterials based on poly(ε-caprolactone) (PCL) has been developed, for example, PPF-*co*-PCL, PCL fumarate (PCLF), PCL diacrylate (PCLDA), and PCL triacrylate (PCLTA) [16-20]. Among these polymers, our research group recently focused on PCLDAs and PCLTAs, which were synthesized via acrylation of PCL diols and triols with different molecular weights, respectively. Photo-crosslinked PCLDAs and PCLTAs have mechanical and thermal properties that can be controlled through crosslinking density and crystallinity, both of which are directly related with the molecular weight of the PCL diol or triol precursor [16,17]. Then PCLDA or PCLTA networks with different stiffnesses were used as model systems to regulate cell behavior [16,17]. PCLDA and PCLTA can also be crosslinked with other polymers such as PPF and hydrophilic methoxyl polyethylene glycol monoacrylate (mPEGA) or

incorporated with inorganic fillers such as hydroxyapatite (HA) nanoparticles to modify the physicochemical characteristics and therefore to regulate the behaviors of different types of mammalian cells [20-22]. PCLTAs with two different molecular weights were also fabricated into microgrooved substrates to promote functions of mouse pre-osteoblastic MC3T3-E1 cells and nerve cells [23,24]. Photo-crosslinked PCLTA substrates with a stiffness gradient along the longitudinal direction could be used to guide rat aortic smooth muscle cell (SMC) migration [17].

Compared with the linear counterpart with the same molecular weight, a branched or multi-arm polymer has the advantages of a lower viscosity and a higher density of terminal end groups [25,26]. In stereolithographical fabrication of PCLA, both a low viscosity and a high density of crosslinkable end groups are desirable as the former means better injectability and processability while the latter means high crosslinking efficiency. In this chapter, I used pentaerythritol and dipentaerythritol as initiators to synthesize PCL tetraols and hexanols with different molecular weights, respectively. The PCL tetraols and hexanols were then converted into photo-crosslinkable PCLAs via acrylation. Thermal properties of the polymers such as melting temperature (T_m) and crystallinity (χ_c) were examined and correlated with their mechanical and rheological properties. Surface properties such as roughness, hydrophilicity, and its capability of adsorbing serum protein from cell culture media were also studied. Then I focused on the roles of surface properties of the photo-crosslinked PCLA networks in influencing SMC attachment, proliferation, spreading, focal adhesions (FAs), and contractile gene expression on them.

4.2 Materials and Methods

4.2.1 Synthesis.

Methylene chloride (CH_2Cl_2) was purchased from Fisher Scientific (Hampton, NH) and all other chemicals used here were purchased from Sigma Aldrich (Milwaukee, WI) unless otherwise noted. As shown as Figure 4.1, pentaerythritol and dipentaerythritol were as the initiators in synthesizing PCL tetraols and hexanols via ring-opening polymerization (ROP) of ε-caprolactone at 130 °C for 12 h in the presence of $Sn(Oct)_2$ as the catalyst, respectively. The molecular weight of PCL tetraol or hexanol was modulated using the monomer to initiator feed ratio. The PCL tetraols and hexaols were added dropwise into diethyl ether to remove the low-molecular-weight oligomer and the precipitate was rotary evaporated. Then acylation of the PCL tetraols and hexanols was performed in the presence of K_2CO_3 as the proton scavenger to form PCLAs [16,27]. PCL tetraol, acryloyl chloride, and K_2CO_3 were measured at a molar ratio of 1:4:4 (1:6:6 for PCL hexanol). PCL tetraol or hexanol was dissolved in methylene chloride (1:2 v/v) and placed in a 50 mL three-neck flask along with K_2CO_3 powder. Acryloyl chloride dissolved in methylene chloride (1:10 v/v) was then added dropwise into the slurry of K_2CO_3/ PCL tetraol or hexanol in methylene chloride. After reaction at room temperature under nitrogen for 24 h, the mixture was filtered to remove the solids and then precipitated in diethyl ether again. The molecular weights of PCL tetraols and hexaols and PCLAs were determined using gel permeation chromatography (GPC; PL-GPC20, Polymer Laboratories) at room temperature with tetrahydrofuran as the eluent and standard monodisperse polystyrene samples (Polymer Laboratories) for calibration. The chemical structures of PCL tetraols and hexaols and PCLAs were determined using ^1H NMR (Varian Mercury 300 spectrometer, 300 MHz) with $CDCl_3$ containing tetramethylsilane (TMS) as solvent.

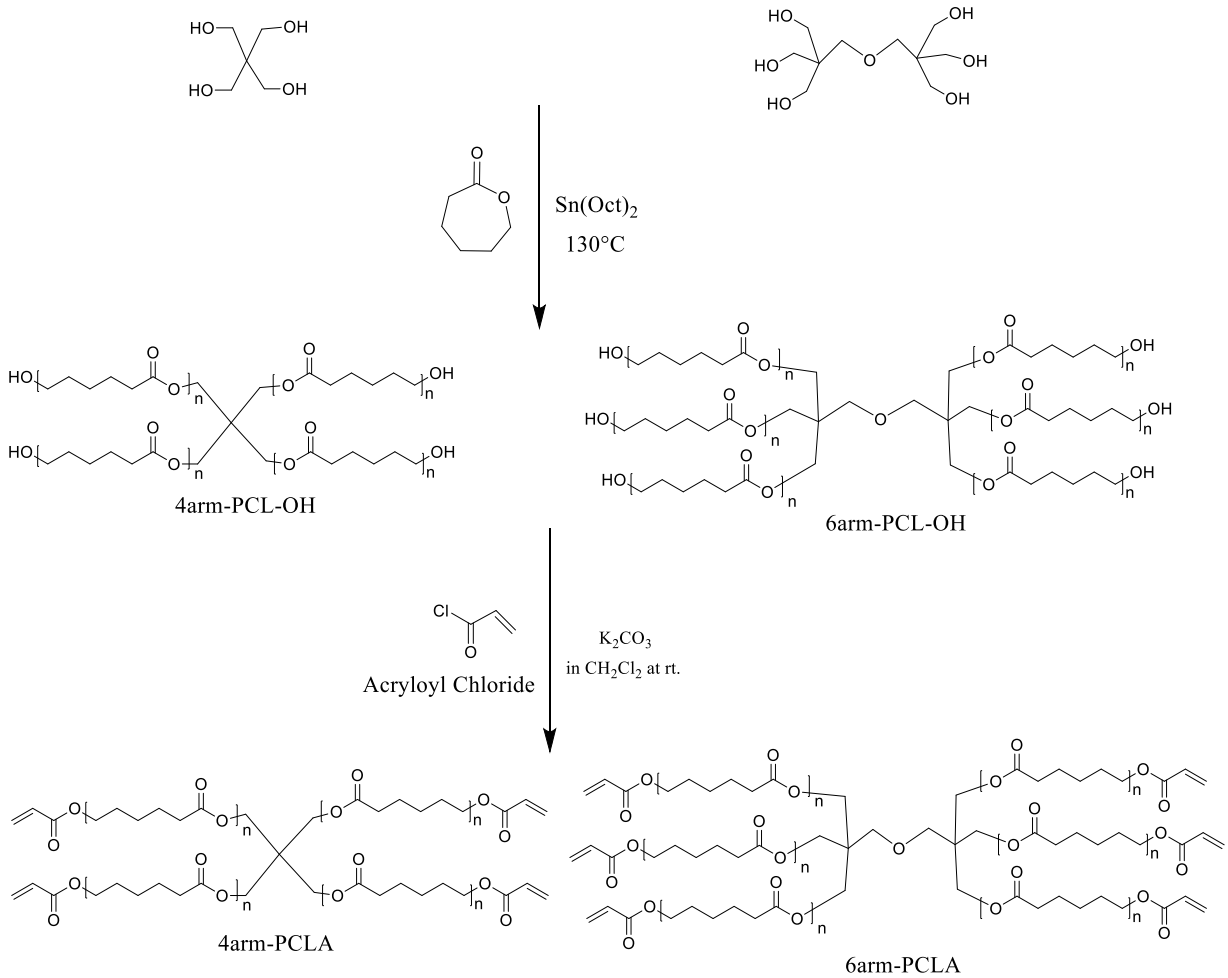

Figure 4.1 Synthesis of PCL-OHs and PCLAs.

4.2.2 Photo-crosslinking of PCLAs.

Photo-initiator, phenyl bis(2,4,6-trimethyl benzoyl) phosphine oxide (BAPO, IRGACURE 819, Ciba Specialty Chemicals, Tarrytown, NY) was used in photo-crosslinking. 75 μL of BAPO/CH_2Cl_2 (300 mg/1.5 mL) solution was mixed with PCLA solution in CH_2Cl_2 (1.5 g/500 μL). The mixture was then transferred into a Teflon mold composed of two glass plates and a Teflon spacer, and then placed under a high-intensity long-wave UV lamp (SB-100P, Spectronics Corp., Westbury, NY, λ= 365 nm, Intensity: 4800 w/cm^2) for 20 min at ~10 cm from the lamp head. After crosslinking, PCLA disks were removed from the mold after cooled down to room temperature and then completely dried in a vacuum oven. The dry PCLA disks were weighed. Based on the measured weights of the original (W_0), fully swollen (W_s, CH_2Cl_2 was used to swell the disks), and dry (W_d,) PCLA disks, the swelling ratio and gel fraction were calculated using the equations of $(W_s\text{-}W_d)/W_d$ and W_d/W_0, respectively [13,16]. Except for the swelling ratio and gel fraction, flat crosslinked PCLA substrates were soaked in acetone for two days to remove the sol fraction and unreacted BAPO, dried completely in vacuum, and compressed between two glass plates at 60 °C and crystallized at room temperature there.

4.2.3 Material characterization.

The thermal properties of PCL tetraols and hexanols, 4arm/6armPCLAs, and crosslinked PCLAs were performed using differential scanning calorimetry (DSC, Q2000, TA instruments, New Castle, DE). The samples were first heated from room temperature to 100 °C and then cooled back to -80 °C, followed by another heating round to 100 °C at a rate of 10 °C/min for all the rounds in dry nitrogen. Linear viscoelastic properties of photo-crosslinked PCLA disks (8 mm × 0.5 mm, diameter × thickness) were measured on a strain-controlled rheometer (RDS-2, Rheometric Scientific) using the dynamic frequency sweep mode in the frequency (ω) range of

0.1-100 rad/s with a strain of 2% at 37 and 60 °C. Zero-shear viscosities (η_0) of PCLAs were measured using dynamic mode in the Newtonian region at temperatures from 60 to 90 °C using the same rheometer. A 25 mm diameter parallel plate flow cell and a gap of ~0.8 mm with a strain of 20% in the frequency range of 0.5-50 rad/s were used in the rheological measurements. The tensile properties of photo-crosslinked PCLA strips (0.5 mm × 0.8 mm × 10 mm, thickness × width× length) were tested at 37 °C using a dynamic mechanical analyzer (DMA, Q800, TA instruments) at a strain rate of 0.005 s^{-1}. The surface morphologies of photo-crosslinked PCLA disks were detected using a multi-mode atomic force microscope (AFM) with a Nanoscope III control system (Veeco Instruments, Santa Barbara, CA). A tapping mode over a scan area of 10 μm × 10 μm at a scan rate of 0.5 Hz was used. Root-mean square roughness (R_{rms}) was measured from the height images using the Nanoscope 7.30 software (Veeco Instruments, Santa Barbara, CA). Water contact angles were measured at 37 °C using a Ramé-Hart NRC C. A. goniometer (model 100-00-230) and analyzed using a tangent method and the ImageJ software (National Institutes of Health, Bethesda, MD) on 20 μL of distilled water (pH = 7.0) injected onto photo-crosslinked PCLA disks after a static time of 30 s. Four disks were used for each photo-crosslinked PCLA to calculate the average and standard deviation.

4.2.4 Protein adsorption.

Photo-crosslinked PCLA disks were sterilized in 70% ethanol solution and dried completely prior to protein adsorption measurements and cell studies. The sterile polymer disks were soaked for 4 h at 37 °C in the culture medium for SMCs, i.e., Dulbecco's modified eagle medium (DMEM; Gibco, Grand Island, NY) supplemented with 10% fetal bovine serum (FBS; HyClone, Thermal Scientific) and 1% penicillin/streptomycin (Gibco). Then the polymer disks were washed using 600 μL of phosphate buffered saline (PBS) three times with 10 min of gentle agitation, followed

by immersion in 300 μL of 1% sodium dodecyl sulfate (SDS) solution for 1 h three times. The total concentration of adsorbed serum proteins in the collected SDS solution was determined using a MicroBCA protein assay kit (Pierce, Rockford, IL) on a microplate reader (SpectraMax Plus 384, Molecular Devices, Sunnyvale, CA). The protein concentration was correlated with the UV absorbance of the SDS solution at 562 nm, based on a calibration curve constructed using solutions of albumin in the kit with known concentrations.

4.2.5 *In vitro* SMC attachment and proliferation.

SMCs were cultured in the culture medium mentioned above. SMCs were seeded onto photo-crosslinked PCLA disks (10 mm × 0.5 mm, diameter × thickness) at a density of 15,000 cells/cm^2 and cultured for 4 h, 1, 2, and 4 days, using tissue culture polystyrene (TCPS) as the positive control. A colorimetric cell metabolic assay (CellTiter 96 Aqueous One Solution, Promega, Madison, WI) was performed in each well to determine the number of attached cells. The cell number was correlated to the UV absorbance of the solution at 490 nm measured on the microplate reader mentioned above and then quantified using a standard curve constructed using known cell numbers. The attached SMCs on the photo-crosslinked PCLA disks were washed with PBS, fixed in 4% paraformaldehyde (PFA, Electron Microscopy Science) solution for 10 min at room temperature, washed with PBS twice, and then permeabilised with 0.1% Triton X-100 at room temperature for another 10 min. Cytoplasm and cell nuclei were then stained using rhodamine-phalloidin (RP, Cytoskeleton, Denver, CO) for 1 h at 37 °C and 4',6-diamidino-2-phenylindole (DAPI) at room temperature, respectively. Then the cells were photographed using an Axiovert 25 light microscope (Carl Zeiss, Germany). Based on the cell images, cell area was determined on more than 50 non-overlapping cells at day 1 by using ImageJ.

4.2.6 Characterization of focal adhesions.

At day 1 post-seeding, SMCs attached on the photo-crosslinked PCLA disks were fixed and permeabilized as described in the last paragraph. Then the disks with attached cells were incubated in 1% bovine serum albumin (BSA)/PBS at 37 °C for 30 min. After being washed with PBS three times, the disks with attached cells were incubated in monoclonal mouse antibody against vinculin (1:1000 in 1% PBS; Sigma) at room temperature for 2 h, followed by PBS washing three times again. Then the disks with attached cells were cultured with goat anti-mouse IgG secondary antibody (1:200 in 1% PBS; Sigma) at room temperature in dark for 2 h. The cells were also stained using RP at 37 °C for another 1 h. The FAs in the SMCs were photographed on a Leica DM6000B fluorescent confocal microscope. The density (defined as the number of FAs per cell), area, and elongation (defined as perimeter^2/4π/area) of the FAs in the SMCs were analyzed and averaged from 15 non-overlapping cells using ImageJ.

4.2.7 Gene expression.

Polymerase chain reaction (PCR) was used to quantify the expression levels of contractile phenotypic markers of smoothlin, calponin, transgelin, and smooth muscle myosin heavy chain (SM-MHC) in SMCs cultured for 4 days on photo-crosslinked PCLA disks. Total RNA was isolated using the RNeasy Mini Kit (Qiagen, Valencia, CA) and the cDNA was synthesized by reverse transcription using DyNAmo cDNA Synthesis Kit (Thermo Scientific, Waltham, MA). The primers for these gene markers were designed using the Oligoperfect software, and their sequences are listed as follows. Smoothlin: forward 5'-TCGGAGTGCTGGTGAATAC-3', reverse 5'-CCCTGTTTCTCTTCCTCTGG-3'; calponin: forward 5'-AGTCTACTCTCTCTTGGCTCTGGCC-3', reverse 5'-CCTGCCTTCTCTCAGCTTCTCAGG-3'; transgelin: forward 5'-GGCAGCTGAGGATTATGGAGTCACG-3', reverse 5'-

TGGGATCTCCACGGTAGTGTCCA-3'; SM-MHC: forward 5'-AAGCAGCTCAAGAGGCAG-3', reverse 5'-AAGGAACAAATGAAGCCTCGTT-3'; and house-keeping gene glyceraldehyde-3-phosphate dehydrogenase (GAPDH): forward 5'-TCTTCACCACCATGGAGAA-3', reverse 5'-ACTGTGGTCATGAGCCCTT-3'. Expression of these gene markers was quantified through PCR with Power SYBR Green PCR Master Mix (Applied Biosystems, Warrington, UK). The amplification and detection process was performed on a Peltier Thermal Cycler fluorescence detection system (MJ Research PTC-200, Bio-Rad Laboratories, Inc, Foster City, CA). The procedure was set as 94 °C for 5 min followed by the cyclic steps of 94 °C for 30 s, 55 °C for 30 s, and 72 °C for 30 s. The expression levels of target gene markers were normalized to that of the GAPDH.

4.2.8 Statistical analysis.

Cell studies were performed in quadruplicates for each group at each time point. All values were expressed as mean ± standard deviation. The statistical significance ($p < 0.05$) in the difference between any two groups was calculated using the student's *t*-test.

4.3 Results and Discussion

4.3.1 Structure characterization and photo-crosslinking.

The molecular weights of the PCL tetraols and hexanols and 4arm/6arm PCLAs determined using GPC are shown in Table 4.1. The 4arm PCLAs with number-average molecular weights (M_n) of 7390, 8770, 9610, 14700, 19900, and 25400 g/mol were named as PCLA ×-7k, 8k, 10k, 14k, 19k, and 25k, respectively. The 6arm PCLAs with M_n of 10200, 13600, 18100, and 30600 g/mol were named as PCLA ∗-10k, 13k, 18k, and 30k, respectively. The polydispersity indexes (PDIs) of these polymers were mostly below 1.30, showing that the polymers were monodisperse.

Table 4.1 Molecular characteristics and thermal properties of the PCL-OHs and PCLAs.

Polymer		M_n (g/mol)	M_w (g/mol)	PDI	Thermal properties				
					T_{cc} (°C)	$T_{m,1}$ (°C)	$T_{m,2}$ (°C)	ΔH_m (J/g)	χ_c (%)
PCL-OH	×-7k	7560	8680	1.15	14.8	41.2	46.3	77.5	58.4
	×-8k	8450	9680	1.15	16.6	41.1	46.5	77.8	58.5
	×-10k	9250	10300	1.11	21.0	45.8	49.4	76.6	57.5
	×-14k	14200	15700	1.11	24.2	49.7	52.8	75.3	56.3
	×-19k	19400	22900	1.12	25.0	51.6	54.3	80.5	60.0
	×-25k	28100	36600	1.30	31.4	53.6	55.8	78.5	58.5
	∗-10k	9990	10900	1.10	15.1	39.8	44.8	76.2	57.9
	∗-13k	12800	14300	1.11	21.8	45.1	48.3	75.3	56.8
	∗-18k	17900	20500	1.14	26.7	48.2	51.0	79.5	59.7
	∗-30k	29600	37700	1.27	29.7	53.1	55.2	80.2	59.9
PCLA	×-7k	7390	8730	1.18	19.2	40.0	46.3	72.9	55.0
	×-8k	8770	9690	1.11	20.4	40.4	46.3	73.1	55.0
	×-10k	9610	10600	1.10	20.4	44.1	49.4	75.5	56.7
	×-14k	14700	16700	1.13	30.0	50.0	53.0	72.8	54.4
	×-19k	19900	23700	1.19	35.7	53.2	54.0	72.6	54.1
	×-25k	25400	34500	1.36	34.0	54.5	56.6	70.5	52.4
	∗-10k	10200	11200	1.10	17.8	39.1	45.6	65.3	49.6
	∗-13k	13600	14700	1.09	20.4	43.9	48.9	70.1	53.0
	∗-18k	18100	20300	1.13	24.3	47.8	51.8	74.1	55.7
	∗-30k	30600	38800	1.27	30.5	54.0	55.9	67.3	50.3

×: 4arm; ∗: 6arm

The chemical structures of the polymers were confirmed using ^{1}H NMR spectra. As shown in Figure 4.2, all the chemical shifts were assigned to the corresponding protons in the polymer structures. Evidently, vinyl groups (-CH=CH_2) with the chemical shift (δ) in the range of 5.7-6.5 ppm can only be seen in the spectra of PCLAs but not in the spectra of PCL tetraols or hexanols. The theoretical molecular weights of PCL tetraols or hexanols were calculated based on the feed molar ratio of the monomer to the initiator with assumption that all the terminal hydroxyl groups initiated the ROP of the monomer. The theoretical molecular weights of PCLAs were calculated by changing the terminal hydroxyl groups into acrylate groups. The molecular weights of the polymers were also calculated from ^{1}H NMR spectra by comparing the integral areas between the methylene protons (-CH_2-) in PCL at δ of 2.3 ppm and the protons connected to the terminal hydroxyl groups (-CH_2-OH, δ = 3.6 ppm) in PCL tetraols and hexanols or the protons of vinyl groups in PCLAs [28]. The chemical shift for the hydroxyl group at 3.6 ppm was significantly smaller in the spectra of the PCLAs than in those of PCL tetraols and hexanols, based on which the acrylation rate was calculated to be always higher than 85%.

High acrylation led to a high crosslinking density and thus it was more precise to modulate the thermal and mechanical properties of the PCLA network. The gel fractions of photo-crosslinked PCLA ×-7k, 8k, 10k, 14k, 19k, and 25k were 0.96 ± 0.02, 0.94 ± 0.04, 0.93 ± 0.02, 0.92 ± 0.02, 0.85 ± 0.02, and 0.82 ± 0.01, respectively. The gel fractions of photo-crosslinked PCLA ∗-10k, 13k, 18k, and 30k were 0.97 ± 0.01, 0.95 ± 0.01, 0.94 ± 0.02, and 0.90 ± 0.02, respectively. When the arm length was the same, photo-crosslinked 6arm PCLAs had the higher gel fractions than photo-crosslinked 4arm PCLAs, which in turn had higher values than photo-crosslinked PCLTAs. This result confirmed that more acrylate end groups in PCLA led to better crosslinking efficiency. The swelling ratios of photo-crosslinked PCLA ×-7k, 8k, 10k, 14k, 19k, and 25k in CH_2Cl_2 were

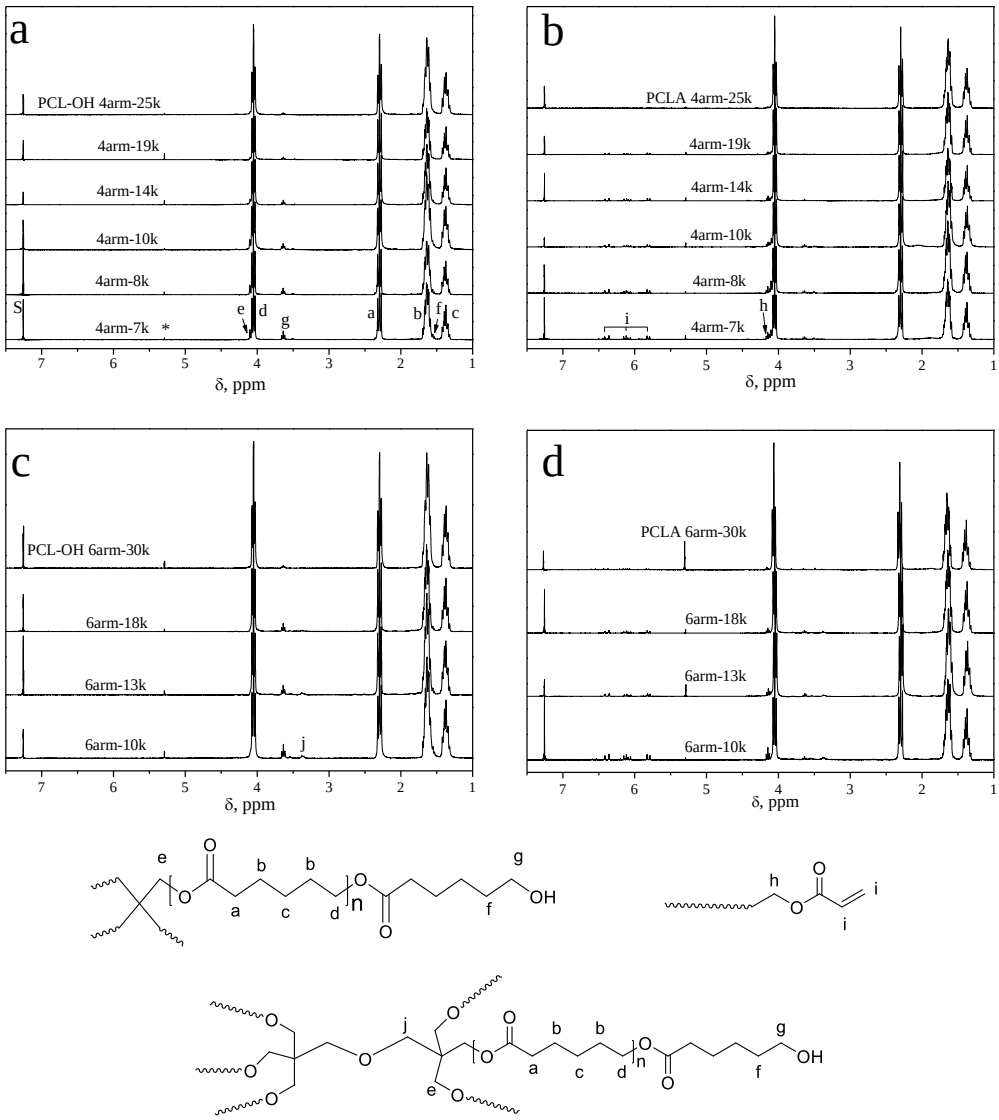

Figure 4.2 ^{1}H NMR (300 MHz, $CDCl_3$, reference TMS) spectra of PCL-OHs and PCLAs (a, 4arm PCL-OH; b, 4arm PCLA; c, 6arm PCL-OH; d, 6arm PCLA). S = solvent. Asterisk denotes the signals due to the residue of CH_2Cl_2.

5.2 ± 0.3, 6.2 ± 0.7, 7.8 ± 0.8, 9.7 ± 0.2, 11.4 ± 0.6, and 17.9 ± 0.9, respectively. The swelling ratios of photo-crosslinked PCLA ∗-10k, 13k, 18k, and 30k were 5.1 ± 0.4, 6.6 ± 0.4, 7.3 ± 0.2, and 11.7 ± 0.8, respectively. For all the PCLAs, the gel fractions decreased and the swelling ratios increased with increasing the molecular weight as the density of acrylate end groups and the crosslinking density both decreased.

4.3.2 Thermal properties.

The thermal properties of PCL tetraols and hexanols, 4arm/6arm PCLAs, and crosslinked PCLAs were determined using the DSC curves in both heating and cooling rounds, as shown in Figure 4.3. The cold crystallization temperature (T_{cc}) was the highest peak temperature of endothermal peaks in the cooling round, while T_m and ΔH_m were the highest peak temperature and the heat of fusion determined from the exothermal peaks in the heating round. χ_c was calculated using the equation of $\chi_c = [\Delta H_m/(\phi_{PCL} \cdot \Delta H_m^c)] \times 100\%$, where ΔH_m^c is the value of 135 J/g for completely crystalline PCL [29], and ϕ_{PCL} was the weight fraction of caprolactone in the polymer. The values of T_{cc}, T_m, ΔH_m and χ_c for uncrosslinked polymers, including PCL tetraols and hexanols and PCLAs are listed in Table 4.1, while the values for photo-crosslinked PCLAs are in Table 4.2. Glass transition could not be detected in the DSC curves. For most of the studied polymers, both T_{cc} and T_m increased with increasing the molecular weight. Regardless of the molecular weight, all the PCL tetraols and hexanols and PCLAs had high crystallinities with two melting peaks, which were attributed to multiple arms. After photo-crosslinking, the crystallinity and T_m decreased significantly and there was only one melting peak as the PCL crystalline domains were strongly restricted by the network [30,31]. Although all the photo-crosslinked PCLAs were still semi-crystalline, the ones made from PCLAs with low molecular weights, ×-7k, ×-8k and ∗-10k, became amorphous at the body temperature (37 °C). The T_ms of photo-crosslinked PCLA

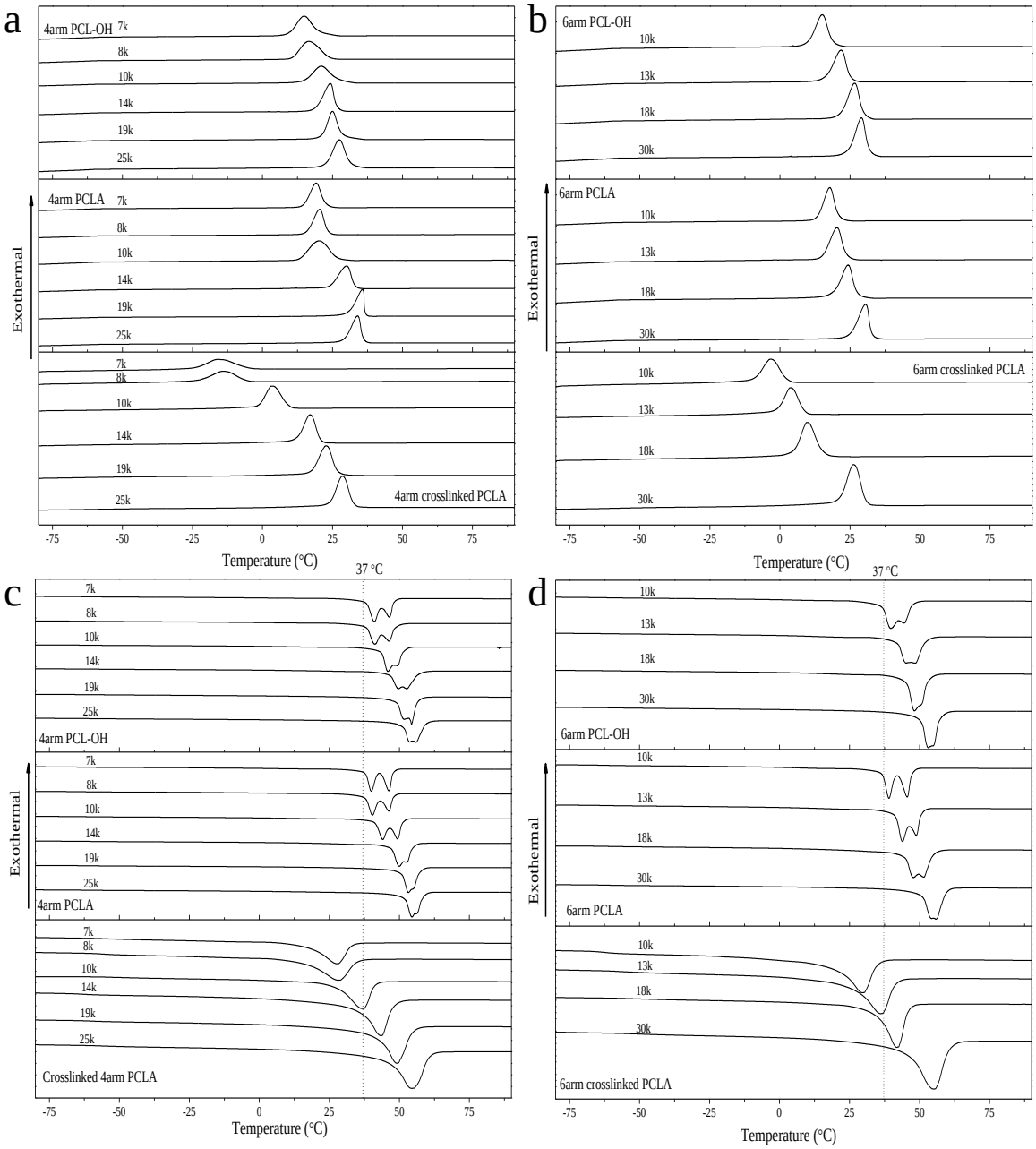

Figure 4.3 DSC curves of 4arm (a, c) and 6arm (b, d) PCL-OHs, PCLAs, and crosslinked PCLAs.

Table 4.2 Thermal and mechanical properties (37 °C) of crosslinked PCLAs.
×: 4arm; ∗: 6arm

Polymer		Thermal properties				Mechanical properties		
		T_{cc} (°C)	T_m (°C)	ΔH_m (J/g)	χ_c (%)	*E* (MPa)	ε_b (%)	*G* (MPa)
Crosslinked PCLA	×-7k	-15.7	27.6	34.0	26.4	14.0 ± 0.3	24 ± 9	0.61
	×-8k	-13.9	28.2	36.4	28.1	7.5 ± 0.3	20 ± 7	0.54
	×-10k	3.3	36.7	42.4	32.6	80.6 ± 4.1	58 ± 13	1.78
	×-14k	17.1	43.4	51.5	39.1	136 ± 7	151 ± 22	2.73
	×-19k	22.8	49.1	58.1	43.8	211 ± 4	215 ± 30	4.31
	×-25k	28.7	54.4	61.1	45.9	229 ± 16	243 ± 26	4.62
	∗-10k	-3.5	29.8	34.9	27.3	5.7 ± 0.2	18 ± 6	0.88
	∗-13k	3.5	36.0	40.8	31.5	48.7 ± 1.2	25 ± 10	2.21
	∗-18k	9.9	41.9	50.3	38.4	159 ± 12	120 ± 19	3.85
	∗-30k	26.1	54.9	60.0	45.3	241 ± 22	253 ± 39	4.73

×-10k and ∗-13k were 36.7 and 36.0 °C, respectively. Based on the M_n values from GPC, PCLA ×-10k and ∗-13k had the arm length of ~2200 g/mol and this value could be considered as the boundary condition for determining whether it was amorphous or semi-crystalline at 37 °C for a PCL-based network. The differences in crosslinking density and crystallinity at 37 °C resulted in their distinct mechanical properties.

4.3.3 Mechanical and rheological properties.

Before photo-crosslinking, all the polymers had melting temperatures higher than 37 °C and were wax-like solid at room temperature. The η_0 values of these PCLDAs at different temperatures above their T_ms were measured and plotted against temperature in Figure 4.4. As expected, η_0 decreased with increasing the temperature or decreasing the molecular weight. At temperatures higher than the T_m, the PCLAs became fluid-like with low viscosities (1-10 Pa·s). After photo-crosslinking, no fluid-like behavior could be observed. As shown in the Figure 4.4, all the photo-crosslinked PCLAs showed that the storage modulus (G') was always much greater than the loss modulus (G''), in which G' was frequency independent, and the viscosity (η) curves showed the shear thinning behavior, indicating perfect polymer networks. Because photo-crosslinked ×-7k, ×-8k, and ∗-10k were amorphous at both test temperatures, there were no significant variances with temperatures for G', G'', and η. In contrast, the other samples showed distinct sets of rheological curves at different temperatures, as they were semi-crystalline at 37 °C but amorphous at 60 °C. At 37 °C, the G' values of semi-crystalline networks were significantly higher than the amorphous networks, and G' increased with increasing the molecular weight. At 60 °C, the G' decreased as the molecular increased, as G' was only determined by the crosslinking density for an amorphous network. Averaged from G' over the frequency range, shear modulus (G) for an amorphous polymer network in Table 4.2 can be used to calculate the average molecular weight

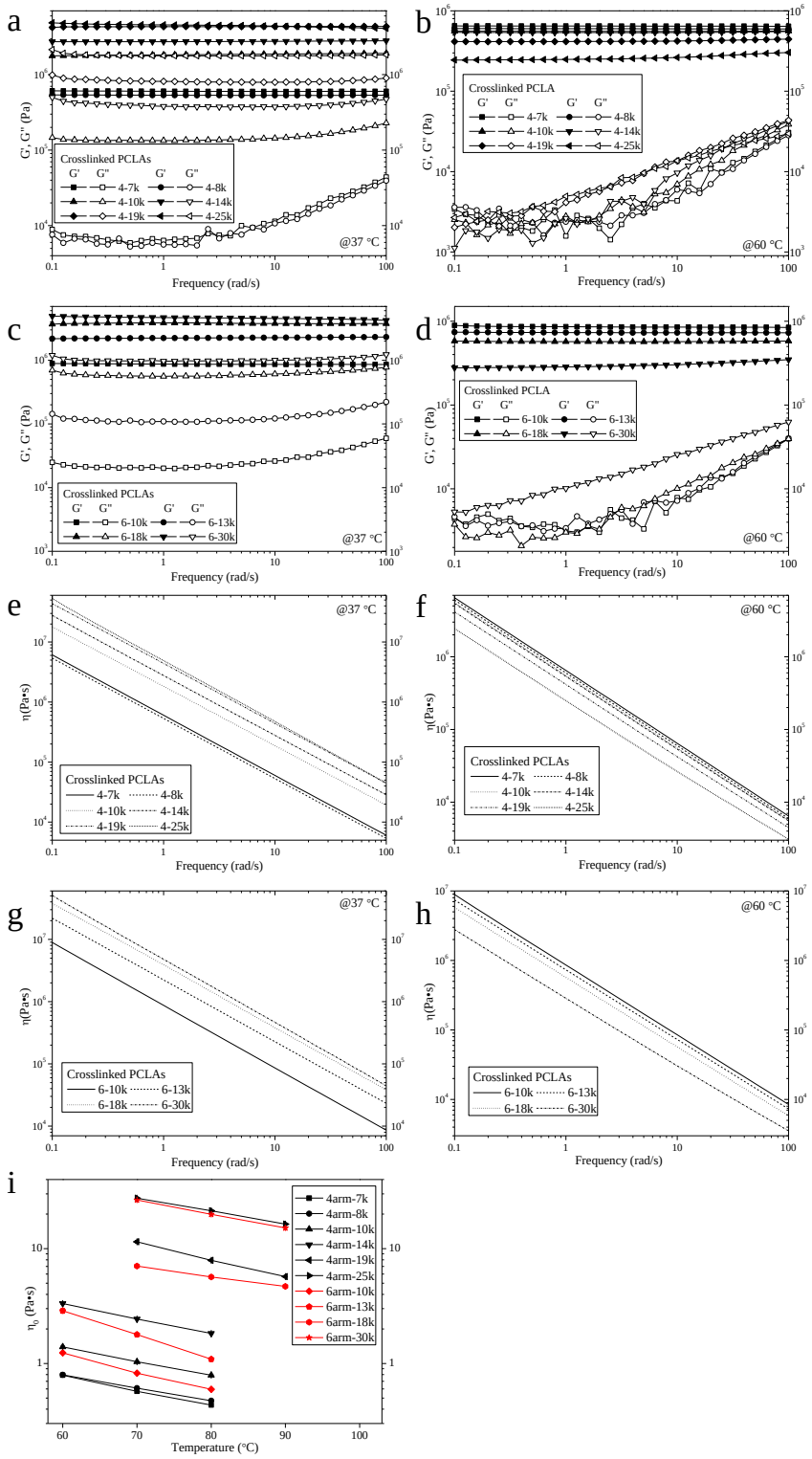

Figure 4.4 Storage modulus G' (solid symbols), and loss modulus G" (open symbols) vs. frequency for crosslinked PCLAs at 37 °C (a, 4arm PCLA; c, 6arm PCLA) and 60 °C (b, 4arm PCLA; d, 6arm PCLA). Viscosity (lines) vs. frequency for crosslinked PCLAs at 37 °C (e, 4arm PCLA; f, 6arm PCLA) and 60 °C (g, 4arm PCLA; h, 6arm PCLA). (i) Temperature dependence of zero-shear viscosity for PCLAs.

(M_c) between two neighboring crosslinks through the equation of $G = \rho RT/M_c$, where ρ is the density of the polymer network in g/cm^3, R is the universal gas constant of 8.3144 J/mol/K, and T is absolute measurement temperature in K [13,32]. In this chapter, M_c was related to the arm molecular weight of PCLA, which was the division of the total molecular weight by the arm number. The crosslinking density n_c (moles of active polymer network chains per unit volume) can be deduced using the equation of $n_c = \rho/M_c$ [13,32]. The n_c values of photo-crosslinked PCLA ×-7k, 8k, 10k, 14k, 19k, and 25k were 940, 870, 800, 780, 600, and 340 mol/m^3, respectively. The n_c values of photo-crosslinked PCLA ∗-10k, 13k, 18k, and 30k were 1860, 1590, 1230, and 620 mol/m^3, respectively. The n_c values of 6arm PCLA were much higher than these of 4arm PCLA with similar arm length.

Representative tensile stress-strain curves of photo-crosslinked PCLAs at 37 °C are shown in Figure 4.5 and the elastic moduli (E) obtained from the initial slope of the curves are summarized in Table 4.2. The amorphous PCLA networks were brittle and broke before showing plastic deformation, while the semi-crystalline PCLA networks were stiff and broke at high strains with demonstrating yielding and necking. For the amorphous PCLA networks, E was only related to the crosslinking density in the chemical network. In contrast, for the semi-crystalline PCLA networks, crystallites formed a physical network to strengthen the chemical network. Therefore, the semi-crystalline networks of PCLA ×-25k and ∗-30k with the highest χ_c had the highest E of 229 ± 16 and 241 ± 22 MPa, and highest strains at break (ε_b) of 243 ± 26% and 253 ± 39%, respectively. Differences were noticed between the two networks of PCLA ×-10k and ∗-13k with T_m near 37 °C as the former showed the necking phenomenon with a ε_b value of 58 ± 13% than the latter (ε_b = 25 ± 10%), although both networks had a low χ_c at 37 °C.

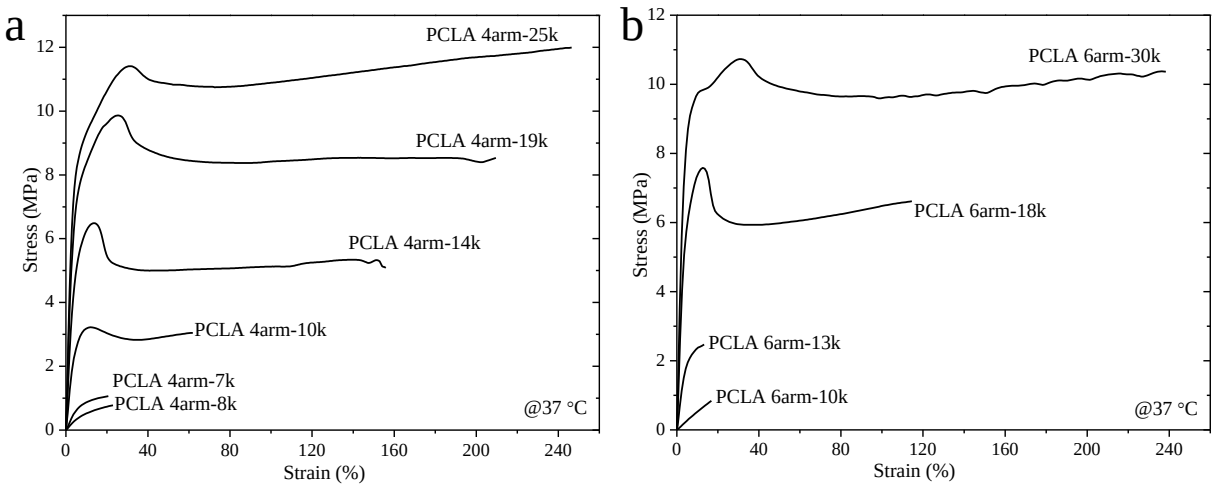

Figure 4.5 Tensile stress-strain curves of crosslinked PCLAs at 37 °C. (a) 4-arm and (b) 6-arm.

The 3D AFM height images of compressed photo-crosslinked PCLA disks are shown in Figure 4.6a. The compressed semi-crystalline photo-crosslinked PCLA disks were much less rough compared with their original ones, as indicated by the R_{rms} values of 16.3 ± 2.1, 17.2 ± 2.0, 19.5 ± 1.9, 21.2 ± 1.3, 17.5 ± 2.8, 18.4 ± 1.2, and 24.3 ± 3.1 nm for ×-10k, 14k, 19k, 25k, ∗-13k, 18k, and 30k, respectively. Lower than those for semi-crystalline ones, the R_{rms} values of the amorphous disks of photo-crosslinked PCLA ×-7k, ×-8k, and ∗-10k were 12.8 ± 1.3, 13.1 ± 1.6, and 11.9 ± 2.4 nm, respectively. It should be noted that the R_{rms} values of the photo-crosslinked PCLA disks at 37 °C should be lower than the above values from the AFM images taken at room temperature.

The difference in χ_c also affected the surface hydrophilicity of photo-crosslinked PCLA disks. As shown in Figure 4.6b, the water contact angle increased while the capability of adsorbing serum proteins from cell culture media decreased with increasing the molecular weight of PCLA, indicating more crystalline PCLAs led to higher hydrophobicity and lower protein adsorption. These results were consistent with the pervious findings on PCL fumarates (PCLFs), PCLDAs, and PCLTAs [16,17,30].

4.3.4 *In vitro* SMC attachment and proliferation.

Consistent with previous reports [16,17,33-35], stiffer disks of photo-crosslinked PCLAs better supported SMC attachment and proliferation. SMC attachment and proliferation in Figures 4.7a and 4.7b followed the same trend as the stiffness of the PCLAs, but the opposite trend as found in protein adsorption, by showing that the cell densities decreased with increasing the molecular weight for amorphous photo-crosslinked PCLAs while increased with increasing the molecular weight for semi-crystalline photo-crosslinked PCLAs. Except for SMC proliferation on the disks of amorphous photo-crosslinked PCLA ×-7k and ×-8k, the differences in SMC attachment and proliferation were significant between any two substrates for both 4arm and 6arm

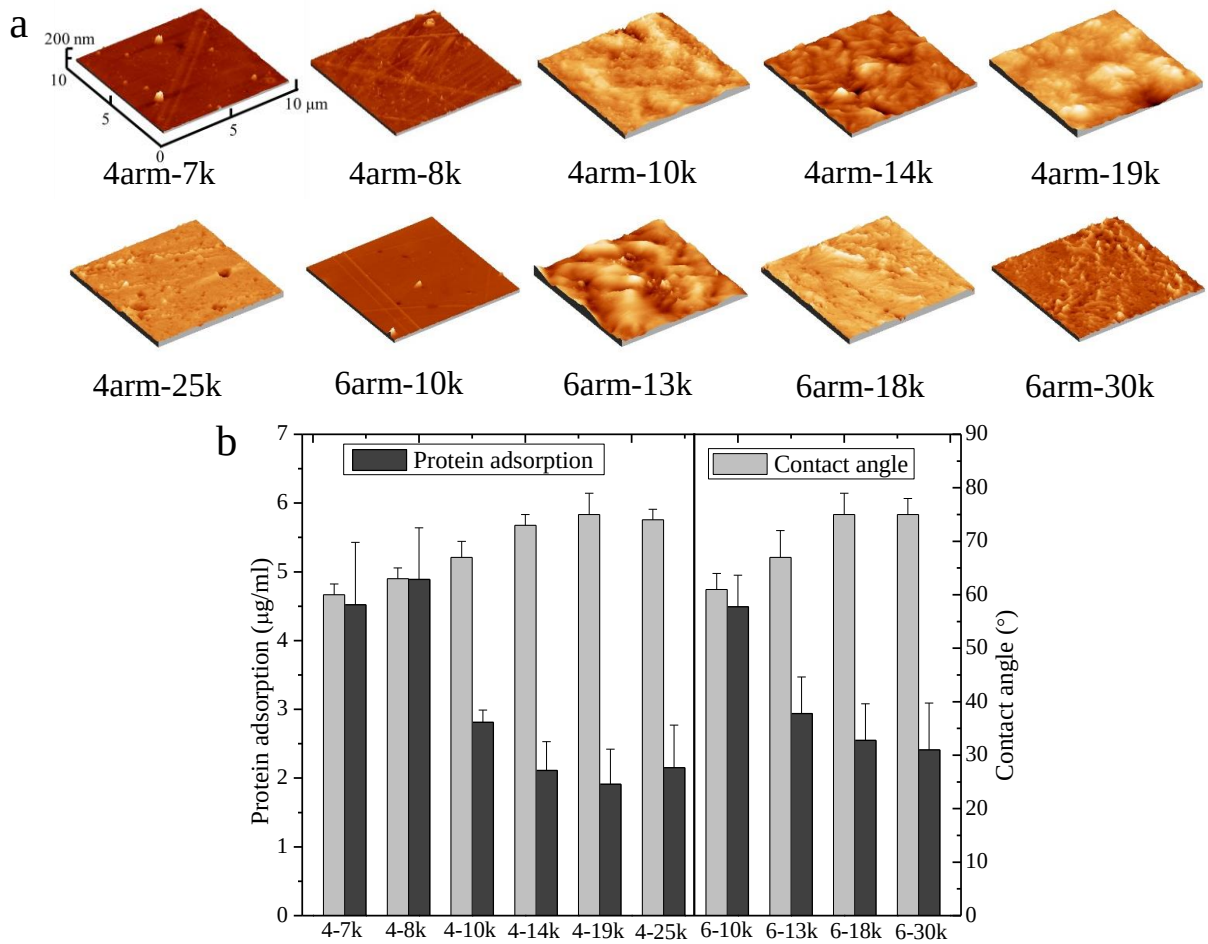

Figure 4.6 (a) AFM 3D height images of compressed crosslinked PCLA disks. (b) Water contact angles and protein adsorptions on crosslinked PCLA disks.

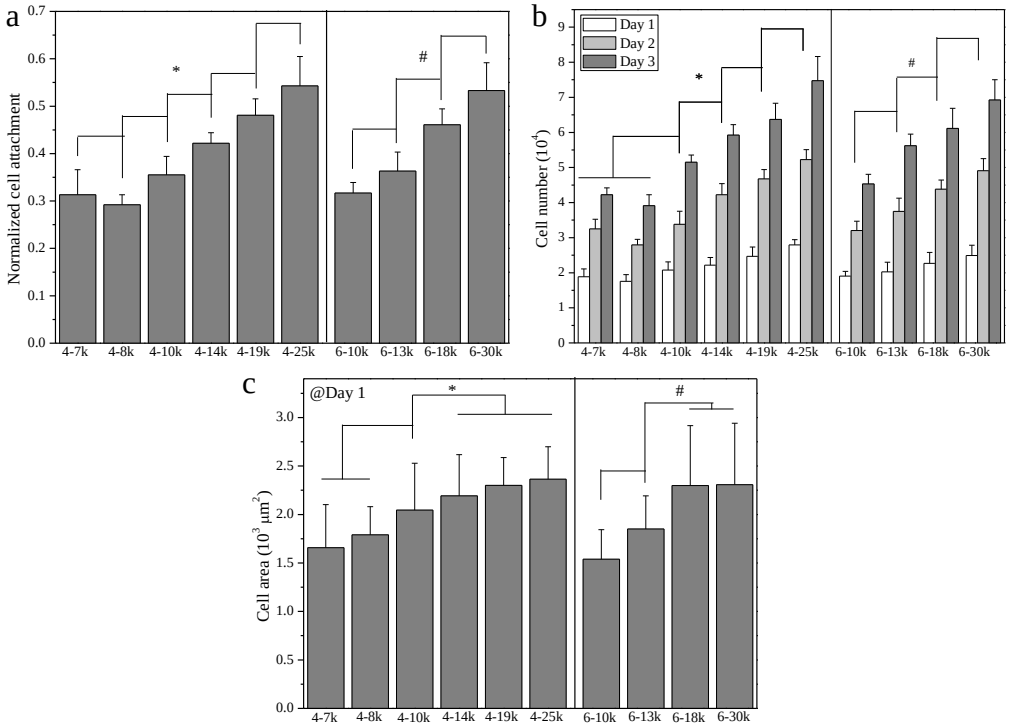

Figure 4.7 (a) Normalized SMC attachment at 4 h post-seeding, (b) SMC numbers at days 1, 2, and 4 post-seeding on the crosslinked PCLA disks, and (c) SMC areas at day 1 post-seeding. $^{*,\#}$: $p < 0.05$ between any two samples marked with the same symbol.

PCLAs. The images of SMCs stained with RP and DAPI at days 1, 2, and 4 are shown in Figure 4.8 and the cell numbers in the images were consistent with the results in Figures 4.7a and 4.7b. The cells on semi-crystalline disks of photo-crosslinked PCLAs were apparently more and could spread better and became confluent at day 4. While on the amorphous disks of photo-crosslinked PCLAs, SMCs were still separated at day 4. The SMCs had better spreading on the PCLAs with higher stiffness than PCLAs with lower stiffness, which was similar with the attachment and proliferation. As shown in Figure 4.7c, the cell spread areas analyzed from the cell images also followed the same trend as the cell attachment and proliferation. However, there was no significant difference between two amorphous groups of photo-crosslinked PCLA ×-7k and ×-8k, or among the three semi-crystalline groups of photo-crosslinked PCLA ×-14k, ×-19k and ×-25k, or between photo-crosslinked PCLA ∗-18k and ∗-30k. Interestingly, the SMC spread areas on the disks of photo-crosslinked PCLA ×-10k and ∗-13k with T_m near 37 °C were significantly smaller than those semi-crystalline ones but also significantly larger than those amorphous ones in their series.

4.3.5 Focal adhesions and gene expression.

FAs serve as the anchorage of a cell and signal carriers to report the ECM condition to cell nucleus and the feedback in turn determines the cell behavior [36,37]. Because FAs are the direct contacts between ECM and cell body, they were the primary component in sensing ECM stiffness and transducing signals to cells through internal signal pathways. Five representative substrates of photo-crosslinked PCLA ×-7k, ×-14k, ×-25k, ∗-18k and ∗-30k were chosen as the substrates to characterize the FAs in the SMCs cultured on them for one day. Based on the fluorescent cell images in Figure 4.9a, FA density and area are shown in Figure 4.9b. FAs on ×-7k, ×-14k, and ∗-18k substrates were less dense and mainly distributed on cell periphery, while FAs on ×-25k

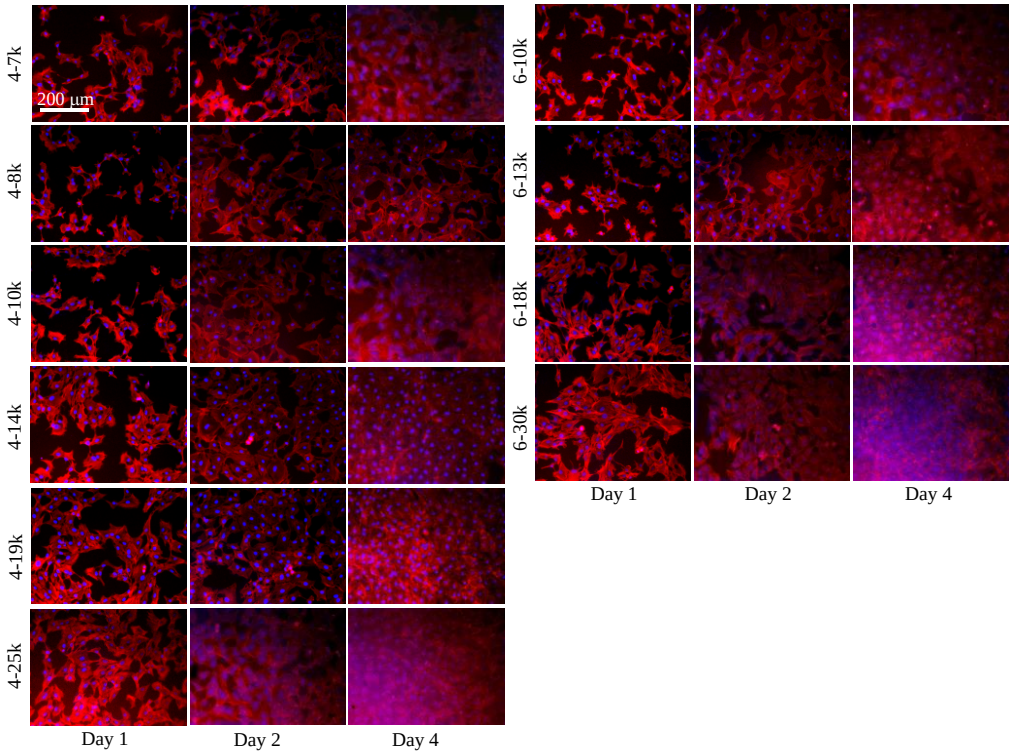

Figure 4.8 SMC images at days 1, 2, and 4 post-seeding stained using RP (red) and DAPI (blue).

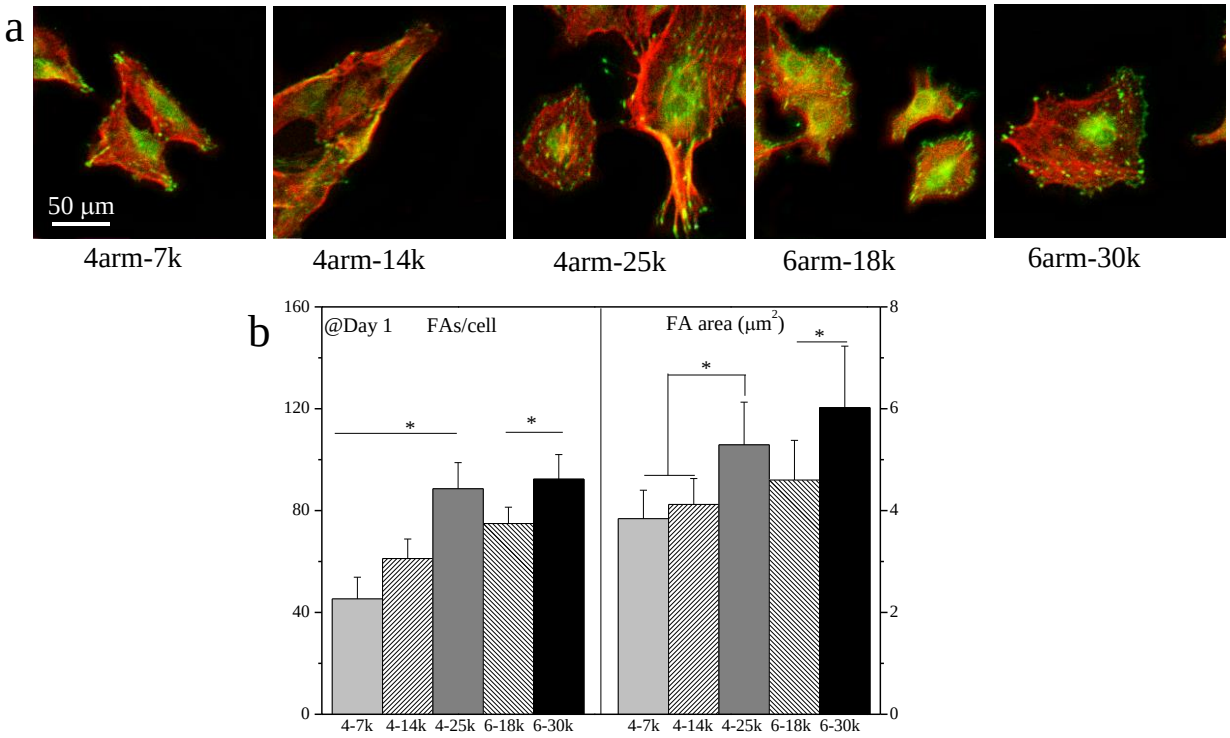

Figure 4.9 (a) Confocal microscope images of SMC filaments and vinculin antibody stained focal adhesions at day 1 post-seeding. (b) FA density, and area. *: $p < 0.05$ between any two samples marked with the same symbol.

and ∗-30k substrates were denser, and located both on cell periphery and inside cell body, as SMCs could sense more surface features of stiffer substrates than softer ones. SMCs on semi-crystalline photo-crosslinked PCLA ×-25k and ∗-30k had higher FA densities than those on the others, while the FA density on amorphous photo-crosslinked PCLA ×-7k was the lowest. Same as FA density, higher FA areas were also observed on the stiffer disks of photo-crosslinked PCLAs, while significant differences were found between ×-25k and the other two, or between ∗-30k and ∗-18k. FA elongation (~1.7) had no significant difference among all these studied photo-crosslinked PCLA disks with flat, featureless surfaces.

Based on the results on SMC attachment and proliferation, photo-crosslinked PCLA ×-7k, ×-14k, ×-25k, ∗-10k, ∗-18k and ∗-30k were chosen as the substrates for culture SMC for 4 days for real-time PCR to determine the mRNA expression levels of four typical contractile gene markers, i.e., smoothlin, calponin, transgelin, and SM-MHC. As shown in Figure 4.10, SMCs cultured on the stiffer substrates had higher contractile phenotypic gene expression levels, consistent with their attachment and proliferation. For all these four contractile gene markers, their expression levels were substantially higher on semi-crystalline photo-crosslinked PCLAs, and the highest levels appeared on the substrates with the highest PCLA molecular weight, i.e., the highest χ_c and E, for both 4arm and 6arm PCLA. The results indicated that stiffer substrates could support a larger portion of functional contractile phenotype and conversion from the proliferative synthetic phenotype. For these substrates with E higher than 100 MPa, the differences in the gene expression levels were smaller compared with the differences from those on the amorphous and compliant substrates. Besides the transgelin expression level on ×-14k and ∗-18k, there was no significant difference between photo-crosslinked disks of the 4arm and 6arm PCLAs with a similar stiffness, for example, ×-7k *vs.* ∗-10k, ×-14k *vs.* ∗-18k, and ×-25k *vs.* ∗-18k). This result indicated that

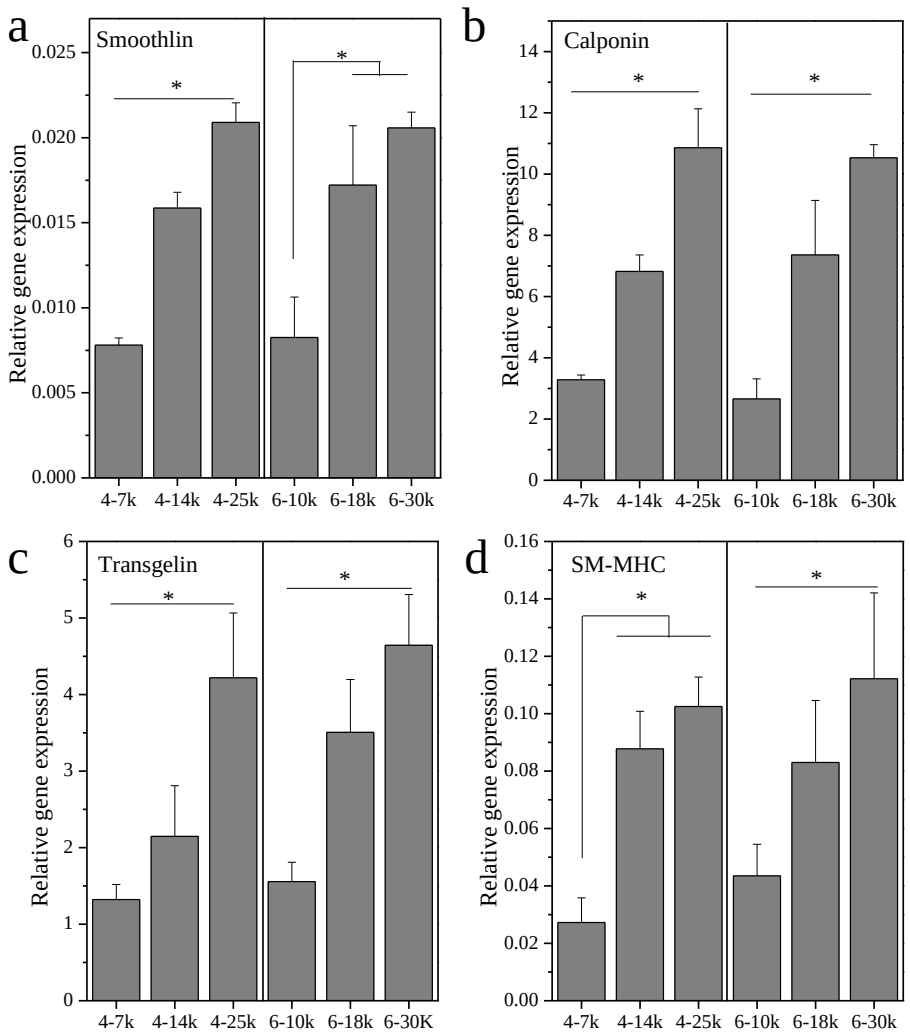

Figure 4.10 Gene expression levels of (a) smoothlin, (b) calponin, (c) transgelin, and (d) SM-MHC relative to GAPDH in SMCs at day 4 post-seeding on crosslinked PCLA disks. *: $p < 0.05$ between any two samples marked with the same symbol.

the gene expression could hardly differentiate the stiffness variance within 30 MPa.

4.3.6 Further discussion.

Compared with the previously reported PCLDAs and PCLTAs [16,17], the 4arm and 6arm PCLAs with different molecular weights used in this chapter had more acrylates in one polymer molecule. Thus photo-crosslinked 4arm and 6arm PCLAs had higher gel fractions and higher crosslinking densities, and more flexible in tuning the thermal and mechanical properties. Although the uncrosslinked sol part was PCLA and had no harm to the tissue, these free polymer chains might affect the mechanical properties and inhibit cell attachment. When PCLAs are used in *in situ* hardening/filling via photo-crosslinking, it will be difficult to remove the uncrosslinked PCLA and thus the sol fraction should be minimized without the need of increasing the crosslinking time. Therefore, compared with PCLDA and PCLTA at the same crosslinking time, 4arm and 6arm PCLAs with the same molecular weight could result in networks with high crosslinking densities and higher gel fractions.

Surface characteristics of photo-crosslinked PCLAs, such as surface roughness and hydrophilicity, were examined. The crystalline surfaces usually were much rougher with larger surface areas than the amorphous or compressed counterparts. The freely crystallized PCL surfaces with spherulitic structures were proved to better support MC3T3-E1 cell attachment and proliferation [38]. However, MC3T3-E1 attachment and proliferation were not evidently influenced by the surface roughness caused by PCL crystallization when semi-crystalline crosslinked PCLDA disks before and after hot compression were compared [16]. In this chapter, all the semi-crystalline PCLA networks were compressed to obtain smoother surfaces and the R_{rms} values were not significantly different from those for the amorphous ones. The hydrophilicity and the capability of adsorbing proteins from the cell culture media decreased with increasing the χ_c

of the PCLA network. Semi-crystalline photo-crosslinked PCLAs with higher *E* enhanced SMC attachment, proliferation, spreading, FAs, and contractile gene expression than the amorphous counterparts. Compared to roughness and hydrophilicity, SMC attachment, proliferation, and spreading were majorly affected by the substrate stiffness. In Chapter 2, I further found that prolonged photo-crosslinking time could render a higher crosslinking density in PCLA networks and consequently improved SMC attachment, proliferation, spreading, and FAs. The semi-crystalline 4arm and 6arm PCLA networks used in this chapter not only had high crosslinking density but also high stiffness, both of which could promote SMC responses to the substrates.

PCLAs with high efficiency of photo-crosslinking can be fabricated into 2D and 3D structures with tunable mechanical and thermal properties. As indicated in the previous discussion, both 4arm and 6arm PCLAs were PCL-dominant, and stiffness was regulated by the molecular weight. The photo-crosslinked 4arm PCLAs had *E* values in the range of 7.5-231MPa, and the photo-crosslinked 6arm PCLAs were between 4.9 and 249 MPa. A wide range of substrate stiffness resulted in distinct SMC attachment, proliferation, spreading, FAs, and gene expression. Nevertheless, further studies are needed to clarify the range of stiffness that is sensitive to cells. Based on the responses of different cell types to these photo-crosslinked PCLAs here and in previous studies in our research group, we can rationally select suitable biomaterials for different applications from hard tissue replacement to soft tissue replacement.

4.4 Conclusions

A series of biodegradable and photo-crosslinkable 4arm and 6arm PCLAs were prepared via the acrylation of PCL tetraols and hexanols were synthesized in the presence of K_2CO_3. These 4arm and 6arm PCLAs were photo-crosslinked with high crosslink efficiency into substrates with

controllable stiffness by varying the crosslinking density and crystallinity, which were simultaneously regulated by varying the PCLA molecular weight. Both amorphous and semi-crystalline PCLA networks were obtained, and their thermal, mechanical and rheological properties, surface roughness and hydrophilicity varied significantly. SMC cultured on these photo-crosslinked PCLA disks for 4 days demonstrated that stiffness affected more on the cell behaviors than surface roughness and hydrophilicity. Stiffer semi-crystalline photo-crosslinked PCLAs induced better attachment, faster proliferation, larger spread area, stronger FAs, and better conversion from the synthetic phenotype to the more functional contractile phenotype of SMCs.

References

1. Bettinger, C. J.; Langer, R.; Borenstein, J. T. *Angew. Chem., Int. Edit.* **2009**, *48*, 5406- 5415.

2. Flemming, R. G.; Murphy, C. J.; Abrams, G. A.; Goodman, S. L.; Nealey, P. F. *Biomaterials* **1999**, *20*, 573-588.

3. Anselme, K.; Bigerelle, M. *Int. Mater. Rev.* **2011**, *56*, 243-266.

4. Dalby, M. J. *Med. Eng. Phys.* **2005**, *27*(9), 730-742.

5. Wong, J. Y.; Leach, J. B.; Brown, X. Q. *Surf. Sci.* **2004**, *570*(1), 119-133.

6. Pozos Vázquez, C.; Boudou, T.; Dulong, V.; Nicolas, C.; Picart, C.; Glinel, K. *Langmuir* 2009, *25*(6), 3556-3563.

7. Wang, H. B.; Dembo, M.; Wang, Y. L. *Am. J. Physiol. Cell Physiol.* **2000**, *279*(5), C1345-C1350.

8. Gray, D. S.; Tien, J.; Chen, C. S. *J. Biomed. Mater. Res. A* **2003**, *66*(3), 605-614.

9. Saltzman, W. M.; Kyriakides, T. R. In *Principles of tissue engineering*, 3rd ed; Lanza, R., Langer, R., Vacanti, J., Eds.; Elsevier Academic Press: San Diego, CA, 2007; pp 279-296.

10. Wong, J. Y.; Leach, J. B.; Brown, X. Q. *Surf. Sci.* **2004**, *570*(1), 119-133.

11. Shi, X. F.; Mikos, A. G. In, Guelcher, S. A.; Hollinger, J. O.; Eds.; Introduction to biomaterials. CRC Press: Boca Raton, 2006; pp 205.

12. Wang, S.; Lu, L.; Yaszemski, M. J. *Biomacromolecules* **2006**, *7*(6), 1976-1982.

13. Wang, S.; Kempen, D. H.; Simha, N. K.; Lewis, J. L.; Windebank, A. J.; Yaszemski, M. J.; Lu, L. *Biomacromolecules* **2008**, *9*, 1229-1241.

14. Peter, S. J.; Miller, M. J.; Yasko, A. W.; Yaszemski, M. J.; Mikos, A. G. *J. Biomed. Mater. Res.* **1998**. *43*(4), 422-427.

15. Khan, Y.; Yaszemski, M. J.; Mikos, A. G.; Laurencin, C. T. J. *Bone Joint Surg. Am.* **2008**, *90*(S1), 36-42.

16. Cai, L.; Wang, S. *Polymer* **2010**, *51*(1), 164-177.

17. Liu, X. 2014. Phenotypic modulation of smooth muscle cells on biodegradable elastomeric substrates. Doctoral dissertation. The University of Tennessee, Knoxville.

18. Wang, S.; Lu, L.; Gruetzmacher, J. A.; Currier, B. L.; Yaszemski, M. J. *Biomaterials* **2006**, *27*(6), 832-841.

19. Wang, S.; Lu, L.; Gruetzmacher, J. A.; Currier, B. L.; Yaszemski, M. J. *Macromolecules* **2005**, *38*(17), 7358-7370.

20. Wang, S.; Kempen, D. H.; De Ruiter, G. C.; Cai, L.; Spinner, R. J.; Windebank, A. J.; Yaszemski, M. J.; Lu, L. *Adv. Funct. Mater.* **2015**, *25*(18), 2715-2724.

21. Cai, L.; Lu, J.; Sheen, V.; Wang, S. *Biomacromolecules* **2012**, *13*(2), 358-368.

22. Cai, L.; Guinn, A. S.; Wang, S. *Acta Biomater.* **2011**, *7*(5), 2185-2199.

23. Wang, K.; Cai, L.; Zhang, L.; Dong, J.; Wang, S. *Adv. Healthc. Mater.* **2012**, *1*(3), 292-301.

24. Cai, L.; Zhang, L.; Dong, J.; Wang, S. *Langmuir* **2012**, *28*(34), 12557-12568.

25. Voit, B. I.; Lederer, A. *Chem. Rev.* **2009**, *109*(11), 5924-5973.

26. Voit, B. *J. Polym. Sci. A Polym. Chem.* **2000**, *38*(14), 2505-2525.

27. Cai, L.; Wang, S. *Biomacromolecules* **2009**, *11*(1), 304-307.

28. Ju, M.; Shen, L.; Gong, F.; Gao, Y.; Zhang, W. *Polym. Int.* **2012**, *61*(9), 1447-1455.

29. Polymer Handbook. 3rd ed. Brandrup, J.; Immergut, E. H.; Eds.; Wiley: New York, 1989.

30. Wang, S.; Yaszemski, M. J.; Gruetzmacher, J. A.; Lu, L. *Polymer* **2008**, *49*(26), 5692-5699.

31. Crystallization of polymers. 2nd ed.; Mandelkern, L. McGraw Hill, New York, 2001; Chapter 7, vol. 1.

32. ‘Introduction to physical polymer science’. 3rd ed.; Sperling, L. H. Wiley: New York,2001; pp 363.

33. Yeung, T.; Georges, P. C.; Janmey, P. A. *Cell Motil. Cytoskel.* **2005**, *60*, 24-34.

34. Schwartz, U. *Soft Matter* **2007**, *3*, 263-266.

35. Choquet, D.; Felsenfeld, D. P.; Sheetz, M. P. *Cell* **1997**, *88*, 39-48.

36. Pelham, R. J.; Wang, Y. L. *Pro. Natl. Acad. Sci. USA* **1997**, *94*, 13661-13665.

37. Burridge, K.; Chrzanowska-Wodnicka, M. *Annu. Rev. Cell Dev. Biol.* **1996**, *12*(1), 463-519.

38. Wang, K.; Cai, L.; Jesse, S.; Wang, S. *Langmuir* **2012**, *28*, 4382-4395.

Chapter V. Roles of Microgroove Dimensions in Promoting Smooth Muscle Cell Functions on Photo-crosslinked Poly(ε-caprolactone) Acrylate Substrates

Abstract

This study was to clarify how microgroove dimensions affected rat aortic smooth muscle cell (SMC) responses to microgrooved substrates of photo-crosslinked poly(ε-caprolactone) acrylates (PCLAs). Using replica molding from micromachined silicon wafer templates, we fabricated photo-cured PCLA substrates with parallel microgrooves (two groove depths of 1 and 12 μm and two groove widths of 5 and 15 μm). These four types of microgrooved substrates, together with the flat one, were used to study SMC attachment, proliferation, alignment, nuclear circularity and distribution, focal adhesion (FA), motility/migration, and gene expression. Most of the microgrooves did not affect SMC attachment and proliferation, while only on the microgrooved substrate with a groove depth of 12 μm and a groove width of 5 μm, cell proliferation decreased at days 2 and 4 post-seeding. The shape and distribution of SMC, as well as the shape and distribution of cell nuclei were significantly altered by the dimensions of the microgrooved substrates. The SMCs on the microgrooved substrates did not show clear FAs, but had higher contractile phenotypic gene expression levels than those on the flat substrates, especially when the groove depth was 12 μm. Both substrate stiffness and microgrooves were proved to promote SMC motility. All microgrooves regulated SMCs to migrate mainly along the groove direction. On the microgrooved substrate with a groove depth of 12 μm and a groove width of 5 μm, SMC migration speed decreased after the cells were trapped inside the microgrooves. In addition, we also found that different culture time periods and different microgroove dimensions had no effect on the SMC motility.

5.1 Introduction

Cell-biomaterial interactions are crucial to the success of implants and tissue-engineering scaffolds [1-3]. There are three major categories of surface physicochemical characteristics in determining cell behavior: surface chemistry, surface mechanical properties, and surface morphology [1-3]. To study how surface morphologies can be used to regulate cell-material interactions, surface micro- and nano-patterning have been used in fabrication of biomaterial substrates [4-14]. Cell responses to different micro- and nano-scale topographies via "contact guidance" as the cytoskeletal arrangements are directly influenced by the surface patterns [15-26]. Among these cell behaviors, cell motility and migration were found to be significantly affected in both the direction and speed [27-33]. Thus polymer substrates and structures that can guide and expedite cell migration and tissue growth, and upregulate gene/protein expression could be desirable for promoting tissue regeneration. Excessive proliferation of vascular smooth muscle cell (SMC) is recognized as one of the characteristics for atherosclerosis [34,35]. Locally control of the migration of vascular SMCs is crucial for the treatment of arterial occlusive disease [36,37].

Biodegradable and photo-crosslinkable polymers with excellent processability can be fabricated into implantable two-dimensional (2D) substrates or three-dimensional (3D) scaffolds with good biocompatibility for regulation of cellular behavior and tissue engineering applications [38,39]. Previously in our research group, both parallel and concentric-microgrooved substrates with various groove widths and depths of photo-crosslinked poly(ε-caprolactone) triacrylates (PCLTAs) were prepared via the replica molding method using micro-machined silicon wafer templates [21-23]. These microgrooved substrates of photo-crosslinked PCLTAs were used to promote alignment and differentiation of mouse pre-osteoblastic MC3T3-E1 cells [21,22], rat pheochromocytoma (PC12) cells [23], and rat Schwann cell precursor line (SPL201) cells [23].

Without showing statistical difference in attachment and proliferation, MC3T3-E1 cell alignment and elongation, distribution of nuclei, and mineralization were found to be better on the stiffer substrates and narrower microgrooves with a groove width of 7.5 μm and a groove depth of 10 μm [21]. The microgroove dimensions showed no effects on the PC12 and SPL201cell proliferation, while PC12 and SPL201 cell alignment, differentiation, and SPL201 cell motility were found to be better on the microgrooved substrates than on the flat substrates [23]. The PC12 and SPL201 cell alignment and differentiation were better on narrower microgrooves, while only SPL201 cell alignment were improved by deeper microgrooves. Moreover, narrower and deeper microgrooves made more SPL201 cell nuclei trapped into the grooves, and the circularity of the nuclei decreased [23]. These previous studies supplied rationale for deliberately selecting suitable mechanical properties and groove dimensions for the present study.

Using the same method and high-molecular-weight 4arm and 6arm PCL acrylates (PCLAs), here I fabricated parallel-microgrooved substrates with designed groove depths of 1 and 12 μm and designed groove widths of 5 and 15 μm. I directly correlated the groove dimensions with rat aortic SMC attachment, proliferation, alignment, distribution and deformation of nuclei, focal adhesions (FAs), and gene expression on the microgrooved substrates. Simultaneously modulated surface stiffness and microgroove dimensions in these photo-crosslinked PCLA substrates were also correlated with SMC in both direction and speed. The findings here could not only improve our fundamental understanding on cell-material interactions but also provide guidance for fabricating polymer scaffolds with appropriate mechanical properties and structural features for cardiovascular tissue engineering applications.

5.2 Materials and Methods

5.2.1 Materials.

Methylene chloride (CH_2Cl_2) was purchased from Fisher Scientific (Hampton, NH) while all other chemicals used here were purchased from Sigma Aldrich (Milwaukee, WI) unless otherwise noted. The polymers utilized to fabricate microgrooved substrates in this chapter were 4arm PCLA (4arm-25k) with a number-average molecular weight (M_n) of 25,400 g/mol and a weight-average molecular weight (M_w) of 34,500 g/mol, and 6arm PCLA (6arm-30k) with M_n of 30,600 g/mol and M_w of 38,800 g/mol, as previously synthesized [40]. PCLA 4arm-25k, 6arm-30k, and another 4arm PCLA (4arm-7k) with M_n of 7,390 g/mol and M_w of 8,730 g/mol were used to prepare flat substrates. Micro-fabricated silicon wafers with parallel microgrooves were prepared as templates or molds using standard stereolithography [21-23]. The microgroove dimensions with two groove depths of 1 and 12 μm, and two groove widths of 5 and 15 μm were used. The groove width was designed to be equal to the ridge width.

5.2.2 Photo-crosslinking of PCLA flat samples and microgrooves.

Photo-initiator, phenyl bis(2,4,6-trimethyl benzoyl) phosphine oxide (BAPO, IRGACURE 819, Ciba Specialty Chemicals, Tarrytown, NY) was used in photo-crosslinking. PCLA/BAPO/CH_2Cl_2 solution (1.5 g/15 mg/500 μL) was transferred onto the silicon molds and photo-crosslinked under a high-intensity long-wave ultraviolet (UV) lamp (SB-100P, Spectronics Corp., Westbury, NY, λ= 365 nm, Intensity: 4800 w/cm^2) for 20 min. Photo-crosslinked PCLA microgrooved substrates were peeled off from the silicon mold and soaked in acetone for two days to remove the sol fraction, followed by complete drying in vacuum. Flat substrates of photo-crosslinked PCLAs were prepared by transferring the polymer solution into a Teflon mold composed of two glass plates and a Teflon spacer, and photo-crosslinked for 20 min, as I

previously reported [40]. Both flat and microgrooved substrates of photo-crosslinked PCLAs were sterilized in 70% ethanol solution and dried completely before the cell studies. The microgrooved structures were characterized using scanning electron microscopy (SEM; S-3500, Hitachi Instruments, Tokyo, Japan) at 5 kV.

5.2.3 *In vitro* SMC attachment, proliferation and alignment.

SMCs were cultured in a growth medium composed of Dulbecco's modified eagle medium (DMEM; Gibco, Grand Island, NY) supplemented with 10% fetal bovine serum (FBS; HyClone, Thermal Scientific) and 1% penicillin/streptomycin (Gibco) in an incubator with 5% CO_2 and 95% relative humidity at 37 °C. SMCs were seeded on the flat and microgrooved substrates at a density of 15,000 cells/cm^2 and cultured for 4 h, 1, 2, and 4 days. A colorimetric cell metabolic assay (CellTiter 96 Aqueous One Solution, Promega, Madison, WI) was performed in each well to determine the number of attached cells, which was correlated to the UV absorbance of the solution at 490 nm measured on a microplate reader (SpectraMax Plus 384, Molecular Devices, Sunnyvale, CA). Cell numbers were then quantified using the standard curve that was constructed using known cell numbers. SMCs attached on the flat and microgrooved substrates were washed with phosphate buffered saline (PBS), fixed in 4% paraformaldehyde (PFA, Electron Microscopy Science) solution for 10 min at room temperature, washed with PBS twice, and then permeabilised with 0.1% Triton X-100 at room temperature for another 10 min. Cytoplasm was then stained using rhodamine-phalloidin (RP, Cytoskeleton, Denver, CO) for 1 h at 37 °C, and cell nuclei were stained using 4',6-diamidino-2-phenylindole (DAPI) at room temperature, respectively. Then the cells were photographed using an Axiovert 25 light microscope (Carl Zeiss, Germany). From the cell images, cell circularity, major/minor axis ratio, area, and perimeter on the flat and microgrooved substrates were determined on more than 25 non-overlapping cells at

day 1. Cell or nuclear circularity defined by the equation of $4\pi \times$ area/perimeter^2 is the measure how close a cell or nucleus is to being perfectly round, in which the circularity is 1. A cell was considered aligned if the angle between the groove direction and the direction of the longer axis of the cell was smaller than 15° [15]. The percentage of aligned cells in the entire cell population was quantified from more than 100 cells at day 1. SMC nuclei circularity and distribution were analyzed from more than 100 cells at day 4. All of these characterizations were determined using the ImageJ software (National Institutes of Health, Bethesda, MD).

5.2.4 Focal adhesions.

After one-day culture, SMCs attached on the flat and microgrooved substrates were washed with PBS, fixed in 4% PFA solution, washed with PBS three times, and permeabilised with 0.1% Triton X-100 at room temperature for 10 min. Then the substrates with attached SMCs were incubated in 1% bovine serum albumin (BSA)/PBS at 37 °C for 30 min. After being washed with PBS three times, the substrates with attached SMCs were incubated in monoclonal mouse antibody against vinculin (1:1000 in 1% PBS; Sigma) at room temperature for 2 h, and then washed with PBS three times again. Then the substrates with attached SMCs were cultured with goat anti-mouse IgG secondary antibody (1:200 in 1% PBS; Sigma) in dark at room temperature for 2 h. The attached SMCs were also stained using RP at 37 °C for another 1 h. The FAs in SMCs on the substrates were then photographed on a Leica DM6000B fluorescent confocal microscope (Buffalo Grove, IL).

5.2.5 Gene expression.

Polymerase chain reaction (PCR) was used to quantify the expression levels of contractile phenotypic markers of smoothlin, calponin, smooth muscle myosin heavy chain (SM-MHC), and transgelin in SMCs cultured for 4 days on the flat and microgrooved substrates of photo-

crosslinked PCLAs. Total RNA was isolated using the RNeasy Mini Kit (Qiagen, Valencia, CA) and the cDNA was synthesized by reverse transcription using DyNAmo cDNA Synthesis Kit (Thermo Scientific, Waltham, MA). The primers for these gene markers were designed using the Oligoperfect software, and their sequences are listed as follows. Smoothlin: forward 5'-TCGGAGTGCTGGTGAATAC-3', reverse 5'-CCCTGTTTCTCTTCCTCTGG-3'; calponin: forward 5'-AGTCTACTCTCTCTTGGCTCTGGCC-3', reverse 5'-CCTGCCTTCTCTCAGCTTCTCAGG-3'; SM-MHC: forward 5'-AAGCAGCTCAAGAGGCAG-3', reverse 5'-AAGGAACAAATGAAGCCTCGTT-3'; transgelin: forward 5'-GGCAGCTGAGGATTATGGAGTCACG-3', reverse 5'-TGGGATCTCCACGGTAGTGTCCA-3'; and house-keeping gene glyceraldehyde-3-phosphate dehydrogenase (GAPDH): forward 5'-TCTTCACCACCATGGAGAA-3', reverse 5'-ACTGTGGTCATGAGCCCTT-3'. Expression of these gene markers was quantified through PCR with Power SYBR Green PCR Master Mix (Applied Biosystems, Warrington, UK). The amplification and detection process was performed on a Peltier Thermal Cycler fluorescence detection system (MJ Research PTC-200). The software procedure was set as 94 °C for 5 min followed by the cyclic steps of 94 °C for 30 s, 55 °C for 30 s, and 72 °C for 30 s. The expression levels of target gene markers were normalized to that of the GAPDH.

5.2.6 Single cell migration.

SMCs with densities of 10,000 and 5,000 cells/cm^2 were first cultured on the flat substrates of photo-crosslinked PCLA 4arm-7k and 4arm-25k, and microgrooved substrates of photo-crosslinked PCLA 4arm-25k for 12 h and 2 days, respectively. Then SMCs were incubated with fluorescent Calcein dye (Calcein AM, Invitrogen) at a concentration of 4 μM for 30 min to receive live staining and then transferred into transparent wells in a flow chamber at 37 °C. Cell migration

was monitored real-time by tracking the same cells every 30 min using the Axiovert 25 light microscope. The cell migration velocity was calculated for more than 100 cells on each substrate by dividing the center-of-mass migration distance of the cell over 30 min. The migration vector of a cell generated in 30 min was presented as a dot in an *XY*-diagram and characterized by its migration distance and direction, according to literature [41].

5.2.7 Statistical analysis.

Cell studies were performed in quadruplicates for each group at each time point. All values were expressed as mean ± standard deviation. The statistical significance ($p < 0.05$) in the difference between two groups was calculated using the student's *t*-test.

5.3 Results and Discussion

5.3.1 Characterization of microgrooved substrates.

Figure 5.1 shows the SEM images of four representative types of microgrooved substrates of photo-crosslinked PCLA 4arm-25k with groove depths of 1 and 12 μm, and groove widths of 15 and 5 μm. Almost identical to the designed values, the actual groove depths/widths determined from the SEM images for these four substrates were 0.9 ± 0.1/16.8 ± 0.5, 1.1 ± 0.1/4.8 ± 0.3, 12.1 ± 0.3/16.4 ± 0.4, and 12.3 ± 0.2/5.0 ± 0.4 μm, respectively. As photo-crosslinked PCLA 6arm-30k had similar properties with PCLA 4arm-25k such as gel fraction (0.82 ± 0.01 for 4arm-25k and 0.90 ± 0.02 for 6arm-30k) and swelling ratio (17.9 ± 0.9 for 4arm-25k and 11.7 ± 0.8 for 6arm-30k), the groove dimensions in the microgrooved substrates of photo-crosslinked PCLA 6arm-30k were also identical to the designed values. For simplification, the four different microgrooved substrates were named as 1-15, 1-5, 12-15, and 12-5, showing the groove depths of 1 and 12 μm, and groove widths of 15 and 5 μm, respectively.

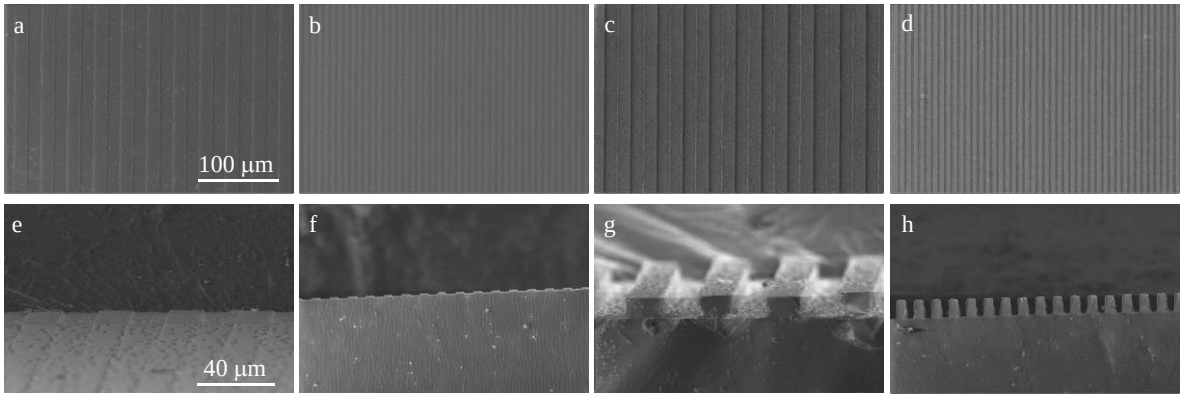

1-15 1-5 12-15 12-5

Figure 5.1 SEM images of the microgrooves with widths of 5 and 15 μm and depths of 1 and 12 μm on crosslinked 4arm-25k PCLA. Scale bar of 100 μm is applicable to a, b, c and d. Scale bar of 40 μm is applicable to e, f, g and h.

5.3.2 *In vitro* SMC attachment and proliferation.

As shown in Figure 5.2, no significant differences were observed in SMC numbers at all the time points between the flat and microgrooved substrates, and among different microgrooved substrates made from the same PCLA, with one exception. This exception was that the cell numbers on the 12-5 microgrooved substrates for both photo-crosslinked PCLA 4arm-25k and 6arm-30k were lower at days 2 and 4 than on the other substrates, and in particular, the difference became significant ($p < 0.05$) at day 4. This decreased SMC proliferation might be due to the entrapment of cytoplasm and cell nuclei that inhibited cell spreading in deep and narrow grooves. Although the microgrooves had limited inhibition on SMC proliferation, they significantly altered the morphology of the cells, as shown in Figure 5.3. The SMCs cultured on the microgrooved substrates were obviously aligned along the groove direction. Significant difference in SMC alignment was observed between the microgrooved substrates with different groove depths. On 12-15 and 12-5 microgrooved substrates, the SMC alignments were still clear at day 4. These experimental phenomena were associated with "contact guidance" that occurred during cell spreading. After the cells attached to the microgrooved substrates, they started to explore their surroundings by extending filopodia [7]. SMC circularity, major/minor axis ratio, area and alignment analyzed from the cell images at day 1 before the cells reached confluency on both photo-crosslinked PCLA 4arm-25k and 6arm-30k are shown in Figure 5.4. The cells on the microgrooved substrates showed much smaller circularities than on the flat substrates. When the groove depth was 12 μm, the circularities of the cells were significantly lower than those on the microgrooved substrates with the groove depth of 1 μm. The cell circularity further decreased from ~0.35 to ~0.25 when the microgrooved substrate changed from 12-15 to 12-5, i.e., when the groove width decreased from 15 to 5 μm. The areas of SMCs on the microgrooved substrates were also

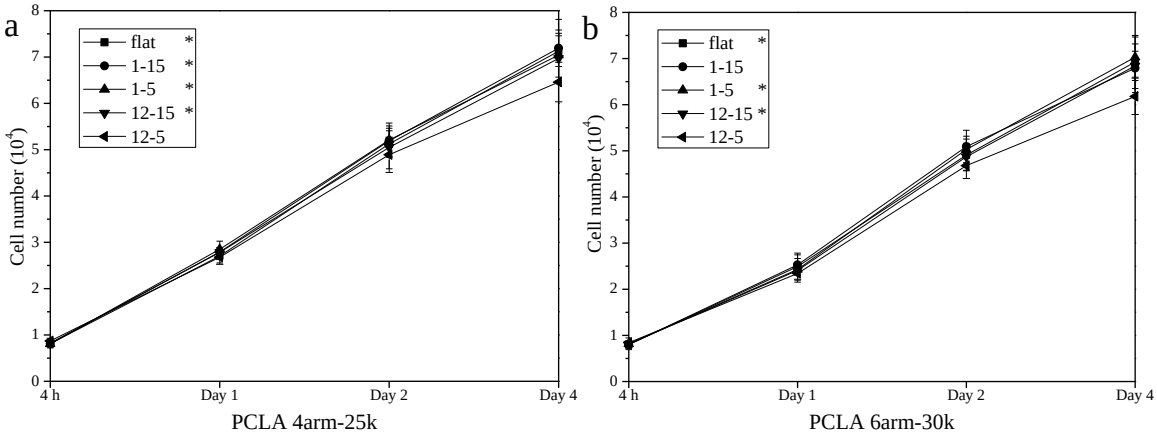

Figure 5.2 SMC numbers at 4 h, days 1, 2, and 4 post-seeding on the microgrooved PCLA disks. *: $p < 0.05$ between the samples marked with the same symbol with the corresponding data on microgrooved disks of 12 μm depth and 5 μm width at day 4 post-seeding.

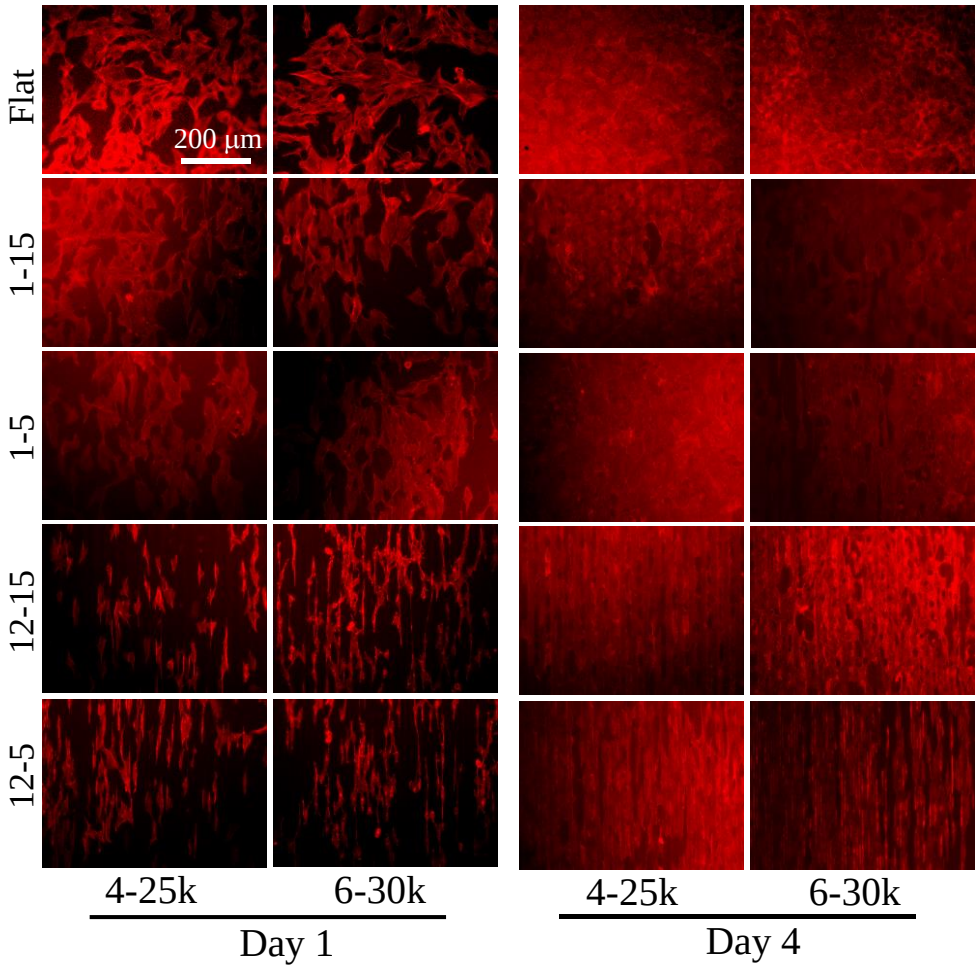

Figure 5.3 SMCs images at days 1 and 4 post-seeding stained using RP (red) on the flat and microgrooved PCLA disks. Scale bar of 200 μm is applicable to all.

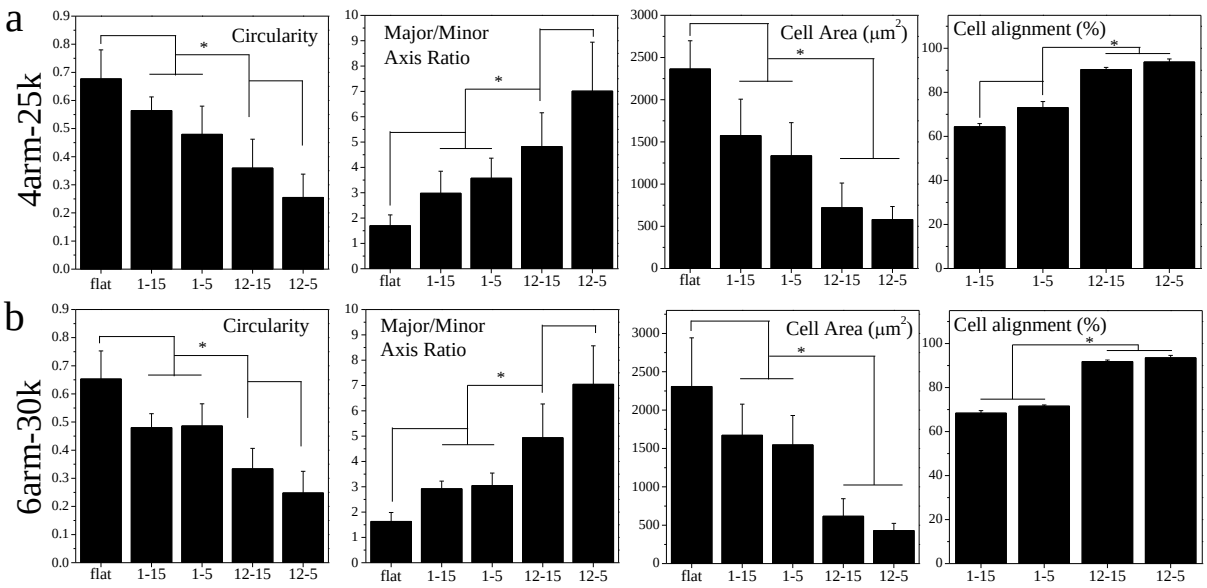

Figure 5.4 SMC circularity, major/minor axis ratio, area and alignment at day 1 post-seeding on the flat and microgrooved substrates of photo-crosslinked PCLA (a, 4arm-25k; b, 6arm-30k). *: $p < 0.05$ between the samples marked with the same symbol.

significantly smaller than that on the flat substrate for both 4arm-25k and 6arm-30k. The cell areas were significantly lower on the microgrooved substrates with the groove depth of 12 μm than on those with the groove depth of 1 μm, while there was no significant difference between the microgrooved substrates with the same groove depth.

Microgroove dimensions also affected both the morphology and distribution of SMC nuclei. The fluorescent images of DAPI-stained SMC nuclei on the microgrooved substrates of photo-crosslinked PCLA 4arm-25k are shown in Figure 5.5a. The average circularity of SMC nuclei and the preference in the grooves analyzed from the images in Figure 5.5a (the images of SMC nuclei on the microgrooved substrates of photo-crosslinked PCLA 6arm-30k are not shown) are shown in Figures 5.5b and 5.5c, respectively. SMC nuclei were aligned along the groove direction and had significantly lower circularities only on the 12-5 microgrooved substrates with the smaller groove width and the groove depth larger than the nuclear diameter (~10 μm) for both PCLA 4arm-25k and 6arm-30k. The circularities of the cell nuclei were ~0.8 for the other three microgrooved substrates, as either the groove width was larger or the groove depth was smaller than the nuclear diameter. The distribution of the cell nuclei over the microgrooved substrates was critical for analysis, and thus I further characterized the percentage of the cell nuclei trapped in the grooves. On the 1-5 microgrooved substrates where the groove depth was only 1 μm and the groove width was smaller than the nuclear diameter, the cell nuclei were evenly distributed. Considering that the groove width was designed to be identical to the ridge width, the percentages of cell nuclei in the grooves on the 1-5 microgrooved substrates of both PCLA 4arm-25k and 6arm-30k were 50%. The percentages of SMC nuclei in the grooves were ~66%, 82%, and 89% for the 1-15, 12-15, and 12-5 microgrooved PCLA 4arm-25k substrates, and ~64%, 80%, and 89% for the 1-15, 12-15, and 12-5 microgrooved PCLA 6arm-30k substrates, respectively. Similar to SMC alignment and area,

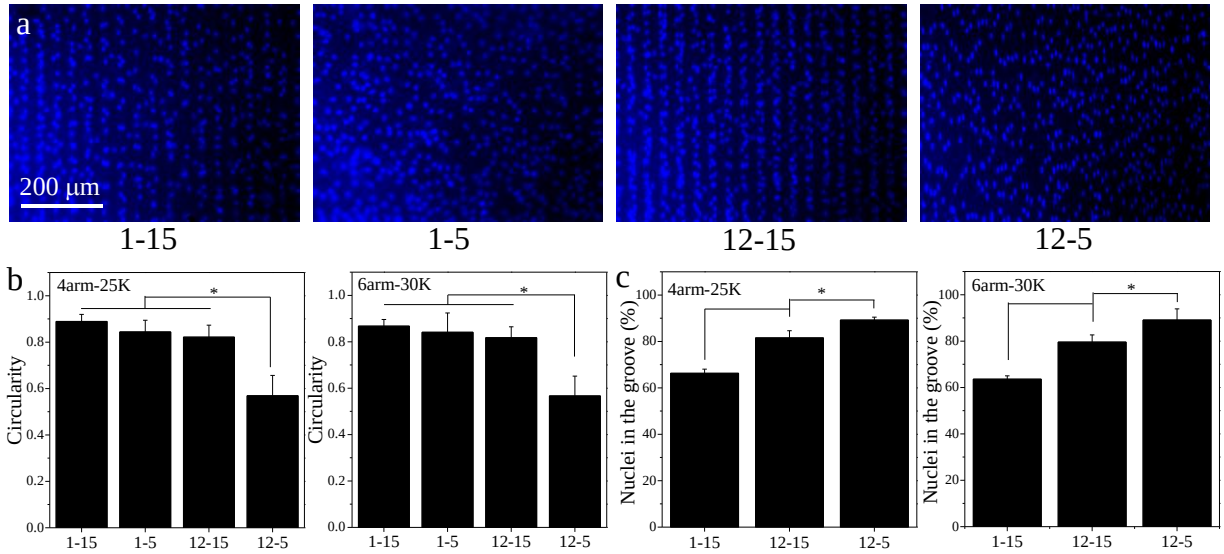

Figure 5.5 (a) Fluorescent images of SMC nuclei stained using DAPI (blue) on the microgrooved substrates of photo-crosslinked PCLA 4arm-25k. Scale bar of 200 μm is applicable to all. SMC nuclear circularities (b), and locations (c) at day 4 post-seeding on the microgrooved PCLA disks. *: $p < 0.05$ between the samples marked with the same symbol.

the groove depth affected more than the groove width in regulating nuclear morphology and distribution as the former varied by a larger factor of 12.

5.3.3 Focal adhesions and gene expression.

Confocal microscopic images of the FAs in the SMCs cultured for one day on the microgrooved substrates of photo-crosslinked PCLA 4arm-25k and 6arm-30k are shown in Figure 5.6. Clear punctate FAs were seen on the microgrooved substrates with the groove depth of 1 μm for both PCLA 4arm-25k and 6arm-30k. In contrast, the FAs formed clusters on the microgrooved substrates with the groove depth of 12 μm as the cells were trapped and crowded inside the grooves.

Real-time PCR was conducted on the SMCs cultured for 4 days on the flat and microgrooved substrates and the mRNA expression levels of four typical contractile gene markers, i.e., smoothlin, calponin, SM-MHC, and transgelin were analyzed, as shown in Figure 5.7. The cells cultured on the microgrooved substrates had higher gene expression levels than the flat ones for both PCLA 4arm-25k and 6arm-30k, in particular, when the groove depth was 12 μm. In contrast to the effect of deep grooves, the variance in the groove width (5 μm *vs.* 15 μm) did not result in obvious differences in gene expression. It should be noted that among all the substrates not all the differences were significant while the differences between the flat substrates and microgrooved substrates with the groove depth of 12 μm were always significant. These results indicated that the presence of microgrooves, especially the deeper ones, upregulated the contractile mRNA level.

5.3.4 SMC migration.

Single-cell migration of the SMCs at 12 h and day 2 post-seeding was studied on the flat substrates of photo-crosslinked PCLA 4arm-7k and 4arm-25k and the four microgrooved substrates of photo-crosslinked PCLA 4arm-25k. The migration vectors of the chosen cells are

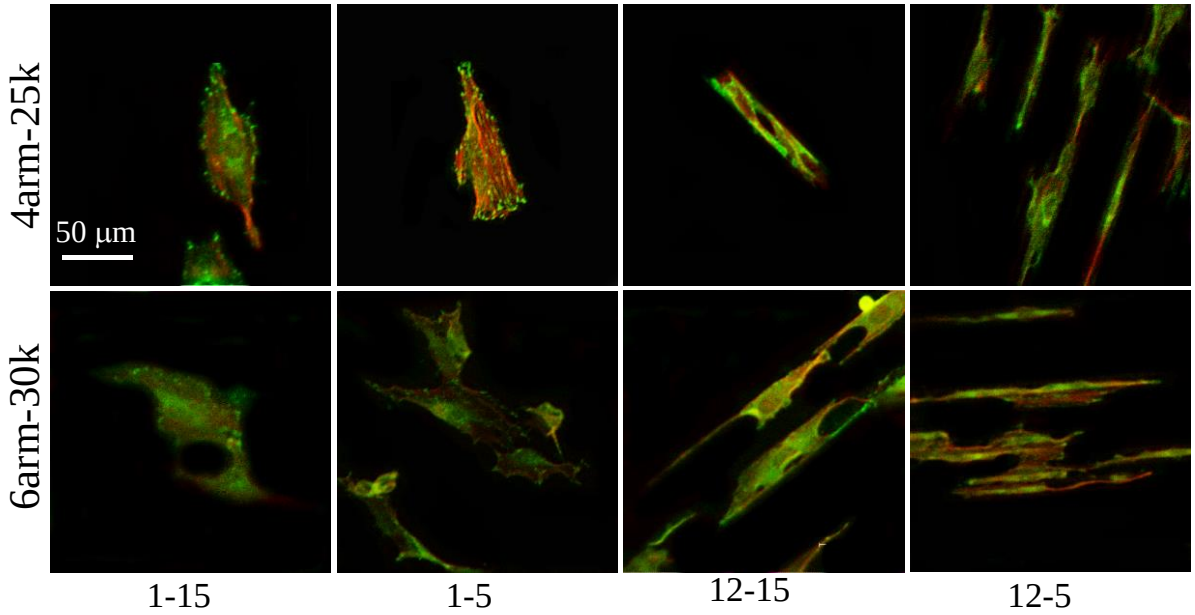

Figure 5.6 Confocal microscope images of SMC filaments and vinculin antibody stained focal adhesions. Scale bar of 50 μm is applicable to all.

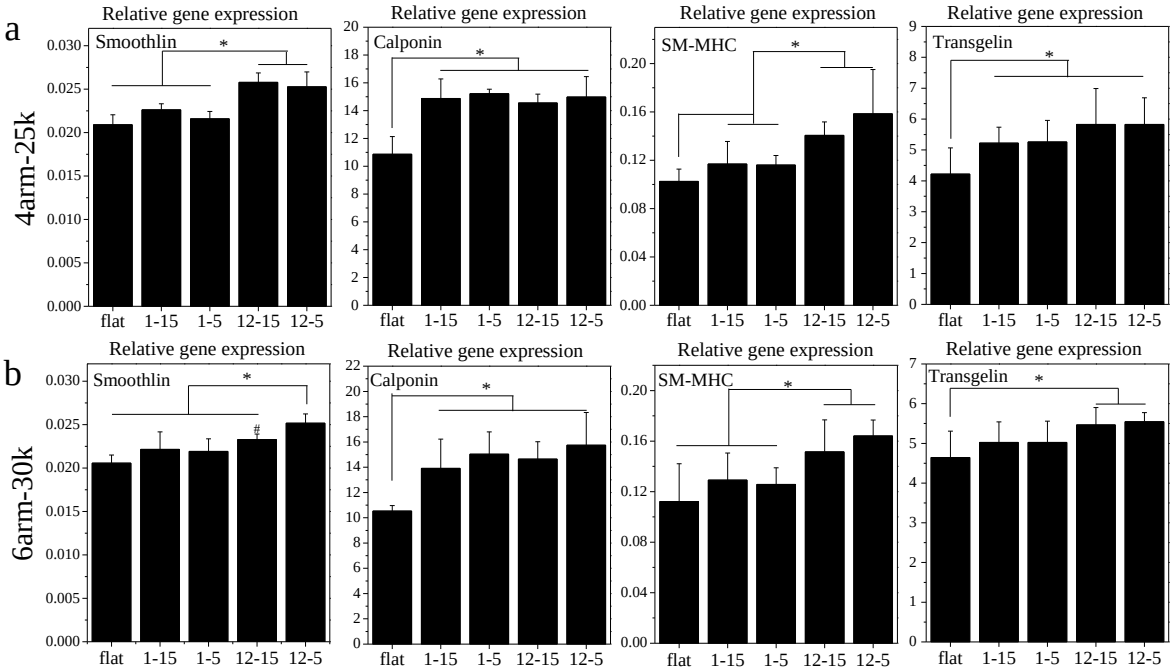

Figure 5.7 Gene expression levels of smoothlin, calponin, SM-MHC, and transgelin relative to GAPDH in SMCs at day 4 post-seeding on the flat and microgrooved PCLA disks (a, 4arm-25k; b, 6arm-30k). *: $p < 0.05$ between the samples marked with the same symbol. #: $p < 0.05$ between the samples marked with the symbol and flat sample.

shown in Figure 5.8. The migration speeds of the cells at 12 h and day 2 are shown in Figure 5.9. In order to avoid the overlap of cells, the cell densities used in the migration study was much lower than the density used in studying cell attachment and proliferation. The comparison between the two flat substrates suggested that the SMC migration favored stiffer substrates in the studied stiffness range, as photo-crosslinked PCLA 4arm-25k with Young's moduli (*E*) of 229 ± 16 MPa was much stiffer than photo-crosslinked PCLA 4arm-7k with *E* of 14.0 ± 0.3 MPa at 37 °C. The migration speeds of the SMCs on the flat substrate of photo-crosslinked PCLA 4arm-25k (~0.12 μm/min) were much higher than those on the PCLA 4arm-7k counterpart (~0.07 μm/min) at both 12 h and day 2. The SMC migration speed did not have vary at different culture time on both flat substrates.

The cell motilities were much higher on the microgrooved substrates than that on the flat one when PCLA 4arm-25k was used. At 12 h, the migration speeds (~0.14 μm/min) of the SMCs did not vary much on the microgrooved substrates with different groove widths and depths. At day 2, the cell migration speeds (~0.15 μm/min) were similar to the values at 12 h on the same microgrooved substrates except the 12-5 one. The cell migration speed at day 2 (~0.11 μm/min) on the 12-5 microgrooved substrate was significant lower than the values on the other three microgrooved substrates and was almost the same as that on the flat substrate made from the same polymer, PCLA 4arm-25k. This impeded cell migration might be attributed to cell entrapment. At 12 h, the SMC nuclei were not fully trapped inside the grooves on the 12-5 microgrooved substrate but they were at day 2. The lower cell motility was also consistent with the above-discussed lower cell densities on the 12-5 microgrooved substrate at day 2.

The average SMC migration distances along and perpendicular to the grooves at 12 h and day 2 are shown in Figure 5.10. For the SMCs on the flat substrates, the migration distances along the

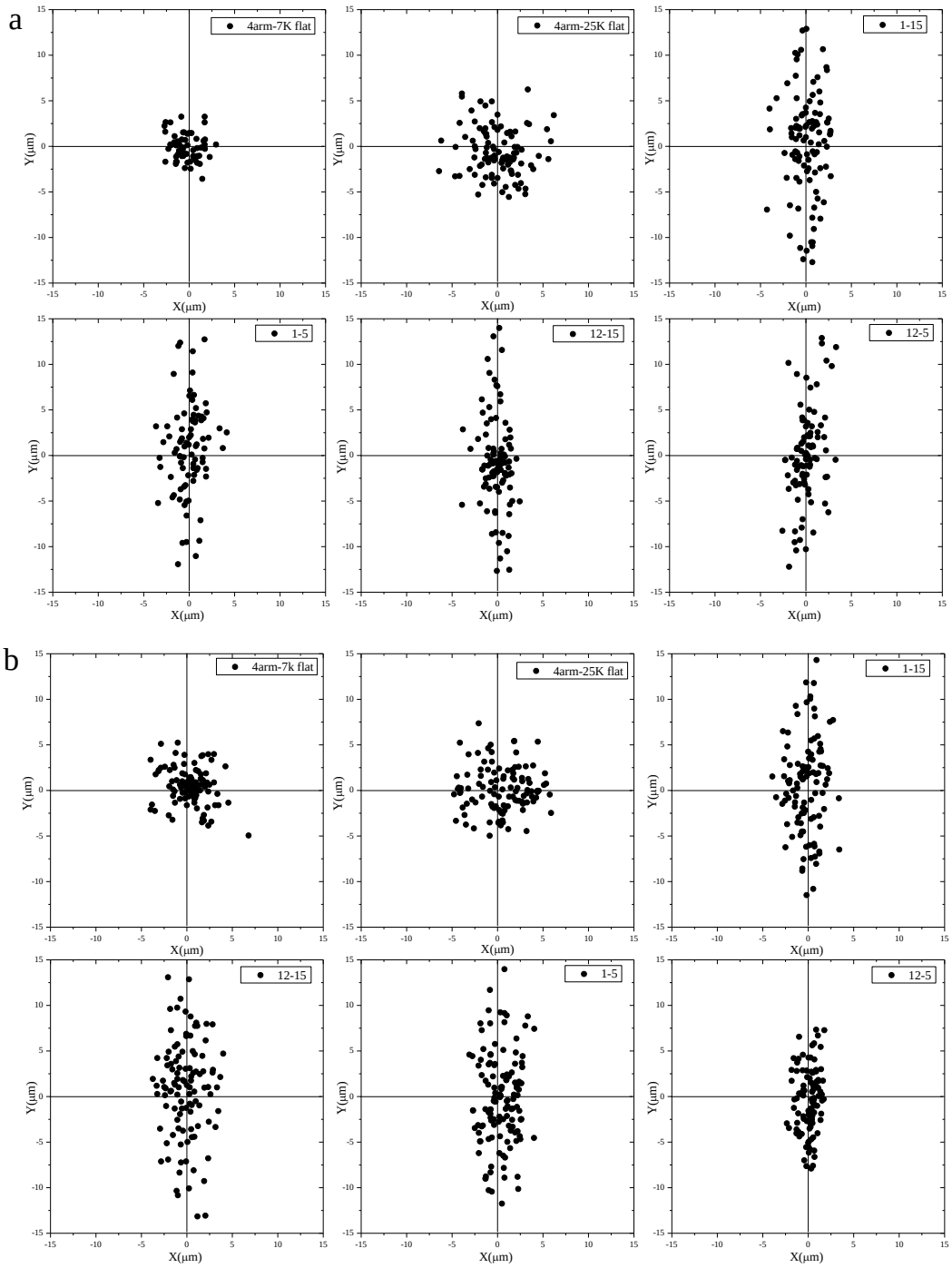

Figure 5.8 SMC migration on flat PCLA 4arm-7k and 4arm-25k substrates, and microgrooved PCLA 4arm-25k substrates, compared with at 12 h (a) and day 2 (b) post-seeding. The migration vector of cells on microgrooves after 30 min expressed as a dot.

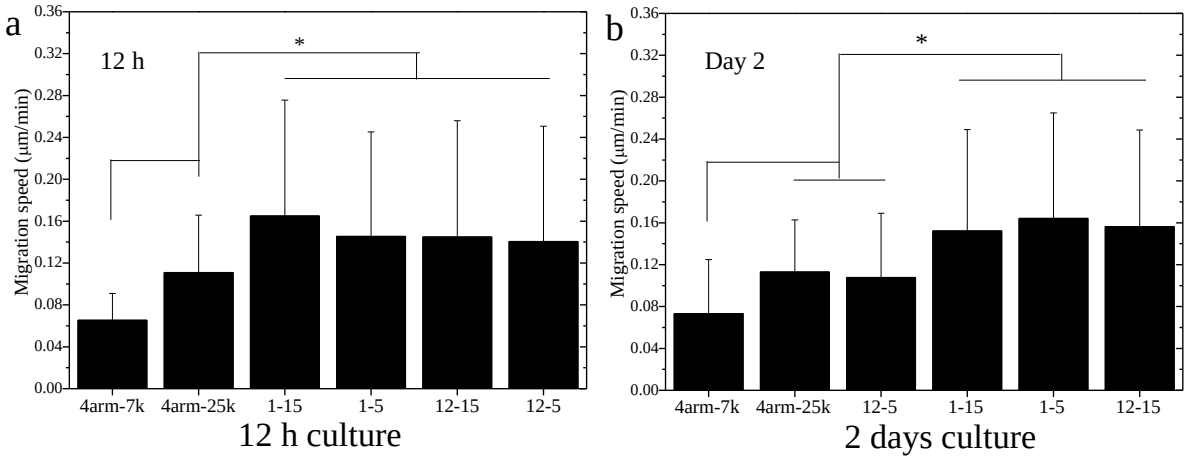

Figure 5.9 SMC migration speeds on flat PCLA 4arm-7k and 4arm-25k substrates, and microgrooved PCLA 4arm-25k substrates at 12 h (a) and day 2 (b) post-seeding. *: $p < 0.05$ between the samples marked with the same symbol.

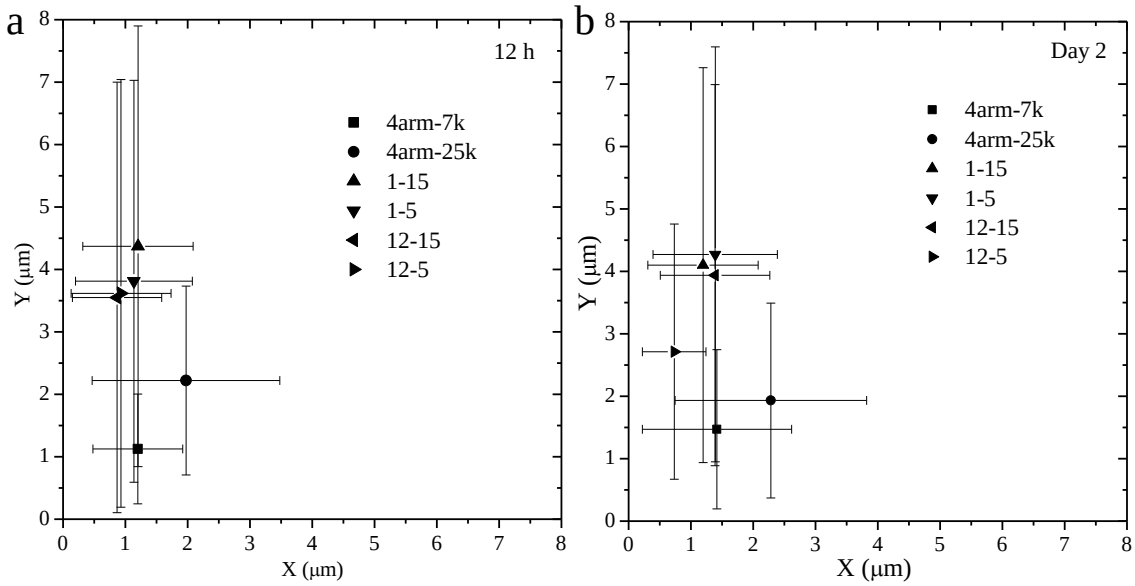

Figure 5.10 SMC migration directions on flat PCLA 4arm-7k and 4arm-25k substrates, and microgrooved PCLA 4arm-25k substrates at 12 h (a) and day 2 (b) post-seeding.

X and *Y* directions were measured. Different from random cell migration along any direction on the flat substrates, the cells on the microgrooved substrates mainly migrated along the groove direction. The ratios between the migration distances along and perpendicular to the grooves were higher than 3 for the cells on the microgrooved substrates, while the ratios were 1 for the cells on the two flat ones.

5.3.5 Further discussion.

In this chapter, I further proved that SMC cytoskeletal and nuclear morphologies could be affected by the microgroove dimensions, which were groove depth and width. The microgrooves did not promote the SMC attachment and proliferation. Instead, the 12-5 microgrooved substrates even prohibited the cell proliferation at day 4. The groove width of 5 μm was smaller while the groove depth of 12 μm was larger than the diameter of SMC nuclei, making both cytoplasm and nuclei deformed and trapped inside the grooves. Microgrooves were well reported in regulating cell morphologies and alignment, nuclear morphologies and distribution, and gene expression [42]. Among the microgroove dimensions, the groove depth was found to be more important than the groove width in regulating cell behaviors [42]. The aspect ratio of the surface feature, obtained by dividing the groove depth by the groove width, was found to be a unified, general factor for regulating human dermal fibroblast alignment and elongation [43]. A lower aspect ratio means that the microgrooved substrate is closer to a flat one. Fibroblasts were better aligned and elongated when the aspect ratio of the surface feature was higher, despite the variations in the cell type and surface feature [43]. Our present results also indicated the microgrooved substrates with the higher groove depth of 12 μm (higher aspect ratios) induced better SMC alignment and elongation when the groove width was fixed as 5 or 15 μm. Similar to the cytoplasm, on the microgrooved substrates with the groove depth of 12 μm, more cell nuclei were attracted into the grooves through “contact

guidance" and gravity. However, only on the 12-5 microgrooved substrates with the deeper and narrower grooves, SMC nuclei were aligned and elongated, while the other microgrooved substrates did not affect the nuclear morphology.

In this chapter, the FAs in the SMCs on the microgrooved substrates formed clusters instead of being individual and thus were not suitable for analyzing cell adhesion. Higher mRNA levels of contractile gene markers in SMCs appeared on the microgrooved substrates, in particular, when the groove depth was 12 μm. It has been proposed that cell alignment and cytoskeletal organization can alter the position of chromosomes and the probability of specific gene expression through deformation of cell nuclei [44,45]. Microgroove patterns were found to induce the differentiation of human embryonic stem cell and human mesenchymal stem cell into the neuronal lineage without the use of any differentiation-inducing agents [12,46] and even to regulate cell reprograming [47].

Another focus of this chapter was to reveal the synergistic effects of substrates stiffness and microgroove dimensions on SMC motility. The phenomenon of higher substrate stiffness promoting cell motility was consistent with other studies on PC12 cell, SPL201 cell, normal (3T3) and cancer (SaI/N) fibroblastic cell, bovine aortic endothelial cell, C2C12 muscle precursor cell, and SMC [23,30,48-50]. Besides substrate stiffness, both groove width and depth were found to be important in regulating SMC motility. Directional migration with a much higher motility was found for the cells on the microgrooved substrates, compared with random migration without a preferred direction of unaligned cells on the flat substrates. Previous studies also demonstrated that microgrooves could expedite cell migration along the groove direction while inhibit transverse movement across the grooves [51,52]. With increasing the microgroove depth, the inhibition of migration across the grooves were more obvious, while the increase of width had less inhibition

on the migration [51,52]. Besides the 12-5 microgrooved substrate at day 2, different aspect ratios of the groove structures had no effects on cell migration speed or direction. The prohibition effect of trapping SMC nuclei on cell motility was demonstrated by comparing the migration speeds at 12 h and day 2 on the 12-5 microgrooved substrate. The cell migration speeds at 12 h were similar on all the microgrooved substrates, while the value at day 2 on the 12-5 microgrooved substrate was significantly lower than the others. Impeded cell migration in deeper microgrooves were also reported by other researchers, in which they found increasing groove depth could decrease the migration speed while the variation of width had no significant influence [51,52].

Cells with a higher motility can travel over a longer distance along the microgrooves to offer a better capability for bridging and curing the injured tissue. Peripheral nerve conduits with microgrooves inside the inner wall was proved to promote nerve cell alignment and axonal growth [53,54]. This chapter showed photo-crosslinked PCLA substrates with surface features such as microgrooves can be readily fabricated for serving as an excellent platform and biomedical devices for cardiovascular applications.

5.4 Conclusions

I fabricated a series of microgrooved substrates of photo-crosslinked PCLAs (4arm-25k and 6arm-30k) with groove depths of 1 and 12 μm and groove widths of 5 and 15 μm via the replica molding method. These biodegradable microgrooved substrates, as well as the flat ones made from the same PCLAs, were used to exam SMC attachment, proliferation, alignment, nuclear circularity and distribution, focal adhesions, gene expression, and migration. The 12-5 microgrooved substrates inhibited SMC proliferation at day 4 compared with the others, on which the cell attachment and proliferation were almost identical. The microgrooves on the substrates were found

to decrease the area, regulate the shape, and generate alignment of SMC cytoskeleton. The SMC nuclei were elongated on 12-5 microgrooved substrates, and the distribution of SMC nuclei were mainly located in the grooves on 1-15, 12-15, and 12-5 microgrooved substrates. The expression levels of contractile gene markers were also elevated by the microgrooves. The groove depth was found to be more important than the groove width in decreasing SMC area, and circularity, regulating alignment, decreasing SMC nuclear circularity, regulating SMC nuclei distribution, and improving contractile gene expression. SMC motility was higher on stiffer substrates when the surface features were identical. SMC motility was promoted by the microgrooved substrates compared with the plat ones when the same PCLA was used. The microgrooves on the substrates also affected the direction of SMC migration by promoting the migration along the grooves and inhibiting the migration perpendicular to the grooves. After the cells were trapped inside the grooves on the 12-5 microgrooved substrate at day 2, the migration speed was significantly suppressed. Except that scenario, the culture time and microgroove dimensions had limited effects on migration speed and direction.

References

1. Saltzman, W. M.; Kyriakides, T. R. In *Principles of tissue engineering*, 3rd ed; Lanza, R.; Langer, R.; Vacanti, J., Eds.; Elsevier Academic Press: San Diego, CA; 2007, pp 279-296.

2. Wong, J. Y.; Leach, J. B.; Brown, X. Q. *Surf. Sci.* **2004**, *570*(1), 119-133.

3. Discher, D. E.; Janmey, P.; Wang, Y. L. *Science* **2005**, *310*(5751), 1139-1143.

4. Huh, D.; Matthews, B. D.; Mammoto, A.; Montoya-Zavala, M.; Hsin, H. Y.; Ingber, D. E. *Science* **2010**, *328*(5986), 1662-1668.

5. Guilak, F.; Cohen, D. M.; Estes, B. T.; Gimble, J. M.; Liedtke, W.; Chen, C. S. *Cell stem cell* **2009**, *5*(1), 17-26.

6. Jeon, H.; Koo, S.; Reese, W. M.; Loskill, P.; Grigoropoulos, C. P.; Healy, K. E. *Nat. Mater.* **2015**, *14*(9), 918-923.

7. Anselme, K.; Bigerelle, M. *Int. Mater. Rev.* **2011**, *56*(4), 243-266.

8. Frey, M. T.; Tsai, I. Y.; Russell, T. P.; Hanks, S. K.; Wang, Y. L. *Biophys. J.* **2006**, *90*(10), 3774-3782.

9. Ghibaudo, M.; Trichet, L.; Le Digabel, J.; Richert, A.; Hersen, P.; Ladoux, B. *Biophys. J.* **2009**, *97*(1), 357-368.

10. Comelles, J.; Caballero, D.; Voituriez, R.; Hortigüela, V.; Wollrab, V.; Godeau, A. L.; Samitier, J.; Martínez, E.; Riveline, D. *Biophys. J.* **2014**, *107*(7), 1513-1522.

11. Berry, C. C.; Campbell, G.; Spadiccino, A.; Robertson, M.; Curtis, A. S. *Biomaterials* **2004**, *25*(26), 5781-5788.

12. Lee, M. R.; Kwon, K. W.; Jung, H.; Kim, H. N.; Suh, K. Y.; Kim, K.; Kim, K. S. *Biomaterials* **2010**, *31*(15), 4360-4366.

13. Biela, S. A.; Su, Y.; Spatz, J. P.; Kemkemer, R. *Acta Biomater.* **2009**, *5*(7), 2460-2466.

14. Han, E. D.; Yoon, S. H.; Kim, B. H.; Seo, Y. H. *Appl. Phys. Lett.* **2013**, *102*(13), 133701.

15. Bettinger, C. J.; Langer, R.; Borenstein, J. T. *Angew. Chem. Int. Ed.* **2009**, *48*, 5406-5415.

16. Clark, P.; Connolly, P.; Curtis, A. S. G.; Dow, J. A. T.; Wilkinson, C. D. W. *Development* **1990**, *108*, 635-644.

17. Flemming, R. G.; Murphy, C. J.; Abrams, G. A.; Goodman, S. L.; Nealey, P. F. *Biomaterials* **1999**, *20*, 573-588.

18. Martínez, E.; Engel, E.; Planell, J. A.; Samitier, J. *Ann. Anat.* **2009**, *191*, 126-135.

19. Wu, X.; Wang, S. *ACS Appl. Mater. Inter.* **2012**, *4*(9), 4966-4975.

20. Wu, X.; Wang, S. *Adv. Healthcare Mater.* **2013**, *2*(2), 326-333.

21. Wang, K.; Harbers, L.; Zhang, L.; Dong, J.; Wang, S. *Adv. Healthcare Mater.* **2012**, *1*, 292-301.

22. Henry, M. G.; Cai, L.; Liu, X.; Zhang, L.; Dong, J.; Chen, L.; Wang, Z.; Wang, S. *Langmuir* **2015**, *31*(9), 2851-2860.

23. Cai, L.; Zhang, L.; Dong, J.; Wang, S. *Langmuir* **2012**, *28*(34), 12557-12568.

24. Chapter 6. Wu, X. 2013. Tuning cell fate on self-assembled structures. Doctoral dissertation. The University of Tennessee, Knoxville.

25. Chapter 5. Liu, X. 2014. Phenotypic modulation of smooth muscle cells on biodegradable elastomeric substrates. Doctoral dissertation. The University of Tennessee, Knoxville.

26. Chapter 6. Liu, X. 2014. Phenotypic modulation of smooth muscle cells on biodegradable elastomeric substrates. Doctoral dissertation. The University of Tennessee, Knoxville.

27. Jiang, X.; Bruzewicz, D. A.; Wong, A. P.; Piel, M.; Whitesides, G. M. *Proc. Natl. Acad. Sci. U.S.A.* **2005**, *102*(4), 975-978.

28. Kim, D. H.; Han, K.; Gupta, K.; Kwon, K. W.; Suh, K. Y.; Levchenko, A. *Biomaterials* **2009**, *30*(29), 5433-5444.

29. Liliensiek, S. J.; Wood, J. A.; Yong, J.; Auerbach, R.; Nealey, P. F.; Murphy, C. J. *Biomaterials* **2010**, *31*(20), 5418-5426.

30. Tzvetkova-Chevolleau, T.; Stéphanou, A.; Fuard, D.; Ohayon, J.; Schiavone, P.; Tracqui, P. *Biomaterials* **2008**, *29*(10), 1541-1551.

31. Wang, X.; Ohlin, C. A.; Lu, Q.; Hu, J. *Biomaterials* **2008**, *29*(13), 2049-2059.

32. Jeon, H.; Hidai, H.; Hwang, D. J.; Healy, K. E.; Grigoropoulos, C. P. *Biomaterials* **2010**, *31*(15), 4286-4295.

33. Miyoshi, H.; Adachi, T.; Ju, J.; Lee, S. M.; Cho, D. J.; Ko, J. S.; Uchida, G.; Yamagata, Y. *Biomaterials* **2012**, *33*(2), 395-401.

34. Schwartz, S. M.; Campbell, G. R.; Campbell, J. H. *Circ. Res.* **1986**, *58*(4), 427-444.

35. Garg, U. C.; Hassid, A. *J. Clin. Invest.* **1989**, *83*(5), 1774-1777.

36. Wong, J. Y.; Velasco, A.; Rajagopalan, P.; Pham, Q. *Langmuir* **2003**, *19*(5), 1908-1913.

37. Zaari, N.; Rajagopalan, P.; Kim, S. K.; Engler, A. J.; Wong, J. Y. *Adv. Mater.* **2004**, *16*(23-24), 2133-2137.

38. Puppi, D.; Chiellini, F.; Piras, A. M.; Chiellini, E. *Prog. Polym. Sci.* **2010**, *35*, 403-440.

39. Lee, K.-W.; Wang, S.; Dadsetan, M.; Yaszemski, M. J.; Lu, L. *Biomacromolecules* **2010**, *11*(3), 682-689.

40. Dou, J.; Zeng, Q.; Wang, S. Smooth muscle cells on photo-cured poly(ε-caprolactone) substrates with varied stiffness and micro-grooves. *Society for Biomaterials*, 2015, Charlotte, NC.

41. Kaiser, J.P.; Bruinink, A. *J. Mater. Sci. Mater. Med.* **2004**, *15*(4), 429-435.

42. Curtis, A.; Wilkinson, C. *Biomaterials* **1997**, *18*(24), 1573-1583.

43. Crouch, A. S.; Miller, D.; Luebke, K. J.; Hu, W. *Biomaterials* **2009**, *30*(8), 1560-1567.

44. Dahl, K. N.; Ribeiro, A. J. S.; Lammerding, J. *Circ. Res.* **2008**, *102*, 1307-1318.

45. Thomas, C. H.; Collier, J. H.; Sfeir, C. S.; Healy, K. E. *Proc. Natl. Acad. Sci. U.S.A.* **2002**, *99*(4), 1972-1977.

46. Yim, E. K.; Pang, S. W.; Leong, K. W. *Exp. Cell. Res.* **2007**, *313*(9), 1820-1829.

47. Downing, T. L.; Soto, J.; Morez, C.; Houssin, T.; Fritz, A.; Yuan, F.; Chu, J.; Patel, S.; Schaffer, D. V.; Li, S. *Nat. Mater.* **2013**, *12*(12), 1154-1162.

48. Charest, J. M.; Califano, J. P.; Carey, S. P.; Reinhart-King, C. A. *Macromol. Biosci.* **2012**, *12*(1), 12-20.

49. Cortese, B.; Gigli, G.; Riehle, M. *Adv. Funct. Mater.* **2009**, *19*(18), 2961-2968.

50. Chapter 4. Liu, X. 2014. Phenotypic modulation of smooth muscle cells on biodegradable elastomeric substrates. Doctoral dissertation. The University of Tennessee, Knoxville.

51. Kaiser, J. P.; Reinmann, A.; Bruinink, A. *Biomaterials* **2006**, *27*(30), 5230-5241.

52. Dalton, B.; Walboomers, X. F.; Dziegielewski, M.; Evans, M. D.; Taylor, S.; Jansen, J. A.; Steele, J. G. *J. Biomed. Mater. Res.* **2001**, *56*(2), 195-207.

53. Hsu, S. H.; Lu, P. S.; Ni, H. C.; Su, C. H. *Biomed. Microdevices* **2007**, *9*(5), 665-674.

54. Lin, Y. L.; Jen, J. C.; Hsu, S. H.; Chiu, M. *Surg. Neurol.* **2008**, *70*, S9-S18.

Chapter VI. Biodegradable Elastomers Based on POSS-Initiated Poly(ε-caprolactone) for Cardiovascular and Peripheral Nerve Repair

Abstract

We used 1,2-propanediol isobutyl polyhedral oligomeric silsesquioxane (POSS) as the initiator to synthesize POSS-poly(ε-caprolactone) (POSS-PCL) diols with different molecular weights (also different POSS weight compositions) via ring-opening polymerization of ε-caprolactone. Then the POSS-PCL diols were further converted to photo-crosslinkable POSS-PCL diacrylates (POSS-PCLDAs) via acrylation in the presence of potassium carbonate (K_2CO_3). POSS-PCLDAs with different POSS compositions were photo-crosslinked into networks with mechanical properties well controlled through the crystallinity and crosslinking density, both of which were determined by the molecular weight of PCL. Because of the steric hindrance induced by the bulky POSS nanocage in the center of POSS-PCLDA, the crystallinities of the photo-crosslinked networks were significantly suppressed. Networks of high-molecular-weight (> 5170 g/mol) POSS-PCLDAs were still semi-crystalline, while the ones prepared from low-molecular-weight POSS-PCLDAs were amorphous and demonstrated elastomeric characteristics at 37 °C. For example, a low elastic modulus of 1.3 MPa and a reversible strain as high as 400% were achieved when the molecular weight of POSS-PCLDA was 4650 g/mol. These novel biodegradable elastomers were evaluated in terms of regulating primary rat aortic smooth muscle cells (SMCs) and rat pheochromocytoma (PC12) cells for potential applications in cardiovascular and peripheral nerve regeneration. Semi-crystalline POSS-PCLDA networks better supported SMC attachment, proliferation, and focal adhesions than amorphous elastomeric POSS-PCLDA networks, while there was no significant difference in SMC behaviors on the latter. In contrast, amorphous elastomeric POSS-PCLDA networks significantly better supported PC12 cell attachment, proliferation, and differentiation than semi-crystalline POSS-PCLDA networks. Flexible nerve

conduits of photo-crosslinked POSS-PCLDA with smooth surfaces and uniform dimensions were fabricated using the elastomeric POSS-PCLDA.

6.1 Introduction

Biodegradable elastomers have attracted much attention as they can provide mechanical properties similar to soft tissues and manufacturing flexibility [1-9]. Biomedical devices for *in vivo* applications are implanted in a mechanically dynamic environment with living tissues of elastomeric properties. Therefore, it requires biomaterials with similar elastomeric properties of being compliant and easy to recover from high deformations [1,2]. Because of these mechanical properties, biodegradable elastomers have better biocompatibility without causing irritation to the surrounding tissues from stress shielding. Different elastomeric biomaterials have been developed from both natural and synthetic polymers. Compared with the natural ones such as elastin and collagen-like peptides, synthetic biomaterials are inexpensive, non-immunologically responsive, thermally stable, and tailorable in structures and physicochemical properties [1,9]. A typical synthetic elastomeric biomaterial is poly(glycerol sebacate) (PGS) that has elastic modulus (E) of 0.05-1.5 MPa and strain at break (ε_b) up to 600% [1,10,11]. However, PGS could fully degrade *in vivo* after 6-10 weeks when the injured tissues were still in the process of recovering [12]. Another widely used synthetic elastomeric biomaterial is polyurethane (PU); however, PUs are slow in biodegradation or unable to fully degrade [13,14].

Based on biodegradable polymers such as poly(propylene fumarate) (PPF) and poly(ε-caprolactone) (PCL), a series of photo-crosslinkable polymers such as PPF-*co*-PCL [15], PCL fumarate (PCLF) [16], and PCL acrylate (PCLA) has been synthesized and photo-crosslinked into cytocompatible polymer substrates and structures with controllable mechanical properties and degradation for diverse tissue engineering applications [17-20]. Among all these polymer systems, PCL-based networks have the advantage of controllable stiffness through both crosslinking density and crystallinity, which can be modulated using the molecular weight of PCL. However, high-

molecular-weight PCLs result in semi-crystalline networks at body temperature and are susceptible to permanent deformation without elastomeric recovery, while networks based on low-molecular-weight PCL were too weak or too brittle and could not hold much deformation.

To modify these polymers, inorganic components such as hydroxyapatite nanoparticles [21,22], polyhedral oligomeric silsesquioxane (POSS) [23,24], β-tricalcium phosphate [25,26], calcium sulfate [27,28] are used as fillers. POSS is a silicon-based nanocage-like molecule and has been used to prepare hybrid systems with biodegradable polymers [29-32]. POSS with a variety of functional groups could be copolymerized, incorporated, or even mixed with polymers to achieve new chemical and physical properties for tissue engineering applications. In most cases, POSS was immiscible with the polymer matrix as macrophase separation occurred when the weight composition of POSS (Φ_{POSS}) was high. Phase separated systems were no longer homogeneous and thus the POSS-rich moiety was different from the POSS-poor moiety in properties. Usually, when Φ_{POSS} was higher than 20% or 30%, POSS cannot enhance the mechanical properties of the polymer matrix any more. The heterogeneously dispersed POSS could even be visible as the nanocomposites were no longer transparent. To homogeneously disperse POSS in polymer matrices, one approach is to incorporate POSS into a polymer backbone and then POSS nanocages can be separated from each other at the molecular level [33-36].

In this chapter, I used 1,2-propanediol isobutyl POSS as the initiator to synthesize POSS-PCL with two hydroxyl end groups (POSS-PCL diols) via ring-opening polymerization (ROP) of ε-caprolactone, the monomer. The molecular weight of POSS-PCL diol could be controlled by varying the ratio of the monomer concentration to the initiator concentration, which was directly related to Φ_{POSS}. Then POSS-PCL diols were converted to photo-crosslinkable POSS-PCL diacrylates (POSS-PCLDAs) via acrylation in the presence of potassium carbonate (K_2CO_3).

POSS-PCLDAs with a variety of Φ_{POSS} from 10% to 50% were crosslinked into networks with tunable crystallinities and crosslinking densities, and thus controllable thermal and mechanical properties. Because of the steric hindrance induced by the bulky POSS nanocages, photo-crosslinked POSS-PCLDA networks with significantly suppressed crystallinities demonstrated elastomeric characteristics such as a low *E* of 1.3 MPa and a reversible strain as high as 400%. The goal of this chapter was to investigate how photo-crosslinked POSS-PCLDAs with different Φ_{POSS} could be used to tailor the network properties and to regulate primary rat aortic smooth muscle cell (SMC) and rat pheochromocytoma (PC12) cell attachment, proliferation, focal adhesion, and differentiation. Elastomeric nerve conduits of photo-crosslinked POSS-PCLDA with excellent flexibility and durability were then fabricated for potential applications in cardiovascular and peripheral nerve regeneration.

6.2 Materials and Methods

6.2.1 Synthesis of POSS-PCL diols and POSS-PCLDAs.

1,2-propanediol isobutyl POSS was purchased from Hybrid Plastics (Hattiesburg, MS). The other chemicals used here were purchased from Sigma-Aldrich (Milwaukee, WI) unless otherwise noted. As shown in Figure 6.1a, POSS-PCL diols were synthesized via ROP of ε-caprolactone at 130 °C for 12 h in the presence of $Sn(Oct)_2$ as the catalyst and 1,2-propanediol isobutyl POSS (shortened as POSS) as the initiator. The Φ_{POSS} used in the synthesis were 10%, 20%, 30%, 40% and 50%, and the molecular weight of POSS-PCL diol was modulated using the monomer to initiator ratio. The POSS-PCL diol was added dropwise into diethyl ether to remove the low-molecular-weight oligomer and the precipitate was rotary evaporated to yield a wax-like product. Then the acylation of the POSS-PCL diols was performed in the presence of K_2CO_3 as the proton

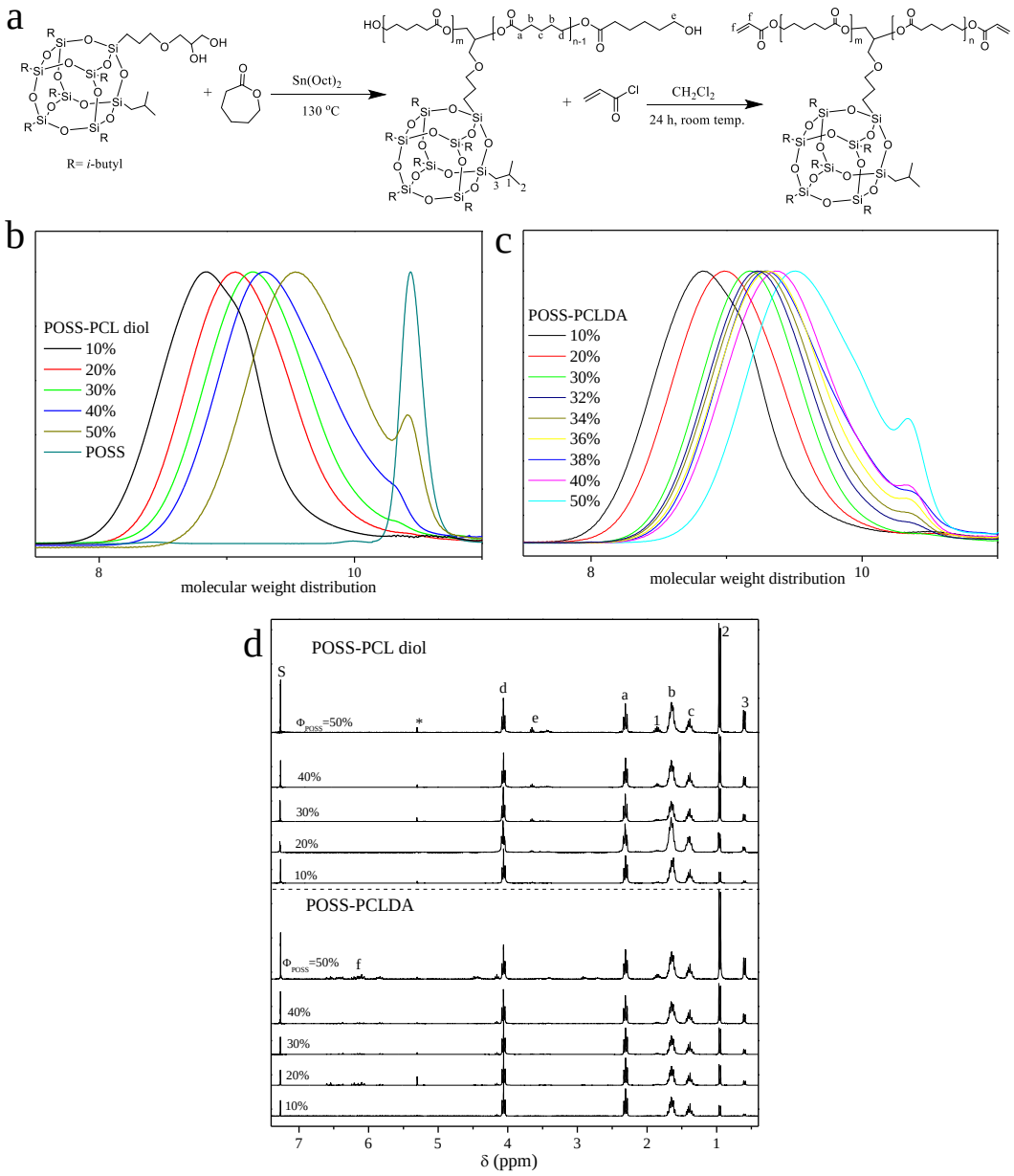

Figure 6.1 Synthesis scheme (a), and GPC curves of POSS-PCL diols (b) and POSS-PCLDAs (c). (d) ^{1}H NMR (300 MHz, $CDCl_3$, reference TMS) spectra of POSS-PCL diols and POSS-PCLDAs. S = solvent. Asterisk denotes the signals due to the residue of CH_2Cl_2.

scavenger to form POSS-PCLDAs [17,37]. POSS-PCL diol, acryloyl chloride, and K_2CO_3 were measured at a molar ratio of 1:3:3. POSS-PCL diol was dissolved in methylene chloride (1:2 v/v) and placed in a 50 mL three-neck flask along with K_2CO_3 powder. Acryloyl chloride dissolved in methylene chloride (1:10 v/v) was then added dropwise into the slurry of K_2CO_3/POSS-PCL diol in methylene chloride. After reaction at room temperature under nitrogen for 24 h, the mixture was filtered to remove the solids and then precipitated in diethyl ether again. The molecular weights of POSS-PCL diols and POSS-PCLDAs were determined using gel permeation chromatography (GPC; PL-GPC20, Polymer Laboratories) at room temperature with tetrahydrofuran as the eluent and standard monodisperse polystyrene samples (Polymer Laboratories) for calibration. The chemical structures of POSS-PCL diols and POSS-PCLDAs were characterized using ^{1}H NMR (Varian Mercury 300 spectrometer, 300 MHz) with $CDCl_3$ containing tetramethylsilane (TMS) as solvent.

6.2.2 Photo-crosslinking of POSS-PCLDAs.

Photo-initiator, phenyl bis(2,4,6-trimethyl benzoyl) phosphine oxide (BAPO, IRGACURE 819, Ciba Specialty Chemicals, Tarrytown, NY), was used in photo-crosslinking. 75 μL of BAPO/CH_2Cl_2 (300 mg/1.5 mL) solution was mixed with POSS-PCLDA solution in CH_2Cl_2 (1.5 g/500 μL). The mixture was then transferred into a Teflon mold composed of two glass plates and a Teflon spacer, and then placed under a high-intensity long-wave ultraviolet (UV) lamp (SB-100P, Spectronics Corp., Westbury, NY, λ= 365 nm, Intensity: 4,800 w/cm^2) for 20 min at a distance of ~10 cm from the lamp head. I also mixed and photo-crosslinked blends of two POSS-PCLDAs with Φ_{POSS} of 40% and 30% at weight ratios of 1:4, 2:3, 3:2, and 4:1, resulting in Φ_{POSS} of 32%, 34%, 36% and 38%, respectively. Flat disks of photo-crosslinked POSS-PCLDA were soaked in acetone for two days to remove the sol fraction, dried in vacuum, and compressed

between two glass plates to smoothen them. The flat disks were sterilized in 70% ethanol solution and dried completely before cell study. Nerve conduits were fabricated by transferring and photo-crosslinking POSS-PCLDA with Φ_{POSS} of 32% precursor solutions into a mold composed of a glass tube, a stainless steel rod, and two Teflon endcaps, as described in literature [16]. The mold loaded with viscous polymer solution was rotated under the UV light for 20 min to facilitate crosslinking. The nerve conduits were soaked in ethanol and acetone for four days to remove the residue of BAPO and sol fraction, followed by complete drying in vacuum. The polymer nerve conduit and its cross-section were examined using scanning electron microscopy (SEM, S-3500, Hitachi Instruments, Tokyo, Japan).

6.2.3 Characterization of photo-crosslinked POSS-PCLDAs.

The gel fraction and swelling ratio of flat crosslinked POSS-PCLDAs were determined in CH_2Cl_2 using the method reported by our research group [17]. The thermal properties of POSS-PCL diols, POSS-PCLDAs, and photo-crosslinked POSS-PCLDAs were measured using differential scanning calorimetry (DSC, Q2000, TA instruments, New Castle, DE). The polymer samples were first heated from room temperature to 200 °C and then cooled to -90 °C, followed by another heating round to 200 °C at a rate of 10 °C/min in dry nitrogen. Linear viscoelastic properties of photo-crosslinked POSS-PCLDA disks (8 mm × 0.5 mm, diameter × thickness) were measured on a strain-controlled rheometer (RDS-2, Rheometric Scientific) at 37 and 60 °C. Thermogravimetric analysis (TGA) for all the crosslinked POSS-PCLDAs was performed on a thermal analyst (Q50, TA instruments) in flowing nitrogen at a heating rate of 20 °C/min from room temperature to 600 °C. The tensile properties of photo-crosslinked POSS-PCLDA strips (0.5 mm × 0.8 mm × 10 mm, thickness × width × length) were tested using a dynamic mechanical analyzer (DMA, Q800, TA instruments) at 37 °C at a strain rate of 0.005 s^{-1}. The surface

morphologies of the crosslinked POSS-PCLDA disks were detected using a multimode atomic force microscope (AFM) with a Nanoscope III control system (Veeco Instruments, Santa Barbara, CA). A tapping mode over a scan area of 20 μm × 20 μm at a scan rate of 0.5 Hz was used. Root-mean-square roughness (R_{rms}) was measured from the height images using the Nanoscope 7.30 software (Veeco Instruments, Santa Barbara, CA). Water contact angles on the crosslinked POSS-PCLDA disks were determined at 37 °C using a Ramé-Hart NRC C. A. goniometer (model 100-00-230) after 20 μL of distilled water (pH = 7.0) was injected onto the sample surface and equilibrated for 30 s. A tangent method was used to measure the contact angle in degrees using the ImageJ software (National Institutes of Health, Bethesda, MD). Three disks were used for each photo-crosslinked POSS-PCLDA to calculate the average and standard deviation.

6.2.4 *In vitro* SMC attachment and proliferation.

Rat primary aortic SMCs were cultured in a growth medium composed of Dulbecco's modified eagle medium (DMEM; Gibco, Grand Island, NY) supplemented with 10% fetal bovine serum (FBS; HyClone, Thermal Scientific) and 1% penicillin/streptomycin (Gibco) in an incubator with 5% CO_2 and 95% relative humidity at 37 °C. SMCs were seeded onto the crosslinked POSS-PCLDA disks (10 mm × 0.5 mm, diameter × thickness) at a density of 15,000 cells/cm^2 and cultured for 4 h, 1, 2, and 4 days. A colorimetric cell metabolic assay (CellTiter 96 Aqueous One Solution, Promega, Madison, WI) was performed in each well to determine the number of attached cells by correlating it to the UV absorbance of the solution at 490 nm measured on a microplate reader (SpectraMax Plus 384, Molecular Devices, Sunnyvale, CA) and a standard curve constructed using known cell numbers. SMCs attached on the photo-crosslinked POSS-PCLDA disks were washed with phosphate buffered saline (PBS), fixed in 4% paraformaldehyde (PFA, Electron Microscopy Science) solution for 10 min at room temperature, washed with PBS twice,

and then permeabilized with 0.1% Triton X-100 at room temperature for another 10 min. SMC cytoplasm was then stained using rhodamine-phalloidin (RP, Cytoskeleton Inc., Denver, CO) for 1 h at 37 °C. Then the cells were photographed using an Axiovert 25 light microscope (Carl Zeiss, Germany), and cell areas were determined by using ImageJ and averaged over 25 non-overlapping cells at day 1 post-seeding.

6.2.5 Characterization of focal adhesions (FAs) in SMCs.

At day 1 post-seeding, SMCs attached on the photo-crosslinked POSS-PCLDA disks were washed with PBS, fixed in 4% PFA solution, washed with PBS three times, and permeabilized with 0.1% Triton X-100 at room temperature for 10 min. Then the polymer disks with attached SMCs were incubated in 1% bovine serum albumin (BSA)/PBS at 37 °C for 30 min. After being washed with PBS three times, the polymer disks with the cells were incubated in monoclonal mouse antibody against vinculin (1:1000 in 1% PBS; Sigma) at room temperature for 2 h, and then washed with PBS three times again. Then the polymer disks with the cells were cultured with goat anti-mouse IgG secondary antibody (1:200 in 1% PBS; Sigma) at room temperature in dark for 2 h. The cells were also stained using RP at 37 °C for another 1 h. The FAs were photographed on a Leica DM6000B fluorescent confocal microscope. The density (FAs per cell), area, and elongation (perimeter^2/4π × area) of FAs were analyzed and averaged from 15 non-overlapping cells using ImageJ.

6.2.6 *In vitro* PC12 cell attachment, proliferation, and differentiation.

Rat PC12 cells (CRL-1721, ATCC, Manassas, VA) were cultured in a growth medium containing F-12K media (Gibco), 15% horse serum, 5% FBS and 1% penicillin/streptomycin in an incubator with 5% CO_2 and 95% relative humidity at 37 °C. PC12 cells were seeded onto crosslinked POSS-PCLDA disks at a density of 15,000 cells/cm^2 and cultured for 4 h, 1, 4, and 7

days. The PC12 cell numbers were determined using the same method for SMCs. For PC12 cell differentiation, neurites were induced in a growth medium supplemented with 50 ng/mL nerve growth factor (NGF) for 7 days. PC12 cells attached on the photo-crosslinked POSS-PCLDA disks were fixed and permeabilized using the same method for SMCs, followed by cytoplasm staining using RP for 1 h at 37 °C and cell nuclear staining using 4′,6-diamidino-2-phenylindole (DAPI) at room temperature. After fluorescent cell images were taken, PC12 cell area and neurites were analyzed and averaged from at least 100 cells using ImageJ. Neurite length, number of neurites per cell, and percentage of differentiation (percentage of cells bearing neurites in entire cells) were quantified. Only neurites longer than the diameter of original PC12 cells (~ 10 μm) were considered as positive neurite extension and cells with at least one neurite extension were counted as neurite-bearing cells.

6.2.7 Statistical analysis.

Cell studies were performed in quadruplicates for each group at each time point. All experimental values were expressed as mean ± standard deviation. The statistical significance ($p < 0.05$) in the difference between two groups was obtained using the student's *t*-test.

6.3 Results and Discussion

6.3.1 Structure characterization and photo-crosslinking.

The number-average molecular weights (M_ns) and weight-average molecular weights (M_ws) of the POSS-PCL diols and POSS-PCLDAs determined using GPC are shown in Table 6.1, and the GPC curves are shown in Figures 6.1b and 6.1c. The theoretical molecular weights of POSS-PCL diols were calculated based on Φ_{POSS}, as the molecular weight was proportional to the feeding molar ratio of the monomer to the initiator, by using the equation of M_{POSS}/Φ_{POSS}, where M_{POSS} is

Table 6.1 Molecular characteristics and thermal properties of the polymers

Polymer	Φ_{POSS}	M_n (g/mol)	M_w (g/mol)	PDI	Thermal properties				
					T_g (°C)	T_{cc} (°C)	T_m (°C)	ΔH_m (J/g)	χ_c (%)
POSS-PCL diol	10%	9670	13900	1.44	-	27.5	50.5 (54.4)	79.2	65.1
	20%	6250	9640	1.54	-	24.5	49.0	69.3	60.5
	30%	4620	7700	1.67	-	18.0	47.0	76.6	52.8
	40%	3400	6180	1.81	13.7[a]	11.7	40.5 (89.1[a])	39.5	40.6
	50%	2530	4280	1.69	-65.3 (13.9[a])	88.9[a]	90.9[a]	10.2[a]	-
POSS-PCLDA	10%	10500	13900	1.32	-	33.0	51.0 (54.6)	74.2	63.0
	20%	6730	8910	1.32	-	27.1	49.1 (53.7)	77.3	63.8
	30%	5170	6870	1.33	-	22.9	46.5 (51.2)	62.0	56.3
	32%	4650	6370	1.37					
	34%	4330	6030	1.39					
	36%	4040	5640	1.40					
	38%	3690	5210	1.41					
	40%	3450	5180	1.56	-	21.9	46.4	54.9	53.1
	50%	2610	4400	1.68	-7.9[a]	65.2[a]	68.3[a]	8.6[a]	-

Data in parenthesis were the second peak values. [a] Data belonged to POSS. -: Data not detected.

the molecular weight of POSS (950 g/mol). The theoretical molecular weights were 9500, 4750, 3160, 2380, and 1900 g/mol for the POSS-PCL diols with Φ_{POSS} of 10%, 20%, 30%, 40%, and 50%, respectively. The M_ns determined using GPC were higher than the theoretical values as the low-molecular-weight moiety was removed during the precipitation. The higher the molecular weight was, the more consistent between the GPC value and the theoretical value. The polydispersity indexes (PDIs) in Table 6.1 showed that the polymers were relatively monodisperse.

The chemical structures of the POSS-PCL diols and POSS-PCLDAs in Figure 6.1a were confirmed using the ^{1}H NMR spectra shown in Figures 6.1d, in which all the chemical shifts could be well assigned to the corresponding protons in the polymer structures. The chemical shifts (δ) at 5.7-6.5 ppm assigned to vinyl groups (-CH=CH_2) could be seen in the spectra for POSS-PCLDAs but not in those for POSS-PCL diols. Meanwhile, the chemical shift at δ of 3.66 ppm ascribed to the hydroxyl (-OH) group was significantly smaller for POSS-PCLDA. Calculated from this chemical shift, the acrylation conversion rate was always higher than 85% for POSS-PCLDAs, rendering their efficient photo-crosslinking. The gel fractions of crosslinked POSS-PCLDAs with Φ_{POSS} of 10%, 20%, 30%, 40% and 50% were 0.83 ± 0.04, 0.85 ± 0.02, 0.88 ± 0.03, 0.92 ± 0.02, and 0.95 ± 0.02, respectively. The corresponding swelling ratios in CH_2Cl_2 were 11.9 ± 1.0, 10.9 ± 0.8, 8.7 ± 0.5, 6.1 ± 0.5, and 3.1 ± 0.3, respectively. The trends in these two parameters indicated that both crosslinking efficiency and crosslinking density increased with increasing Φ_{POSS} and decreasing the molecular weight. Unlike PPF-*co*-POSS copolymerized from condensation previously reported in our research group [29], POSS in this chapter was the initiator for ROP and thus there was only one POSS nanocage located in the center of each polymer chain. Meanwhile, photo-crosslinked POSS-PCLDAs did not swell in PBS, suggesting the scaffolds made from them can stay intact in *in vivo* implantation.

6.3.2 Thermal and mechanical properties.

The DSC heating and cooling curves of POSS-PCL diols, POSS-PCLDA, and photo-crosslinked POSS-PCLDAs are shown in Figures 6.2a and 6.2b. From the DSC curves, glass transition temperature (T_g) was the midpoint temperature of the glass transition in the heating round, the cold crystallization temperature (T_{cc}) was the highest peak temperature of the exothermal peaks in the cooling round, and the melting temperature (T_m) was the highest peak temperature of the exothermal peaks in the heating round. Crystallinity (χ_c) can be calculated using the equation of $\chi_c = [\Delta H_m/(\Phi_{PCL} \cdot \Delta H_m^c)] \times 100\%$, where ΔH_m was the heat of fusion obtained from the exothermal peak area in the DSC curve and ΔH_m^c is 135 J/g for completely crystalline PCL [38]. All the thermal properties are listed in Table 6.1 for POSS-PCL diols and POSS-PCLDAs and Table 6.2 for crosslinked POSS-PCLDAs. The pure POSS had a small pre-melting peak at around -10 °C and a melting peak at 173 °C [29,39]. The crystalline structure of POSS in polymer was destroyed as POSS was incorporated into the polymer chain. The melting peaks of POSS could only be observed in POSS-PCL diols with Φ_{POSS} of 40% and 50% and POSS-PCLDA with Φ_{POSS} of 50%. After photo-crosslinking, the melting peaks belonging to POSS disappeared completely in all the samples even when Φ_{POSS} was as high as 50% as the result of separation of POSS nanocages and suppression of crosslinks. Before crosslinking, the T_{cc}s and T_ms of PCL for all the polymers decreased with increasing Φ_{POSS} from 10% to 40%, and eventually both crystallization peak and melting peak for PCL disappeared at Φ_{POSS} of 50%. Instead, there were small melting peaks at ~85 °C for POSS-PCL diols with Φ_{POSS} of 40% and 50% and at ~70 °C for POSS-PCLDA with Φ_{POSS} of 50% in the DSC heating curves. These peaks ascribed to the crystalline domains of POSS were consistent with the previous findings on PPF-*co*-POSSs. Except POSS-PCL diol and POSS-PCLDA with Φ_{POSS} of 50%, all the other polymers showed crystalline

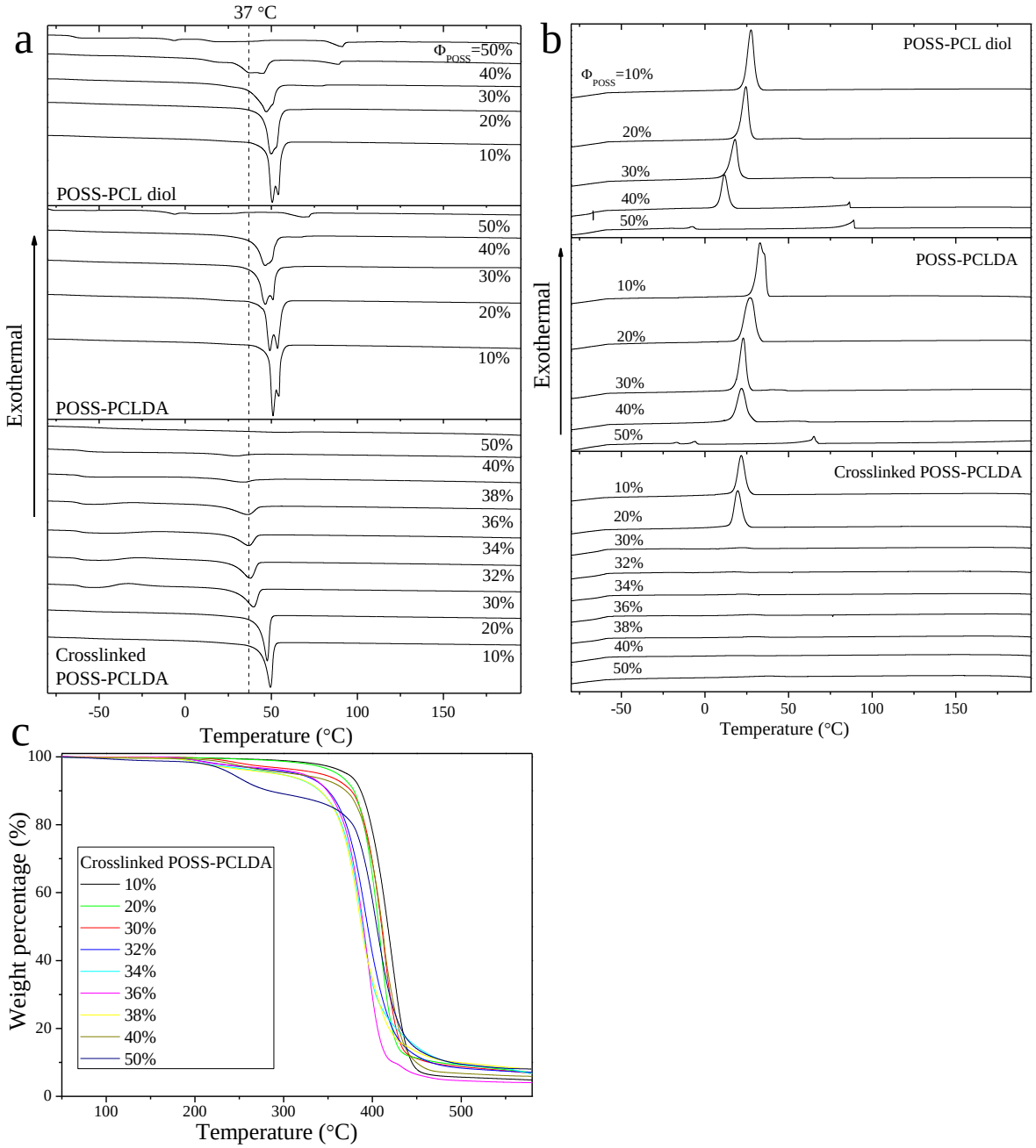

Figure 6.2 DSC heating (a) and cooling (b) curves of POSS-PCL diols, POSS-PCLDAs, and crosslinked POSS-PCLDAs. (c) TGA curves of crosslinked POSS-PCLDAs.

Table 6.2 Thermal properties and mechanical properties of crosslinked PCLAs at 37 °C

Polymer	Φ_{POSS}	Thermal properties						Mechanical properties		
		T_g (°C)	T_{cc} (°C)	T_m (°C)	ΔH_m (J/g)	χ_c (%)	T_d (°C)	*E* (MPa)	ε_b (%)	*G* (MPa)
Crosslinked POSS-PCLDA	10%	-	21.8	49.5	56.8	46.3	393	115.9 ± 9.5	248 ± 43	42.7
	20%	-	19.6	47.6	49.7	42.9	390	76.8 ± 6.2	222 ± 41	27.1
	30%	-61.4	-	39.6	33.9	30.6	388	51.3 ± 5.5	119 ± 23	1.57
	32%	-61.4	-	37.7	30.0	28.0	388	1.3 ± 0.4	435 ± 49	-
	34%	-59.9	-	36.8	29.5	27.9	363	2.2 ± 0.7	384 ± 64	-
	36%	-61.3	-	36.0	23.1	22.4	361	3.8 ± 0.8	212 ± 47	-
	38%	-61.2	-	33.8	14.0	13.9	366	4.8 ± 0.6	221 ± 47	-
	40%	-59.3	-	29.2	6.5	6.3	360	10.8 ± 2.1	254 ± 58	0.90
	50%	-	-	-	0	0	375	16.5 ± 0.9	42 ± 13	2.53

structures of PCL and the crystallinity did not vary much between POSS-PCL diol and POSS-PCLDA at the same Φ_{POSS}. The T_{cc}s and T_ms of PCL for photo-crosslinked POSS-PCLDAs also decreased with increasing Φ_{POSS}. When Φ_{POSS} was higher than 30%, the crystallization peaks were no longer visible in the DSC cooling curves. Photo-crosslinked POSS-PCLDAs were semi-crystalline up to Φ_{POSS} of 40% in the studied range. However, photo-crosslinked POSS-PCLDAs with lower molecular weights (or when Φ_{POSS} was higher than 30%) were amorphous at the physiological temperature of 37 °C. The differences in the crosslinking density and crystallinity at 37 °C resulted in the distinct mechanical properties of photo-crosslinked POSS-PCLDAs, in particular, when the Φ_{POSS} was 30% or 32%, at which the T_ms were near 37 °C. Thermal stability of photo-crosslinked POSS-PCLDA was evaluated by using TGA (Figure 6.2c), and the on-set thermal degradation temperatures (T_d) are shown in Table 6.2. POSS exhibited a lower T_d of 292 °C than PCL network (~390 °C) [29,30], and could be still seen in the photo-crosslinked POSS-PCLDAs with Φ_{POSS} higher than 30%. Thermal stabilities of the photo-crosslinked POSS-PCLDAs decreased in T_d from 393 to 360 °C with increasing Φ_{POSS}, consistent with the behavior of crosslinked PPF-*co*-POSS copolymers and PCLTA/POSS networks reported by our groups [29,30].

The rheological properties of photo-crosslinked POSS-PCLDAs at 37 and 60 °C were measured using the dynamic frequency sweep mode. As shown in the Figures 6.3a-d, all curves showed that the storage modulus (G') was much greater than the loss modulus (G'') and shear thinning occurred in the studied frequency range. All the G' curves were frequency independent, suggesting that the networks were perfect. For the crosslinked POSS-PCLDAs that were amorphous at both test temperatures (Φ_{POSS} = 30%, 40%, and 50%), both G' and viscosity (η) showed little variance with temperature. In contrast, photo-crosslinked POSS-PCLDAs with Φ_{POSS}

of 10% and 20% showed distinct sets of rheological curves at different temperatures, as they were semi-crystalline at 37 °C but amorphous at 60 °C. Thus at 60 °C, *G'* increased with increasing Φ_{POSS}, as the molecular weight decreased and crosslinking density increased.

Representative tensile stress-strain curves of photo-crosslinked POSS-PCLDA strips at 37 °C are shown in Figure 6.3e with mechanical properties summarized in Table 6.2. The cyclic stress-strain curve (cycle number = 2) for photo-crosslinked POSS-PCLDA with Φ_{POSS} of 34% is shown in Figure 6.3f to demonstrate the reversible elastomeric properties. Similar to photo-crosslinked PCLAs, the *E* of crosslinked POSS-PCLDA was efficiently controlled by the molecular weight because it determined both the crosslinking density and crystallinity simultaneously [17]. When the molecular weight was high, the POSS-PCLDA network was semi-crystalline and stiffer than the amorphous counterparts made from lower molecular weights. Photo-crosslinked POSS-PCLDAs with Φ_{POSS} of 10%, 20%, and 30% were plastic and showed yielding during the tensile test, while the others were elastomeric. The Φ_{POSS} dependences of *E*, T_m, and χ_c of photo-crosslinked POSS-PCLDAs are shown in Figure 6.3g. Interestingly, the *E* values of photo-crosslinked POSS-PCLDAs with Φ_{POSS} of 30% and 32% were significantly different at 37 °C. Although the compositions were similar, the *E* value dropped dramatically when the POSS-PCLDA network became amorphous. It should be noted that photo-crosslinked POSS-PCLDA with Φ_{POSS} of 30% was more likely to be amorphous on the top surface when used for culturing cells at 37 °C although the bulk was still semi-crystalline. The semi-crystalline POSS-PCLDA networks showed the necking phenomenon at the strain of ~20%, while the amorphous POSS-PCLDA networks were elastomeric without showing the necking phenomenon, unlike amorphous PCLA networks, which were quite brittle and had the ε_b values of less than 35% [20]. The ε_b values were higher than 200% for most of the amorphous POSS-PCLDA networks except the one with

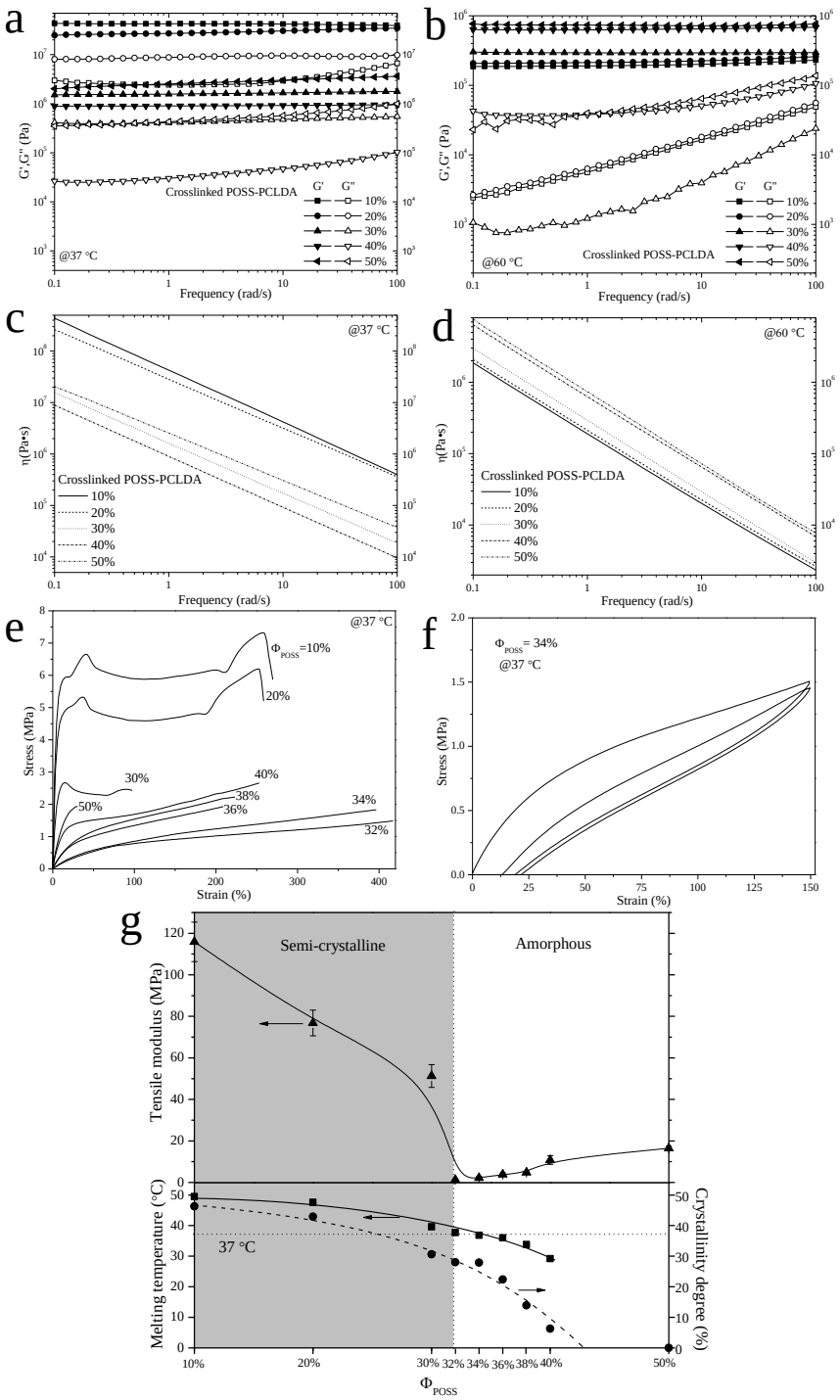

Figure 6.3 Storage modulus G' (solid symbols), and loss modulus G'' (open symbols) vs. frequency for crosslinked POSS-PCLDAs at 37 °C (a) and 60 °C (b). Viscosity (lines) vs. frequency for crosslinked POSS-PCLDAs at 37 °C (c) and 60 °C (d). (e) Tensile stress-strain curves for crosslinked POSS-PCLDAs at 37 °C. (f) Cyclic stress–strain curve (cycle = 2) for POSS-PCLDA (Φ_{POSS} = 34%). (g) Tensile modulus, melting temperature, and crystallinity degree change based on POSS compositions of crosslinked POSS-PCLDAs.

Φ_{POSS} of 50%, and the elongation could recover after removing the applied force. After 1 h or at a higher temperature (45 °C), the elongation could be fully recovered. The largest ε_b value was 435 ± 49% for photo-crosslinked POSS-PCLDA with Φ_{POSS} of 32%.

The optical images of crosslinked POSS-PCLDA disks at 25, 37, and 60 °C were shown in Figure 6.4a. At 25 °C, photo-crosslinked POSS-PCLDA disks with Φ_{POSS} lower than 34% were opaque, indicating the disks were semi-crystalline. At 37 °C, only POSS-PCLDA disks with Φ_{POSS} lower than 30% were opaque. At 60 °C, all the disks were transparent. The optical image was consistent with the DSC data. Semi-crystalline polymer networks usually had higher surface roughnesses because of the surface rearrangement from purification in acetone and then crystallization. To minimize the effect of surface roughness on cell behaviors, photo-crosslinked POSS-PCLDA disks were compressed and smoothened between two glass plates. The surface morphologies of the disks were characterized using AFM, as shown in Figure 6.4b. The surfaces of the photo-crosslinked POSS-PCLDA disks with Φ_{POSS} of 10% and 20% were still rougher than the others, but the R_{rms} values were all less than 20 nm. As another important surface characteristic that can affect cell-material interactions, surface hydrophilicity or wettability was characterized using the water contact angles on all the photo-crosslinked POSS-PCLDA disks at 37 °C, as shown in Figure 6.4c. The water contact angle depended on Φ_{POSS} in a parabolic or non-monotonic manner. The water contact angles were 80° and 78° on the semi-crystalline photo-crosslinked POSS-PCLDA disks with Φ_{POSS} of 10% and 20%, respectively. As I mentioned above, the photo-crosslinked POSS-PCLDA disk with Φ_{POSS} of 30% actually had an amorphous surface despite the semi-crystalline bulk, as evidenced by the lowest water contact angle of 61°. Then the value increased dramatically from 69° to 91° with further increasing Φ_{POSS} from 30% to 50%, as the content of hydrophobic POSS increased.

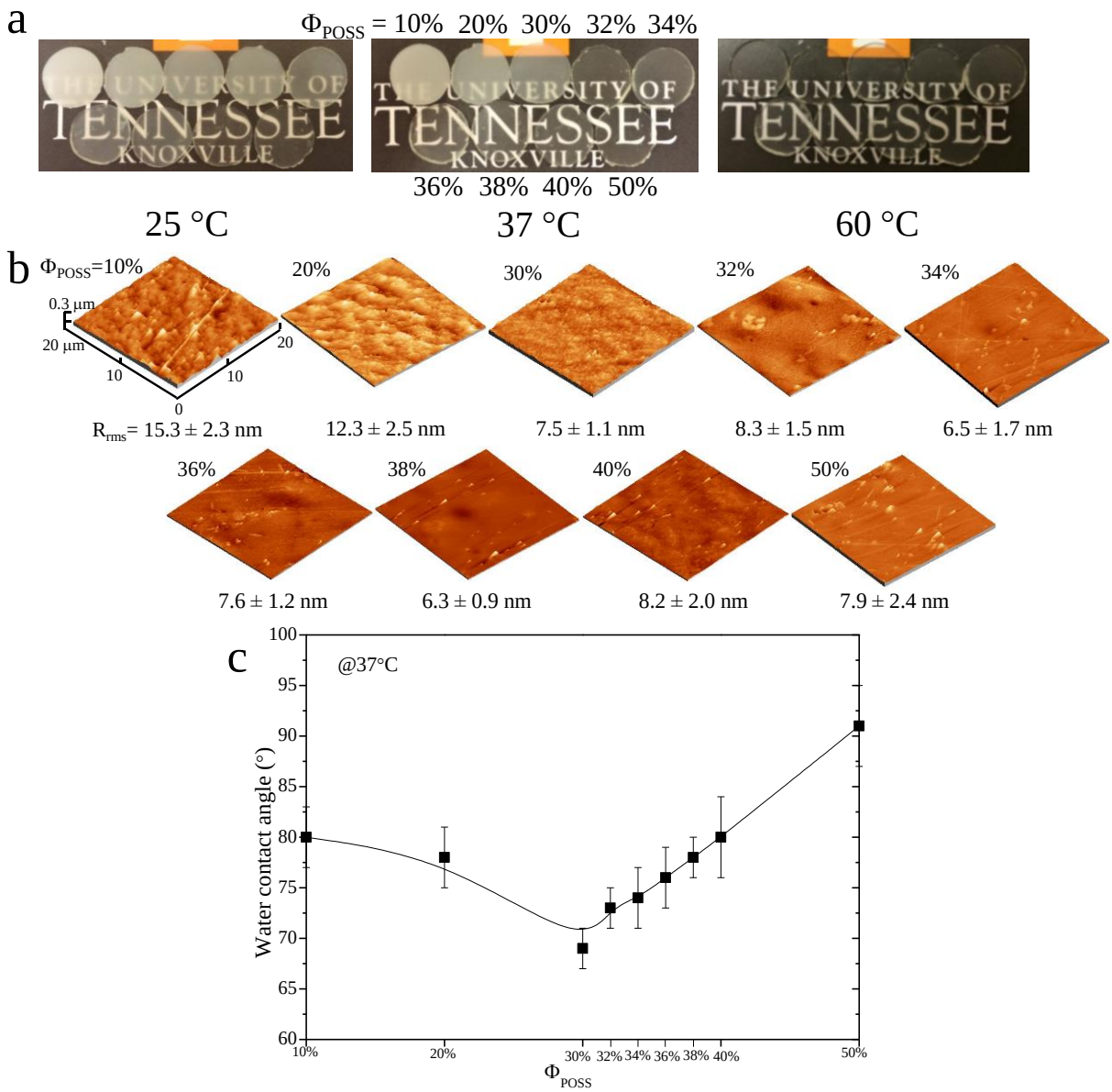

Figure 6.4 (a) Optical images of crosslinked POSS-PCLDA disks at 25, 37, and 60 °C. (b) AFM 3D height images and (c) water contact angles of compressed crosslinked POSS-PCLDA disks.

6.3.3 *In vitro* SMC attachment and proliferation.

Consistent with the previous studies [40-44], stiffer substrates of semi-crystalline POSS-PCLDA networks with Φ_{POSS} of 10% and 20% could better support SMC attachment and proliferation than any other samples, as shown in Figure 6.5b,c. Photo-crosslinked POSS-PCLDA disks with Φ_{POSS} of 10% had higher SMC attachment and proliferation than the ones with Φ_{POSS} of 20%, although only cell attachment showed significant difference. On the more compliant photo-crosslinked POSS-PCLDA disks, SMC attachment and proliferation did not show significant difference. Similar SMC numbers from 4 h to day 4 post-seeding were found on the amorphous POSS-PCLDA networks, as well as photo-crosslinked POSS-PCLDA with Φ_{POSS} of 30%. The SMC images stained with RP shown in Figure 6.5a were consistent with the cell numbers calculated using the MTS assay. SMC spreading followed a similar trend as the substrate stiffness varied, as the cell spread area (~2000 μm^2) decreased with increasing the molecular weight for amorphous photo-crosslinked POSS-PCLDA disks while it increased with increasing the molecular weight for semi-crystalline ones. However, the differences were not significant among all the samples except for photo-crosslinked POSS-PCLDA with Φ_{POSS} of 10%.

6.3.4 Focal adhesions in SMCs.

FAs with functional diversity serve as the anchorage of a cell and signal carriers to report the extracellular matrix (ECM) condition to cell nucleus and the feedback in turn affects the cell behavior [45]. The FAs in the SMCs cultured on the photo-crosslinked POSS-PCLDA disks were characterized at day 1 post-seeding, as shown in Figure 6.6. The FA density, area, and elongation quantified from the cell images followed a similar trend as the cell proliferation did on different photo-crosslinked POSS-PCLDA disks. The highest FA density, area, and elongation were found at Φ_{POSS} of 10% when the substrate stiffness was the highest. The FA area and elongation on photo-

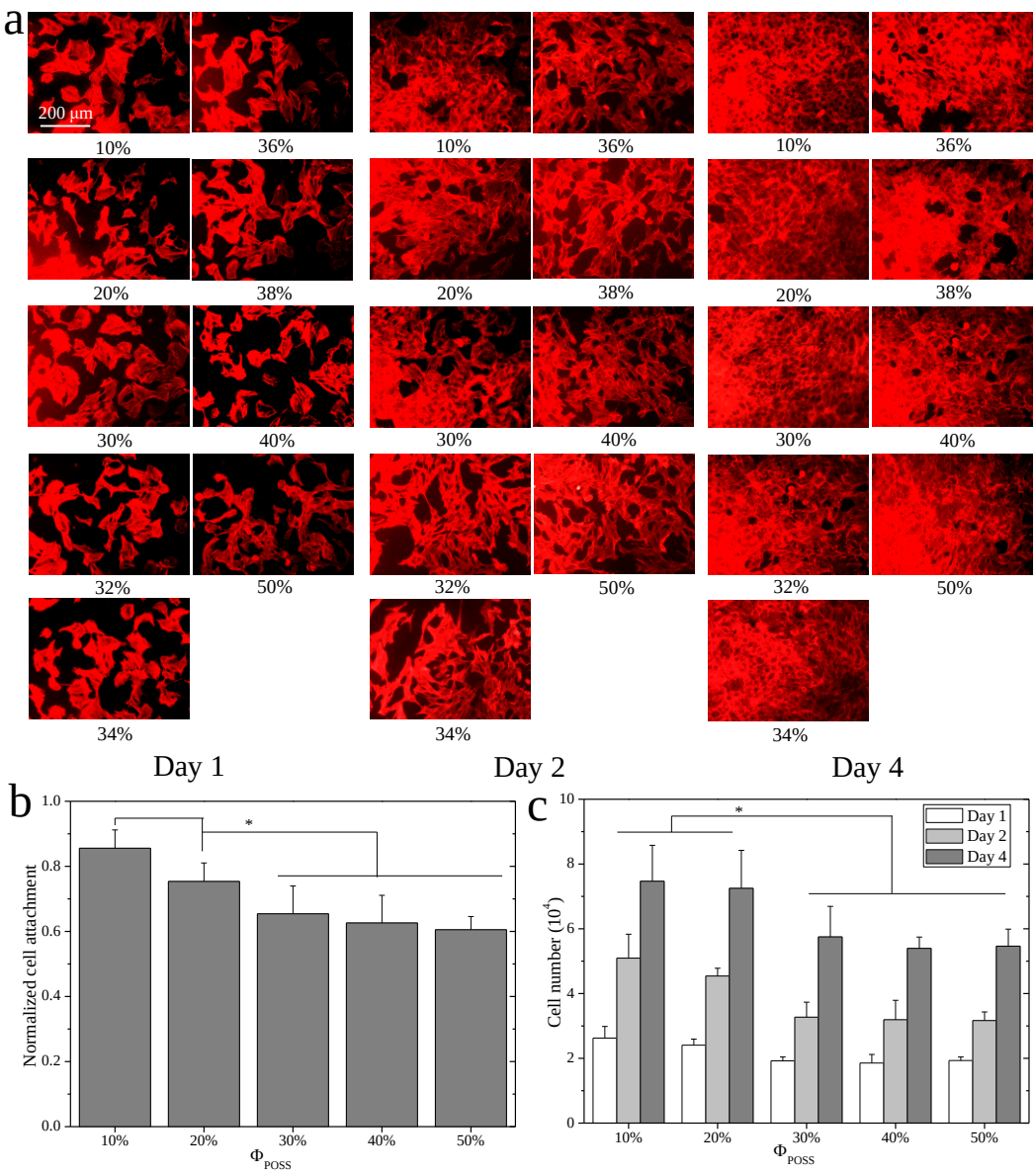

Figure 6.5 (a) SMCs images at days 1, 2, and 4 post-seeding stained using RP (red). Scale bar of 200 µm is applicable to all. (b) Normalized SMC attachment at 4 h post-seeding. (c) SMC numbers at days 1, 2, and 4 post-seeding on the crosslinked POSS-PCLDA disks. *: $p < 0.05$ between any two samples marked with the same symbol.

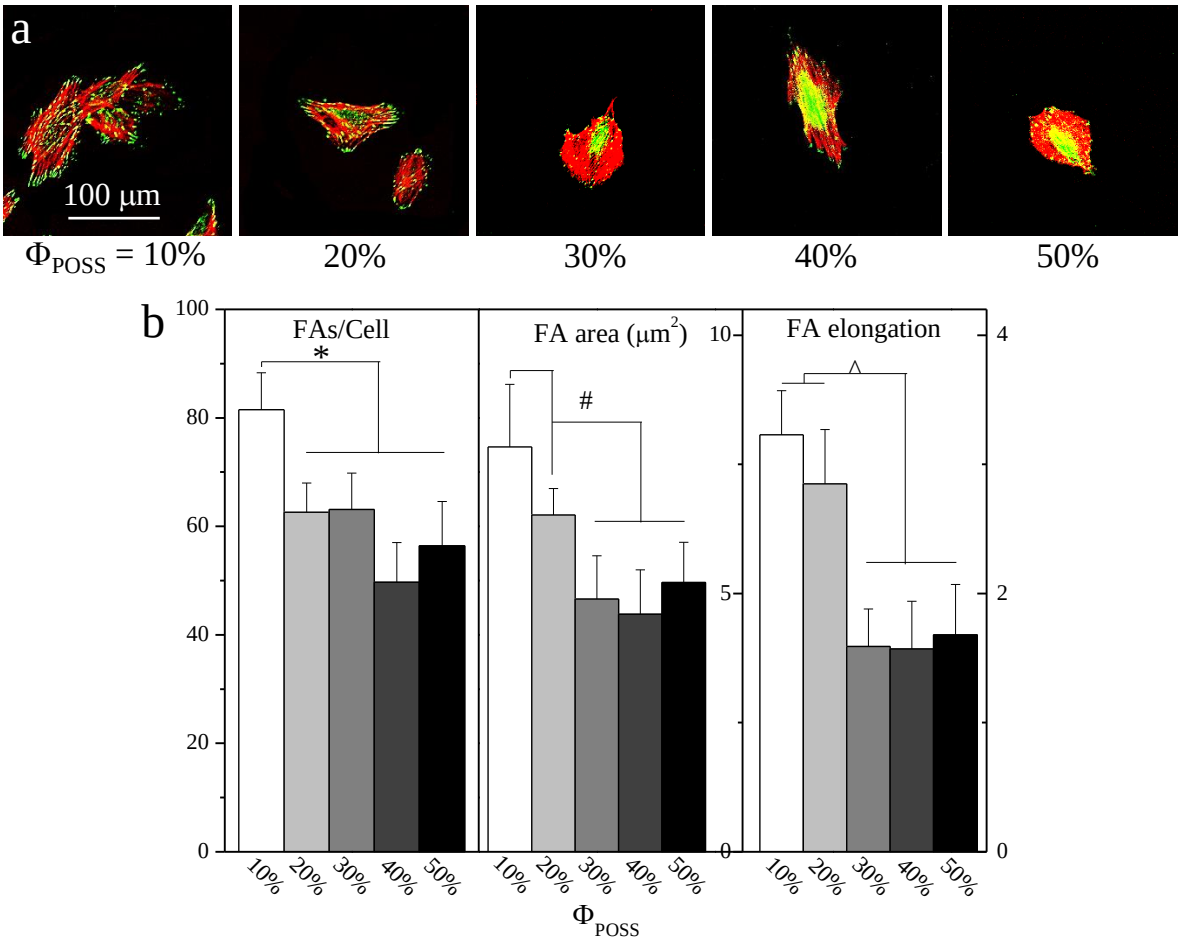

Figure 6.6 (a) Confocal microscope images of SMC filaments and vinculin antibody stained focal adhesions. Scale bar of 100 μm is applicable to all. (b) FA density, FA area, and FA elongation. $*^{,\#,\wedge}$: $p < 0.05$ between the samples marked with the same symbol.

crosslinked POSS-PCLDA disks with Φ_{POSS} of 20% were higher than those on more compliant disks. Among the disks with Φ_{POSS} of 30%, 40% and 50%, there was no significant difference in the density, area, and elongation of FAs. The above results of SMC attachment, proliferation, and FAs indicated that SMCs preferred the stiffer substrates.

6.3.5 *In vitro* PC12 cell attachment, proliferation, and differentiation.

In contrast with the results of the SMC study, neuronal-natured PC12 cell attachment, proliferation, and differentiation all showed non-monotonic or parabolic dependences on Φ_{POSS} when they were seeded and cultured on the photo-crosslinked POSS-PCLDA disks. PC12 cell proliferation over 7 days are shown in Figure 6.7. The fluorescent images of RP-stained PC12 cells on photo-crosslinked POSS-PCLDA disks at days 1, 4, and 7 post-seeding in Figures 6.7a demonstrate proliferation levels. PC12 cells formed clusters on all the POSS-PCLDAs. As reported previously, PC12 cells preferred softer substrates [46,47]. Thus PC12 attachment and proliferation were significantly lower on photo-crosslinked POSS-PCLDA disks with Φ_{POSS} of 10% and 20% than on the disks with higher Φ_{POSS} of 30-36%. PC12 cell attachment and proliferation did not vary much when Φ_{POSS} increased from 10% to 20% and the E value decreased from 115.9 to 76.8 MPa. The effect of surface stiffness on PC12 cell behavior might be less prominent on the substrates with E higher than a critical value. Higher surface hydrophobicity of photo-crosslinked POSS-PCLDAs with Φ_{POSS} of 40% and 50% also significantly limited PC12 cell attachment and proliferation. The highest PC12 cell attachment and proliferation appeared on the photo-crosslinked POSS-PCLDA with Φ_{POSS} of 30%, which had the lowest water contact angle and the lowest E when immersed into the culture media at 37 °C. With increasing Φ_{POSS} from 32%-36%, both E and water contact angle increased for photo-crosslinked POSS-PCLDA while the PC12 cell number decreased without showing significant difference. The fluorescent images

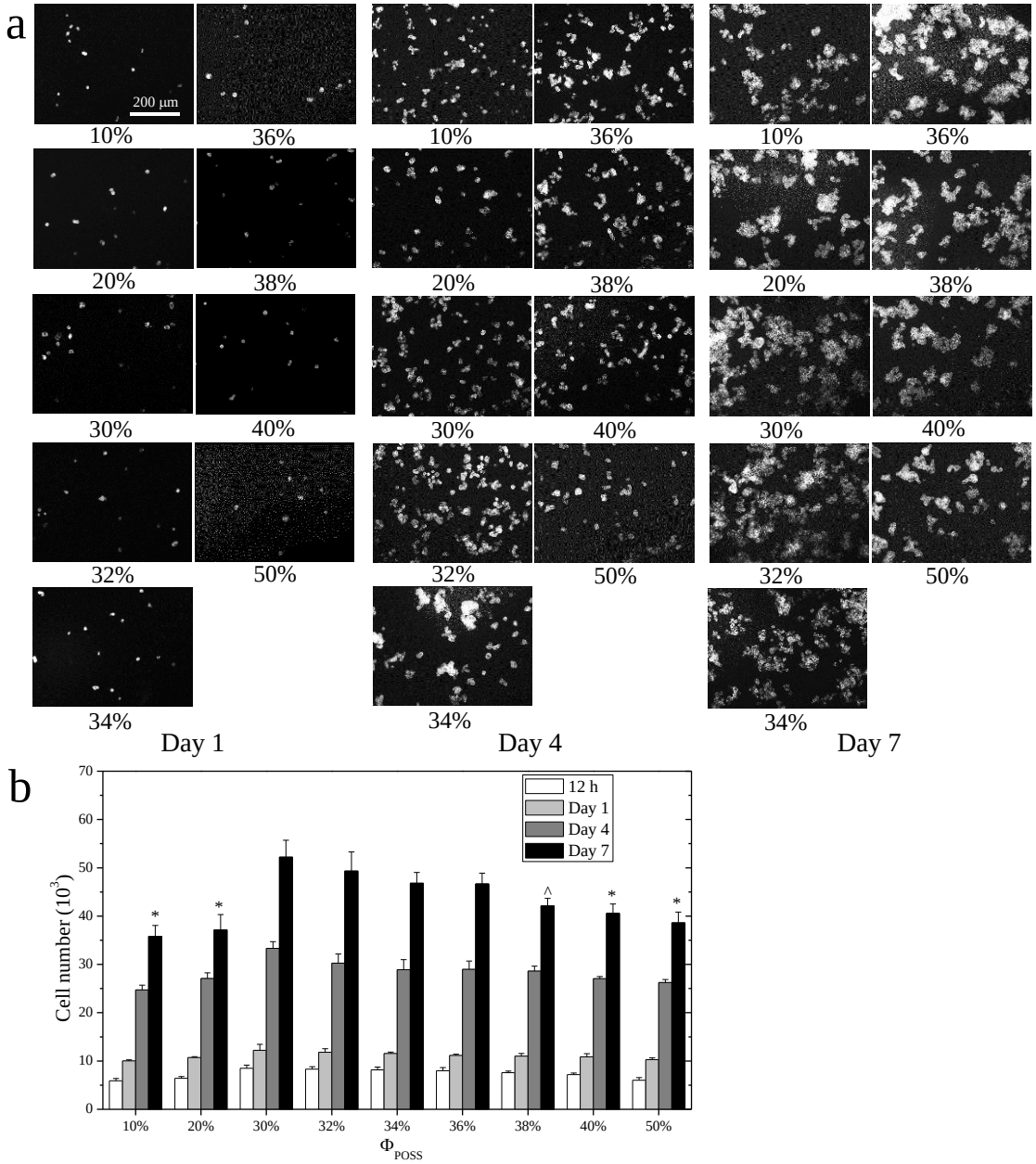

Figure 6.7 (a) PC12 cell images at days 1, 4, and 7 post-seeding stained using RP. Scale bar of 200 µm is applicable to all. (b) PC12 cell numbers at 12 h, days 1, 2, and 4 post-seeding on the crosslinked POSS-PCLDA disks. *: $p < 0.05$ between the sample marked with the symbol and POSS-PCLDAs (Φ_{POSS} = 30%, 32%, 34% and 36%). ^: $p < 0.05$ between the sample marked with the symbol and POSS-PCLDA (Φ_{POSS} = 30%).

of PC12 cells were consistent with the cell numbers obtained using the MTS assay.

PC12 cell differentiation also showed a similar trend as in the cell proliferation, as shown in Figure 6.8. Upon NGF treatment, neurite lengths were significantly higher on the photo-crosslinked POSS-PCLDA disks with Φ_{POSS} of 30% and 32% than on the others by showing average values of 123 and 103 μm, respectively. The percentages of differentiated PC12 cells, i.e., the cells bearing neurites, were also significantly higher on the photo-crosslinked POSS-PCLDA disks with Φ_{POSS} of 30-36% than on the photo-crosslinked POSS-PCLDA disks with Φ_{POSS} of 10% and 20%. As discussed earlier on PC12 cell attachment and proliferation, higher hydrophobicity on the disks of photo-crosslinked POSS-PCLDAs with Φ_{POSS} of 40% and 50% also resulted in less PC12 cell differentiation. The above results showed the amorphous elastomeric POSS-PCLDA networks with higher hydrophilicity and lower *E* could promote PC12 cell differentiation better.

6.3.6 Fabrication of nerve conduits.

Photo-crosslinking of POSS-PCLDA with Φ_{POSS} of 32% was efficient in fabricating nerve conduits free of defects, as shown in Figure 6.9. The fabricated nerve conduit was transparent at 37 °C and had smooth surfaces with an inner diameter of ~1.2 mm and an average thickness of 280 μm. The photo-crosslinked POSS-PCLDA nerve conduit had no swelling in PBS solution, but could slightly swell in 70% ethanol solution. The swelling in ethanol solution was helpful for removing leachable and potentially toxic components if they existed [16,18]. Because of the elastomeric properties at body temperature, nerve conduits made from POSS-PCLDA with Φ_{POSS} of 32% had sufficient flexibility and resistance to tear during *in vivo* implantation. The suturability was also excellent to satisfy the basic requirements for guiding peripheral nerve regeneration [16,18,48].

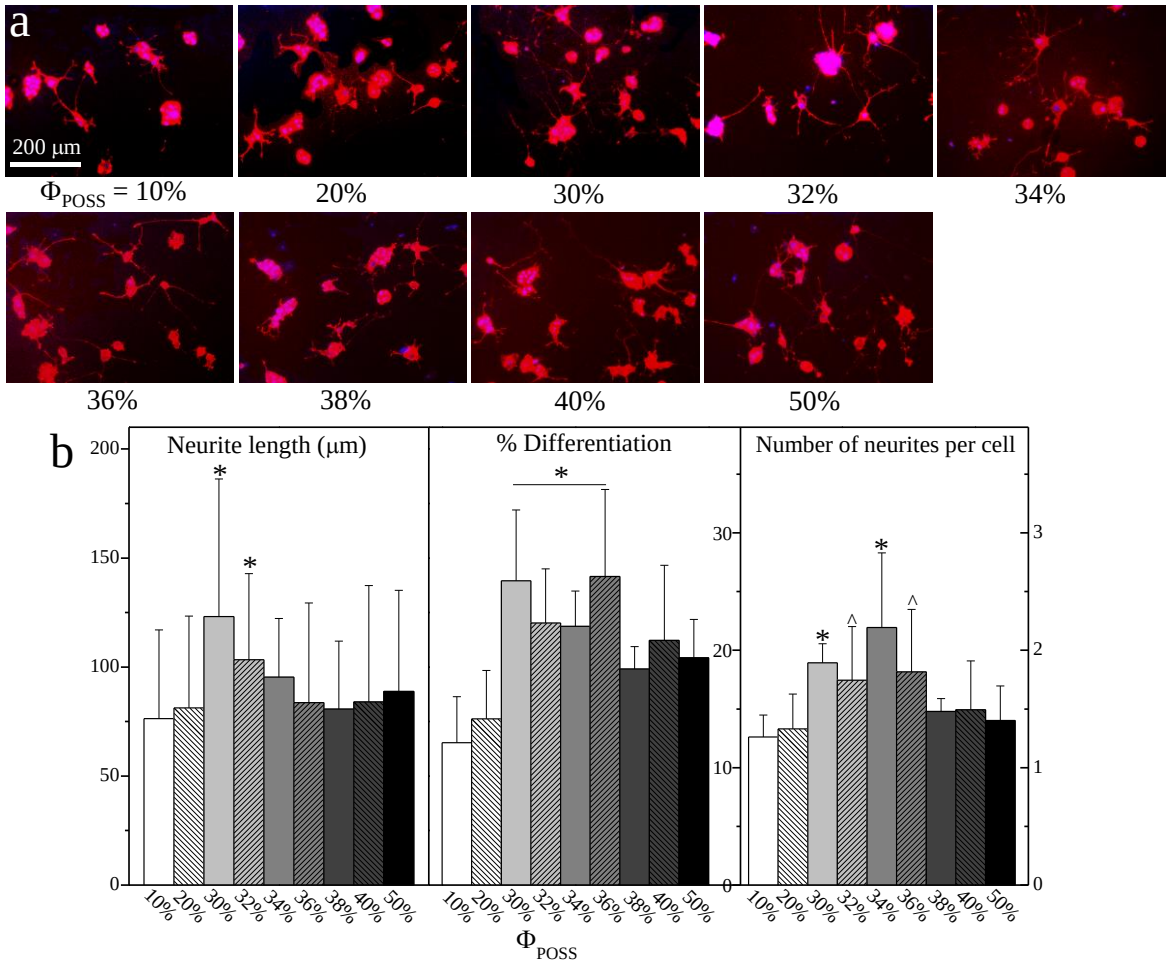

Figure 6.8 (a) Fluorescent images of NGF-induced PC12 cell differentiation stained using RP (red) and DAPI (blue) at day 7 post-seeding. Scale bar of 200 μm is applicable to all. (b) Quantification of PC12 neurites at day 7 using the number of neurites per cell, percentage of differentiated cells, and neurite lengths. *: $p < 0.05$ between the marked samples and any other samples. ^: $p < 0.05$ between the marked samples and POSS-PCLDA (Φ_{POSS} = 10% and 20%).

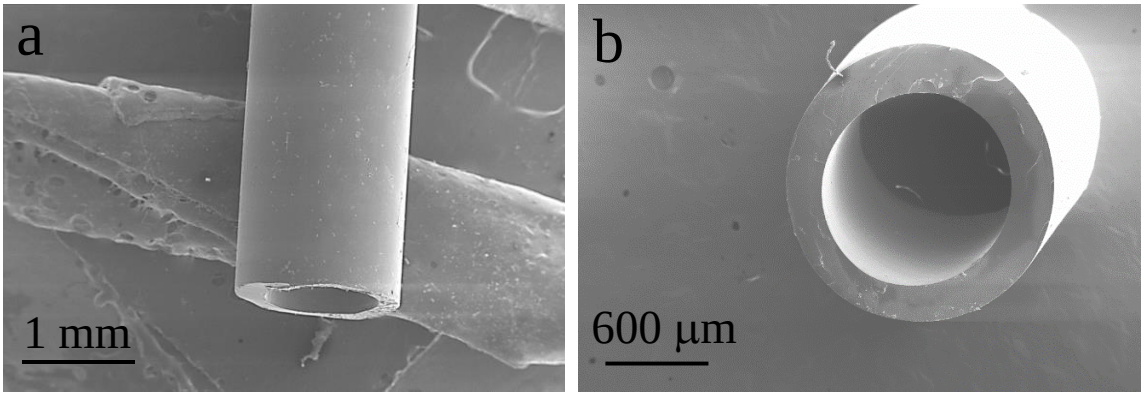

Figure 6.9 SEM images of (a) a crosslinked POSS-PCLDA (Φ_{POSS} = 32%) conduit and (b) the cross sections.

6.3.7 Further discussion.

In this chapter, I introduced a POSS nanocage into the PCL chain by using 1,2-propanediol isobutyl POSS to initiate the ROP of ε-caprolactone. Usually, addition of POSS into a polymer matrix can enhance thermal and mechanical properties without introducing cytotoxicity [49-52]. However, POSS nanocages started to aggregate and show phase separation at high Φ_{POSS}, resulting in non-uniform properties. Therefore, Φ_{POSS} could be only limited to be less than 30%, leaving it difficult to further improve the properties of the composites. Through the present method, each POSS nanocage was located and confined in the center of a PCL chain and there was no crystallization of POSS after crosslinking even at Φ_{POSS} of 50%. This finding was different from the previous reports [33,34], in which similar methods were applied but the crystallization of POSS was still found in the polymer networks with Φ_{POSS} of 34-42%. Removal of the low-molecular-weight moiety in the precipitation step in this chapter might be crucial in preventing aggregation and crystallization of POSS after crosslinking. Usually, networks made from low-molecular-weight PCLs were amorphous and elastic but brittle with low values of ε_b (<35% for PCLDA, <80% for PCLTA, and <50% for PCLF) [16,17,20]. In contrast, networks made from high-molecular-weight PCL were elastomeric with a low *E* at temperatures higher than its T_m but they became semi-crystalline and tough with significantly increased *E* when the temperature was lower than its T_m. However, the T_m was usually higher than 37 °C for the networks made from high-molecular-weight PCL and thus the semi-crystalline PCL networks were not elastomeric at body temperature. The networks made from POSS-PCLDA could not only prevent aggregation and phase separation of POSS but also suppress the crystallization of both POSS and PCL. The bulky POSS nanocage in the center of POSS-PCLDA in this chapter was mainly to suppress the crystallinity of the polymer network, instead of strengthening the network. Compared with

PCLDA networks [17], POSS-PCLDA networks could be amorphous at 37 °C even at a higher PCL molecular weight and thus could more likely form elastomers. Specifically, photo-crosslinked POSS-PCLDA with Φ_{POSS} of 32% had a low *E* value of 1.3 MPa and a reversible strain as high as 400% without showing the necking phenomenon.

The surface chemical, topological, and mechanical properties of biomaterials are three major cues to affect cell-biomaterial interactions [53-55]. As surface roughness was very low and did not vary among all the compressed disks of photo-crosslinked POSS-PCLDAs, this factor was first ruled out. I further proved that SMC attachment and proliferation could be majorly affected by substrate stiffness through mechanotransduction that involves integrins, FAs, and actin-myosin associations [3,40,41,56]. Stiffer substrates can enhance integrin expression and encourage FA maturation of some cell types such as pre-osteoblastic cells and SMCs, and thus further promote other cell functions. However, SMC attachment and proliferation did not vary significantly for amorphous networks although there was a slight increment in the substrate stiffness when Φ_{POSS} increased from 30% to 50%. Our SMC results also indicated photo-crosslinked POSS-PCLDA with Φ_{POSS} of 30% was sensed by the cells as an amorphous network in the cell culture environment instead of a semi-crystalline network as determined using DSC. Without the enhancement of crystalline domains, the stiffness of the POSS-PCLDA network increased with increasing the crosslinking density that was decided by the molecular weight of PCL, which was inversely proportional to Φ_{POSS}. Therefore, the *E* value of the surface layer of photo-crosslinked POSS-PCLDA with Φ_{POSS} of 30% was much lower in the cell culture environment than that measured in the tensile test at 37 °C, and even smaller than that of photo-crosslinked POSS-PCLDA with Φ_{POSS} of 32%. For all these amorphous POSS-PCLDA networks, with increasing Φ_{POSS} from 32% to 50%, *E* increased from 1.3 to 16.5 MPa and the water contact angle also

increased greatly. A higher substrate stiffness usually improved SMC attachment and proliferation, while a water contact angle higher than ~50° [53], i.e., lower surface hydrophilicity, hindered cell attachment and proliferation. The decreased hydrophilicity might offset the effect of increased substrate stiffness in regulating cell behaviors. Therefore, given the low substrates stiffness and low hydrophilicity of these amorphous POSS-PCLDA networks, their elastomeric properties did not benefit the SMC behaviors.

The elastomeric amorphous POSS-PCLDA networks were proved to better support PC12 cell attachment, proliferation, and differentiation than their stiffer semi-crystalline counterparts, confirming that more compliant substrates are more suitable for PC12 cells. As discussed earlier, POSS-PCLDA network with Φ_{POSS} of 30% demonstrated elastomeric properties with the lowest surface stiffness and highest hydrophilicity in the cell culture environment best supported PC12 cell attachment, proliferation, and differentiation. Since photo-crosslinked POSS-PCLDA with Φ_{POSS} of 30% was not uniform network in the cell culture environment as the surface were amorphous and compliant while the inner part was semi-crystalline and stiff, I choose POSS-PCLDA with Φ_{POSS} of 32% to prepare nerve conduits. Although the elastomeric POSS-PCLDA networks were proved to support PC12 cell attachment, proliferation and differentiation, the low surface hydrophilicity still limited the biomedical applications. Our research group previously reported methoxyl poly(ethylene glycol) monoacrylate (mPEGA) and photo-polymerizable poly(L-lysine) (PLL) with one end-capped double bond [46,57,58]. These polymers could be photo-crosslinked into hydrophobic polymer networks to improve the hydrophilicity and/or introduce positive charge. With less than 5% of these polymers incorporating into the network, the surface hydrophilicity and density of positive charges can be significantly improved without changing too much on mechanical and thermal properties [46,57,58]. Further improvements of the

POSS-PCLDA system are under investigation to explore the tissue engineering applications of PCL-based networks.

6.4 Conclusions

POSS-PCLs with two hydroxyl end groups and different molecular weights were synthesized with 1,2-propanediol isobutyl POSS as the initiator in the ROP of ε-caprolactone and further acrylated to photo-crosslinkable POSS-PCLDAs. POSS nanocages were homogenously incorporated into the polymer network after photo-crosslinking. The thermal and mechanical properties of the POSS-PCLDA networks could be well controlled by Φ_{POSS}. Amorphous photo-crosslinked POSS-PCLDAs exhibited elastomeric properties with a high strain at break without showing the necking phenomenon. Both semi-crystalline stiff and amorphous elastomeric POSS-PCLDA networks were evaluated for supporting SMC and PC12 cell attachment and proliferation, and PC12 cell differentiation. Stiff and semi-crystalline POSS-PCLDA networks could significantly better support SMC attachment, proliferation, spreading, and FAs than their elastomeric amorphous counterparts, among which no significant differences were found in SMC behaviors. In clear contrast, elastomeric amorphous POSS-PCLDA networks better supported PC12 cell attachment, proliferation, and differentiation, showing the great promise as a potential biomaterial for fabricating flexible nerve conduits used in guided peripheral nerve regeneration.

References

1. Wang, Y.; Ameer, G. A.; Sheppard, B.J.; Langer, R. *Nat. Biotechnol.* **2002**, *20*(6), 602-606.

2. Zhang, Y.; Tran, R. T.; Gyawali, D.; Yang, J. *Int. J. Biomater. Res. Eng.* **2011**, *1*(1), 18.

3. Yang, J.; Webb, A. R.; Ameer, G. A. *Adv. Mater.* **2004**, *16*(6), 511-516.

4. Yang, J.; Webb, A. R.; Pickerill, S. J.; Hageman, G.; Ameer, G. A. *Biomaterials* **2006**, *27*(9), 1889-1898.

5. Gyawali, D.; Tran, R. T.; Guleserian, K. J.; Tang, L.; Yang, J. *J. Biomater. Sci., Polym. Ed.* **2010**, *21*(13), 1761-1782.

6. Dey, J.; Xu, H.; Shen, J.; Thevenot, P.; Gondi, S. R.; Nguyen, K. T.; Sumerlin, B. S.; Tang, L.; Yang, J. *Biomaterials* **2008**, *29*(35), 4637-4649.

7. Daemi, H.; Rajabi-Zeleti, S.; Sardon, H.; Barikani, M.; Khademhosseini, A.; Baharvand, H. *Biomaterials* **2016**, *84*, 54-63.

8. Amsden, B. G.; Misra, G.; Gu, F.; Younes, H. M. *Biomacromolecules* **2004**, *5*(6), 2479-2486.

9. Lee, L. Y.; Wu, S. C.; Fu, S. S.; Zeng, S. Y.; Leong, W. S.; Tan, L. P. *Eur. Polym. J.* **2009**, *45*(11), 3249-3256.

10. Chen, Q.Z.; Bismarck, A.; Hansen, U.; Junaid, S.; Tran, M. Q.; Harding, S. E.; Ali, N. N.; Boccaccini, A. R. *Biomaterials* **2008**, *29*(1), 47-57.

11. Pereira, M. J. N.; Ouyang, B.; Sundback, C. A.; Lang, N.; Friehs, I.; Mureli, S.; Pomerantseva, I.; McFadden, J.; Mochel, M. C.; Mwizerwa, O.; del Nido, P. *Adv. Mater.* **2013**, *25*(8), 1209-1215.

12. Chen, Q.; Jin, L.; Cook, W. D.; Mohn, D.; Lagerqvist, E. L.; Elliott, D. A.; Haynes, J. M.; Boyd, N.; Stark, W. J.; Pouton, C. W.; Stanley, E. G. *Soft Matter* **2010**, *6*(19), 4715-4726.

13. Santerre, J. P.; Labow, R. S.; Duguay, D. G.; Erfle, D.; Adams, G. A. *J. Biomed. Mater. Res.* **1994**, *28*(10), 1187-1199.

14. Lavrador, C.; Mascarenhas, R.; Coelho, P.; Brites, C.; Pereira, A.; Gogolewski, S. *J. Mater. Sci. Mater. Med.* **2016**, *27*(3), 1-12.

15. Wang, S.; Lu, L.; Gruetzmacher, J. A.; Currier, B. L.; Yaszemski, M. J. *Macromolecules* **2005**, *38*(17), 7358-7370.

16. Wang, S.; Yaszemski, M. J.; Knight, A. M.; Gruetzmacher, J. A.; Windebank, A. J.; Lu, L. *Acta Biomater.* **2009**, *5*(5), 1531-1542.

17. Cai, L.; Wang, S. *Polymer* **2010**, *51*(1), 164-177.

18. Wang, S.; Kempen, D. H.; De Ruiter, G. C.; Cai, L.; Spinner, R. J.; Windebank, A. J.; Yaszemski, M. J.; Lu, L. *Adv. Funct. Mater.* **2015**, *25*(18), 2715-2724.

19. Wang, K.; Cai, L.; Zhang, L.; Dong, J.; Wang, S. *Adv. Healthcare Mater.* **2012**, *1*(3), 292-301.

20. Liu, X. 2014. Phenotypic modulation of smooth muscle cells on biodegradable elastomeric substrates. Doctoral dissertation. The University of Tennessee, Knoxville.

21. Wei, G.; Ma, P. X. *Biomaterials* **2004**, *25*(19), 4749-4757.

22. Sun, F.; Zhou, H.; Lee, J. *Acta Biomater.* **2011**, *7*(11), 3813-3828.

23. Xie, M.; Ge, J.; Lei, B.; Zhang, Q.; Chen, X.; Ma, P. X. *Macromol. Biosci.* **2015**, *15*(12), 1656-1662.

24. Yildirimer, L.; Buanz, A.; Gaisford, S.; Malins, E. L.; Becer, C. R.; Moiemen, N.; Reynolds, G. M.; Seifalian, A. M. *Sci. Rep.* **2015**, *5*.

25. Rai, B.; Oest, M. E.; Dupont, K. M.; Ho, K. H.; Teoh, S. H.; Guldberg, R. E. *J. Biomed. Mater. Res. Part A* **2007**, *81*(4), 888-899.

26. Kikuchi, M.; Koyama, Y.; Yamada, T.; Imamura, Y.; Okada, T.; Shirahama, N.; Akita, K.; Takakuda, K.; Tanaka, J. *Biomaterials* **2004**, *25*(28), 5979-5986.

27. La Gatta, A.; De Rosa, A.; Laurienzo, P.; Malinconico, M.; De Rosa, M.; Schiraldi, C. *Macromol. Biosci.* **2005**, *5*(11), 1108-1117.

28. Murariu, M.; Ferreira, A. D. S.; Degée, P.; Alexandre, M.; Dubois, P. *Polymer* **2007**, *48*(9), 2613-2618.

29. Cai, L.; Chen, J.; Rondinone, A. J.; Wang, S. *Adv. Funct. Mater.* **2012**, *22*(15), 3181-3190.

30. Cai, L.; Foster, C. J.; Liu, X.; Wang, S. *Polymer* 2014, *55*(16), 3836-3845.

31. Kannan, R. Y.; Salacinski, H. J.; Butler, P. E.; Seifalian, A. M. *Acc. Chem. Res.* **2005**, *38*(11), 879-884.

32. Filion, T. M.; Xu, J.; Prasad, M. L.; Song, J. *Biomaterials* **2011**, *32*(4), 985-991.

33. Alvarado-Tenorio, B.; Romo-Uribe, A.; Mather, P. T. *Macromolecules* **2011**, *44*(14), 5682-5692.

34. Lee, K. M.; Knight, P. T.; Chung, T.; Mather, P. T. *Macromolecules* **2008**, *41*(13), 4730-4738.

35. McMullin, E.; Rebar, H. T.; Mather, P. T. *Macromolecules* **2016**, *49*(10), 3769-3779.

36. Du, Y.; Yu, M.; Chen, X.; Ma, P. X.; Lei, B. *ACS Appl. Mater. Interfaces* **2016**, *8*(5), 3079-3091.

37. Cai, L.; Wang, S. *Biomacromolecules* **2009**, *11*(1), 304-307.

38. Brandrup, J.; Immergut, E. H.; editors. Polymer Handbook. 3rd ed. New York, Wiley; 1989.

39. Kopesky, E. T.; Haddad, T. S.; Cohen, R. E.; McKinley, G. H. *Macromolecules* **2004**, *37*(24), 8992-9004.

40. Pelham, R. J.; Wang, Y. L. *Proc. Natl. Acad. Sci.* **1997**, *94*(25), 13661-13665.

41. Yeung, T.; Georges, P. C.; Flanagan, L. A.; Marg, B.; Ortiz, M.; Funaki, M.; Zahir, N.; Ming, W.; Weaver, V.; Janmey, P. A. *Cell Motil. Cytoskel.* **2005**, *60*(1), 24-34.

42. Schwarz, U. *Soft Matter* **2007**, *3*(3), 263-266.

43. Choquet, D.; Felsenfeld, D. P.; Sheetz, M. P. *Cell* **1997**, *88*(1), 39-48.

44. Hadjipanayi, E.; Mudera, V.; Brown, R. A. *Cell Motil. Cytoskel.* **2009**, *66*(3), 121-128.

45. Burridge, K.; Chrzanowska-Wodnicka, M. *Annu. Rev. Cell Dev. Biol.* **1996**, *12*, 463-519.

46. Cai, L.; Lu, J.; Sheen, V.; Wang, S. *Biomacromolecules* **2012**, *13*(2), 358-368.

47. Gunn, J. W.; Turner, S. D.; Mann, B. K. *J. Biomed. Mater. Res. Part A* **2005**, *72*(1), 91-97.

48. Schmidt, C. E.; Leach, J. B. *Annu. Rev. Biomed. Eng.* **2003**, *5*(1), 293-347.

49. Wu, J.; Mather, P. T. *Polym. Rev.* **2009**, *49*(1), 25-63.

50. Cordes, D.B.; Lickiss, P. D.; Rataboul, F. *Chem. Rev.* **2010**, *110*(4), 2081-2173.

51. Kuo, S. W.; Chang, F. C. *Prog. Polym. Sci.* **2011**, *36*(12), 1649-1696.

52. Hartmann-Thompson, C. Polyhedral oligomeric silsesquioxanes in electronics and energy applications. In *Applications of Polyhedral Oligomeric Silsesquioxanes*; Springer: Netherlands, 2011; pp 247-325.

53. Harbers, G. M.; Grainger, D. W. Cell-material interactions: fundamental design issues for tissue engineering and clinical considerations. In *An introduction to biomaterials*; CRC: New York, 2006; pp 15-45.

54. Wong, J. Y.; Leach, J. B.; Brown, X. Q. *Surf. Sci.* **2004**, *570*(1), 119-133.

55. Saltzman, W. M.; Kyriakides, T. R. Cell interactions with polymers. In *Principles of tissue engineering*; Elsevier Inc., 1997; *3*.

56. Cai, L.; Zhang, L.; Dong, J.; Wang, S. *Langmuir* **2012**, *28*(34), 12557-12568.

57. Cai, L.; Wang, K.; Wang, S. *Biomaterials* **2010**, *31*(16), 4457-4466.

58. Cai, L.; Lu, J.; Sheen, V.; Wang, S. *Biomacromolecules* **2012**, *13*(2), 342-349.

Chapter VII. Epitaxial Crystallization and Surface Segregation in Modulating Pre-osteoblastic Cell Behavior on Polymer Substrates

Abstract

Poly(ε-caprolactone) (PCL) and its blends with 5% and 10% polyethylene glycol (PEG) were used to prepare crystallized polymer films on different substrates: glass, silicon (Si) and polytetrafluoroethylene (PTFE). Both the free surface (the top surface exposed to air) and the confined surface (the bottom surface contacting the substrate) of the crystallized polymer films were studied in terms of roughness and hydrophilicity. Glass and Si substrates did not affect polymer crystallization, while PTFE could induce epitaxial crystallization that resulted in much smaller spherulites. Different surface morphologies, surface segregation of hydrophilic PEG, as well as the different interactions with air or substrates affected mouse pre-osteoblastic MC3T3-E1 cell responses to these polymer surfaces. Polymer surfaces with regular spherulites could support better MC3T3-E1 cell attachment, proliferation, and focal adhesions (FAs) than the surfaces with epitaxial crystals. Addition of PEG into PCL also improved MC3T3-E1 cell attachment, proliferation, and FAs. Free polymer surfaces on glass/Si substrates supported MC3T3-E1 cells better than the confined surfaces, while the two sides of the polymer films crystallized on the PTEF substrate did not differ much.

7.1 Introduction

Cell-biomaterial interactions are crucial for the tissue engineering applications of biomaterials. Cellular responses to the underlying substrates can be regulated by three major categories of surface properties, such as surface chemistry, topography, and mechanical properties [1-4]. Among these factors, surface morphological features include ordered patterns and random roughness at both the micrometer and nanometer scales [5-11]. Compared with smooth surfaces, rough surfaces induced by polymer crystallization can have different surface morphologies and physicochemical properties controlled by isothermal crystallization temperature (T_c), composition, molecular weight, and film thickness for regulating cell behaviors [12-17]. Amorphous, flat materials such as glass and quartz are often used as substrates for polymer crystallization. When another crystalline material is used as the substrate, epitaxial crystallization, defined as the oriented overgrowth of a crystalline phase upon the surface of a substrate which is also crystalline, can happen and significantly affect the morphology and crystalline structure of the polymer film on it [18-25]. Polymers with low surface energies were also found to induce epitaxial crystallization even when they are amorphous [19-21]. Polytetrafluoroethylene (PTFE), a semi-crystalline polymer with a low surface energy, is often used as the substrate to induce epitaxial crystallization of another semi-crystalline polymer.

Poly(ε-caprolactone) (PCL) is a widely used biodegradable, semi-crystalline polymer with excellent biocompatibility and mechanical properties. Spherulites can form in pure PCL and its miscible blends with an amorphous or semi-crystalline component at appropriate compositions and T_cs [26-29]. Besides of the spherulites of pure PCL, PCL spherulites can also been observed in miscible blends of PCL with polymethacrylates, poly(styrene-*co*-acrylonitrile), poly(vinyl chloride), poly(vinyl methyl ether), in which the spherulites were usually banded-like [27-32]. The

epitaxial crystallization of PCL can be induced on high-orientated high-density polyethylene (HDPE) [33,34] and PTFE [35,36]. The epitaxial PCL crystalline structure not only occurs in the contact layer but also from the interface into the PCL melt [33]. The epitaxial crystallization of PCL in thin films was mainly edge-on structure at the interface, but flat-on structure with the further grown, while in thick films the epitaxial crystallization of PCL generated a semi-periodic lamellar twisting [34]. PCL crystalline showed different orientations on PTFE substrates, by either minimizing the lattice mismatch between PTFE and PCL, or showing graphoepitaxial nucleation [35]. The epitaxial PCL films on PTFE also provided 'contact guidance' to align smooth muscle cells [36]. Polyethylene glycol (PEG) is also a semi-crystalline polymer and is well used in improving surface hydrophilicity/wettability and inhibiting immunogenic activities, which are crucial for the tissue compatibility of a material [37-40].

Although epitaxial crystallization of PCL has been well studied, how mammalian cells respond to different morphologies resulted from epitaxial crystallization and to different interfaces, i.e., the top surface exposed to air and the bottom surface that contacts the substrate are largely unknown. Here I isothermally crystallized PCL and its binary blends with weight compositions of PEG (Φ_{PEG}) of 5% and 10% on three different substrates, glass, silicon (Si), and PTFE, and studied on both the top and bottom surfaces shown in Figure 7.1. Both epitaxial crystallization of PCL on PTFE and surface segregation of PEG occurred in the blends and further influenced the top and bottom surfaces of the crystallized film, which were reported to have different compositions and morphologies previously [41-45]. First I present the spherulitic morphologies, root-mean-square surface roughness (R_{rms}) values, and hydrophilicity of the top and bottom surfaces of the films of PCL and PCL/PEG blends isothermally crystallized on these three substrates. Then I discuss the

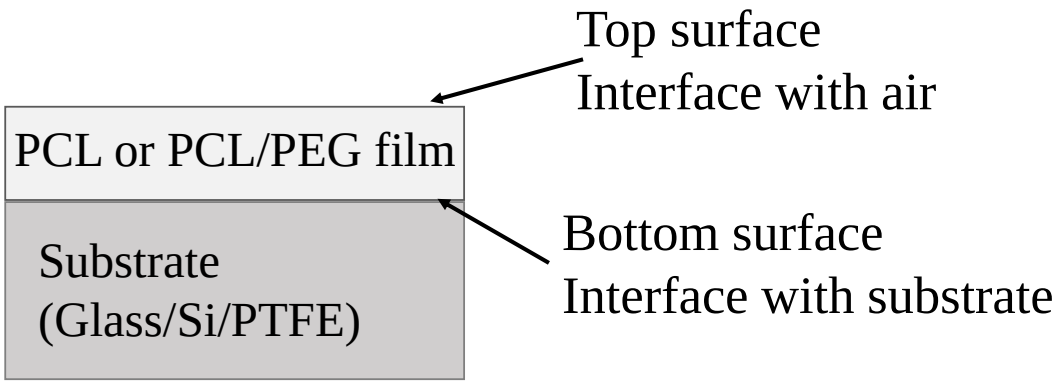

Figure 7.1 Polymer films coated on different substrates

capabilities of these surfaces to adsorb serum proteins from cell culture media and mouse pre-osteoblastic MC3T3-E1 cell attachment, proliferation and focal adhesions on these surfaces.

7.2 Experimental Section

7.2.1 Film preparation and characterization.

PCL and PEG purchased from Sigma Aldrich (Milwaukee, WI). PCL had a number-average molecular weights (M_n) of 98000 and a weight-average molecular weight (M_w) of 144000 g/mol, and PEG had a M_n of 14500 g/mol and a M_w of 15300 g/mol. Solutions of PCL and PCL/PEG blends with ϕ_{PEG} of 5% and 10% were prepared by dissolving 1 g of the polymer in 10 mL of CH_2Cl_2. About 100 μL of the polymer solution was drop-coated onto glass coverslips, silicon wafers, and PTFE plates. After the polymer films on the substrates were fully dried in a vacuum oven, they were melted at 85 °C for 5 min and quickly transferred onto a hot stage for isothermal crystallization at 45 °C. A polarized optical microscope (POM; Nikon Optiphot-2, POL) equipped with a Mettler Toledo FP82HT hot stage and a PixeLink digital camera was used to monitor and record the isothermal crystallization. Morphologies of the top and bottom surfaces of the polymer films crystallized on different substrates were characterized at room temperature using a multi-mode atomic force microscope (AFM) with a Nanoscope III control system (Veeco Instruments, Santa Barbara, CA). Images over a scan area of 100 μm × 100 μm were acquired using the tapping mode at a scan rate of 0.5 Hz. Surface topography was recorded with a standard silicon tapping tip on a beam cantilever, and R_{rms} was calculated from the height profiles using the Nanoscope 7.30 software (Veeco Instruments, Santa Barbara, CA). To characterize surface hydrophilicity, water contact angles were determined using the ImageJ software (National Institutes of Health, Bethesda, MD) 30 s after 20 μL of distilled water (pH = 7.0) was injected onto the film surface at 37 °C using

a Ramé-Hart NRC C.A. goniometer (Model 100-00-230, Mountain Lakes, NJ). Polymer films were peeled off from the substrates and attached onto flat glass slips and three samples were used for each surface to calculate the average and standard deviation.

7.2.2 Protein adsorption.

All the polymer films were washed by deionized water and exposed under ultraviolet (UV) light for 24 h to be sterilized before protein adsorption and cell studies. Then the films were soaked for 4 h at 37 °C in the culture medium for MC3T3-E1 cells, i.e., α-Minimum Essential Medium (α-MEM; Gibco, Grand Island, NY) supplemented with 10% fetal bovine serum (FBS; HyClone, Thermal Scientific) and 1% penicillin/ streptomycin (Gibco). Then the polymer films were washed three times using 600 μL of phosphate buffered saline (PBS) with 10 min of gentle agitation. Then each film was immersed in 300 μL of 1% sodium dodecyl sulfate (SDS) solution for 1 h three times. The total concentration of adsorbed serum proteins in the collected SDS solution was determined using a MicroBCA protein assay kit (Pierce, Rockford, IL) on a microplate reader (SpectraMax Plus 384, Molecular Devices, Sunnyvale, CA). The protein concentration was correlated with the UV absorbance of the SDS solution at 562 nm, based on a calibration curve constructed using solutions of albumin in the kit with known concentrations.

7.2.3 *In vitro* MC3T3-E1 cell attachment and proliferation.

MC3T3-E1 cell (CRL-2593, ATCC, Manassas, VA) attachment and proliferation were examined on the top and bottom surfaces of the polymer films crystallized on different substrates. The polymer films were attached onto the well bottom of 24-well plates using autoclaved inert silicon-based vacuum grease (Dow Corning, Midland, MI). MC3T3-E1 cells were seeded on the polymer films and tissue-culture polystyrene (TCPS) positive control wells at a density of ~15,000 cells/cm^2. After 4 h, 1, 2, and 4 days, a colorimetric cell metabolic assay (CellTiter 96 Aqueous

One Solution, Promega, Madison, WI) was performed in each well to obtain the number of viable cells by correlating it to the UV absorbance of the solution at 490 nm measured on the microplate reader, with assistance of a standard curve constructed using known cell numbers. The polymer films with attached cells were washed twice with PBS, fixed in 4% paraformaldehyde (PFA) solution for 10 min, and then permeabilized with 0.2% Triton X-100 for 10 min at room temperature. The filaments in cytoplasm were stained using rhodamine-phalloidin (RP) for 1 h at 37 °C and cell nuclei were stained using 4′,6-diamidino-2-phenylindole (DAPI) at room temperature for 5 min. Then the cells were photographed using an Axiovert 25 light microscope (Carl Zeiss, Germany), and cell spread area was determined using ImageJ and averaged over 15 non-overlapping cells at day 1.

7.2.4 Focal adhesions (FAs) in MC3T3-E1 cells.

As described in the last paragraph, MC3T3-E1 cells were cultured on the polymer films for 24 h and fixed and permeabilized, followed by incubated in 1% bovine serum albumin (BSA)/PBS for 1 h at 37 °C to block unspecific antibody binding sites. After being washed three times in PBS, the cells were treated with monoclonal mouse antibody against vinculin (1:1000 in PBS; Sigma) at room temperature with gentle shaking for 2 h, followed by washing three times with PBS again and then incubation at 37 °C for 2 h with goat anti-mouse IgG secondary antibody (1:200 in PBS; Sigma). The actin filaments of MC3T3-E1 cells were stained using RP at 37 °C for another 1 h prior to photographing on a Leica DM6000B fluorescent confocal microscope (Buffalo Grove, IL). The area, perimeter, density (defined as the number of FAs per cell) and elongation (defined as $\text{perimeter}^2/4\pi/\text{area}$) of the focal adhesions in MC3T3-E1 cells were determined and averaged over 15 non-overlapping cells using ImageJ.

7.2.5 Statistical analysis.

Protein adsorption and cell studies were performed in triplicates for each sample and each time point, and repeated to confirm the results. The student's *t*-test was performed to assess the statistical significance ($p < 0.05$) of the differences in the results between any two groups.

7.3 Results and Discussion

7.3.1 Surface roughness and hydrophilicity.

To prepare polymer films with sufficient mechanical strength and steady morphologies after detachment from the substrate and during the cell studies, the drop-coated polymer films were much thicker than the spin-coated ones and the film thickness was controlled to be 30-40 μm using the volume of polymer solution. PEG with a high molecular weight of 14,500 g/mol was used as it had similar melting temperature (T_m) [46] and was miscible with PCL. Then a uniform isothermal crystallization process could be used for both PCL and two PCL/PEG blends. Meanwhile, this high-molecular-weight PEG embedded in hydrophobic PCL had a low leaching-out rate during the cell studies. I checked the spherulitic structures under POM after immersing the polymer films into the culture medium and PBS at 37 °C for 4 days, and did not find evident changes compared with the original films. Thus, the PCL/PEG blends were considered stable in the duration of 4 days for the cell studies.

The spherulitic surfaces of PCL and PCL/PEG blends crystallized on different substrates were distinct in morphology, hydrophilicity, and roughness. As shown in the POM images in Figure 7.2, regular polymer spherulites with lamellar structures extending radially from nucleation sites were observed when the polymers were crystallized on glass and Si substrates. In contrast, significantly smaller spherulites were found in all the polymers crystallized on the PTFE substrate

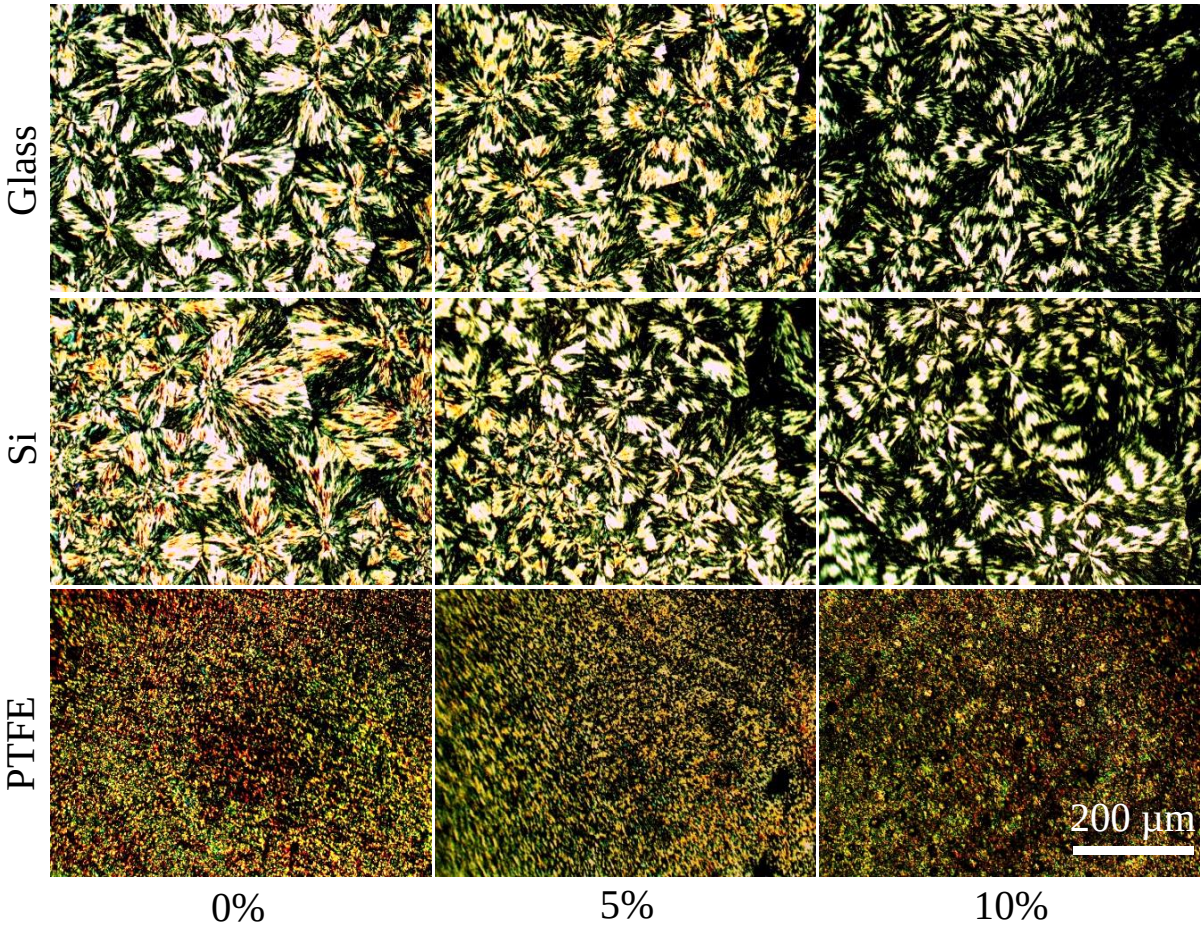

Figure 7.2 POM images of the spherulites on different substrates

as the result of epitaxial crystallization. The average diameter of the polymer spherulites on the glass and Si substrates were 180 and 160 μm, respectively, while the value on the PTFE substrate was hard to measure. In addition, there was no obvious difference between the spherulite structures of the same polymer on the glass and Si substrates, indicating the absence of epitaxial crystallization on these two inert, featureless inorganic substrates. The subtle differences in the spherulite size and roughness discussed later were believed to result from the differences in the surface roughness and wettability for glass clips and Si wafer. In contrast, the semi-crystalline PTFE substrate could provide much more nucleation centers for the polymers to crystallize from. Although it was impossible to monitor the real-time crystallization of the PCL and PCL/PEG blends on the opaque PTFE substrate through POM, I observed that the crystallization process was complete in less than 1 h, much shorter than 3-5 hours on the glass or Si substrates at the same T_c of 45 °C.

Unlike pure PCL, the miscibility was critical for the PCL/PEG blends, especially when the two components were semi-crystalline. PCL/PEG blends were considered as immiscible under certain circumstances by showing biphasic constructions [47-53]. In the present chapter, no obvious phase separation between PCL and PEG could be observed during crystallization. The result might be attributed to the low Φ_{PEG} of 5% and 10%, at which the PEG chains were included within the PCL spherulites rather than being excluded from them during isothermal crystallization. Instead of showing biphasic spherulites, uniform spherulites with more clearly banded structures could be seen on the glass and Si substrates when 5% or 10% PEG were added into PCL, which were also evidence for the miscibility between the two components [52-54].

It could be observed from the AFM images in Figure 7.3 that the bottom surfaces of PCL and PCL/PEG blends on the glass and Si substrates usually were less rough than the top surfaces. But

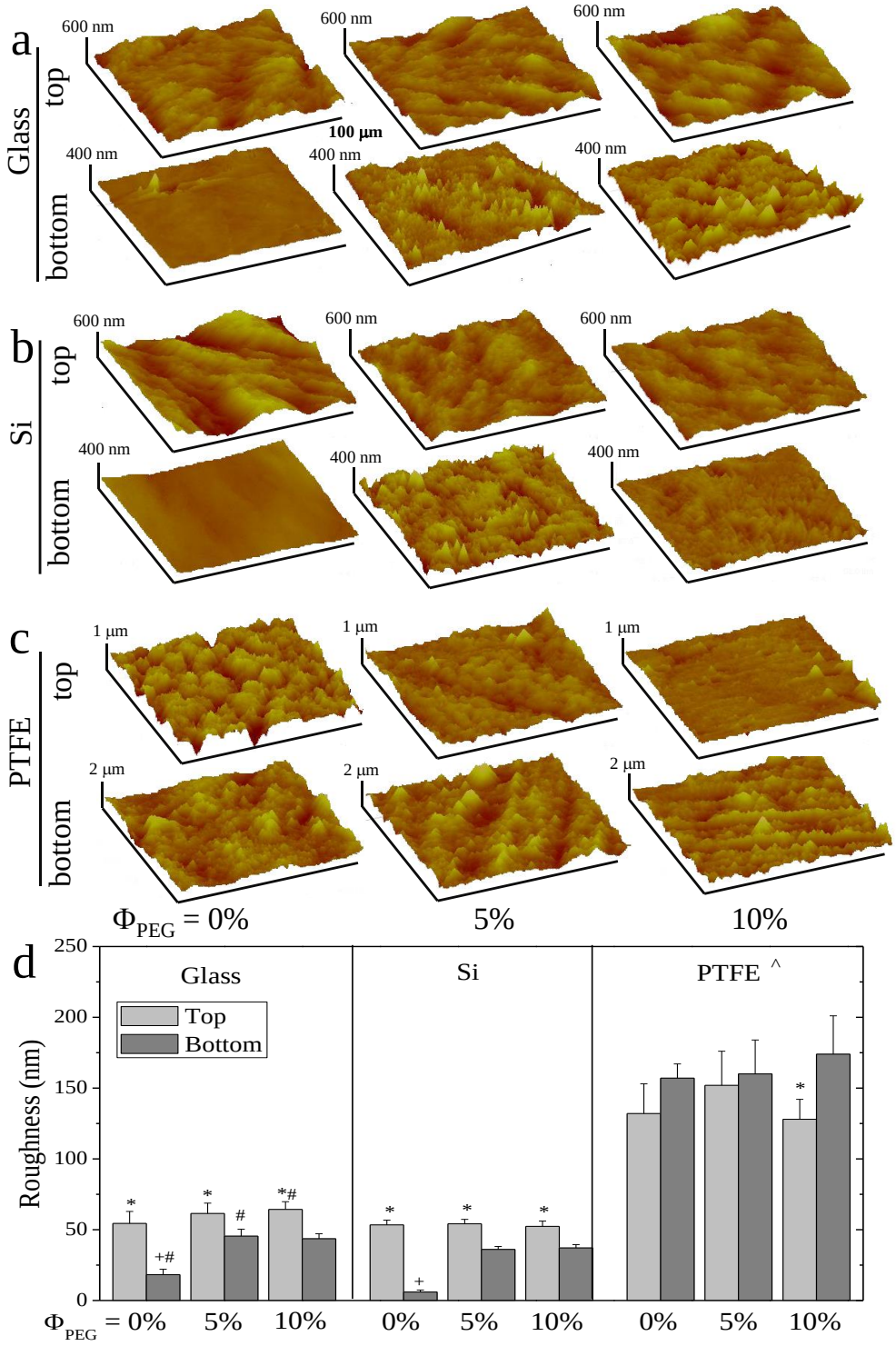

Figure 7.3 AFM images of the interfaces in the PCL/PEG films on glass (a), Si (b), and PTFE (c). The scale of the images is 100 µm. (d) Surface roughness of the polymer films. *: $p < 0.05$ relative to the bottom surface of the same film. +: $p < 0.05$ relative to the bottom surfaces of 5% and 10% films on same substrates. #: $p < 0.05$ relative to the Si counterparts. ^: $p < 0.05$ relative to the glass and Si counterparts.

for the polymer films crystallized on the PTFE substrate, the bottom surfaces were rougher than their top surfaces and all the surfaces on the glass and Si substrates. As indicated in Figure 7.3d and Table 7.1, the R_{rms} values of the polymer films on the PTFE substrate were at least two times higher than those on the glass and Si substrates. The surface of the PTFE substrate was much rougher than the glass and Si substrates. Moreover, the PTFE substrate used here was also semi-crystalline and could induce epitaxial crystallization of PCL and PCL/PEG blends, and thus the crystallized polymer films obviously differed from the regular spherulites. Addition of PEG resulted in rougher films, no matter on the top or bottom surfaces when the glass and Si substrates were used. In contrast, the differences were not significant on the PTFE substrate. The R_{rms} values of the films crystallized on the glass substrate were slightly higher than those on the Si substrate. Addition of hydrophilic PEG into more hydrophobic PCL increased the surface hydrophilicity and thus decreased the water contact angle (4-8 degrees with increasing Φ_{PEG}) (Figure 7.4a, and Table 7.1) on all the surfaces of the polymer films crystallized on all the substrates. It should also be noted that almost all the bottom surfaces were more hydrophilic than their corresponding top surfaces, in particular, when on the glass and Si substrates.

7.3.2 Protein adsorption.

The ability to adsorb serum proteins from culture medium is important for later cell responses to the material and it can be influenced by surface morphology, roughness, and hydrophilicity [55]. As shown in Figure 7.4b, the total amounts of adsorbed proteins on the surfaces of the polymer films crystallized on the PTFE substrate were significantly higher than the corresponding surfaces obtained from the glass and Si substrates, especially for the PCL/PEG blends. Addition of PEG into PCL improved protein adsorption on the both surfaces of the polymer films, especially on the bottom surfaces. This result was different from the previous reports that PEG could reduce protein

Table 7.1 Surface roughnesses and water contact angles of the polymer samples

	sample	Glass		Si		PTFE	
		R_{rms} (nm)	Contact angle (º)	R_{rms} (nm)	Contact angle (º)	R_{rms} (nm)	Contact angle (º)
top	PCL	54.4 ± 8.5	74 ± 1	53.4 ± 3.4	76 ± 1	132 ± 21	74 ± 2
	PCL/PEG 5%	61.4 ± 7.3	70 ± 1	54.2 ± 3.1	72 ± 1	152 ± 24	70 ± 1
	PCL/PEG 10%	64.3 ± 5.5	69 ± 1	52.4 ± 3.7	69 ± 1	128 ± 14	67 ± 2
bottom	PCL	18.2 ± 4.0	70 ± 1	6.0 ± 1.4	71 ± 1	157 ± 10	72 ± 1
	PCL/PEG 5%	45.4 ± 5.0	65 ± 1	36.1 ± 2.0	64 ± 2	160 ± 24	68 ± 1
	PCL/PEG 10%	43.6 ± 3.5	63 ± 1	37.1 ± 2.3	64 ± 1	174 ± 27	68 ± 1

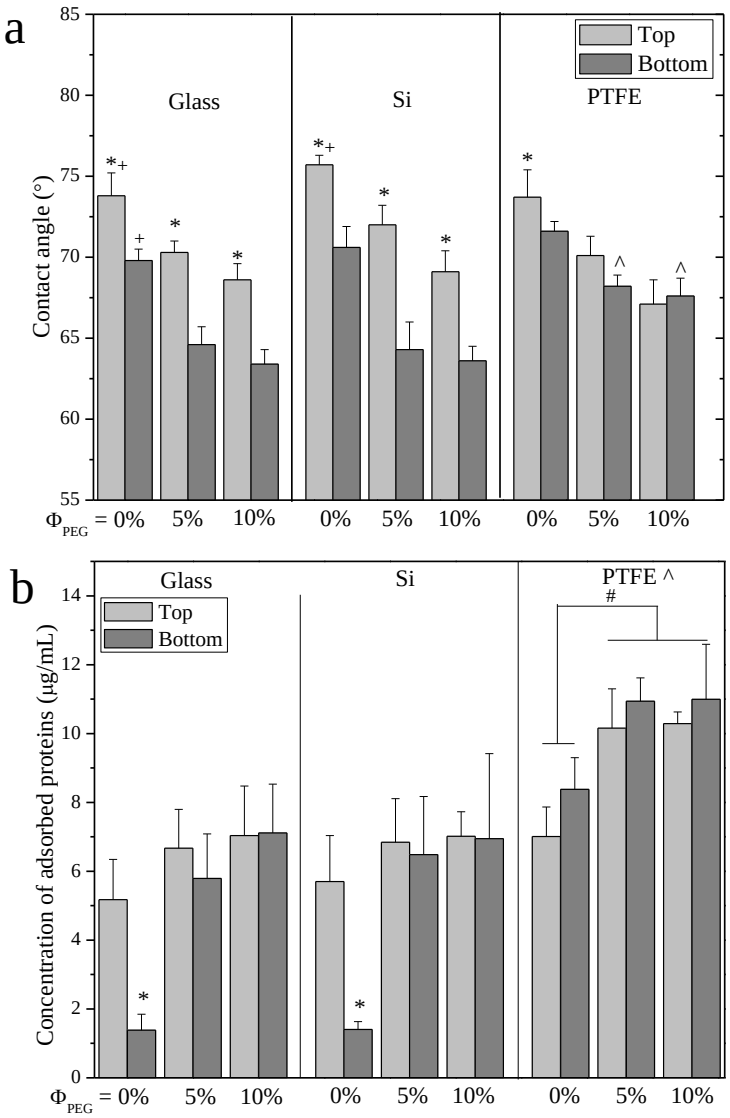

Figure 7.4 (a) Water contact angles of the polymer films. *: $p < 0.05$ relative to the bottom surface of the same film. +: $p < 0.05$ relative to the top or bottom surfaces of 5% and 10% films on same substrates. ^: $p < 0.05$ relative to the glass and Si counterparts. (b) Protein adsorptions of the polymer films. *: $p < 0.05$ relative to the 0% top surface, 5% and 10% bottom surfaces on same substrates. #: $p < 0.05$ between any two samples marked with the same symbol. ^: $p < 0.05$ relative to the glass and Si counterparts except the 0% top.

adsorption [56,57], because the PEG used in this chapter had a high molecular weight and crystallized together with PCL to form an intertwined lamellar structure. The bottom surfaces of the PCL/PEG films crystallized on the glass and Si substrates usually had similar amounts of adsorbed serum proteins but the ones for the significantly smoother PCL films obtained from the glass and Si substrates had much lower values of 1.25 ± 0.42 and 1.26 ± 0.20 μg/cm^2, respectively. Based on these results, the increment in protein adsorption could be attributed to rougher surfaces with larger areas. Moreover, addition of PEG increased the surface hydrophilicity to make it easier to wet the film surfaces in the culture media but did not prohibit protein adsorption.

7.3.3 Cell attachment and proliferation.

To explore how MC3T3-E1 cells respond to the top and bottom surfaces of the PCL and PCL/PEG blend films crystallized from three different substrates, extensive characterizations of cell attachment, proliferation, and focal adhesions were performed in the duration of 4 days. Figure 7.5a shows actin filaments stained with RP and nuclei stained with DAPI of MC3T3-E1 cells at day 2 on the films. MC3T3-E1 cell attachment was monitored at 4 h post-seeding by normalizing the cell numbers on the samples to the TCPS positive control value. As shown in Figures 7.5a and and 7.5b, MC3T3-E1 cell attachment and proliferation over 4 days, represented by the cell densities at 4 h, days 1, 2, and 4, were better on the top surfaces than on the bottom surface for all these three polymer samples when the glass and Si substrates were used. In contrast, no significant differences in the cell attachment and proliferation were found between the two surfaces and among these three polymer samples when the PTFE substrate was used. Addition of PEG into PCL improved MC3T3-E1 cell attachment and proliferation on all the interfaces, and the effect was more prominent when Φ_{PEG} was higher, 10%. Representative fluorescence images of the MC3T3-E1 cells in Figure 7.5a were consistent with the cell densities in Figure 7.5c. From the images, I

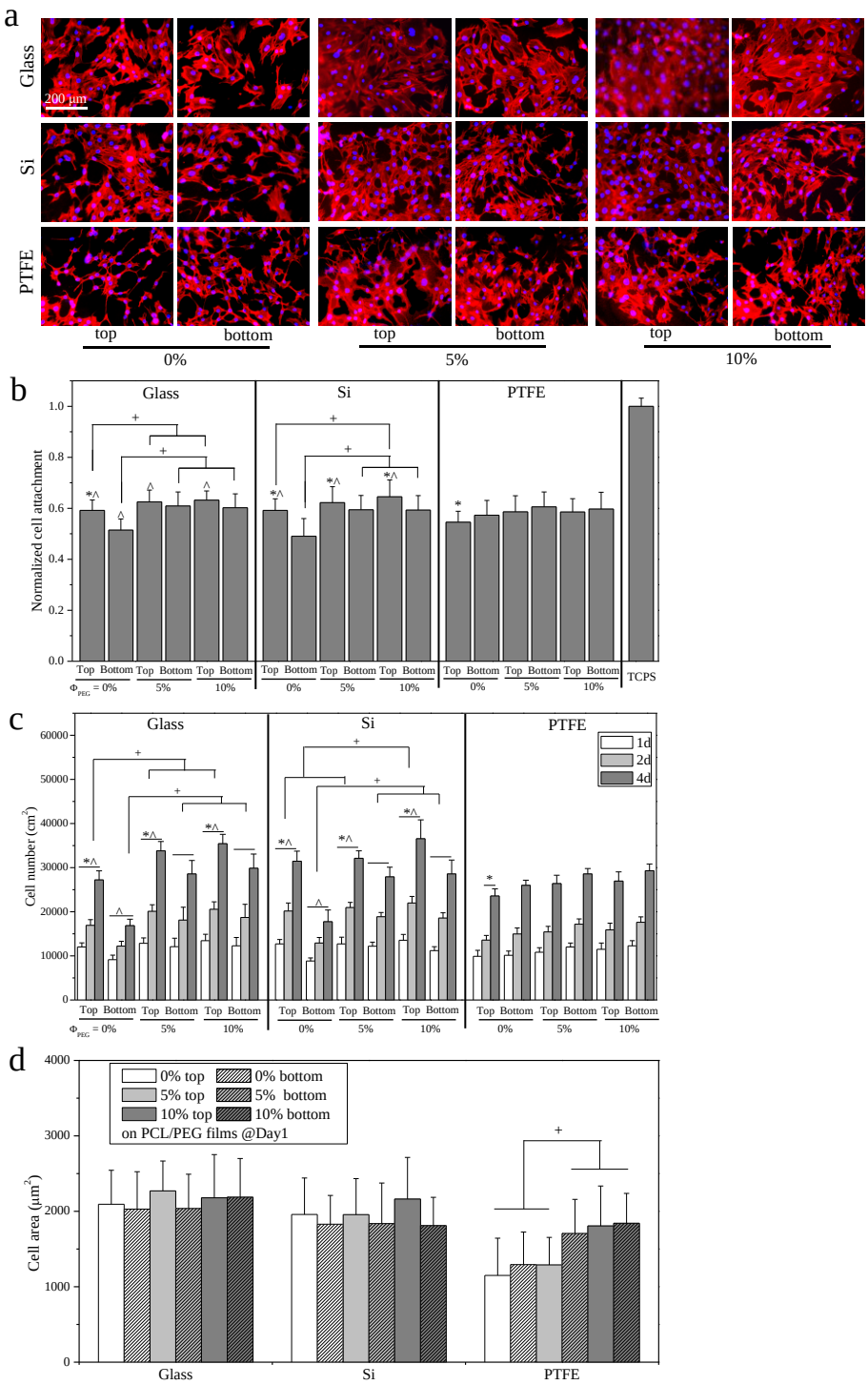

Figure 7.5 (a) Fluorescent images of MC3T3-E1 cells stained with RP (red) and DAPI (blue) on the PCL/PEG films at day 2 post-seeding. Scale bar of 200 µm is applicable to all. (b) Normalized MC3T3-E1 cell attachment at 4 h post-seeding on the PCL/PEG films. (c) MC3T3-E1 cell proliferation indicated by cell numbers at days 1, 2, and 4 post-seeding on the PCL/PEG films. (d) MC3T3-E1 cell areas at day 1 post-seeding on PCL/PEG films. *: $p < 0.05$ relative to the bottom surface of the same film. +: $p < 0.05$ between two samples marked with the same symbol. ^: $p < 0.05$ relative to the PTFE counterparts.

also found that the cell spreading at day 1 quantified as cell spread areas in Figure 7.5d followed the similar trend with the cell attachment and proliferation. When the glass and Si substrates were used, the cell spread area did not show significant difference with an average cell area of ~2000 μm^2. However, when the PTFE substrate was used, the cell areas were significantly smaller on the top and bottom surfaces of PCL and the top surface of the PCL/PEG (Φ_{PEG} = 5%) films than on the other surfaces.

7.3.4 Focal adhesions.

FAs are dynamic anchoring protein complexes mostly located at the cell periphery to provide a structural connection between the internal cytoskeleton and the extracellular substrates [58]. Upon receiving mechanical stimulation, FAs adjust their morphology and size to form various adhesion subtypes and simultaneously trigger signal transductions that relate to cell growth, spreading, and migration [59,60]. The FAs in the MC3T3-E1 cells were stained green using immunofluorescent monoclonal vinculin primary antibody and the F-actin in cytoplasm was stained red using RP, as shown in Figures 7.6a, 7.6b and 7.6c. Compared to the bottom surfaces when glass and Si substrates were used, on which the FAs were less dense and mainly distributed on cell periphery, FAs on top surfaces were denser, and located both on cell periphery and inside cell body. Increasing the Φ_{PEG} also caused the FA denser. FA density, area, and elongation were quantified, as shown in Figures 7.6d, 7.6e and 7.6f. A similar trend was found in FA density and area as in MC3T3-E1 cell attachment and proliferation. Higher FA densities and areas were observed on the top surfaces than on the corresponding bottom surfaces when the glass and Si substrates were used. Addition of PEG into PCL increased FA density and area on all the surfaces and the increment was more prominent at the higher Φ_{PEG} of 10%. The difference in FA area was insignificant among the surfaces when the PTFE substrate was used except the bottom surfaces of

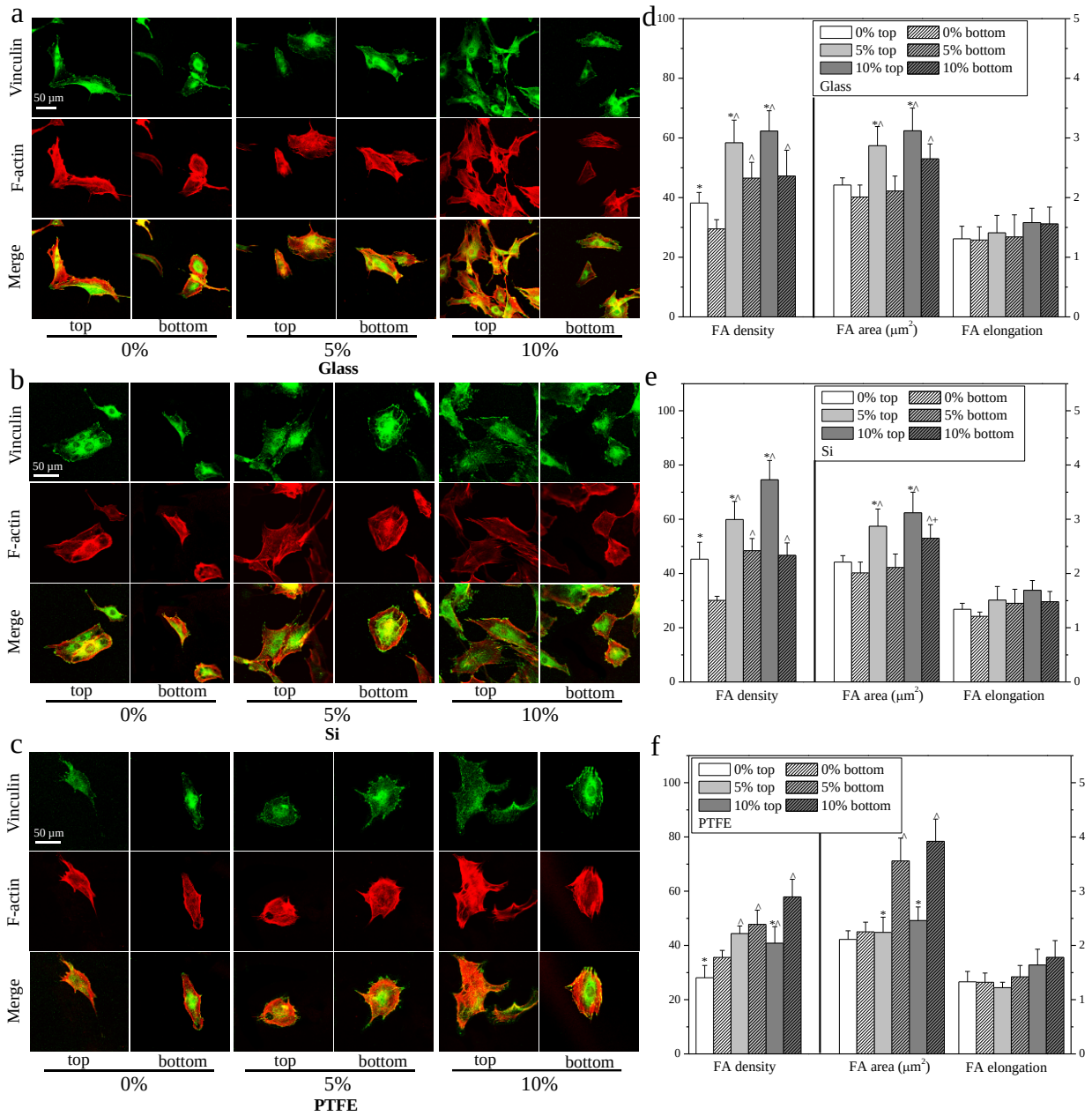

Figure 7.6 Confocal microscope images of MC3T3-E1 cell filaments and vinculin antibody stained focal adhesions, on the surfaces of the PCL/PEG films crystallized on the (a) glass, (b) Si, and (c) PTFE substrates. Scale bar of 50 µm is applicable to all. (d-f) FA density, FA area, and FA elongation of the MC3T3-E1 cell of a-c, respectively. *: $p < 0.05$ relative to the bottom surface of the same film. ^: $p < 0.05$ relative to the top or bottom surfaces of 0% films on same substrates. +: $p < 0.05$ relative to the bottom surface of 5% films on same substrates.

PCL/PEG films, on which significantly higher FA areas were found, especially at Φ_{PEG} of 10%. For all the surfaces and all the substrates, FA elongation (~1.46) did not show any significant difference.

7.3.5 Further discussion.

Epitaxial crystallization has been a method to regulate the microstructures of polymer thin films. Nucleation during epitaxial crystallization is promoted by surfaces of foreign bodies, which is called heterogeneous nucleation, while the nucleation during isothermal crystallization is called homogeneous nucleation [18-25,61,62]. Owing to the special intermolecular interactions between the overgrowth and the substrate crystal planes, the morphology, structure, and even the kinetics of the overgrowth polymers can be controlled [18-25]. High-orientated PTFE, isotactic polypropylene (iPP), and HDPE are commonly used to cause epitaxial crystallization [23-25,61]. To our best knowledge, for the first time three important factors were found in regulating MC3T3-E1 cell behavior: epitaxial crystallization, surface segregation, and top (free)/bottom (confined) surfaces. The significance of this chapter lies in the fact that the substrate for preparing polymer films and different interfaces can be critical in determining the surface properties and cell-material interactions. Without inducing epitaxial crystallization of PCL and PCL/PEG blends, glass and Si substrates were similar in regulating the characteristics of the top and bottom surfaces and MC3T3-E1 cellular responses. Unlike glass and Si substrates, the PTFE substrate induced epitaxial crystallization, as demonstrated by the significantly smaller spherulites, which in turn significantly affected MC3T3-E1 cell attachment, proliferation, and FAs.

Moreover, surface segregation and enrichment of PEG could occur in films at 37 °C and played an important role in determining the cell fate. In general, a polymer with a higher mobility is liable to appear on the top surface when it is blended with another polymer with a lower mobility

[29,63,64]. In our previous report, for hetero-blends composed of PCL and polypropylene fumarate (PPF) and homo-blends composed of two PCLs with molecular weights of 80k and 2k, the high-mobility component of amorphous, low-molecular-weight, and low glass transition temperature (T_g) PPF or the lower-molecular-weight PCL could dramatically inhibit cell attachment and proliferation even when its composition was low [12,65]. In this chapter, both the top and bottom interfaces of the PCL/PEG blend films could be rich of PEG at 37 °C, evidenced by the significantly decreased water contact angle compared with the corresponding surfaces with pure PCL on the same substrates. Meanwhile, the bottom surfaces of the PCL/PEG films showed higher PEG enrichment, especially when glass and Si were used as the substrates, as the water contact angles on them were much smaller than their corresponding top surfaces. When super-hydrophobic PTFE was used as the substrate, the difference in the water contact angle between the top surface and the bottom surface was smaller and the values on the bottom surfaces of the PCL/PEG films were much higher than those ones from the glass and Si substrates. This finding might suggest that low-surface-energy PTFE preferred to attract more hydrophobic component, i.e., PCL, from the PCL/PEG blends.

Beside the surface segregation effect in inducing different surface hydrophilicity, I also found that even the top and bottom surfaces of pure PCL films were different. The reason might be that, unlike the top free interface showing a water contact angle of ~74° for high-molecular-weight PCL [66,67], the bottom surface was confined by the substrate and this confinement might affect chain orientation and distribution of the amorphous moiety of the polymer chain.

7.4 Conclusions

The spherulitic top and bottom surfaces of PCL and PCL/PEG blends crystallized on the glass, Si, and PTFE substrates have been studied. Regular spherulites were observed in the polymers crystallized on the glass and Si substrates, while significantly smaller spherulites were found on the PTFE substrate as the result of epitaxial crystallization. Addition of 5% or 10% PEG into PCL resulted in more hydrophilic and rougher films, which could adsorb more serum proteins from the culture media. The films crystallized on the PTFE substrates had rougher surfaces and better protein adsorption. Bottom surfaces of the polymer films when glass and Si were used as substrates had lower surface roughness, lower water contact angle and lower protein adsorption than corresponding top surfaces. Only the top and bottom surfaces of pure PCL films had significant difference in protein adsorption. Moreover, bottom surfaces of the polymer films when PTFE was used as substrates were slightly rougher, and had slightly lower water contact angle and higher protein adsorption than top surfaces. Addition of 5% or 10% PEG into PCL improved MC3T3-E1 cell attachment, proliferation, and FAs on all the surfaces. Distinct MC3T3-E1 cell attachment, proliferation, and FAs were found on the top and bottom surfaces of the polymer films when glass and Si were used as substrates, while there were no significant differences between the top and bottom surfaces when PTFE was used as the substrate. MC3T3-E1 cells attached and proliferated better, and had better FAs on the top surfaces of the polymer films crystallized on the glass and Si substrates than those on the films crystallized on the PTFE substrate.

References

1. Harbers, G. M.; Grainger, D. W. Cell-material interactions: fundamental design issues for tissue engineering and clinical considerations. In *Introduction to biomaterials*; Guelcher, S. A., Hollinger, J. O., Eds.; CRC Press, 2005; Boca Raton, FL, pp15-45.

2. Saltzman, W. M.; Kyriakides, T. R. Cell interactions with polymers. In *Principles of Tissue Engineering*; Lanza, R., Langer, R., Vacanti, J., Eds.; 3rd ed. Elsevier Academic Press, 2007; San Diego, CA, pp 279-296.

3. Peyton, S. R.; Putnam, A. J. *J. Cell Physiol.* **2005**, *204(1)*, 198-209.

4. Discher, D. E.; Janmey, P.; Wang, Y. L. *Science* **2005**, *310(5751)*, 1139-1143.

5. Curtis, A.; Wilkinson, C. *Biomaterials* **1997**, *18(24)*,1573-1583.

6. Flemming, R. G.; Murphy, C. J.; Abrams, G. A.; Goodman, S. L.; Nealey, P. F. *Biomaterials* **1999**, *20*, 573-588.

7. Bettinger, C. J.; Langer, R.; Borenstein, J. T. *Angew. Chem., Int. Ed.* **2009**, *48*, 5406-5415.

8. Wang, K.; Cai, L.; Zhang, L.; Dong, J.; Wang, S. *Adv. Healthcare Mater.* **2012**, *1*, 292-301.

9. Cai, L.; Zhang, L.; Dong, J.; Wang, S. *Langmuir* **2012**, *28*, 12557-12568.

10. Henry, M. G.; Cai, L.; Liu, X.; Zhang, L.; Dong, J.; Chen, L.; Wang, Z.; Wang, S. *Langmuir* **2015**, *31*, 2851-2860.

11. Wu, X.; Wang, S. *Polymer* **2014**, *55*, 1756-1762.

12. Wang, K.; Cai, L.; Jesse, S.; Wang, S. *Langmuir* **2012**, *28*, 4382-4395.

13. Keller, A. *J. Polym. Sci.* **1955**, *17*, 291-308.

14. Chen, H. L.; Li, L. J.; Ou-Yang, W. C.; Hwang, J. C.; Wong, W. Y. *Macromolecules* **1997**, *30*, 1718-1722.

15. Phillips, P. J.; Rensch, G. J.; Taylor, K. D. *J. Polym. Sci., Part B: Polym. Phys.* **1987**, *25*, 1725-1740.

16. Ong, C. J.; Price, F. P. *J. Polym. Sci. Polym. Symp.* **1978**, *63*, 45-58.

17. Mareau, V. H.; Prud'Homme, R. E. *Macromolecules* **2002**, *35*, 5338-5341.

18. Schonhorn, H.; Drobek, J. *Science* **1968**, *162*, 1483-1484.

19. Kim, J.; Cho, J.; Ryba, E.; Bai, J. *Polym. J.* **2003**, *35*, 929-937.

20. Schonhorn, H. *Macromolecules* **1968**, *1(2)*, 145-151.

21. Chatterjee, A. M.; Price, F. P.; Newman, S. *J. Polym. Sci., Part B: Polym. Phys.* **1975**, *13*, 2369-2383.

22. Fitchmun, D.; Newman, S. *J. Polym. Sci., Part B: Polym. Lett.* **1969**, *7*, 301-305.

23. Luongo, J. P.; Schonhorn, H. *J. Polym. Sci., Part A-2: Polym. Phys.* **1968**, *6*, 1649-1658.

24. Chatterjee, A. M.; Price, F. P.; Newman, S. *J. Polym. Sci., Part B: Polym. Phys.* **1975**, *13*, 2385-2390.

25. Chatterjee, A. M.; Price, F. P.; Newman, S. *J. Polym. Sci., Part B: Polym. Phys.* **1975**, *13*, 2391-2400.

26. Wang, Z.; Alfonso, G. C.; Hu, Z.; Zhang, J.; He, T. *Macromolecules* **2008**, *41*, 7584-7595.

27. Woo, E. M.; Mandal, T. K.; Lee, S. C. *Colloid Polym. Sci.* **2000**, *278*, 1032-1042.

28. Wang, Z.; Jiang, B. *Macromolecules* **1997**, *30*, 6223-6229.

29. Cheung, Z. L.; Weng, L. T.; Chan, C. M.; Hou, W. M.; Li, L. *Langmuir* **2005**, *21*, 7968-7970.

30. Su, C. C.; Lin, J. H. *Colloid Polym. Sci.* **2004**, *283*(2), 182-193.

31. Neo, M. K.; Goh, S. H. *Eur. Polym. J.* **1991**, *27*(9), 927-930.

32. Yam, W. Y.; Ismail, J.; Schmidt, H.; Kummerlöwe, C. *Polymer* **1999**, *40*(20), 5545-5552.

33. Chang, H.; Zhang, J.; Li, L.; Wang, Z.; Yang, C.; Takahashi, I.; Ozaki, Y.; Yan, S. *Macromolecules* **2009**, *43*(1), 362-366.

34. Liu, J.; Li, H.; Yan, S.; Xiao, Q.; Petermann, J. *Colloid Polym. Sci.* **2003**, *281*(7), 601-607.

35. Beekmans, L. G. M.; Vallée, R.; Vancso, G. J. *Macromolecules* **2002**, *35*(25), 9383-9390.

36. Wang, Y.; Jiang, S.; Shi, H.; Zhang, W.; Qiao, J.; Wu, M.; Tian, Y.; Niu, Z.; Huang, Y. *Chem. Comm.* **2013**, *49*(88), 10421-10423.

37. Lee, J. H.; Lee, H. B.; Andrade, J. D. *Prog. Polym. Sci.* **1995**, *20*, 1043-1079.

38. Chaikof, E. L.; Merrill, E. W.; Callow, A. D.; Connolly, R. J.; Verdon, S. L.; Ramberg, K. *J. Biomed. Mater. Res.* **1992**, *26*, 1163-1168.

39. Nagaoka, S.; Mori, Y.; Takiuchi, H.; Tanzawa, H.; Nishiumi, S. Interaction between blood components and hydrogels with poly(oxyethylene) chains. In *Polymers as biomaterials*: Shalaby, S. W., Hoffman, A. S., Ratner, B. D., Horbett, T. A., Eds; Plenum Press, 1984; New York, pp 361-374.

40. Mougin, K.; Lawrence, M. B.; Fernandez, E. J.; Hillier, A. C. *Langmuir* **2004**, *20*, 4302-4305.

41. Gautam, K. S.; Schwab, A. D.; Dhinojwala, A.; Zhang, D.; Dougal, S. M.; Yeganeh, M. S. *Phys. Rev. Lett.* **2000**, *85*, 3854.

42. Gautam, K. S.; Dhinojwala, A. *Phys. Rev. Lett.* **2002**, *88*, 145501.

43. Li, G.; Dhinojwala, A.; Yeganeh, M. S. *J. Phys. Chem. B* **2009**, *113*, 2739-2747.

44. Kline, R. J.; McGehee, M. D.; Toney, M. F. *Nat. Mater.* **2006**, *5*, 222-228.

45. Coulon, G.; Russell, T. P.; Deline, V. R.; Green, P. F. *Macromolecules* **1989**, *22*, 2581-2589.

46. Lin, W. J.; Lu, C. H. *J. Membrane Sci.* **2002**, *198*(1), 109-118.

47. Chuang, W. T.; Shih, K. S.; Hong, P. D. *J. Polym. Res.* **2005**, *12*(3), 197-204.

48. Huo, H.; Guo, C.; Zhou, J.; Zhao, X. *Colloid Polym. Sci.* **2014**, *292*(4), 971-983.

49. Hou, W. M.; Zhou, J. J.; Gan, Z. H.; Shi, A. C.; Chan, C. M.; Li, L. *Polymer* **2007**, *48*(17), 4926-4931.

50. Chuang, W. T.; Jeng, U. S.; Hong, P. D.; Sheu, H. S.; Lai, Y. H.; Shih, K. S. *Polymer* **2007**, *48*(10), 2919-2927.

51. Qiu, Z.; Ikehara, T.; Nishi, T. *Polymer* **2003**,*44*(10), 3101-3106.

52. Causa, A.; Filippone, G.; Domingo, C.; Salerno, A. *RSC Advances* **2015**, *5*(73), 59354-59363.

53. Luo, C.; Chen, W.; Gao, Y. *Polym. Sci. Ser. A* **2016**, *58*(2), 196-205.

54. Wang, S.; Lu, L.; Gruetzmacher, J. A.; Currier, B. L.; Yaszemski, M. J. *Macromolecules* **2005**, *38*(17), 7358-7370.

55. Lord, M. S.; Foss, M.; Besenbacher, F. *Nano Today* **2010**, *5*, 66-78.

56. Jo, S.; Park, K. *Biomaterials* **2000**, *21*(6), 605-616.

57. Lazos, D.; Franzka, S.; Ulbricht, M. *Langmuir* **2005**, *21*(19), 8774-8784.

58. Burridge, K.; Chrzanowska-Wodnicka, M. *Annu. Rev. Cell Dev. Biol.* **1996**, *12*, 463-519.

59. Parsons, J.T.; Horwitz, A.R.; Schwartz, M. A. *Nat. Rev. Mol. Cell Biol.* **2011**, *11*, 633-643.

60. Zamir, E.; Geiger, B. *J. Cell Sci.* **2001**, *114*, 3583-90.

61. Mauritz, K. A.; Baer, E.; Hopfinger, A. J. *J. Polym. Sci.-Macromol. Rev.* **1978**, *13*(1), 1-61.

62. Takahashi, T.; Inamura, M.; Tsujimoto, I. *J. Polym. Sci., Part B: Polym. Lett.* **1970**, *8*(9), 651-657.

63 Bhatia, Q. S.; Pan, D. H. K.; Koberstein, J. T. *Macromolecules* **1988**, 21, 2166-2175.

64 Nishino, T.; Matsumoto, T.; Nakamae, K. *Polym. Eng. Sci.* **2000**, *40*, 336-343.

65. Wang, K.; Cai, L.; Hao, F.; Xu, X.; Cui, M.; Wang, S. *Biomacromolecules* **2010**, *11*, 2748-2759.

66. Cai, L.; Lu, J.; Sheen, V.; Wang, S. *Biomacromolecules* **2012**, *13*, 358-368.

67. Cai, L; Wang, S. *Polymer* **2010**, *51*, 164-177.

Chapter VIII. Smooth Muscle Cell Responses to PHB Spherulites

Abstract

Banded spherulites with concentric alternating succession of ridges and valleys were observed on poly(3-hydroxybutyrate) (PHB) films when they were isothermally crystallized at certain temperatures. Their thermal properties and surface morphology (spherulites and cracks) were examined. The melting temperatures and crystallinity degrees did not vary much, while the surface roughness of the spherulites was higher when crystallization temperature was higher. *In vitro* rat primary aortic smooth muscle cell (SMC) attachment, proliferation, alignment and nuclear morphologies were assessed on the hot-compressed flat films and spherulites-roughened films of PHB. The number of attached SMCs and the proliferation rate were smaller on the rougher surfaces, and the highest values were on the flat films. Although cracks were found on all the spherulitic PHB films, cells only had obvious alignment along the circular cracks. Roughness and cracks did not affect cell nuclear localization and morphology.

8.1 Introduction

Semi-crystalline polymeric biomaterials such as poly(ε-caprolactone) (PCL) and poly(L-lactic acid) (PLLA) can crystallize into non-banded and banded spherulitic surfaces for investigating cell-substrate interactions [1-4]. Polyhydroxyalkanoates (PHAs) are a group of bioderived and biodegradable polyesters, among which poly(3-hydroxybutyrate) (PHB) is a typical example with a glass transition temperature (T_g) of ~0 °C, a melting temperature (T_m) of ~175 °C, and a crystallinity of 60-90% [5-7]. Banded spherulites with regular concentric rings can be formed when PHB is crystallized isothermally and the crystallization temperature (T_c) can greatly affect the spherulitic morphologies and the band width in the banded structures [8-11].

Previously our research group has cultured mouse pre-osteoblastic MC3T3-E1 cells on the PCL spherulites and found that rougher banded spherulites induced higher cell attachment and proliferation and the peak-valley structure regulated nuclear distribution [1]. The banded spherulites of PHB were more regular than those of PCL under polarized optical microscopy (POM), and thus I explored to elucidate whether this advantage could be used to regulate cellular responses in a better defined manner. Unlike PHB thick disks in literature reports [12,13], here I used PHB thin films with controllable cracks that are liable to break and detach from their substrates. Flat, banded spherulitic, and non-banded spherulitic morphologies were prepared at different conditions by varying T_c and film thickness. Primary aortic smooth muscle cells (SMCs) were used to examine their responses to these different surface morphologies of PHB films. For the banded spherulitic morphologies, different cracks formed when the film thickness was different and then the effect of these cracks on SMC behavior was also investigated.

8.2 Experimental Section

8.2.1 Materials and sample preparation.

PHB was purchased from Sigma-Aldrich (Milwaukee, WI) and used as received. PHB solution was prepared by dissolving 1 g PHB into 10 mL of chloroform at 60 °C in reflux. PHB films were prepared by drop-casting PHB solution directly onto round glass coverslips and completely drying in vacuum. Then PHB films were melted at 190 °C for 10 min and then quickly transferred to a hot stage with a preset isothermal crystallization temperature (T_c = 45, 65, 80, and 90 °C). After crystallization was finished, the PHB films were cooled down to room temperature at 1 °C/min. The film thickness was controlled using the solution volume, which was ~25 μm for the samples crystallized at different T_cs, and ~45 μm for extra thicker films crystallized at T_c of 80 and 90 °C. Flat PHB films as the control group were prepared by compressing PHB melts between two polyimide films at 190 °C and cooled down to room temperature naturally, and the thickness of the flat PHB films was ~300 μm.

8.2.2 Polymer characterizations.

After PHB films were completely crystallized, their T_ms and crystallinities were determined using a TA Q2000 differential scanning calorimeter (DSC), through a heating ramp from room temperature to 200 °C at a rate of 10 °C/min in a dry nitrogen atmosphere. The crystalline structures of the PHB films were observed using POM (Nikon Optiphot-2, POL). At least 10 spherulites for each sample were measured and averaged to obtain the bandwidths and spherulite diameters. The surface morphologies of the polymer films were detected using a multimode atomic force microscope (AFM) with a Nanoscope III control system (Veeco Instruments, Santa Barbara, CA). A tapping mode over a scan area of 50 μm × 50 μm or 100 μm × 100 μm at a scan rate of 0.5 Hz was used. Root-mean square roughness (R_{rms}) was measured from the height images (five

images for each sample) using the Nanoscope 7.30 software (Veeco Instruments, Santa Barbara, CA).

8.2.3 *In vitro* SMC attachment, proliferation, and alignment.

Prior to cell studies, the dried PHB films were immersed in PBS for 10 min for cleaning and exposed under UV light for 24 h for sterilization. SMCs were cultured in a growth medium composed of Dulbecco's modified eagle medium (DMEM; Gibco, Grand Island, NY) supplemented with 10% fetal bovine serum (FBS; Sera-Tech, Germany) and 1% penicillin/streptomycin (Gibco) in an incubator with 5% CO_2 and 95% relative humidity at 37 °C. SMCs were seeded on the PHB films at a density of ~15000 cells/cm^2 and cultured for 4 h and 1, 2, and 4 days. A colorimetric cell metabolic assay (CellTiter 96 Aqueous One Solution, Promega, Madison, WI) was performed in each well to determine the number of attached cells by correlating to the UV absorbance of the solution at 490 nm measured on the microplate reader (SpectraMax Plus 384, Molecular Devices, Sunnyvale, CA). Cell numbers were then quantified using the standard curve that was constructed using known cell numbers. The cells attached on the PHB films were washed with PBS, fixed with 4% paraformaldehyde (PFA) solution for 10 min at room temperature, rinsed with PBS twice, and permeabilized with 0.2% Triton X-100 solution at room temperature for another 10 min. Cytoplasm was stained using rhodamine-phalloidin (RP) for 1 h at 37 °C and cell nuclei were stained using 4′,6-diamidino-2-phenylindole (DAPI) at room temperature. Then the cells were photographed using an Axiovert 25 light microscope (Carl Zeiss, Germany). Cell areas and circularities defined as $4\pi \times \text{area/perimeter}^2$ were determined by using ImageJ software and averaged over 25 non-overlapping cells at day 1. For scanning electron microscopy (SEM) imaging, the cells cultured on the flat PHB films and those crystallized at 80 °C (with or without circular cracks) for 1 day were fixed in 4% PFA for 10 min and rinsed with

PBS twice. Then the films were dehydrated with gradient ethanol solutions (30%, 50%, 70%, 95%, and 100%) for 20 min at each concentration and dried completely in vacuum. After being sputter-coated with a gold layer, the films were observed using SEM (S-3500, Hitachi Instruments, Tokyo, Japan) at an accelerating voltage of 5 kV.

8.2.4 Gene expression.

Polymerase chain reaction (PCR) was used to quantify the expression levels of contractile phenotypic markers of smoothlin, calponin, transgelin, and smooth muscle myosin heavy chain (SM-MHC) in SMCs cultured for 4 days on the flat PHB films and those crystallized at 80 ºC (with and without circular cracks). Total RNA was isolated using the RNeasy Mini Kit (Qiagen, Valencia, CA) and the cDNA was synthesized by reverse transcription using DyNAmo cDNA Synthesis Kit (Thermo Scientific, Waltham, MA). The primers for these gene markers were designed using Oligoperfect software, and their sequences are listed as follows. Smoothlin: forward 5'-TCGGAGTGCTGGTGAATAC-3', reverse 5'-CCCTGTTTCTCTTCCTCTGG-3'; calponin: forward 5'-AGTCTACTCTCTCTTGGCTCTGGCC-3', reverse 5'-CCTGCCTTCTCTCAGCTTCTCAGG-3'; transgelin: forward 5'-GGCAGCTGAGGATTATGGAGTCACG-3', reverse 5'-TGGGATCTCCACGGTAGTGTCCA-3'; SM-MHC: forward 5'-AAGCAGCTCAAGAGGCAG-3', reverse 5'-AAGGAACAAATGAAGCCTCGTT-3'; and house-keeping gene glyceraldehyde-3-phosphate dehydrogenase (GAPDH): forward 5'-TCTTCACCACCATGGAGAA-3', reverse 5'-ACTGTGGTCATGAGCCCTT-3'. Expression of these gene markers was quantified through PCR with Power SYBR Green PCR Master Mix (Applied Biosystems, Warrington, UK). The amplification and detection process was performed on a Peltier Thermal Cycler fluorescence detection system (MJ Research PTC-200). The software procedure was set as 94 ºC for 5 min

followed by the cyclic steps of 94 ºC for 30 s, 55 ºC for 30 s, and 72 ºC for 30 s. The expression levels of target gene markers were normalized to that of the GAPDH.

8.2.5 Statistical analysis.

Cell studies were performed in quadruplicates for each group at each time point. All values were expressed as mean ± standard deviation. The statistical significance ($p < 0.05$) in the difference between two groups was calculated using student's *t*-test.

8.3 Results and Discussion

8.3.1 Characterizations of PHB spherulites.

Figure 8.1a shows the DSC curves of the PHB samples after they were fully crystallized at different T_c of 45, 65, 80, and 90 °C, as well as the flat one crystallized at room temperature for determining the T_m and the heat of fusion (ΔH_m). The crystallinity (χ_c) of the PHB sample was calculated using the equation of $\chi_c = (\Delta H_m/\Delta H_m^c) \times 100\%$, where ΔH_m^c is 146 J/g for completely crystalline PHB [8]. The T_ms and χ_c values were 164.8, 162.3, 162.4, 163.0, and 162.7 °C, and 66.1%, 65.2%, 64.8%, 65.3%, and 61.4% for the flat PHB and PHB films with T_c of 45, 65, 80, and 90 °C, respectively. Both T_m and χ_c obtained from the DSC curves did not vary much when the sample was crystallized at different temperatures; however, the flat PHB had higher T_m and χ_c than other isothermally crystallized films. Normally a polymer can have a more ordered lamellar structure with higher values of T_m and χ_c when the crystallization is conducted slowly at a T_c slightly lower than its T_m. In the present chapter, even the highest isothermal T_c of 90 °C was still far below the T_m of ~175 °C and crystallization ended in a few minutes at all these four T_cs. The slightly higher values of T_m and χ_c for the flat PHB film might be attributed to its thicker dimension

and processing method of hot compression between glass plates. Since all the samples had similar crystallinities, identical density and stiffness were assumed among them in the discussion.

As demonstrated in Figure 8.1, POM was used to observe the crystalline structures of the PHB samples crystallized at different temperatures as well as its flat film. The flat PHB sample (Figure 8.1b) and the one crystallized at 45 °C (Figure 8.1c) showed small non-banded spherulites with an average diameter of ~40 μm. In contrast, banded spherulites because of lamellar twisting were formed on the freely crystallized samples when the T_c was 65, 80, or 90 °C with clear alternating dark and bright concentric rings and dark Maltese crosses especially when the T_c was 80 or 90 °C, as shown in Figures 8.1d-f [1,9,14]. The concentric rings are ridge-valley structures with a ridge-to-ridge band width or spacing that differs for different polymer types and can be regulated by the polymer composition and T_c [15]. The inner part of the flat PHB film still showed spherulites although the surface was smooth without typical spherulitic morphologies because of the confined crystallization. The bandwidth and spherulite diameter for the PHB films crystallized at 65 °C (Figure 8.1d) were 11.3 ± 0.8 and ~80 μm, respectively. For thin PHB films with the thickness of ~25 μm crystallized at 80 and 90 °C (Figures 8.1e and 8.1f), the bandwidths were 17.5 ± 4.6, and 35.2 ± 9.7 μm, and the diameters of the spherulites were ~460 and 780 μm, respectively. Increasing the film thickness to ~45 μm resulted in more the nucleation centers, thus reducing the spherulite diameter significantly to ~200 and ~360 μm, and meanwhile decreasing the band width slightly to 14.3 ± 2.3 and 24.5 ± 5.2 μm for the PHB films crystallized at 80 and 90 °C (Figures 8.1g and 8.1h), respectively.

Crystallized PHB thin films are usually brittle with inevitable cracks. As the result of the different radial and circumferential thermal expansion coefficients [11], there are two different center [10]. As reported in literature, the cracks can be controlled by T_c, film thickness, substrate

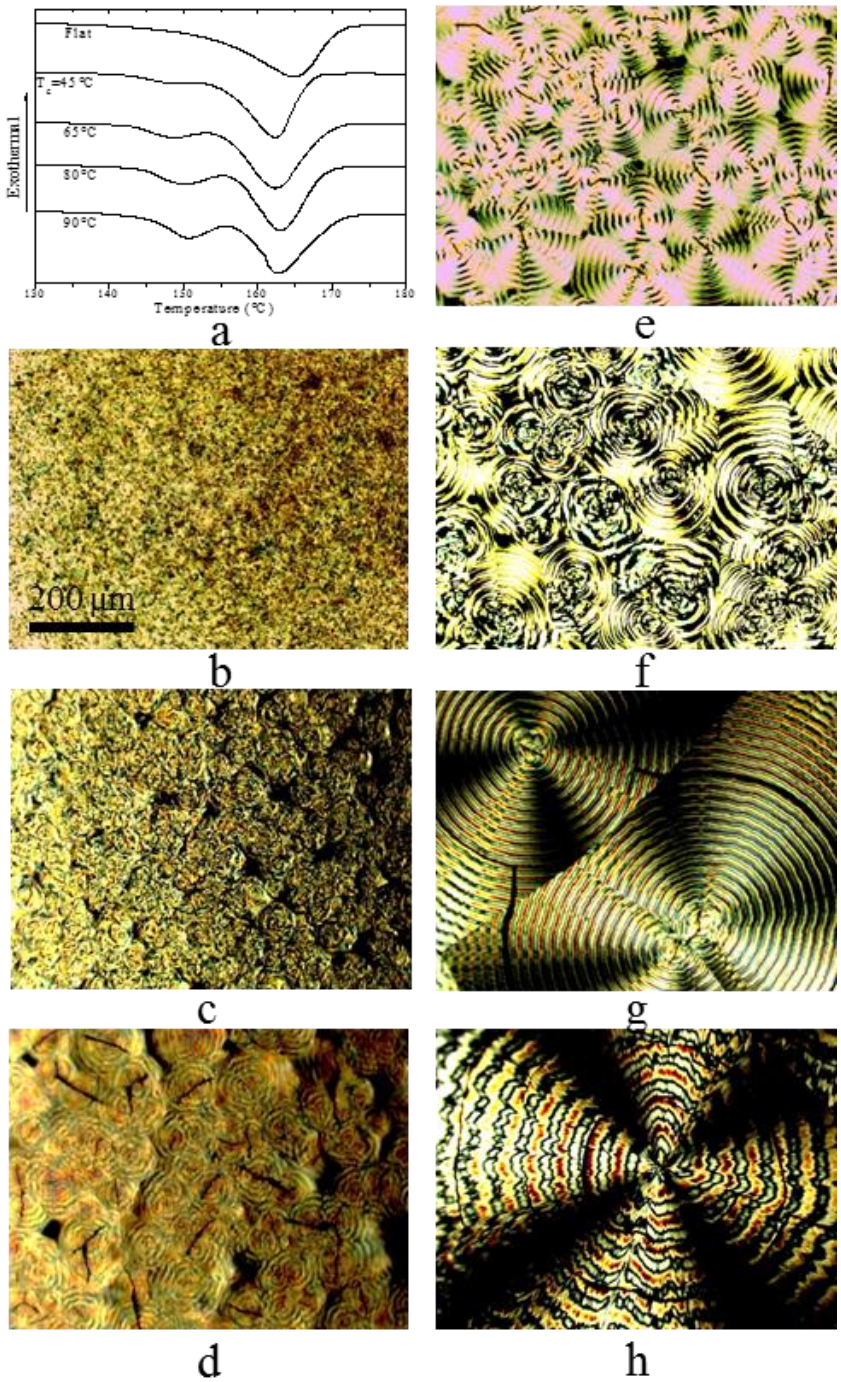

Figure 8.1 (a) DSC curves of PHB crystallized at different conditions. (b-h) POM images of the PHB spherulites crystallized with different conditions, T_c= b: 45 °C; c: 65 °C; d: 80 °C without circular cracks; e: 90 °C without circular cracks; g: 80 °C with circular cracks; h: 90 °C with circular cracks. Scale bar of 200 µm is applicable to all images.

type, and spherulite size [5,7,10,11]. During the crystallization of PHB and also in the later cooling at room temperature, small and narrow cracks grew and joined into long and wide ones. Long radial cracks in PHB spherulites could be minimized by lowering the cooling rate to 1 °C/min. However, circular cracks and radial cracks in the spherulite centers happened during the crystallization, regardless of the cooling rate (Figure 8.2). Circular cracks only formed when the spherulites were larger than a critical size (Figure 8.3), as also reported previously [7,10]. Thus, circular cracks were only found in large PHB spherulites obtained at T_c of 80 and 90 °C and when the film thickness was ~25 μm. At T_c of 80 °C, circular cracks (solid arrowhead in Figure 8.2d) with a length of 200-1500 μm either formed whole circles in a single spherulite or joined with the circular cracks in neighboring spherulites without being connected by radial cracks, as shown in Figures 8.3a and 8.3c. As indicated using a hollow arrow-head in Figure 8.2d, the radial cracks with a length of 10-50 μm in the spherulite centers had a width smaller than 1.5 μm and nearly did not extend to other cracks. At T_c of 90 °C, more radial cracks with a length of 20-50 μm appeared to connect with the circular cracks that had a length of 100-500 μm, as shown in Figures 8.3b and 8.3d. The width of the above-discussed cracks was ~2 μm with some larger exceptions of 9 μm. The crack depth was normally smaller than the film thickness; however, a few deep cracks were indeed developed later to break the films. The circular cracks were found to exist in both peak and valley regions without preference and the inter-circular-crack distance was random with a range of 30-300 μm, which was different with the previous report [11].

The topographies of the PHB films were characterized using AFM, as shown in Figure 8.4. Because the cracks were deeper than the AFM tip, I only scanned the spherulites without cracks. The flat PHB film had a smooth surface with a R_{rms} value of 12.4 ± 1.9 nm. With a higher R_{rms} value of 26.4 ± 8.9 nm, non-banded spherulites of PHB crystallized at 45 °C displayed a typical

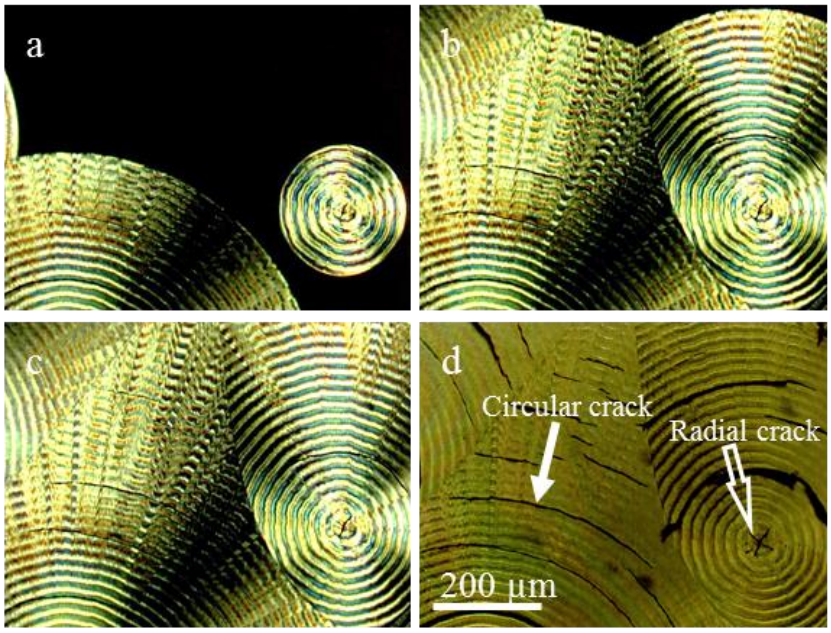

Figure 8.2 Formation of circular cracks during the crystallization process of PHB at 80 °C for (a) 30 s, (b) 90 s, (c) 3 min, and (d) cooling down to room temperature. Scale bar of 200 µm in (d) is applicable to all images.

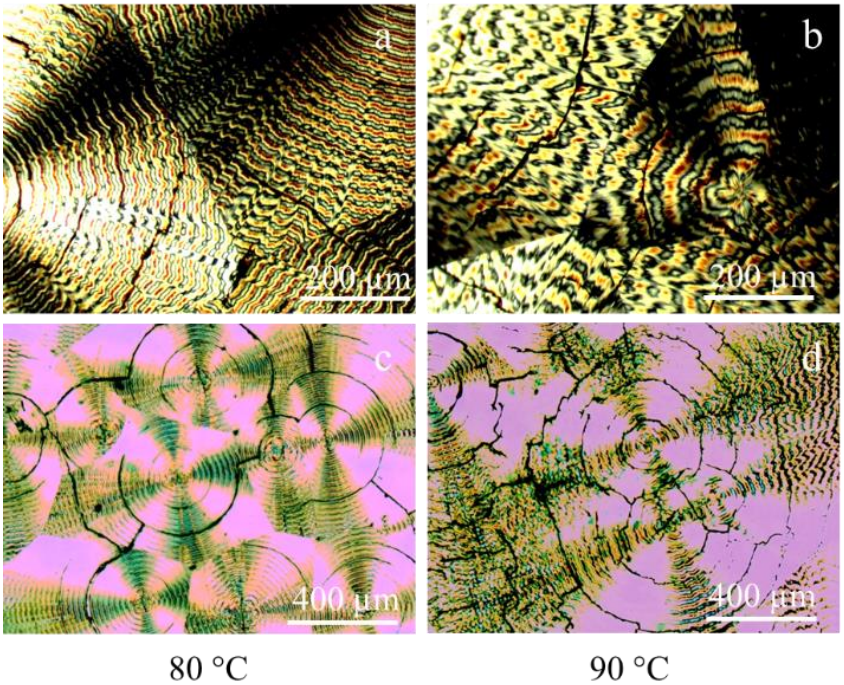

Figure 8.3 Circular cracks on PHB spherulites crystallized at 80 °C (a,c), and at 90 °C (b,d).

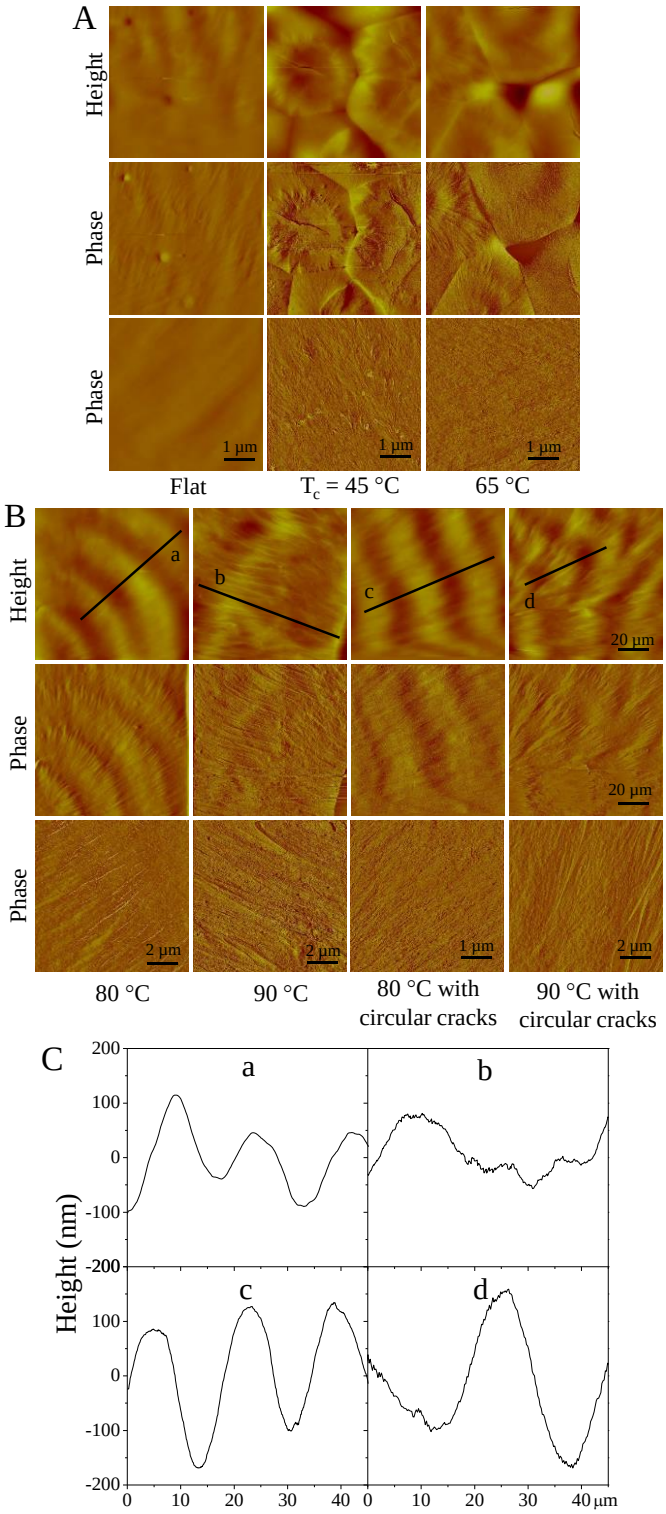

Figure 8.4 (A) AFM images of flat PHB film, and PHB films crystallized at 45 and 65 °C. (B) AFM images of PHB films (with and without circular cracks) crystallized at 80 and 90 °C. The scales of unmarked images are 50 µm. (C) Height curves (a, b, c, and d) were corresponding to the line in the AFM images (B).

lamellae radiating from the center. The surfaces of the banded spherulites were rougher and the R_{rms} value increased from 39.1 ± 6.5 nm for T_c of 65 °C to 70.4 ± 12.8 nm for T_c of 80 °C and 75.5 ± 18.3 nm for T_c of 90 °C. In absence of circular cracks, the PHB thicker films crystallized at 80 and 90 °C had lower R_{rms} values of 52.3 ± 6.9 and 69.4 ± 11.0 nm, respectively. In banded spherulites, alternating concentric rings along the radial direction were evident and their corresponding depth profiles in Figure 8.4B indicated that the peak-valley depths of ~250 or ~300 nm for the thin films with circular cracks and ~150 or ~180 nm for the thick ones without circular cracks, when the T_c was 80 or 90 °C, respectively. Unlike PCL banded spherulites with flat-on lamellar orientation in the valleys and the edge-on orientation in the ridges, only edge-on orientation was found in the ridges of the PHB banded spherulites without showing clear flat-on lamellae in the valleys, possibly because the PHB films used here were thicker than the ridge-valley depth.

8.3.2 Cell attachment, proliferation and alignment.

In order to elucidate how the spherulitic morphologies and the cracks in PHB affected the cellular behavior, SMCs were cultured on all the above-discussed samples, i.e., the banded and non-banded spherulites of PHB and the flat one. As shown in Figures 8.5 and 8.6, the densities of SMCs on the flat PHB films at 4 h, days 1, 2, and 4 post-seeding were always higher than those on the spherulitic films and the lowest value was found on the large banded spherulites with circular cracks crystallized at 90 °C. This finding was opposite to our previous observation that MC3T3-E1 cell proliferation was enhanced on rougher spherulitic surfaces of PCL, especially the banded ones, as rougher surfaces resulted in larger areas and higher protein adsorption [11]. On the other hand, the trend in SMC proliferation on the PHB films was similar to the reports that cell

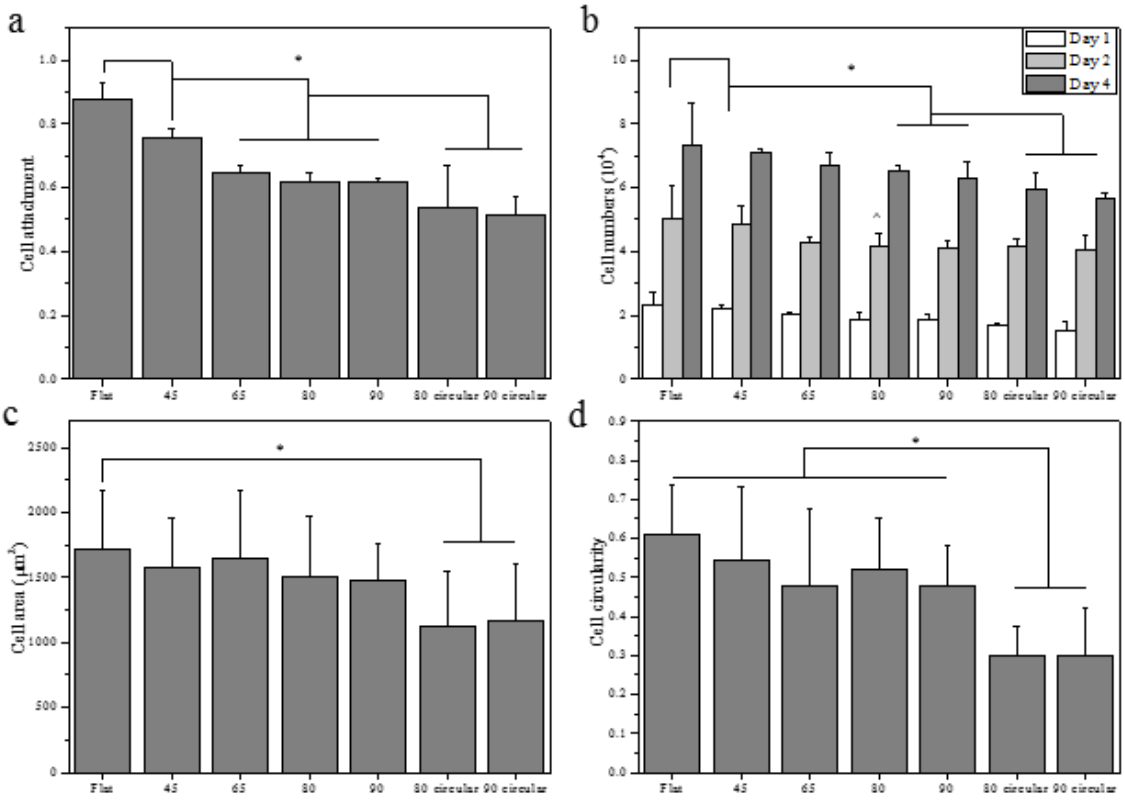

Figure 8.5 (a) Normalized SMC attachment at 4 h post-seeding on the PHB films crystallized at different conditions. (b) SMC proliferation indicated by cell numbers at days 1, 2, and 4 post-seeding on the PHB films crystallized at different conditions. SMC areas (c) and circularities (d) at day 1 post-seeding on PHB films. *: $p < 0.05$ between two samples marked with the same symbol.

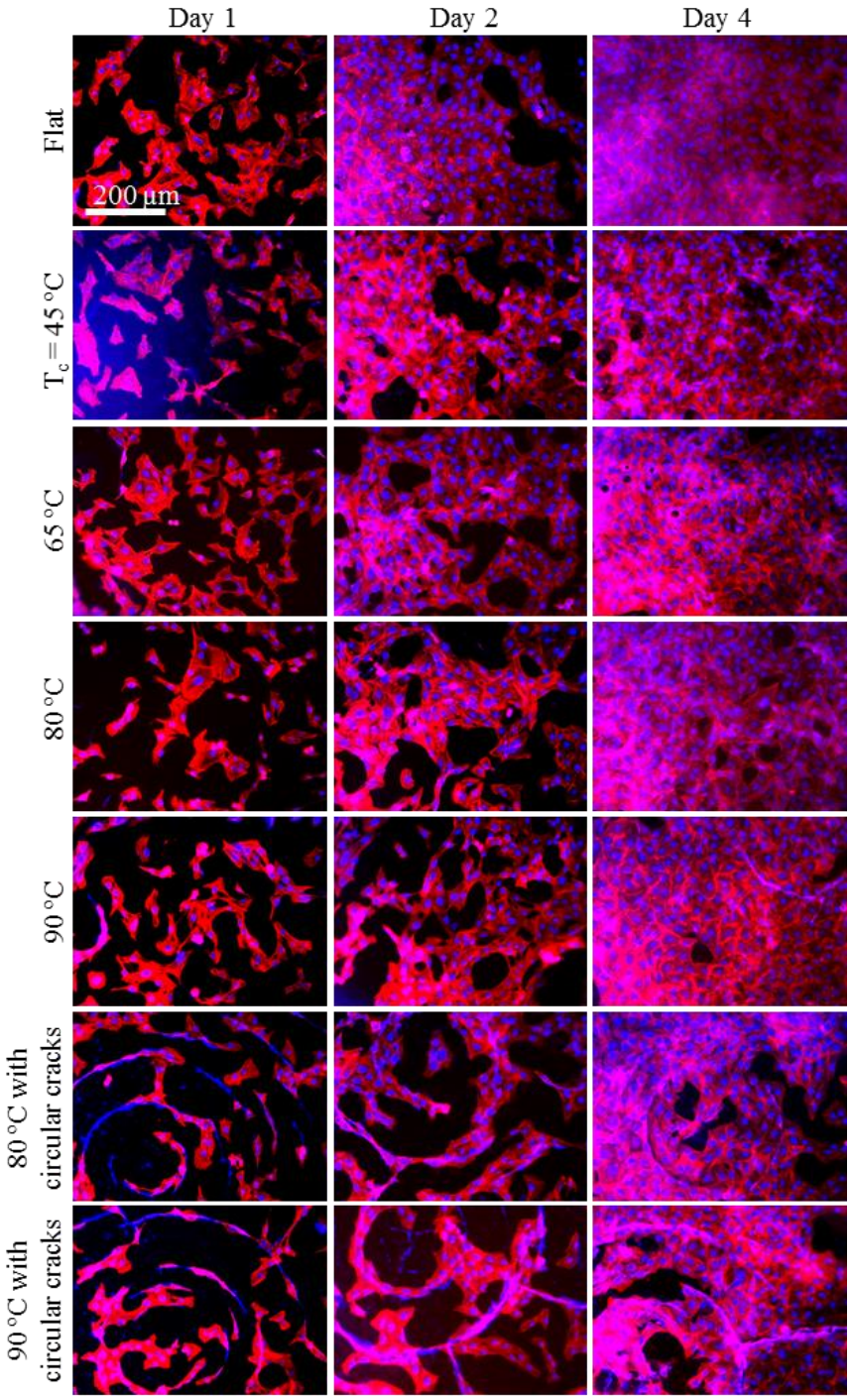

Figure 8.6 Fluorescent images of SMCs stained with RP (red) and DAPI (blue) on the PHB films at days 1, 2, and 4 post-seeding. Scale bar of 200 µm is applicable to all images.

proliferation was slower on the rougher spherulitic surfaces of PLLA than on its quenched amorphous and smooth counterpart [16-20]. Unlike PCL with low T_g (-60 °C) and T_m (60 °C) and a relatively low stiffness (Young's modulus, E = 200-300 MPa) at 37 °C, PHB (E = 1-2 GPa) and PLLA (E = 2-5 GPa) are much stiffer [1,5,21].

The representative fluorescence images of the cells stained with RP and DAPI at days 1, 2, and 4 post-seeding in Figure 8.6 were consistent with the corresponding cell densities in Figure 8.5a and 8.5b. Without being aligned along the circular bands or the radial lamellae, the cells grew and spread randomly on the PHB films without circular cracks (Figures 8.6 and 8.7). Figure 8.7 showed the merged images of cell and spherulites on PHB films with and without circular cracks crystallized at 80 and 90 °C at day 1 post-seeding. The cells on the PHB films without circular cracks distributed randomly and had no alignment. On the PHB films with circular cracks, it was clearly to be seen that the cells aligned along the cracks not the bands. Although spherulites and crack morphologies were different with different crystallization temperatures, the trend of cell alignment did not change. On the PHB films with circular cracks, the cells were evidently aligned along the cracks at both days 1 and 2 post-seeding, before the films were fully covered by the cells at day 4 post-seeding. At day 1, ~73% of all the attached cells on the PHB films with circular cracks prepared at T_c of 80 °C were aligned on the cracks, among which ~68% was caused by the circular cracks while only ~5% by the radial cracks. This number increased to ~79% (~70% on the circular cracks, ~9% on the radial cracks) on the films prepared at T_c of 90 °C.

As shown in Figures 8.5 c and 8.5d, the circularities and areas of the cells at day 1 varied little (~0.5 for circularity and ~1600 μm^2 for cell area) on the PHB films without circular cracks; however, the values (~0.3 for circularity and ~1200 μm^2 for cell area) were significantly smaller on the PHB films with circular cracks because of the alignment along the cracks.

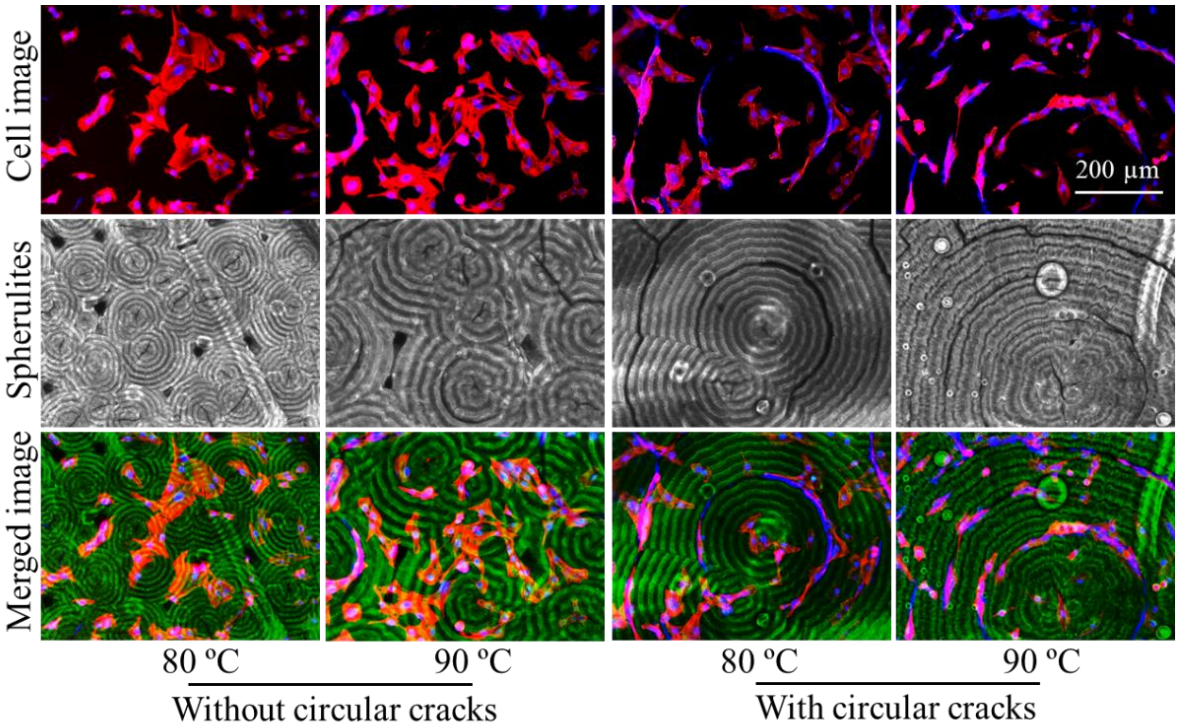

Figure 8.7 SMC alignment on PHB films with and without circular cracks crystallized at 80 and 90 °C. Scale bar of 200 μm is applicable to all images.

The surface morphologies of the SMCs on the flat PHB films and PHB films crystallized at 80 °C (with and without circular cracks) are shown in the SEM images in Figure 8.8. The peak-valley structures of PHB banded spherulites could be roughly seen with clear cracks. The average width of the cracks was larger than the value determined using AFM, mainly because of the further enlargement of cracks during the ethanol treatment in SEM characterization. Compared with well-spread cells on the flat PHB films and those without circular cracks, the cells were obviously aligned along the circular cracks.

8.3.3 Gene expression of contractile markers.

Regulation of synthetic to contractile phenotypic conversion process is of critical importance for SMCs in cardiovascular tissue engineering [22]. Here I chose four typical contractile gene markers, smoothlin, calponin, transgelin and SM-MHC, to evaluate phenotypic conversion in SMCs [23]. Three representative samples, flat PHB film and those crystallized at 80 °C (with and without circular cracks), were chosen to study the gene expression. As shown in Figure 8.9, all the four contractile gene markers had highest expression levels in SMCs on the flat PHB films. Meanwhile, the expression levels on the PHB films without circular cracks were slightly higher than the values on the PHB films with circular cracks. The above gene expression results suggested that the surface roughness formed in crystallization resulted in different phenotypic conversion in SMCs.

8.3.4 Cell nuclear shape and distribution.

The shape and area of cell nuclei are critical for gene expression and cell functions, thus I characterized the nuclei of SMCs on the PHB films. Unlike the results in cytoplasm, the nuclear circularity (~0.65) and area (~160 μm^2) did not vary significantly among all the PHB films. The distribution of the cell nuclei on the banded spherulites of PHB was also characterized from the

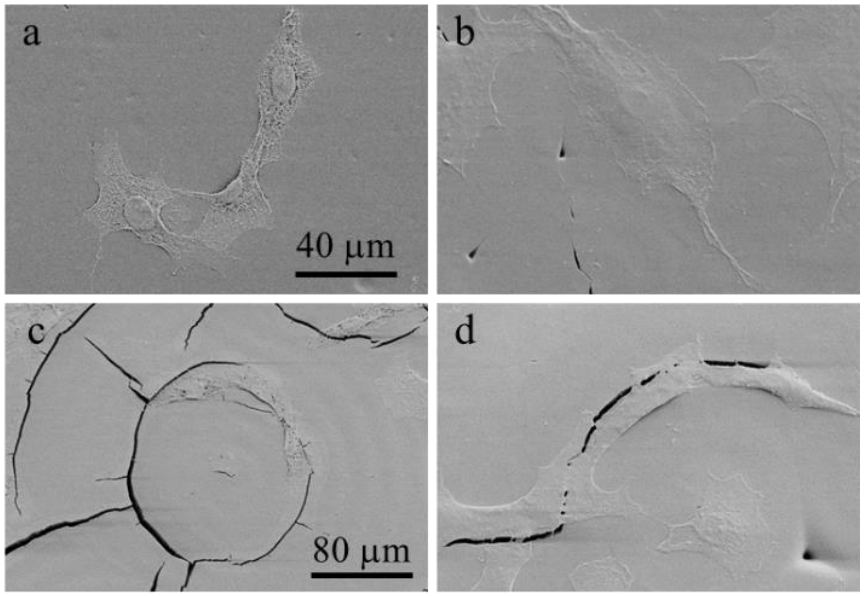

Figure 8.8 SEM images of SMCs on the flat PHB films (a), PHB films without circular cracks crystallized at 80 °C (b), and PHB films with circular cracks crystallized at 80 °C (c: large scale, and d: small scale). Scale bar of 200 μm is applicable to a, c, and d.

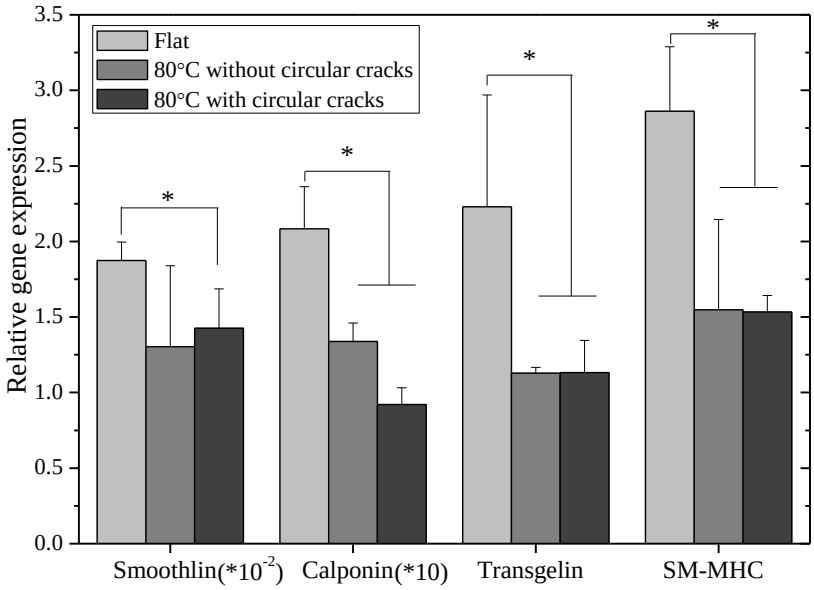

Figure 8.9 Relative gene expression levels of four contractile gene markers of SMCs on flat PHB films, and PHB films with and without circular cracks crystallized at 80 °C. *: $p < 0.05$ between two samples marked with the same symbol.

merged images of stained cell nuclei and their substrate background in Figure 8.10. Previously our research group found that mouse MC3T3-E1 cells preferred (~78%) to stay in the valleys of the banded spherulites, although not absolutely. In the present chapter, the nuclei of the SMCs also showed preference to stay in the valleys than on the ridges. The percentages of cell nuclei located in the valleys of the banded spherulites were just ~60% for the PHB films, regardless of the sample differences in T_c and the presence of circular cracks. It should be noted that the width ratio between the ridges and valleys in the banded spherulites was approximately 3:2, meaning the valleys had a rather lower area but attracted more cell nuclei. The ridge-valley depths of <350 nm for all the banded structures were much lower than the band widths of 17-35 μm and thus the aspect ratio of the structure was not sufficiently large for confining and aligning/distorting all the cells. In comparison, the cracks in PHB specimens here, especially the circular cracks, affected the cells and their nuclei more significantly.

8.3.5 Further discussion.

Aligned cytoskeleton can distort cell nuclei through mechanotransduction as the alignment of actin structure sensitively influences intermediate filaments transferring the applied force from actin to nuclei [25-28]. In this chapter, SMCs on the PHB films without circular cracks spread only randomly without being affected by the surface features and thus their nuclei were not expected to be distorted. Even for the aligned cells along the circular cracks existing on the two groups of PHB films, their nuclei did not alter either.

The difference in T_c (45-90 °C) for preparing the PHB films in this chapter was not expected to significantly change the mechanical properties, in particular, stiffness. PHB is known to thermally degrade at temperatures higher than its T_m. In this chapter, the same thermal history (melting at 190 °C for 10 min) was applied before isothermal crystallization, which happened at

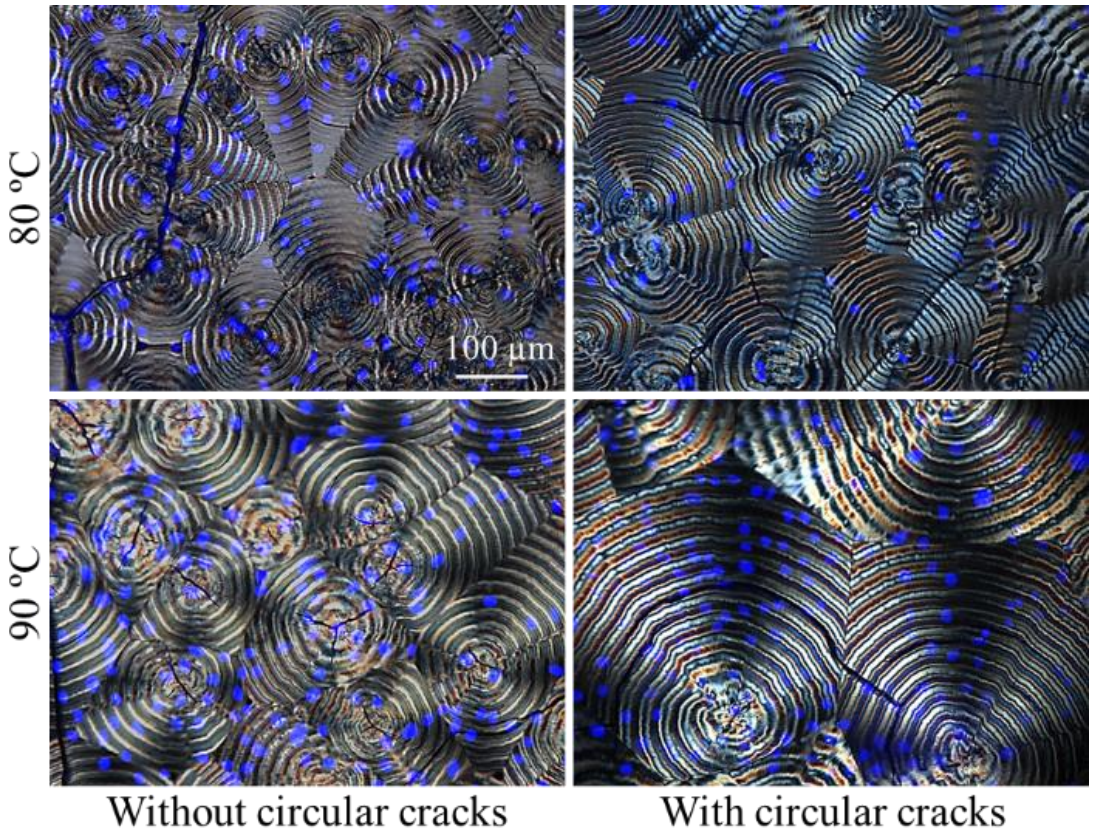

Figure 8.10 SMC nuclear distribution at day 2 post-seeding on banded PHB spherulites with and without circular cracks crystallized at 80 and 90 °C, respectively. Merged image of polarizing optical micrograph as the background, and fluorescent image of DAPI-stained cell nuclei. Scale bar of 100 µm is applicable to all images.

T_c much lower than the T_m, and thus the degree of thermal degradation in the PHB films should be similar. Therefore, the main reason to explain the different results in SMC behavior should be the surface features, including both the roughness and cracks. Different isothermal crystallization temperatures resulted in spherulites with differences in the size and banded structure. Surface roughness is believed as one important factor to regulate cell-substrate interactions, by itself or through a synergistic way with other factors such as surface energy and protein adsorption [16,29]. As our research group noted in an earlier report [1], cell behaviors were opposite on crystallized PCL and PLLA when the comparison was made between a hot-compressed flat surface and a freely crystallized spherulitic film, i.e., cells usually preferred the rougher surfaces of PCL while not in the PLLA case. Now the present chapter put PHB together with PLLA. PHB and PLLA have similarities in their high moduli and high T_m/χ_c. In addition, the surface roughness in this chapter only affected SMC attachment and proliferation, but not the area or distribution of both cytoplasm and nuclei.

To our best knowledge, this is the first time to find that cracks in the PHB films played a more important role in aligning cytoplasm along the crack direction. At days 1 and 2 post-seeding, SMCs preferred to attach and proliferate near the circular cracks. At day 4, SMCs migrated and proliferated to be confluent on the whole spherulitic surfaces and thus there were unaligned cells on the area without cracks. Compared with the banded spherulites, the deep cracks in the PHB films had sharp edges with micrometer-scale length and width are reminiscent of the substrates with microgrooves, in which deeper (15 μm) and narrower (5 μm) microgrooves could significantly trap and align both cytoplasm and nuclei [30,31]. Except for those extended and connected with the circular cracks, the short radial cracks in the PHB films did not affect SMC behavior much if the cells attached there. On the PHB films crystallized at 45 and 65 °C, there

were often no cells around or along the radial cracks. The knowledge about cellular responses to the different PHB spherulitic substrates with variances in surface roughness, spherulitic structure, and cracks offers better understanding in cell-material interactions and helps further explore of using PHB in biomedical applications.

8.4 Conclusions

Banded and non-banded spherulitic surfaces of PHB prepared through isothermal crystallization as well as the hot-compressed samples were prepared. The effect of surface roughness and cracks on SMC behaviors was studied. SMC attachment and proliferation were lower on the rougher spherulitic surfaces of PHB films than on the flat, compressed ones. SMCs were aligned by the circular cracks formed in big spherulites, not by the concentric ridges in the banded spherulites. After the circular cracks were minimized, SMCs spread randomly with a moderately higher cell number.

References

1. Wang, K.; Cai, L.; Jesse, S.; Wang, S. *Langmuir* **2012**, *28*, 4382-4395.

2. Simon Jr., C.; Eidelman, Naomi; Kennedy, S. B.; Sehgal, A.; Khatria, C. A.; Washburn, N. R. *Biomaterials* **2005**, *26*, 6906-6915.

3. Ajami-Henriquez, D.; Rodrıguez, M.; Sabino, M.; Castillo, R. V.; Muller, A. J.; Boschetti-de-Fierro, A.; Abetz, C.; Abetz, V.; Dubois, P. *J. Biomed. Mater. Res. Part A* **2008,** *87A(2)*, 405-417.

4. Martínez, E. C.; Ivirico, J. E.; Criado, I. M.; Ribelles, J. G.; Pradas, M. M; Sánchez, M. S. *J. Mater. Sci. Mater. Med.* **2007**, *18(8)*, 1627-1632.

5. Holmes, P. A. Biologically Produced (*R*)-3-hydroxy-alkanoate polymers and copolymers. In *Developments in crystalline polymers*. Springer Netherlands, 1988; pp 1-65.

6. Barham, P. J. *J. Mater. Sci.* **1984**, *19*, 3826-3834.

7. Hobbs, J. K.; McMaster, T. J.; Miles, M. J.; Barham, P. J. *Polymer* **1996**, *37*, 3241-3246.

8. Barham, P. J.; Keller, A.; Otun, E. L.; Holmes, P. A. *J. Mater. Sci.* **1984**, *19*, 2781-2794.

9. Hobbs, J. K.; Binger, D. R.; Keller, A.; Barham, P. J. *J. Polym. Sci., Part B: Polym. Phys.* **2000**, *38*, 1575-1583.

10. Barham, P. J.; Keller, A. *J. Polym. Sci.* **1986**, *24*, 69-77.

11. Martinez-Salazar, J.; Sanchez-Cuesta, M.; Barham, P. J.; Keller, A. *J. Mater. Sci. Lett.* **1989**, *8*, 490-492.

12. Tezcaner, A.; Bugra, K.; Hasirci, V. *Biomaterials* **2003**, *24*, 4573-4583.

13. Deng, Y.; Lin, X.; Zheng, Z.; Deng, J.; Chen, J.; Ma, H.; Chen, G. *Biomaterials* **2003**, *24*, 4273-4281.

14. Xu, J.; Guo, B.; Zhou, J.; Li, L.; Wu, J.; Kowalczuk, M. *Polymer* **2005**, *46*, 9176-9185.

15. Jiang, Y.; Luo, Y.; Fan, Z.; Wang, X.; Xu, J.; Guo, B.; Li, L. *Sci. China Ser. B* **2003**, *46*, 152-159.

16. Washburn, N. R.; Yamada, K. M.; Simon Jr, C. G.; Kennedy, S. B.; Amis, E. J. *Biomaterials* **2004**, 25, 1215-1224.

17. Simon Jr, C. G. *J. Microsc.* **2004**, 216, 153-155.

18. Bernardo, V.; Luz, G. M.; Alves, N. M.; Mano, J. F. *Mater. Lett.* **2012**, *87*, 105-108.

19. Park, A.; Cima, L. G. *J. Biomed. Mater. Res.* **1996**, *31*, 117-130.

20. Xu, C.; Yang, F.; Wang, S.; Ramakrishna, S. *J. Biomed. Mater. Res. Part A* **2004**, *71A(1)*, 154-161.

21. Södergård, A.; Stolt, M. *Prog. Polym. Sci* **2002**, *27(6)*, 1123-1163.

22. Chan-Park, M. B.; Shen, J.; Cao, Y.; Xiong, Y.; Liu, Y.; Rayatpisheh S.; Kang, G. C.; Greisler, H. P. *J. Biomed. Mater. Res. A* **2009**, *88(4)*, 1104-1121.

23. Sobue, K.; Hayashi, K.; Nishida, W. *Mol. Cell Biochem.* **1999**, *190*, 105-118.

24. Wang, C.; Yin, S.; Cen, L.; Liu, Q.; Liu, W.; Cao, Y.; Cui, L. *Tissue Eng. Part A* **2010**, *6(4)*, 1201-1213.

25. Nikolovski, J.; Mooney, D. J. *Biomaterials* **2000**, *21*, 2025-2032.

26. Anselme, K.; Bigerelle, M. *Int. Mater. Rev.* **2011**, *56(4)*, 243-266.

27. Maniotis, A. J.; Chen, C. S.; Ingber, D. E. *Proc. Natl. Acad. Sci. USA* **1997**, *94*, 849-854.

28. Dalby, M. J.; Riehle, M. O.; Yarwood, S. J.; Wilkinson, C. D. W.; Curtis, S. G. *Exp. Cell Res.* **2003**, *284*, 274-280.

29. Lord, M. S.; Foss, M.; Besenbacher, F. *Nano Today* **2010**, *5*(1), 66-78.

30. Henry, M. G.; Cai, L.; Liu, X.; Zhang, L.; Dong, J.; Chen, L.; Wang, Z.; Wang, S. *Langmuir* **2015**, *31*, 2851-2860.

31. Cai, L.; Zhang, L.; Dong, J.; Wang, S. *Langmuir* **2012**, *28*, 12557-12568.

Chapter IX. Cell Responses to Poly(L-lactic acid) Banded and Non-banded Spherulites

Abstract

We report that spherulites-roughened poly(L-lactic acid) (PLLA) surfaces regulated cell behaviors. Banded and nonbanded spherulites were observed on drop-coated films of PLLA binary homoblends composed of high- and low-molecular-weight components when they were isothermally crystallized at certain temperatures. The spherulitic patterns showed strong dependence on the crystallization temperature (T_c), the blend composition, and the annealing process. PLLA films with Φ_{PLLA3k} of 30% were found to be able to have better banded structures, and were chosen to regulate cell behaviors. The surface roughness of these spherulites showed parabolic trend with the T_cs. *In vitro* rat primary aortic smooth muscle cell (SMC), mouse pre-osteoblastic MC3T3-E1 cell, and rat pheochromocytoma (PC12) cell attachment and proliferation, and PC12 cell differentiation were assessed on spherulites-roughened PLLA films. The SMCs and MC3T3-E1 cells attachment and proliferation were better on the surfaces with less roughness. MC3T3-E1 cells showed alignment along the radial direction on nonbanded spherulites. PLLA spherulites coated with poly(D-lysine) showed no significant effect on PC12 cell attachment, proliferation and differentiation. The nuclei of MC3T3-E1 cell and PC12 cell had distribution preference by showing more nuclei located in the valleys than on the ridges.

9.1 Introduction

Surface topography is one of the most important parameters in the cell-material interactions [1-4]. Both pre-designed surface patterns and surface roughness affect cell behaviors, in particular, spherulitic surfaces have been used to study the responses of cells cultured on them [5-8]. Semi-crystalline poly(L-lactic acid) (PLLA) is a widely used biomaterial with a melting temperature (T_m) of 170-180 °C and crystallinity (χ_c) of 30-50% [9-10]. Various PLLA surface morphologies were achieved at different crystallization conditions and cellular responses to them were examined. Compared with the smooth amorphous surface, crystallized surfaces were rougher and the cell growth rate on them were lower [5,11-15]. Similar results were also found in the blends of PLLA with amorphous poly(D,L-lactic acid) (PDLLA), and PLLA-poly(ε-caprolactone) (PCL) copolymers [16,17]. Moreover, different spherulitic morphologies also had different effects on cell spreading or orientation [18-21]. Human articular chondrocytes were elongated on larger PLLA spherulites but showed spread-stellate-like morphologies on smaller PLLA spherulites and avoided inter-crystallite microcavities [18,19]. L929 mouse fibroblast cells were reported to proliferate less but spread better on the quenched PLLA films with more areas of spherulites [20]. The growth rates of both mouse fibroblast 3T3-Swiss albino cells and pre-osteoblastic MC3T3-E1 cells were found to be lower on the spherulitic PLLA films than on the amorphous counterparts, while only fibroblasts were oriented along the perimeter [21].

PCL, PLLA, and poly(3-hydroxybutyrate) (PHB) can form banded and non-banded spherulitic surfaces at different crystallization temperatures (T_c) [6,22,23]. Banded spherulites are spherulites with alternating concentric rings along the radial direction, which are ridge-valley structures. The bandwidth in these banded spherulites, i.e., the spacing between two neighboring ridges, differs for different polymer types and can be regulated by the polymer composition and T_c [24].

Previously our research group found that MC3T3-E1 cells cultured on the PCL spherulites (in particular, banded ones) of PCL attached and proliferated better than on the hot-compressed surfaces and cell nuclei preferred to stay in the valley [6]. Recently I also studied the behaviors of primary rat aortic smooth muscle cells (SMCs) on PHB spherulites and found that rougher banded spherulites resulted in worse SMC proliferation and the circular cracks in the banded spherulites aligned the cells [23]. Despite the earlier investigations, how spherulitic surfaces of different semi-crystalline polymers (e.g., PCL *vs.* PHB or PLLA) affect cellular responses and how different cell types respond to PLLA spherulitic surfaces are still unclear. In this chapter, I used PLLA with a higher Young's modulus *E* of 2-5 GPa and a higher glass transition temperature (T_g) of 55-80 °C, compared with PCL and PHB studied earlier [6,25,26].

Unlike PCL, it is difficult for high-molecular-weight PLLA to form banded spherulites while the spherulitic film of low-molecular-weight PLLA is unstable in water because of hydrolysis and brittle in the presence of cracks [14,27,28]. Blending or copolymerize a semi-crystalline polymer with an amorphous one is a commonly used method to form banded spherulites, for example, PCL homoblends (i.e., blends of two different molecular weight but the same polymer species) and PCL blends or copolymers with polypropylene fumarate (PPF) [6,7,29]. This strategy was also applied in forming banded spherulites of PLLA as two different weight-average molecular weights (M_w) of 120,000 and 1,600-2,400 g/mol [30]. Here I examined the spherulitic structures of PLLA binary homoblends with various composition ratios and crystallization conditions. Both banded and non-banded spherulites were formed and different bandwidths were achieved. Then these controllable spherulitic surfaces of PLLA were used as the substrates for examining SMC, MC3T3-E1 cell, and rat pheochromocytoma (PC12) cell responses when these three different cell types were cultured on them.

9.2 Experimental Section

9.2.1 Materials.

The chemicals used here were purchased from Sigma-Aldrich Co. (Milwaukee, WI) unless otherwise noted. Two PLLAs were synthesized through ring-opening polymerization of L-lactide [31]. As shown in Table 9.1, these two samples with number-average molecular weights (M_n) of 148000 and 2970 g/mol were named as PLLA150k and PLLA3k, respectively. Using these two PLLA samples, homoblends with different PLLA3k weight compositions (Φ_{PLLA3k}) of 20%, 30%, and 40% were prepared by dissolving 0.5 g of the blends in 10 mL of methylene chloride and drop-casting directly onto round glass coverslips, followed by complete drying in vacuum. The formed PLLA films were first melted at 210 °C for 10 min and then directly transferred to a hot stage with a preset T_c (110-135 °C) for isothermal crystallization, or annealed at 160 °C for 30 min before isothermal crystallization. Crystallization time varied from 15 min to 12 h for different compositions and T_c. Based on the solution volume used in solution casting, the obtained PLLA films had a thickness of ~20 μm. Prior to cell studies, the crystallized PLLA films were immersed in PBS for 10 min for cleaning and exposed under UV light for 24 h for sterilization.

9.2.2 Polymer characterization.

The crystalline structures of all the PLLA films were observed using polarized optical microscopy (POM, Nikon Optiphot-2, POL). The molecular weights of PLLA with Φ_{PLLA3k} of 30% (original, after melting, and after annealing) were determined using gel permeation chromatography (GPC; PL-GPC20, Polymer Laboratories) at room temperature with tetrahydrofuran as the eluent and standard monodisperse polystyrene samples (Polymer Laboratories) for calibration. The surface morphologies of the PLLA films with Φ_{PLLA3k} of 30% were characterized using a multimode atomic force microscope (AFM) with a Nanoscope III

Table 9.1 Molecular weight change of the PLLA homoblends after melting and annealing process

PLLA	M_n (g/mol)	M_w (g/mol)	PDI	M_n (g/mol)	M_w (g/mol)	PDI
Original	148000	281000	1.9	2970	3560	1.2
After melting	66300	114000	1.7	3080	4190	1.4
After annealing	53100	84100	1.6	3070	4360	1.4

control system (Veeco Instruments, Santa Barbara, CA). A tapping mode over a scan area of 50 μm × 50 μm or 80 μm × 80 μm at a scan rate of 0.25 Hz was used. Root-mean square roughness (R_{rms}) was measured from the height images using the Nanoscope 7.30 software (Veeco Instruments, Santa Barbara, CA).

9.2.3 *In vitro* SMC attachment and proliferation.

SMCs were cultured in a growth medium composed of Dulbecco's modified eagle medium (DMEM; Gibco, Grand Island, NY) supplemented with 10% fetal bovine serum (FBS; HyClone, Thermal Scientific) and 1% penicillin/streptomycin (Gibco, Grand Island, NY) in an incubator with 5% CO_2 and 95% relative humidity at 37 °C. SMCs were seeded on the PLLA films at a density of ~15,000 cells/cm^2 and cultured for 4 h and 1, 2, and 4 days. A colorimetric cell metabolic assay (CellTiter 96 Aqueous One Solution, Promega, Madison, WI) was performed in each well to determine the number of attached cells by correlating to the UV absorbance of the solution at 490 nm measured on a microplate reader (SpectraMax Plus 384, Molecular Devices, Sunnyvale, CA). Cell numbers were then quantified using the standard curve that was constructed using known cell numbers. Cell attachment at 4 h post-seeding was calculated through normalizing the cell density on the sample by the value on the tissue culture well. The cells attached on the PLLA films were washed with PBS, fixed with 4% paraformaldehyde (PFA, Electron Microscopy Science) solution for 10 min at room temperature, rinsed with PBS twice, and permeabilized with 0.2% Triton X-100 solution at room temperature for another 10 min. Cytoplasm was stained using rhodamine-phalloidin (RP, Thermal Scientific) for 1 h at 37 °C. Then the cells were photographed using an Axiovert 25 light microscope (Carl Zeiss, Germany). Based on the cell images, cell area and circularity (defined as $4\pi \times \text{area}/\text{perimeter}^2$) were determined on more than 50 non-overlapping cells at day 1 by using ImageJ software (National Institutes of Health, Bethesda, MD).

9.2.4 *In vitro* MC3T3-E1 cell attachment, proliferation, and alignment.

MC3T3-E1 cells were cultured in a growth medium composed of α-Minimum Essential Medium (α-MEM; Gibco, Grand Island, NY) supplemented with 10% FBS and 1% penicillin/streptomycin in an incubator with 5% CO_2 and 95% relative humidity at 37 °C. Cells were seeded onto the PLLA films at a density of ~15,000 cells/cm^2. The MC3T3-E1 cell numbers were determined and the cells were stained and analyzed using the same method for SMCs. Cell alignment was quantified using the percentage of aligned cells in the total cells along the radial direction. Cells were considered as aligned when the angle between the long axis and the radial direction of the spherulite was smaller than 15°. MC3T3-E1 cell nuclei at day 2 post-seeding were stained using 4′,6-diamidino-2-phenylindole (DAPI) at room temperature for photographing and characterizing nuclear distribution.

9.2.5 *In vitro* PC12 cell attachment, proliferation, and differentiation.

Prior to cell studies, the sterilized PLLA films were immersed in poly(D-lysine) (PDL) aqueous solution (100 μg/mL) at 37 °C for 1 h, washed with PBS three times, and then dried completely. Rat PC12 cells were cultured in a growth medium containing F-12K media (Gibco, Grand Island, NY), 15% horse serum, 5% FBS and 1% penicillin/streptomycin in an incubator with 5% CO_2 and 95% relative humidity at 37 °C. PC12 cells were seeded onto PLLA films with and without PDL coating at a density of 15,000 cells/cm^2 and cultured for 12 h, 1, 4, and 7 days. For differentiation, PC12 cell neurites were induced in a growth medium supplemented with 50 ng/mL NGF for 7 days. PC12 cell numbers were determined, and the cells were stained and analyzed using the same method for SMCs. PC12 cell areas and neurites were analyzed and averaged from at least 100 cells using ImageJ. Nuclei of PC12 cell at day 2 post-seeding were also

stained using DAPI at room temperature and photographed for characterization of nuclear distribution.

9.2.6 Statistical analysis.

Cell studies were performed in quadruplicates for each group at each time point. All values were expressed as mean ± standard deviation. The statistical significance ($p < 0.05$) in the difference between two groups was calculated using student's *t*-test.

9.3 Results and Discussion

9.3.1 Characterizations of PLLA spherulites.

The crystalline structures of the PLLA binary homoblends were observed using POM, as demonstrated in Figure 9.1. The spherulitic patterns varied with T_c and the blend composition, as well as the annealing process. PLLA150k and PLLA3k had different crystallization temperature ranges, and the binary homoblends with different compositions showed distinct crystalline structures. Banded spherulites with clear alternating dark and bright concentric rings were unable to form when Φ_{PLLA3k} in the PLLA homoblends was lower than 20% or higher than 40%. The average bandwidths of the PLLA banded spherulites with Φ_{PLLA3k} of 20%, 30%, and 40% are shown in Table 9.2. The bandwidth increased with increasing T_c, and annealing at 160 °C for 30 min increased both the spherulite size and the bandwidth. Among these three compositions, spherulites with clearer banded structures were observed at higher Φ_{PLLA3k}; however, the films were more brittle. Thus, Φ_{PLLA3k} of 30% were chosen to prepare PLLA substrates for regulating cell behaviors. In the banded spherulites in Figure 9.1, the bright bands were ridges, the dark bands were valleys, and their width ratios were ~3:2.

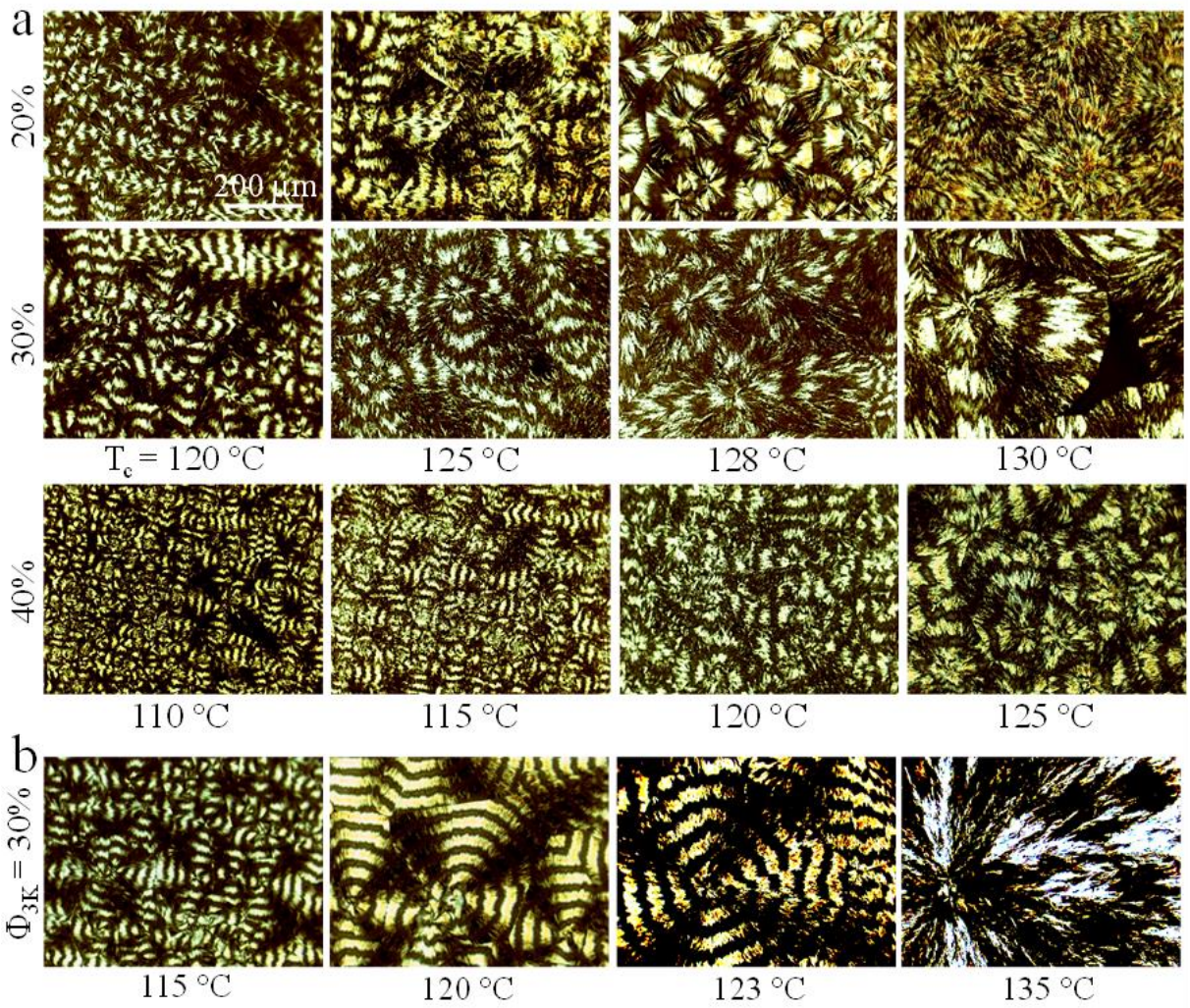

Figure 9.1 POM images of the PLLA spherulites prepared under different crystallized temperatures. (a) Without annealing at 160 °C. (b) Annealing at 160 °C.

Table 9.2 Band widths (μm) of the PLLA spherulites prepared under different T_cs. a: annealing at 160 °C. -: samples not prepared.

$Ф_{PLLA3k}$	110 °C	115 °C	120 °C	123 °C	125 °C	128 °C	130 °C
20%	-	-	33.8 (39.2[a])	-	48.0	89.1	116.2
30%	-	31.7[a]	41.0 (51.5[a])	65.9[a]	67.7	110.8	167.5
40%	24.1	29.4	48.1 (50.3[a])	-	102.6	-	-

To prepare banded spherulites with clear peak-valley structures, T_cs of 115, 120, and 123 °C were used with annealing before isothermal crystallization. The PLLA films crystallized at 135 °C (Figure 9.1b) showed large non-banded spherulites (~1400 μm, diameter), while the average diameters of the banded spherulites were ~450, 600, and 700 μm at T_c of 115, 120, and 123 °C, respectively. Cracks occurred only to non-banded spherulites in both radial and circular directions.

PLLA thermal degradation at temperatures higher than T_m was characterized using the changes in the molecular weights before and after the melting and annealing processes, as shown in Table 9.1. The PLLA150k in the homoblends degraded dramatically after the melting and the molecular weight further decreased after the annealing process. The molecular weight of the lower-molecular weight component, PLLA3k, in the homoblends seemingly increased as PLLA150k degraded into shorter chains that had higher molecular weights than that of PLLA3k. After thermal degradation, the polydispersity index (PDI) of PLLA150k decreased while that of PLLA3k increased slightly.

The topographies of the PLLA films were characterized using AFM, as shown in Figure 9.2. The banded structures were seen in the AFM height images in Figure 9.2a. The surface roughness (R_{rms}) values of the PLLA films prepared at T_c of 115, 120, 123, and 135 °C were 66.6, 87.2, 83.5, and 76.8 nm, respectively. In the PLLA banded spherulites, alternating concentric rings along the radial direction were evident (Figure 9.2a). Their corresponding depth profiles in Figure 9.2b indicated that the peak-valley depths were ~710, 870, and 900 nm at T_c of 115, 120, and 123 °C, respectively. The AFM images in Figure 9.2c and 9.2d demonstrated the marked valley (or dark) and peak (or bright) areas in PLLA spherulites crystallized at 115 °C. Distinct difference could be seen in these two areas, as the edge-on orientation of lamellae was dominant in the peak area while the flat-on orientation was found in the valley area. This finding was also reported in PCL banded spherulites [6,24].

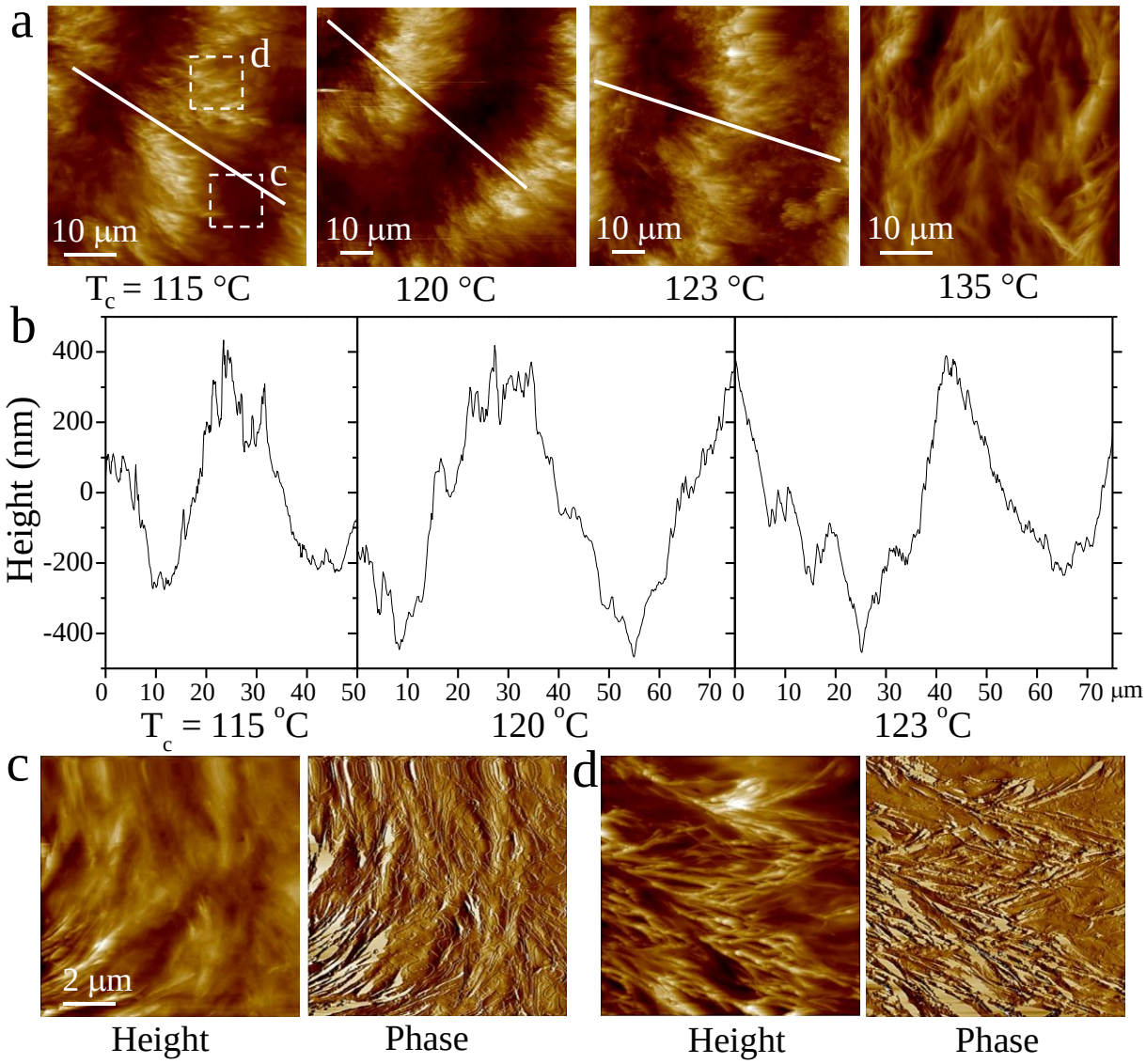

Figure 9.2 AFM images of PLLA (Φ_{PLLA3k} = 30%) spherulites with different T_cs. (a) Height images of the spherulites. (b) Height curves corresponding to the lines in (a). Height and phase images of valley (c) and ridge (d) in (a). Scale bar of 2 μm is applicable to all images in (c) and (d).

9.3.2 Cellular responses to PLLA spherulites.

To elucidate how the PLLA spherulitic morphologies affect cellular behavior and compare with the literature findings, three different cell types (i.e., SMCs, MC3T3-E1 cells, and PC12 cells) were cultured on the banded and non-banded spherulites of the PLLA films. Fluorescent images of SMCs on the PLLA spherulites are shown in Figure 9.3. As shown in Figures 9.3b and 9.3c, the densities of SMCs on the PLLA films crystallized at 120 °C were always lower than those on the other PLLA films at all the time points (4 h and days 1, 2, and 4), although the normalized cell attachment at 4 h showed no significant difference among all the samples. The trend in cell densities with increasing T_c was opposite to that in R_{rms} and the highest cell densities appeared on the non-banded spherulites crystallized at 135 °C. Representative fluorescence images of the SMCs stained with RP in Figures 9.3a were consistent with the cell densities in Figure 9.3c. Despite the significantly different cell proliferation, the circularity and area of the SMCs at day 1 varied little (~0.55 for circularity and ~2400 μm^2 for cell area) on all the PLLA films.

MC3T3-E1 cell images, attachment, and proliferation on the banded and non-banded spherulites of the PLLA films are shown in Figure 9.4. Similar to SMCs discussed above, the densities of MC3T3-E1 cells in Figures 9.4b and 9.4c also were the lowest on the roughest PLLA films at all the time points. However, except this film, MC3T3-E1 cell attachment and proliferation were not significantly different among the other three PLLA films. Representative fluorescence images of the MC3T3-E1 cells stained with RP are shown in Figures 9.4a. Unlike SMCs, MC3T3-E1 cells were aligned along the radial directions on the non-banded PLLA film, and over 35% of the cells were aligned at day 1. However, this cell alignment did not result in significant differences in cell circularity and cell area, which were around ~0.51 and 3000 μm^2, respectively. PC12 cells are neuronal-like cells that can respond to NGF by growing neurites and serve as an excellent

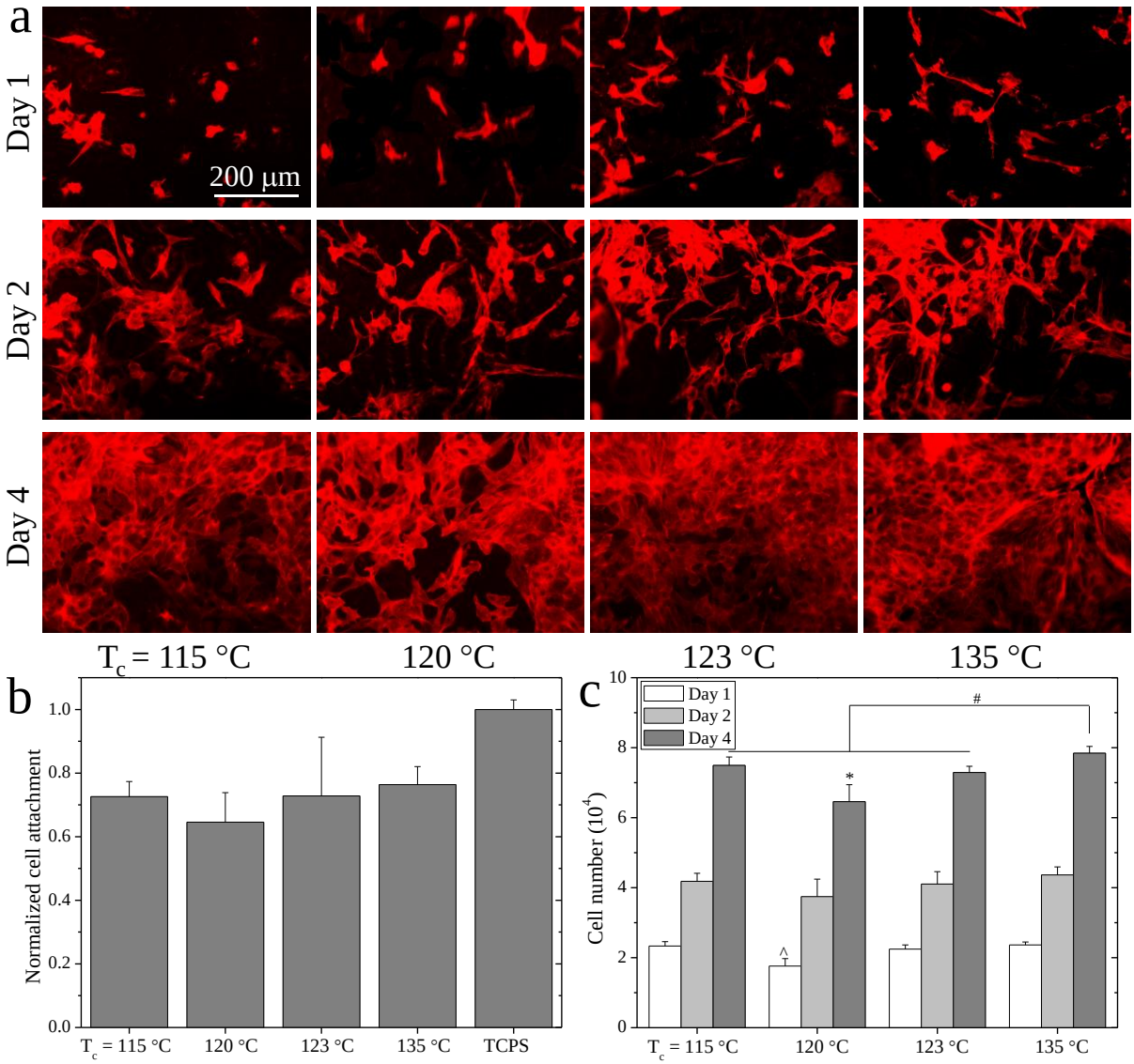

Figure 9.3 (a) SMC images at days 1, 2, and 4 post-seeding stained using RP (red) on PLLA spherulites. Scale bar of 200 μm is applicable to all. (b) Normalized SMC attachment at 4 h post-seeding. (c) SMC numbers at days 1, 2, and 4 post-seeding. *, ^: significantly smaller ($p < 0.05$) than the corresponding data on the other samples. #: $p < 0.05$ between the samples marked with the same symbol.

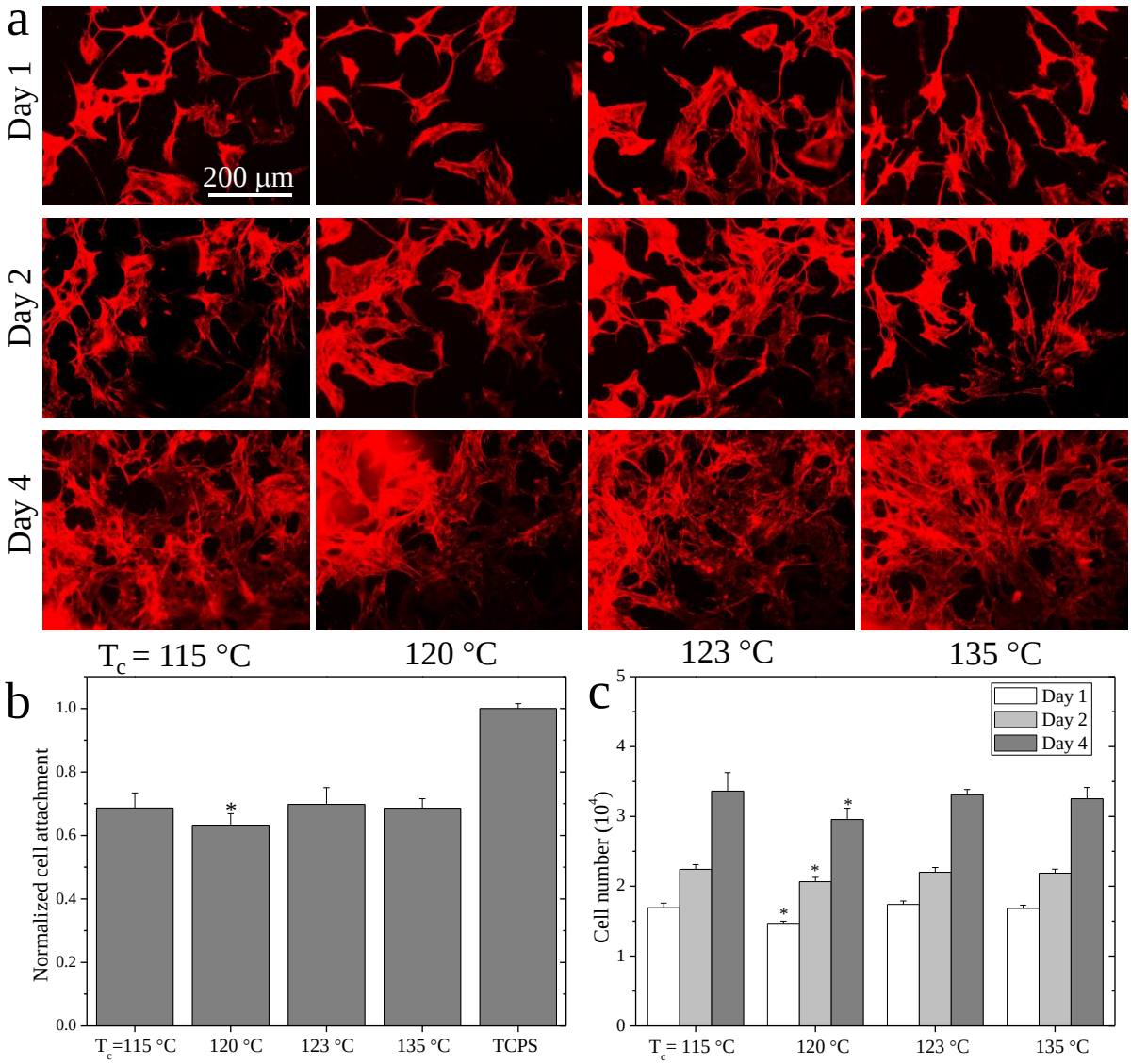

Figure 9.4 (a) MC3T3-E1 cell images at days 1, 2, and 4 post-seeding stained using RP (red) on PLLA spherulites. Scale bar of 200 μm is applicable to all. (b) Normalized MC3T3-E1 cell attachment at 4 h post-seeding. (c) MC3T3-E1 cell numbers at days 1, 2, and 4 post-seeding. *: significantly smaller ($p < 0.05$) than the corresponding data on the other samples.

model for studying cell signaling and neuronal communication [32]. Different from SMCs and MC3T3-E1 cells, PC12 cells could hardly attach on the pristine PLLA films. Figure 9.5 showed PC12 cell images, attachment, proliferation, and NGF-induced differentiation on the banded and non-banded spherulites of the PDL-coated PLLA films. There was no significant difference in PC12 cell attachment and proliferation among all the PDL-coated PLLA films. Representative fluorescence images of the PC12 cells stained with RP in Figure 9.5a also indicated similar cell densities on the PLLA films, and the cell area and circularity (~0.78 for circularity and ~150 μm^2 for cell area) had no difference among different PLLA films. PC12 cell differentiation or neurite extension was quantified using the average neurite length, percentage of differentiated cells, and number of neurites per cell. Most of these parameters had no significant differences, except the neurite number was lower on the PLLA film crystallized at 115 °C than those on the other films. Besides that, the neurites grew randomly along all directions without showing any preference along the ridge/groove or the radial direction.

9.3.3 Cell nuclear shape and distribution.

The shape and area of cell nuclei are critical for gene expression and cell functions, thus I characterized the nuclei of MC3T3-E1 cells and PC12 cells on the PLLA films. The nuclear circularity (~0.71 for MC3T3-E1 cells and ~0.82 for PC12 cells) and area (~240 μm^2 for MC3T3-E1 cells and ~75 μm^2 for PC12 cells) did not vary significantly among all the PLLA films. The nuclear distribution of the MC3T3-E1 cells and PC12 cells on the banded spherulites of PLLA was characterized from the merged images of DAPI-stained cell nuclei and their substrate background in Figure 9.6. In contrast with the nuclei shape and area, the nuclei of the MC3T3-E1 cells and PC12 cells preferred to stay in the valleys than on the ridges. The percentages of MC3T3-E1 cell nuclei located in the valleys of the banded spherulites were ~60%, 62%, and 65% for the

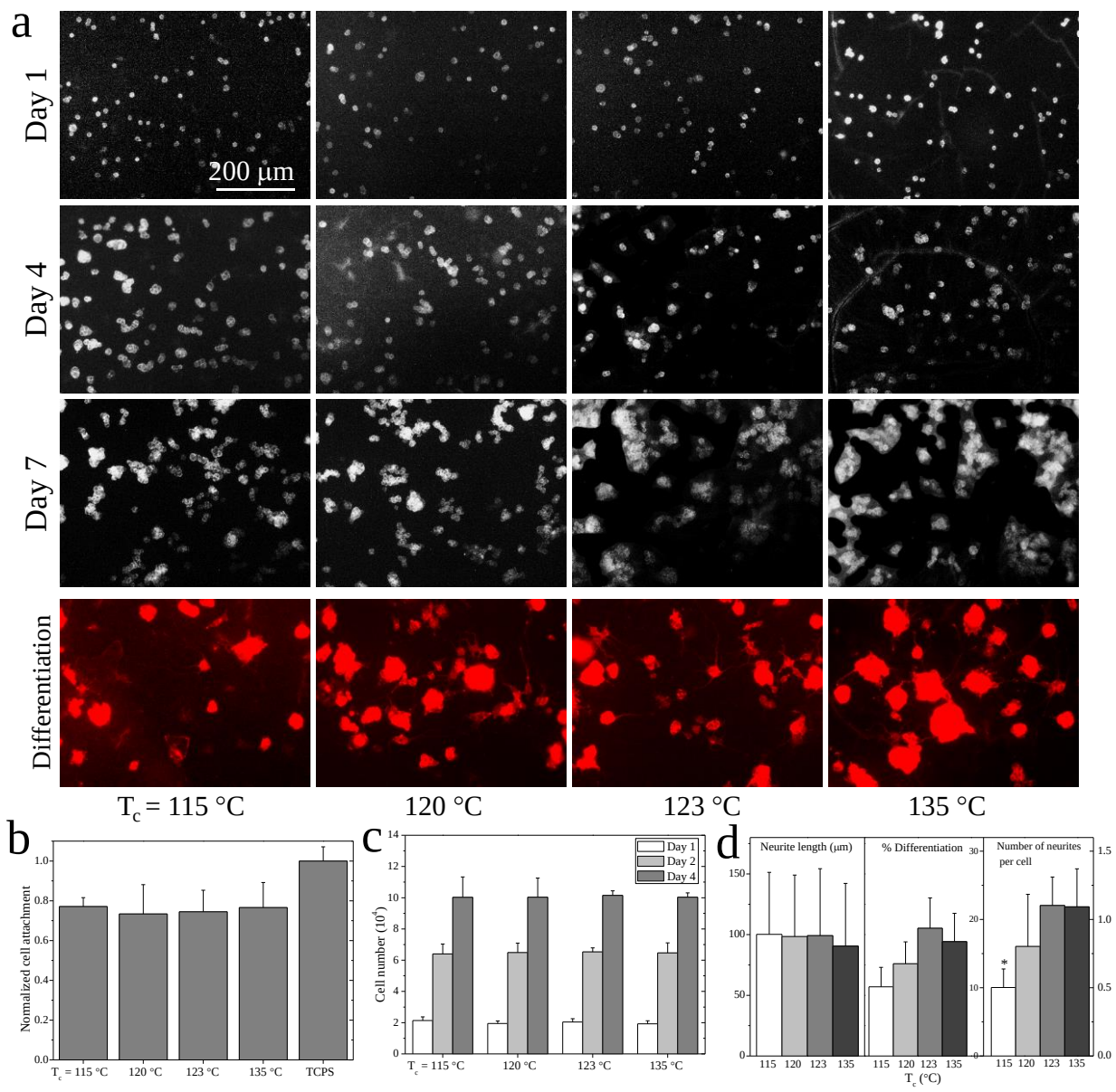

Figure 9.5 (a) PC12 cell images at days 1, 4, and 7 post-seeding, and differentiation images at day 7 post-seeding stained using RP (red) on PLLA spherulites. Scale bar of 200 µm is applicable to all images. (b) Normalized PC12 cell attachment at 4 h post-seeding. (c) PC12 cell numbers at days 1, 4, and 7 post-seeding. (d) Quantification of PC12 neurites at day 7 post-seeding using the neurite lengths, percentage of differentiated cells, and number of neurites per cell. *: significantly lower ($p < 0.05$) than the other samples.

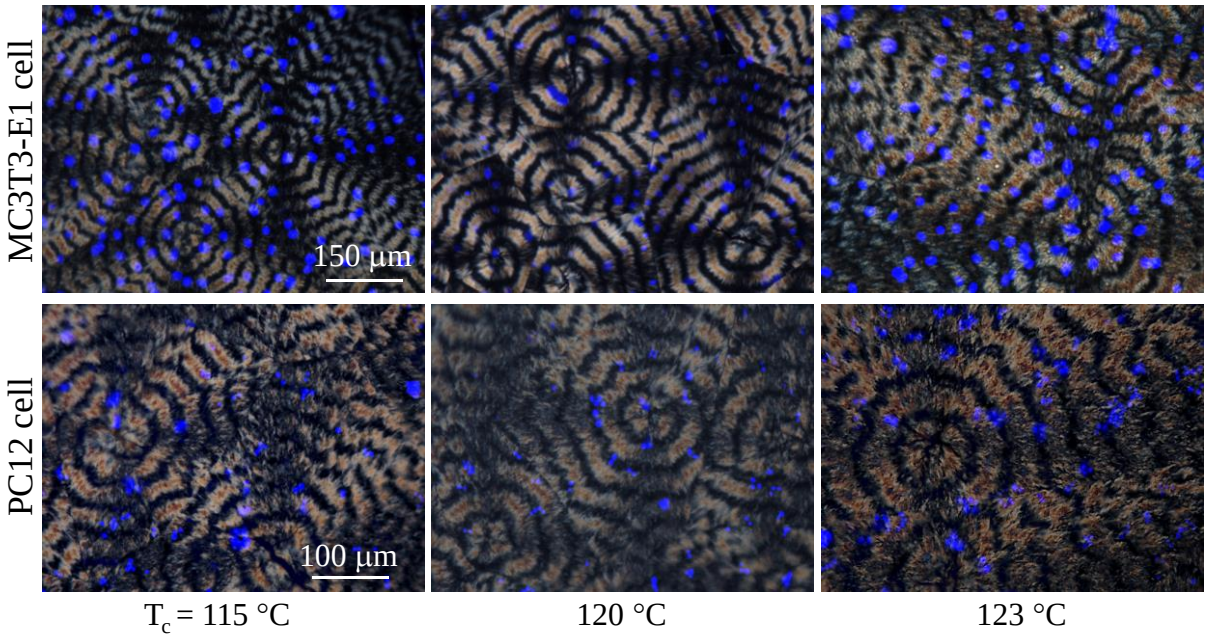

Figure 9.6 MC3T3-E1 and PC12 cell nuclear distribution at day 2 post-seeding on banded PLLA spherulites with different crystallization temperatures. Merged image of polarizing optical micrograph as the background, and fluorescent image of DAPI-stained cell nuclei. Scale bar of 150 μm is applicable to images of MC3T3-E1 cells, and 100 μm to images of PC12 cells.

PLLA films crystallized at 115, 120, and 123 °C, respectively. The percentages of PC12 cell nuclei located in the valleys of the banded spherulites were ~54%, 56%, and 58% for the PLLA films at T_c of 115, 120, and 123 °C, respectively. As mentioned earlier, the valleys had lower areas (ridge-valley area ratio of 3:2) than the ridges but attracted more cell nuclei.

9.3.4 Further discussion.

PLLA is known to degrade thermally at temperatures higher than its T_m [33]. In this chapter, the same thermal history (melting at 210 °C and annealing at 160 °C) was applied before isothermal crystallization for the PLLA films used in the cell study. Based on the molecular weights determined using GPC (Table 9.1), I can conclude that the degradation of PLLA mainly occurred in the melting step. Thermal degradation in the PLLA films during the crystallization was negligible as the T_cs of 115-135 °C were all much lower than the values in the melting and annealing steps. Thus, the PLLA homoblends crystallized at different T_cs were considered as the same in terms of component molecular weights and composition. Spherulites with different sizes and banded structures, and consequently different surface roughnesses were resulted by varying the T_c. Surface roughness can often affect surface energy and capability of adsorbing serum proteins from the culture media. However, as found earlier for PLLA films, surface energy did not vary with T_c [13] and surface roughness did not affect the protein adsorption significantly [5].

In contrast with the non-banded spherulites of PCL and PHB, PLLA non-banded spherulites were formed at a T_c higher than the values for forming banded spherulites. When T_c is low, no lamellar twisting occurs and thus non-banded spherulites form. PLLA non-banded spherulites observed here might be apparent ones that actually contained crystals twisting with a period larger than the spherulite radius [27]. Rough spherulitic polymer surfaces were generated in crystallization, and the surface roughness usually increased with increasing T_c [5,6]. In this

chapter, surface segregation of the low-molecular-weight component also affected surface roughness of the PLLA homoblends. At higher T_cs, surface segregation was more significant because of the different crystallization rates of the PLLA components with different molecular weights. A higher T_c was closer to the T_m of the low-molecular-weight PLLA, and therefore, its crystallization rate was lower than that of the high-molecular-weight one. The low-molecular-weight PLLA was still an amorphous melt when the high-molecular-weight PLLA started to crystallize. As the result, the low-molecular-weight PLLA melt with a higher chain mobility aggregated on the surface, causing surface enrichment and decreased surface roughness. The R_{rms} values of crystallized PLLA homoblends in this chapter were higher than those of PCL and PHB spherulites reported earlier by our research group. Cracks only appeared on the PLLA spherulites at the highest T_c of 135 °C as the low-molecular-weight PLLA that was more liable to generate cracks enriched on the surface [28]. Since the cracks were sparse on the spherulites, no effect on the cell behavior was noticed.

The findings in this chapter demonstrated the correlation between surface roughness and cell behaviors on PLLA spherulitic surfaces. This correlation was believed to relate to substrate stiffness via mechanotransduction. For soft substrates such as PCL, rougher surfaces increased the surface area for cell adhesion and protein adsorption, and consequently supported cell proliferation better. For stiff substrates such as PHB and PLLA, surface roughness may inhibit the cell attachment. The roughness difference between amorphous and crystalline PLLA, and that among different PLLA spherulites both could affect cell behaviors. For SMCs and MC3T3-E1 cells, the surface roughness of PLLA only affected their attachment and proliferation, but not the shape and area of both cytoplasm and nuclei. PC12 cells could only attach and proliferate on the films coated with PDL, but not on the bare PLLA films possibly because of its high stiffness. PDL was an

alternative to poly(L-lysine) (PLL) with the same function to avoid possible digestion of PLL [34-36]. The PDL coating layer on the PLLA surface was ~20 nm and did not significantly change the surface roughness [37]. PC12 cells might only interact with the PDL layer and thus did not show significantly different attachment and proliferation among all the PDL-coated PLLA films. PLLA non-banded spherulites caused MC3T3-E1 cell alignment along the radial direction, while its banded spherulites did not align the cells. The radial alignment of MC3T3-E1 cells was also found on the spherulites of PLLA-polyethylene glycol-PLLA comb-dendritic copolymers in our research group [38]. Although radial cracks were found on the PLLA non-banded spherulites, MC3T3-E1 cell alignment was irrelevant to them.

The ridge-to-valley depth of the PLLA banded spherulites increased from 0.7 to 0.9 μm when the T_c increased from 115 to 123 °C. Although the depth in this chapter was higher than the value of PCL banded spherulites (~0.35 μm), it was still much smaller than the dimension of the cell nuclei and the bandwidth. As our research group noted in a previous report, MC3T3-E1 cells preferred (~78%) to stay in the valleys of the banded spherulites, although not absolutely [6]. In this chapter, both MC3T3-E1 cell and PC12 cell nuclei were also found to prefer to stay in valley, in particular, the preference was obvious considering the ridge-valley area ratio was 3:2. Moreover, at a higher T_c, the ridge-to-valley depth was higher and more cell nuclei were located in the valley. The preference of nuclear location slightly increased when increasing the ridge-to-valley depth. Different from separate nuclei of the MC3T3-E1 cells, PC12 cell nuclei tended to agglomerate together and extended to the ridge from the valley, resulting a smaller fraction of PC12 cell nuclei in the valley than MC3T3-E1 cell nuclei. Noticeable elongation and orientation of cell nuclei were not seen on the ridge-valley structure, in agreement with our previous reports on the cells cultured on PCL and PHB banded spherulites [6,23]. The aspect ratio of the surface feature is important in

“contact guidance” and regulating cytoplasm and nuclei deformation, as proved using the microgrooved structures [39-41]. Compared with the microgrooved structures, the aspect ratio of the PLLA banded spherulites, calculated by dividing the ridge-to-valley depth by the bandwidth, was not sufficiently large (~0.014-0.022) for confining and aligning of cell nuclei and cytoplasm. However, it is still unclear why MC3T3-E1 cells were aligned along the radial direction on the non-banded spherulites. The present findings on different cellular responses to PLLA spherulitic substrates with variance in surface roughness and spherulitic morphology offers better understanding in how cells interact with polymer crystalline substrates.

9.4 Conclusions

Spherulites of PLLA binary homoblends were prepared through isothermal crystallization. Addition of low-molecular-weight PLLA3k into the high-molecular-weight one was critical in forming PLLA banded spherulites, and the annealing process at 160 °C for 30 min resulted in spherulites with larger bandwidth and size. The highest roughness was found on the PLLA films with Φ_{PLLA3k} of 30% crystallized at 120 °C, on which the lowest attachment and proliferation of SMCs and MC3T3-E1 cells were observed. PC12 cells could not attach on the bare PLLA films except being coated with PDL, but they did not differ in attachment, proliferation, and differentiation among all the PLLA films coated with PDL. MC3T3-E1 cells were aligned along the radial direction on the PLLA non-banded spherulites. The nuclei of both MC3T3-E1 cells and PC12 cells preferred to stay in the valley, and the fraction of the MC3T3-E1 cell nuclei in the valley was higher than that of PC12 cell nuclei.

References

1. Harbers, G. M.; Grainger, D. W. In *Introduction to biomaterials*; Guelcher, S. A., Hollinger, J. O., Eds.; CRC Press, **2006**; Boca Raton, FL, pp 15-45.

2. Saltzman, W. M.; Kyriakides, T. R. In *Principles of tissue engineering*; Lanza, R., Langer, R., Vacanti, J., Eds.; 3rd ed. Elsevier Academic Press, **2007**; San Diego, CA, pp 279-296.

3. Wong, J. Y.; Leach, J. B.; Brown, X. Q. *Surf. Sci.* **2004**, *570*(1), 119-133.

4. Anselme, K.; Bigerelle, M. *Int. Mater. Rev.* **2011**, *56(4)*, 243-266.

5. Washburn, N. R.; Yamada, K. M.; Simon Jr, C. G.; Kennedy, S. B.; Amis, E. J. *Biomaterials* **2004**, 25, 1215-1224.

6. Wang, K.; Cai, L.; Jesse, S.; Wang, S. *Langmuir* **2012**, *28*, 4382-4395.

7. Wang, K.; Jesse, S.; Wang, S. *Macromol. Chem. Phys.* **2012**, *213*(12), 1239-1250.

8. Cui, H.; Sinko, P. J. *Front. Mater. Sci.* **2012**, *6*(1), 47-59.

9. Lasprilla, A. J.; Martinez, G. A.; Lunelli, B. H.; Jardini, A. L.; Maciel Filho, R. *Biotechnol. Adv.* **2012**, *30*(1), 321-328.

10. Garlotta, D. *J. Polym. Environ.* **2001**, *9*(2), 63-84.

11. Alves, N. M.; Shi, J.; Oramas, E.; Santos, J. L.; Tomás, H.; Mano, J. F. *J. Biomed. Mater. Res. Part A* **2009**, *91*(2), 480-488.

12. Simon Jr, C. G. *J. Microsc.* **2004**, 216, 153-155.

13. Park, A.; Cima, L. G. *J. Biomed. Mater. Res.* **1996**, *31*, 117-130.

14. Xu, C.; Yang, F.; Wang, S.; Ramakrishna, S. *J. Biomed. Mater. Res. Part A* **2004**, *71A(1)*, 154-161.

15. Ribeiro, C.; Sencadas, V.; Areias, A. C.; Gama, F. M.; Lanceros-Méndez, S. *J. Biomed. Mater. Res. Part A* **2015**, *103*(7), 2260-2268.

16. Simon Jr., C.; Eidelman, Naomi; Kennedy, S. B.; Sehgal, A.; Khatria, C. A.; Washburn, N. R. *Biomaterials* **2005**, *26*, 6906-6915.

17. Ajami-Henriquez, D.; Rodrıguez, M.; Sabino, M.; Castillo, R. V.; Muller, A. J.; Boschetti-de-Fierro, A.; Abetz, C.; Abetz, V.; Dubois, P. *J. Biomed. Mater. Res. Part A* **2008,** *87A(2)*, 405-417.

18. Martínez, E. C.; Ivirico, J. E.; Criado, I. M.; Ribelles, J. G.; Pradas, M. M; Sánchez, M. S. *J. Mater. Sci. Mater. Med.* **2007**, *18(8)*, 1627-1632.

19. Martínez, E. C.; Hernández, J. C. R.; Machado, M.; Mano, J. F.; Ribelles, J. L. G.; Pradas, M. M.; Sánchez, M. S. *Tissue Eng. Part A* **2008**, *14*(10), 1751-1762.

20. Degirmenbasi, N.; Ozkan, S.; Kalyon, D. M.; Yu, X. *J. Biomed. Mater. Res. Part A* **2009**, *88*(1), 94-104.

21. Bernardo, V.; Luz, G. M.; Alves, N. M.; Mano, J. F. *Mater. Lett.* **2012**, *87*, 105-108.

22. Xu, J.; Guo, B.; Zhou, J.; Li, L.; Wu, J.; Kowalczuk, M. *Polymer* **2005**, *46*, 9176-9185.

23. Dou, J.; de Menezes, J. G.; Wang, S. Smooth muscle cell responses to PHB spherulites. *World Biomaterials Congress*, 2016, Montreal, Quebec, Canada.

24. Jiang, Y.; Luo, Y.; Fan, Z.; Wang, X.; Xu, J.; Guo, B.; Li, L. *Sci. China Ser. B* **2003**, *46*, 152-159.

25. Holmes, P. A. Biologically produced (*R*)-3-hydroxy-alkanoate polymers and copolymers. In *Developments in crystalline polymers*. Springer Netherlands, **1988**; pp 1-65.

26. Södergård, A.; Stolt, M. *Prog. Polym. Sci* **2002**, *27(6)*, 1123-1163.

27. Wang, Y.; Mano, J. F. *J. Appl. Polym. Sci.* **2007**, *105*(6), 3500-3504.

28. Nurkhamidah, S.; Woo, E. M. *J. Appl. Polym. Sci.* **2011**, *122*(3), 1976-1985.

29. Wang, S.; Lu, L.; Gruetzmacher, J. A.; Currier, B. L.; Yaszemski, M. J. *Macromolecules* **2005**, *38*(17), 7358-7370.

30. Sun, G.; Chan, C. M. *Colloid. Polym. Sci.* **2013**, *291*(6), 1495-1501.

31. Leenslag, J. W.; Pennings, A. J. *Macromol. Chem. Phys.* **1987**, *188*(8), 1809-1814.

32. Vaudry, D.; Stork, P. J. S.; Lazarovici, P.; Eiden, L. E. *Science* **2002**, *296*(5573), 1648-1649.

33. Jamshidi, K.; Hyon, S. H.; Ikada, Y. *Polymer* **1988**, *29*(12), 2229-2234.

34. Greene, L. A.; Sobeih, M. M.; Teng, K. K. Methodologies for the culture and experimental use of the PC12 rat pheochromocytoma cell line. In *Culturing nerve cells*. MIT Press, **1991**; Cambridge, MA, pp 207-226.

35. Yavin, E.; Yavin, Z. *J. Cell Biol.* **1974**, *62*(2), 540-546.

36. McKeehan, W. L.; Ham, R. G. *J. Cell Biol.* **1976**, *71*(3), 727-734.

37. Colville, K.; Tompkins, N.; Rutenberg, A. D.; Jericho, M. H. *Langmuir* **2009**, *26*(4), 2639-2644.

38. Wu, X. 2013. Tuning cell fate on self-assembled structures. Doctoral dissertation. The University of Tennessee, Knoxville.

39. Crouch, A. S.; Miller, D.; Luebke, K. J.; Hu, W. *Biomaterials* **2009**, *30*, 1560-1567.

40. Wang, K.; Cai, L.; Zhang, L.; Dong, J.; Wang, S. *Adv. Healthcare Mater.* **2012**, *1*(3), 292-301.

41. Cai, L.; Zhang, L.; Dong, J.; Wang, S. *Langmuir* **2012**, *28*, 12557-12568.

Chapter X. Conclusions

To supply an extensive database of physical and chemical properties of poly(ε-caprolactone) acrylates (PCLAs), in this thesis, (1) the crosslinking efficiency and degradation of PCL triacrylates (PCLTAs) were studied, and I further investigated the regulation of cell behaviors by using PCLTAs with different crosslinking time, and different hydrolysis time. (2) To further improve the crosslink efficiency and gel fraction, 4arm and 6arm PCLAs were prepared, and microgrooved substrates were also fabricated by photo-crosslinking 4arm and 6arm PCLAs. Cell responses to these substrates and microgrooved structures were investigated. (3) 1,2-propanediol isobutyl polyhedral oligomeric silsesquioxane (POSS) was used as initiator to prepare POSS-PCL diacrylate (POSS-PCLDA) with different POSS contents. Both cardiovascular cell and nerve cell responses to the crosslinked POSS-PCLDAs were investigated.

To investigate the effect of crosslinking time on the polymer network properties and cellular behaviors, PCLAs with different molecular weights were crosslinked under UV light for time ranging from 1 to 60 min. The crosslinking efficiency of PCLA increased with decreasing the molecular weight and increasing crosslinking time could increase the gel fraction and network stiffness and decrease the swelling ratio. Primary rat aortic smooth muscle cell (SMC) attachment, proliferation, spreading, and focal adhesions all increased when the PCLTA molecular weight increased from 8k to 10k and then to 20k at the same crosslinking time. For the same PCLTA, SMC attachment, proliferation, spreading, and focal adhesions increased with increasing the crosslinking time, in particular, between the substrates crosslinked for less than 3 min and longer than 5 min.

Photo-crosslinked networks of PCLTA and methoxyl polyethylene glycol monoacrylate (mPEGA)/PCLTA with a weight fraction of mPEGA of 5% were degraded in sodium hydroxide (NaOH) aqueous solution at 37 °C via expedited hydrolysis for different time periods of 24, 48

and 60 h to obtain different surface topographies and roughnesses. Longer NaOH hydrolysis time resulted in rougher surfaces and lower water contact angles for both PCLTA and mPEGA/PCLTA networks. At all hydrolysis time periods, SMCs were found to have better attachment, proliferation, spreading, and focal adhesions on mPEGA/PCLTA networks than on PCLTA networks, as the addition of a small amount of mPEGA increased surface hydrophilicity without significantly decreasing the stiffness. For both PCLTA and mPEGA/PCLTA networks, longer NaOH hydrolysis time resulted in better SMC attachment, proliferation, spreading, and focal adhesions. I also found that the mPEGA/PCLTA network degraded faster and had higher water adsorption than the PCLTA network in both phosphate buffered saline (PBS) and NaOH aqueous solution. Both PCLTA and mPEGA/PCLTA networks could be fully degraded in NaOH solution in 40 days while they were quite stable in PBS for over 16 months with weight residue of higher than 80%, and the both networks remained high degrees of crystallinity (higher than 36.0%) during the degradation.

4arm and 6arm PCLAs with different molecular weights were synthesized through acrylation of PCL tetraols and hexanols, which were prepared via ring-opening polymerization of ε-caprolactone initiated with pentaerythritol and dipentaerythritol, respectively. The multi-arm PCLAs showed high photo-crosslinking efficiency and the resulted PCLA networks had gel fractions higher than 82%. By varying the molecular weight of PCLA, both amorphous and semi-crystalline PCLA networks were obtained. Photo-crosslinked 4arm and 6arm PCLAs with number-average molecular weights (M_ns) higher than 10000 g/mol and 13000 g/mol were semi-crystalline at physiological temperature, which showed distinct thermal and mechanical properties. Compared to amorphous PCLA networks, semi-crystalline PCLA networks had higher stiffness, rougher surface, lower hydrophilicity and lower protein adsorption. Among all the surface characteristics,

other than surface hydrophilicity and roughness, substrate stiffness was the main factor in promoting SMC attachment, proliferation, spreading, focal adhesions, and contractile gene expression.

To clarify how microgroove dimensions affected rat aortic SMC responses to microgrooved substrates of photo-crosslinked PCLAs, photo-cured PCLA substrates were fabricated with parallel microgrooves (two groove depths of 1 and 12 μm and two groove widths of 5 and 15 μm) using replica molding from micromachined silicon wafer templates. Most of the microgrooves did not affect SMC attachment and proliferation, while only on the microgrooved substrate with a groove depth of 12 μm and a groove width of 5 μm, cell proliferation decreased at days 2 and 4 post-seeding. The microgrooves on the substrates were found to decrease the area, regulate the shape, and generate alignment of SMC cytoskeleton. The SMC nuclei were elongated on 12-5 microgrooved substrates, and the distribution of SMC nuclei were mainly located in the grooves on 1-15, 12-15, and 12-5 microgrooved substrates. The SMCs on the microgrooved substrates did not show clear focal adhesions, but had higher contractile phenotypic gene expression levels than those on the flat substrates, especially when the groove depth was 12 μm. Both substrate stiffness and microgrooves were proved to promote SMC motility. All microgrooves regulated SMCs to migrate mainly along the groove direction. On the microgrooved substrate with a groove depth of 12 μm and a groove width of 5 μm, SMC migration speed decreased after the cells were trapped inside the microgrooves. In addition, different culture time periods and different microgroove dimensions had no effect on the SMC motility.

1,2-propanediol isobutyl POSS was used as the initiator to synthesize POSS-PCL diols with different molecular weights (also different POSS weight compositions, Φ_{POSS}) via ring-opening polymerization of ε-caprolactone. Then the POSS-PCL diols were further converted to photo-

crosslinkable POSS-PCLDAs via acrylation in the presence of K_2CO_3. POSS-PCLDAs with different POSS compositions were photo-crosslinked into networks with mechanical properties well controlled through the crystallinity and crosslinking density, both of which were determined by the molecular weight of PCL. Because of the steric hindrance induced by the bulky POSS nanocage in the center of POSS-PCLDA, the crystallinities of the photo-crosslinked networks were significantly suppressed. Networks of high-molecular-weight POSS-PCLDAs (M_n higher than 5170 g/mol, Φ_{POSS} smaller than 30%) were still semi-crystalline, while the ones prepared from low-molecular-weight POSS-PCLDAs were amorphous and demonstrated elastomeric characteristics at 37 °C. For example, a low elastic modulus of 1.3 MPa and a reversible strain as high as 400% were achieved when the M_n of POSS-PCLDA was 4650 g/mol (Φ_{POSS} = 32%). Semi-crystalline POSS-PCLDA networks better supported SMC attachment, proliferation, and focal adhesions than amorphous elastomeric POSS-PCLDA networks, while there was no significant difference in SMC behaviors on the latter. In contrast, amorphous elastomeric POSS-PCLDA networks significantly better supported rat pheochromocytoma (PC12) cell attachment, proliferation, and differentiation than semi-crystalline POSS-PCLDA networks. Flexible nerve conduit was fabricated using the elastomeric POSS-PCLDA, which showed uniform diameter and thickness.

The study of spherulites in regulating cell behaviors help us better understand cell-material interaction. The origin and mechanism of distinct cell responses to crystallization-induced surface characteristics was carefully studied. In this thesis, (1) the crystallization of PCL/ polyethylene glycol (PEG) blends on different substrates was studied, and the cell responses to the epitaxial crystallization, and different interfaces (free with air or confined with substrates) were studied. (2)

Both banded and nonbanded spherulites of poly(3-hydroxybutyrate) (PHB) were prepared, and the effects of PHB spherulite topographies and cracks on cell behaviors were studied. (3) Poly(L-lactic acid) (PLLA) homoblends were used to prepare spherulites with different morphologies, and the regulation of cell behaviors was studied.

PCL and its blends with 5% and 10% PEG were used to prepare crystallized polymer films on different substrates: glass, Si and polytetrafluoroethylene (PTFE). Both the free surface (the top surface exposed to air) and the confined surface (the bottom surface contacting the substrate) of the crystallized polymer films were studied in terms of roughness and hydrophilicity. Glass and Si substrates did not affect polymer crystallization, while PTFE could induce epitaxial crystallization that resulted in much smaller spherulites. Different surface morphologies, surface segregation of hydrophilic PEG, as well as the different interactions with air or substrates affected mouse pre-osteoblastic MC3T3-E1 cell responses to these polymer surfaces. Polymer surfaces with regular spherulites could support better MC3T3-E1 cell attachment, proliferation, and FAs than the surfaces with epitaxial crystals. Addition of PEG into PCL also improved MC3T3-E1 cell attachment, proliferation, and FAs. Free polymer surfaces on glass/Si substrates supported MC3T3-E1 cells better than the confined surfaces, while the two sides of the polymer films crystallized on the PTEF substrate did not differ much.

Banded spherulites with concentric alternating succession of ridges and valleys were observed on PHB films when they were isothermally crystallized at certain temperatures. Their thermal properties and surface morphology (spherulites and cracks) were examined. The melting temperatures and crystallinity degrees did not vary much, while the surface roughness of the spherulites was higher when crystallization temperature was higher. The number of attached SMCs and the proliferation rate were smaller on the rougher surfaces, and the highest values were on the

hot-compressed flat films. Although cracks were found on all the spherulitic PHB films, SMCs only had obvious alignment along the circular cracks. Roughness and cracks did not affect SMC nuclear localization and morphology.

Banded and non-banded spherulites were observed on drop-coated films of PLLA binary homoblends composed of high- and low-molecular-weight components when they were isothermally crystallized at certain temperatures. The spherulitic patterns showed strong dependence on the T_c, the blend composition, and the annealing process. PLLA films with Φ_{PLLA3k} of 30% were found to be able to have better banded structures, and were chosen to regulate cell behaviors. The surface roughness of these spherulites showed parabolic trend with the T_cs. The SMCs and MC3T3-E1 cells attachment and proliferation were better on the surfaces with less roughness. MC3T3-E1 cells showed alignment along the radial direction on non-banded spherulites. PLLA spherulites coated with poly(D-lysine) showed no significant effect on PC12 cell attachment, proliferation and differentiation. The nuclei of MC3T3-E1 cell and PC12 cell had distribution preference by showing more nuclei located in the valleys than on the ridges.

Vita

Jinbo Dou was born in Shandong, China. He attended Northwestern Polytechnical University, Xi'an, China from 2005-2012, where he received a B.S. degree in Chemical Engineering and Technology, and a Master degree in Chemical Technology. In the fall of 2012, he enrolled in the doctoral program and joined Prof. Shanfeng Wang's group in the Department of Materials Science and Engineering at the University of Tennessee, Knoxville. He received a Doctor of Philosophy degree in Materials Science and Engineering from the University of Tennessee in May 2017.